The Hadronic Vacuum Polarization Contribution to $(g-2)_\mu$ from Lattice QCD with Coordinate-Space Methods

Dissertation zur Erlangung des Grades
"Doktor der Naturwissenschaften“

am Fachbereich Physik, Mathematik, Informatik

JOHANNES GUTENBERG UNIVERSITÄT MAINZ

JG|U

vorgelegt von **Julian Valentino Parrino**
geboren in Frankfurt am Main

Betreuer: Harvey B. Meyer
Zweitgutachter: Stefan Weinzierl

Abgabe der Dissertation: 24. September 2024
Tag der Promotionsprüfung: 11. Dezember 2024

Abstract

Precision calculations are nowadays of central interest for the physics community. They serve on one hand as a test of the standard model and on the other hand as a window into the search for new physics. The anomalous magnetic moment of the muon a_μ has represented a puzzle for many years now. At the 0.20 ppm level of accuracy, the experimental measurement is in strong tension with the theoretical prediction. On the theory side, the main source of uncertainty is due to hadronic contributions, which cannot be evaluated perturbatively. The hadronic vacuum polarization (HVP) is the largest such contributions. To obtain this quantity, there are two methods: The dispersive approach, which relies on experimental input from e^+e^--scattering data and lattice QCD, as a framework to obtain hadronic observables from first principles. In recent years, the lattice community has made tremendous effort in order to reach sub-percent precision in the determination of the HVP contribution a_μ^{hvp}.

In this thesis, we want to investigate a covariant coordinate-space (CCS) approach for the calculation of a_μ^{hvp}, which has some advantages compared to the traditional time-momentum representation (TMR) used in the community. We develop a method for estimating finite-size effects in this new method based on a field theory approach. We present a full lattice calculation of the quark-connected light and strange component to the intermediate distance window quantity at an unphysical pion mass of $m_\pi = 350$ MeV. This calculation verifies the result obtained using the TMR method. We furthermore give a blueprint for computations of other observables in the CCS representation, especially with applications for very large lattices, which will become more relevant as computing resources become more powerful.

We then turn to the evaluation of isospin breaking corrections to a_μ^{hvp}. These need to be included in order to match the accuracy of the experimental measurement. We propose a scheme for regularizing the effects from quantum electrodynamics (QED) by introducing a Pauli-Villars regulator in the photon propagator. We present a calculation of one UV-finite diagram that constitutes a major part of the QED corrections to a_μ^{hvp}. This is performed on several ensembles with pion masses ranging from approximately 132 MeV to 422 MeV. We furthermore employ a calculation of the dominant charged pion and pseudoscalar meson contribution using an effective field theory approach to support the lattice calculation. We obtain a physical result for this partial contribution that can be seen as a benchmark quantity for the lattice calculation of QED corrections to the HVP contribution.

List of publications

The work presented in this thesis has led to the following peer-reviewed publications

1. Volodymyr Biloshytskyi, Antoine Gérardin, Jeremy R. Green, Franziska Hagelstein, Harvey B. Meyer, **Julian Parrino**, Vladimir Pascalutsa, "Forward light-by-light scattering and electromagnetic correction to hadronic vacuum polarization", JHEP 03 (2023) 194, arxiv:2209.02149 [hep-lat]

2. En-Hung Chao, Harvey B. Meyer, **Julian Parrino**, "Coordinate-space calculation of the window observable for the hadronic vacuum polarization contribution to $(g-2)_\mu$", Phys.Rev.D 107 (2023) 5, 054505, arxiv: 2211.15581 [hep-lat]

Several milestones of this thesis were presented at the Lattice conference in 2022, 2023 and 2024. Summaries of these presentation have been published in the following proceedings

1. En-Hung Chao, Harvey B. Meyer, **Julian Parrino**, "The $(g-2)$ intermediate window quantity from a coordinate-space method", PoS LATTICE2022, 326 (2022), DOI: 10.22323/1.430.0326

2. En-Hung Chao, Harvey B. Meyer, **Julian Parrino**, "Coordinate-space calculation of QED corrections to the hadronic vacuum polarization contribution to $(g-2)_\mu$", PoS LATTICE2023, arxiv:2310.20556 [hep-lat]

3. En-Hung Chao, Harvey B. Meyer, **Julian Parrino**, "Coordinate-space calculation of QED corrections to the
hadronic vacuum polarization contribution to $(g-2)_\mu$ with SU(3) flavor symmetry" EDJ Web of Conferences (to be published)

Contents

1 Motivation

"Every theoretical physicist who is any good knows six or seven different theoretical representations for exactly the same physics."

Richard Feynman[1]

In the modern era of precision calculations, Richard Feynman's quote is more relevant than ever. If two methods that both rely on the same physical principles do not agree on a final result there is something off. For the case of the anomalous magnetic moment of the muon, such a situation seems to arise nowadays. Determinations of this quantity have a long history, starting in the early twentieth century. But since 2006, the experimental measurement at BNL [1] with an accuracy of 0.54ppm is in tension with the theoretical prediction. This puzzle seems to turn now into a disagreement between two competing methods for the leading hadronic contribution, which dominates the uncertainty of the theory prediction currently. A major motivation for this thesis is to contribute to the understanding of this problem.

On the other hand, there are various examples, where a different viewpoint on a physical problem has led to new breakthroughs. Quantum field theories have their have their origin in the unification of classical field theory with quantum mechanics. The realization that classical electrodynamics exhibits a $U(1)$ gauge symmetry played a crucial role in the development of quantum electrodynamics (QED), which itself sparked the idea for non-abelian gauge theories by extending the symmetry group to more complicated Lie-group such as $SU(2) \times U(1)$ for the electroweak theory [2, 3]. It was now possible to describe the weak interaction that is responsible for β-decays in terms of interactions between fermions and the $W^{\pm}$ and Z^0 vector-bosons. These particles are expected to be massless, but measuring their energy signature in particle detectors one finds their masses to be $m_W = 80.377(12)$ GeV and $m_Z = 91.1876(21)$ GeV, which appears to contradict the formulation as a local gauge theory [2,3]. However, due to the interpretation of their rest mass as an effect of the interaction with the Higgs boson, the contradiction was resolved.

For the theoretical description of the strong interaction in the 1960s there were several competing theories. Today we know that the strong interaction on the fundamental level is described by a $SU(3)$ gauge theory that describes the interaction between several species of quarks and eight gluons, which

[1] The Character of Physical Law (MIT Press, 1965), p. 168.

we call quantum chromo dynamics (QCD) [4]. Another description of hadronic physics relies on pions as the force carrier particles, which has ultimately led to the development of chiral perturbation theory as a low energy effective theory of QCD, which has still many applications today [5]. Even string theory has its origin in the 1970s as a theory for the strong interaction and was picked up only many years later again as a candidate for a theory of everything [6].

The discovery of the Higgs particle in 2012 [7] completed the standard model (SM) of particle physics as it is today. However, it is clear that it is not the most fundamental theory of nature, as it fails to explain some well known phenomena. It assumes neutrinos to be massless, which in reality cannot be the case, since there is experimental evidence for neutrino oscillation [8–10]. It furthermore yields no explanation for the abundance of dark matter in the universe. And even gravity itself can not be described within the standard model due to the fact that we have not yet been able to find a consistent theory of quantum gravity.

Still, the standard model withstands some of the most extensive precision tests that have been made in the history of physics. The anomalous magnetic moment of the electron has been measured experimentally with a remarkable precision of 0.24 ppb [11, 12]. This is in full agreement with the theoretical calculation that has achieved a precision of 0.66 ppb [13, 14]. To this level of precision the uncertainty is dominated by the QED contribution that is calculated up to $O(\alpha^5)$ in the fine-structure constant α.

The anomalous magnetic moment of the muon is a different case. It has been a long standing puzzle that the measurement of its anomalous magnetic moment with a precision of 0.20 ppm [1,15,16] does not agree with the prediction from the standard model [17] up to 5.2σ. The fact the the muons mass is roughly 200 times larger than the electrons mass amplifies the contributions from the weak and strong interactions. Especially the effects from hadronic processes play a major role in understanding this tension, since these are the dominant source of error nowadays. In this thesis, we want to focus precisely on these hadronic contributions to the anomalous magnetic moment of the muon in order to examine if the tension between the standard model prediction and the measurement is due to our lack of understanding of hadronic effects. Or, if this tension is evidence for physics beyond the standard model.

1.1 The anomalous magnetic moment of the muon

The magnetic moment $\boldsymbol{\mu}$ of a particle with spin $\boldsymbol{S}$, charge q and mass m is given by [18]:

$$\boldsymbol{\mu} = g\frac{q}{2m}\boldsymbol{S}. \tag{1.1}$$

The proportionality factor g is called gyromagnetic ratio or Landè factor. Dirac's theory for fermions predicts a factor of $g = 2$. We denote any deviation from this for a given lepton $l = e, \mu, \tau$ by the

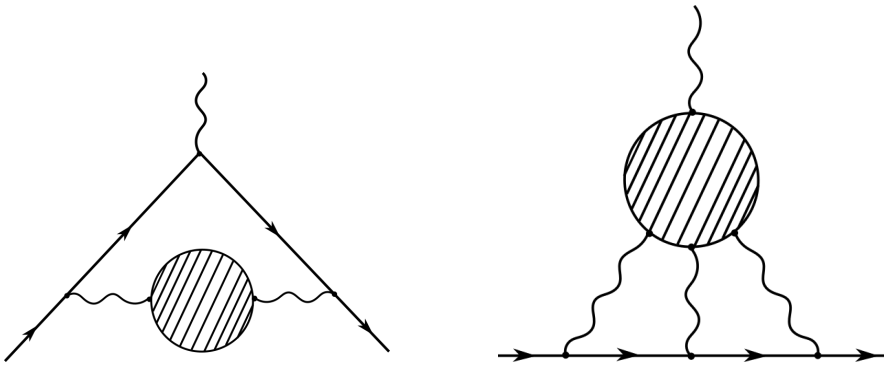

(a) Hadronic vacuum polarization **(b)** Hadronic light-by-light scattering

Figure 1.1: Leading hadronic contributions to the anomalous magnetic moment of the muon

anomalous magnetic moment

$$a_l = \frac{g_l - 2}{2}. \tag{1.2}$$

In the standard model (SM), the magnetic moment receives quantum corrections from QED, the electroweak (EW) and hadronic (had) interactions

$$a_l = a_l^{QED} + a_l^{EW} + a_l^{had}. \tag{1.3}$$

By far the largest contribution stems from QED corrections that can be treated by perturbation theory in the fine-structure constant α. The one-loop correction to the vertex was calculated first by Julian Schwinger (1948) [19]. It is universal for each lepton $l = e, \mu, \tau$ and given by [18]

$$a_l^{QED,1} = \frac{\alpha}{2\pi}. \tag{1.4}$$

Since then, QED corrections have been calculated up to $O(\alpha^5)$. These corrections dominate the error for the case of the electron's anomalous magnetic moment. With a precision of 0.66 ppb [13, 14] the result calculated within the SM is in perfect agreement with the experimental measurement that achieved a precision of 0.24 ppb [11, 12]. The anomalous magnetic moment of the muon is a different case [17]. In comparison to the electrons anomalous magnetic moment, quantum corrections from virtual particles, coupling to the photon are enhanced by a factor of $\left(\frac{m_\mu}{m_e}\right)^2 \sim 40000$ for a_μ. This leads to a drastic enhancement of the contributions from the weak and strong interaction. At the current level of precision of the experimental measurement of the muon's anomalous magnetic moment with 0.20 ppm [16], these interactions need to be taken into account carefully.

Electroweak corrections, like QED corrections, can be calculated with perturbation theory. Results exist up to two-loop order [17], see table 1.1. Hadronic contributions enter the a_μ only indirectly via their coupling to virtual photons. These corrections can not be treated perturbatively, since the anomalous magnetic moment is very sensitive to effects from small energies where the coupling of

Table 1.1: The different standard model contributions to the anomalous magnetic moment of the muon a_μ taken from the theory White Paper [17]. Since the publication of the White Paper in 2020 several new results from lattice QCD [21–29] and from dispersive calculations [30–33] have been published. A new experimental measurement of a_μ was conducted at Fermilab with first results published in Ref. [15, 16] agreeing with previous the experimental result given in the table [1].

Contribution	Value $\times 10^{11}$	References
Experiment	116 592 089(63)	Ref. [1]
HVP LO (e^+e^-)	6931(40)	Refs. [34–39]
HVP NLO (e^+e^-)	-98.3(7)	Ref. [39]
HVP NNLO (e^+e^-)	12.4(1)	Ref. [40]
HVP LO (lattice, udsc)	7116(184)	Refs. [41–49]
HLbL (phenomenology)	92(19)	Refs. [20, 50–61]
HLbL NLO (phenomenology)	2(1)	Ref. [62]
HLbL (lattice, uds)	79(35)	Ref. [63]
HLbL (phenomenology + lattice)	90(17)	Refs. [20, 50–61, 63]
QED	116 584 718.931(104)	Refs. [13, 64]
Electroweak	153.6(1.0)	Ref. [65, 66]
HVP (e^+e^-, LO + NLO + NNLO)	6845(40)	Refs. [34–40]
HLbL (phenomenology + lattice + NLO)	92(18)	Refs. [20, 50–63]
Total SM Value	116 591 810(43)	Refs. [13, 34–40, 50–56, 62–66]
Difference: $\Delta a_\mu := a_\mu^{exp} - a_\mu^{SM}$	279(76)	

the strong interaction α_s is large [20]. However, they can be classified by the order in the electromagnetic coupling α in which they appear. The largest hadronic contribution is the hadronic vacuum polarization (HVP), Fig. 1.1a, contributing at $O(\alpha^2)$. At the order $O(\alpha^3)$ the hadronic light-by-light scattering contribution, shown in Fig. 1.1b, is one of the hardest to compute. For these diagrams the hadronic "blob" has to be evaluated by non-perturbative means. Although by far the largest contribution to a_μ stems from QED corrections, the total uncertainty is completely dominated by the hadronic contributions, see table 1.1.

In 2020, the muon g-2 theory initiative published a result for a_μ [17] with similar precision that is in 5.0σ tension with the newest experimental measurement [16]. This tension could potentially be a hint for new physics. However, it is still an ongoing effort to narrow down the uncertainty from hadronic contributions.

Here, we see an interesting development in the field in the last few years. The traditional method to compute hadronic corrections, using a dispersive approach, relying on data from e^+e^- scattering experiments, shows a discrepancy to the calculation from first principles in lattice QCD [22]. In the spirit of Feynman's quote from the start one expects both methods to be perfectly consistent with each other. It is an ongoing effort in the community to resolve this tension and ultimately to explain the experimentally measured anomalous magnetic moment of the muon.

In this thesis, we want to focus on the calculation of the HVP contribution from lattice QCD. To this end, we will in many cases use results from chiral perturbation theory to support the lattice

calculation, for example in controlling finite-size effects or extrapolating results that are computed with unphysical pion masses to the physical point.

The chapters 2-5 can be seen as a general introduction relying mostly on material from introductory textbooks. In chapters 6-11 we will concentrate on the specific calculation of the HVP contribution. In chapter 6 we will review the dispersive framework, as well as the time-momentum representation, which is commonly used by lattice practitioners to obtain the HVP contribution to a_μ. Then, we will focus on the covariant coordinate-space (CCS) representation as a new framework to calculate a_μ^{hvp} in chapter 7. In this representation we will work out the calculation of finite-volume effects in chapter 8 and present results on the light and strange connected contribution to the intermediate window observable in chapter 9. We will then discuss the computation of isospin breaking corrections using the CCS method in 10 and present some preliminary results on a specific UV finite QED correction to the HVP contribution in chapter 11.

2 Euclidean quantum field theory

In this chapter, we want to establish the basic formalism that is used throughout this work, as well as review some key concepts such as the computation of correlation functions and Wick rotation. This introduction is based on the textbooks of Peskin & Schroeder [3], Weinberg [2] and Srednicki [67]. We assume that the reader is familiar with the basic concepts of quantum field theory, discussed in these sources. Some introductory parts are taken from the authors master's thesis [68]. Especially sections 2.1.2-2.2.1 and 2.4 show some overlap with Ref. [68].

2.1 Computing correlation functions

We are ultimately interested in the computation of expectation values of hermitian field operators $\hat{O}(x)$ depending on the coordinates x of the underlying spacetime manifold acting on the ground state $|\Omega\rangle$ of the theory in Hilbert space

$$\langle\Omega|\hat{O}(x)|\Omega\rangle = o(x), \tag{2.1}$$

where $\langle\cdot|\cdot\rangle$ is the inner product of that Hilbert space. The resulting real number $o(x)$ is a physical quantity that can in principle be compared with an experimental measurement. In this thesis, we will only discuss the case of flat spacetime. We will first write down the equations in Minkowski space with metric tensor $\eta = \text{diag}(1,-1,-1,-1)$ and work out the connection to the formulation in Euclidean space in section 2.2. We denote coordinates in Minkowski space by x_M.
Physical interactions are governed by the action functional

$$S[\Phi] = \int d^4x_M \mathscr{L}[\Phi(x_M)] \tag{2.2}$$

that depends on quantum fields $\Phi(x_M)$ [1], which themselves are functions of the spacetime coordinates x_M. The physical equations of motion are obtained by minimizing the action functional, while taking into account all symmetries of spacetime, i.e. the isometries of the Poincaré group, as well as the internal gauge symmetries of the Lagrangian density $\mathscr{L}$.

[1] We use the notation $\Phi(x_M)$ for a general quantum field content, not specifying under which irreducible representation of the Lorentz group it transforms (Scalar, Spinor, $\cdots$)

A systematic approach to the computation of correlation functions [2] is the path integral formalism, first used in the theory of statistical mechanics. We define the generating functional [3]

$$Z[\xi] = \int \mathscr{D}\Phi \exp\Big(i \int d^4x_M (\mathscr{L}[\Phi(x_M)] + \xi \hat{O}[\Phi(x_M)])\Big). \tag{2.3}$$

for a gauge invariant operator $\hat{O}[\Phi]$. The formal integral $\int \mathscr{D}\Phi$ sums over all possible field configurations. Using the functional derivative we can obtain n-point correlation functions of this operator by writing

$$\langle \Omega | T\{\hat{O}[\Phi(x_M)]\hat{O}[\Phi(y_M)](\ldots)\}|\Omega\rangle = Z[\xi]^{-1}\Big(-i\frac{\delta}{\delta\xi(x_M)}\Big)\Big(-i\frac{\delta}{\delta\xi(y_M)}\Big)\Big(\ldots\Big)Z[\xi]\Big|_{\xi=0}, \tag{2.4}$$

where T stands for the time-ordered product, defined as

$$T\{\hat{O}[\Phi(x_M)]\hat{O}[\Phi(y_M)]\} = \theta(x_0-y_0)\hat{O}[\Phi(x_M)]\hat{O}[\Phi(y_M)] + \theta(y_0-x_0)\hat{O}[\Phi(y_M)]\hat{O}[\Phi(x_M)]. \tag{2.5}$$

2.1.1 The free scalar propagator

At first we want to discuss the case of a free scalar field theory with the Klein-Gordon Lagrangian density

$$\mathscr{L} = \frac{1}{2}(\partial_\mu\phi)(\partial^\mu\phi) - \frac{m^2}{2}\phi^2. \tag{2.6}$$

Let us use the path integral formalism defined in Eq.2.4 to derive the expression for the time-ordered two-point function $\langle 0|T\{\phi(x_M)\phi(y_M)\}|0\rangle$ [67]. We define

$$S_\xi[\phi] = \int d^4x_M(\mathscr{L} + \xi\phi(x_M)) = \int d^4x_M\Big(\frac{1}{2}(\partial_\mu\phi(x_M))(\partial^\mu\phi(x_M)) - \frac{m^2}{2}(\phi(x_M))^2 + \xi\phi(x_M)\Big), \tag{2.7}$$

and use four-dimensional Fourier transformation

$$\widetilde{\phi}(p_M) = \int d^4x_M e^{-ip_Mx_M}\phi(x_M), \qquad \phi(x_M) = \int \frac{d^4p_M}{(2\pi)^4} e^{-ip_Mx_M}\widetilde{\phi}(p_M), \tag{2.8}$$

to rewrite the action as [67]

$$S_\xi[\widetilde{\phi}] = \frac{1}{2}\int \frac{d^4p_M}{(2\pi)^4}\Big(-\widetilde{\phi}(p_M)(p_M^2-m^2)\widetilde{\phi}(-p_M) + \widetilde{\xi}(p_M)\widetilde{\phi}(-p_M) + \widetilde{\xi}(-p_M)\widetilde{\phi}(p_M)\Big). \tag{2.9}$$

where $p_M^2 = p_0^2 - \boldsymbol{p}^2$. We use the notation $\widetilde{\cdot}$ for variables in momentum space. Now we apply the change of variables

$$\widetilde{\chi}(p_M) = \widetilde{\phi}(p_M) + \frac{\widetilde{\xi}(p_M)}{p_M^2 - m^2 + i\epsilon}, \tag{2.10}$$

[2] A correlation function is defined as an expectation value of multiple hermitian field operators

thus obtaining

$$S_\xi[\widetilde{\phi}] = \frac{1}{2}\int \frac{d^4p_M}{(2\pi)^4}\Big(\frac{\widetilde{\xi}(p_M)\widetilde{\xi}(-p_M)}{p_M^2 - m^2 + i\epsilon} + \widetilde{\chi}(p_M)(p_M^2 - m^2)\widetilde{\chi}(-p_M)\Big). \tag{2.11}$$

The $i\epsilon$ is necessary to regulate the p_M integral at the poles $p_0 = \pm\sqrt{\boldsymbol{p}^2 + m^2 - i\epsilon}$. We will consider the limit $\epsilon \to 0$ for terms that are not multiplying any pole contribution. We see now that the second term in Eq. 2.11 is not dependend on $\widetilde{\xi}$. This means that when we evaluate the generating functional Eq.2.3 this term will give us exactly $Z[0]$. For the first term of Eq. 2.11 we have

$$\frac{1}{2}\int \frac{d^4p_M}{(2\pi)^4}\Big(\frac{\widetilde{\xi}(p_M)\widetilde{\xi}(-p_M)}{p_M^2 - m^2 + i\epsilon}\Big) = \frac{1}{2}\int d^4x_M d^4x'_M \xi(x_M) G_m(x_M - x'_M)\xi(x'_M), \tag{2.12}$$

where we have defined

$$G_m(x_M - x'_M) = \int \frac{d^4p_M}{(2\pi)^4}\frac{i}{p_M^2 - m^2 + i\epsilon}e^{-ip_M(x_M - x'_M)}. \tag{2.13}$$

This yields for the generating functional

$$Z[\xi] = \exp\Big[\frac{i}{2}\int d^4x_M d^4x'_M \xi(x_M)G_m(x_M - x'_M)\xi(x'_M)\Big]Z[0]. \tag{2.14}$$

So, to achieve our goal we only need to calculate the functional derivative according to Eq. 2.4

$$\begin{aligned}
\langle 0|T\{\phi(x_M)\phi(y_M)\}|0\rangle &= Z[\xi]^{-1}\Big(-i\frac{\delta}{\delta\xi(x_M)}\Big)\Big(-i\frac{\delta}{\delta\xi(y_M)}\Big)Z[\xi]\Big|_{\xi=0} \\
&= Z[\xi]^{-1}\Big(-i\frac{\delta}{\delta\xi(x_M)}\Big)i\int d^4x'_M G_m(y_M - x'_M)\xi(x'_M)Z[\xi]\Big|_{\xi=0} \\
&= G_m(y_M - x_M).
\end{aligned} \tag{2.15}$$

The function $G_m(y_M - x_M)$ is known as the *Feynman propagator*. It turns out that the regularization prescription of using $+i\epsilon$ in the denominator of Eq.2.13 is exactly the right one in order to ensure time ordering of the field operators [3]. For a general n-point correlation function, we have [67]

$$\langle 0|T\{\phi(x_M^1)\dots\phi(x_M^{2n})\}|0\rangle = \sum_{\text{pairs}} G_m(x_M^{i_1} - x_M^{i_2})\dots G_m(x_M^{i_{2n-1}} - x_M^{i_{2n}}). \tag{2.16}$$

This result is known as *Wick's theorem*. Using Eq. 2.13, it is easy to check that the Feynman propagator is a Green´s function of the Klein-Gordon operator,

$$(\partial_\mu^{(x_M)}\partial^{(x_M)\mu} + m^2)G_m(x_M - y_M) = \delta^{(4)}(x_M - y_M). \tag{2.17}$$

It is furthermore possible to evaluate the integral in Eq. 2.13 explicitly. In Ref. [69] the authors derived a closed expression for one time and $D-1$ spatial dimensions. Using the parameter $\lambda = \frac{D}{2} - 1$, the

result reads

$$\begin{aligned} G_m^\lambda(x-y) &= \theta\Big((x-y)^2\Big)\frac{(-i)^{2\lambda+1}m^\lambda}{2^{\lambda+2}\pi^\lambda((x-y)^2-i\epsilon)^{\lambda/2}}H_\lambda^{(2)}\Big(m\sqrt{(x-y)^2-i\epsilon}\Big) \\ &\quad +\theta\Big(-(x-y)^2\Big)\frac{m^\lambda}{(2\pi)^{\lambda+1}(-(x-y)^2+i\epsilon)^{\lambda/2}}K_\lambda\Big(m\sqrt{-(x-y)^2+i\epsilon}\Big) \end{aligned} \tag{2.18}$$

where $H_\lambda^{(2)}(x)$ is the Hankel function of the second kind of order λ and $K_\lambda(x)$ is the modified Bessel function of the second kind of order λ. In this form we see that the position-space propagator has poles at $x^{(0)} = \pm\sqrt{(\boldsymbol{x})^2+i\epsilon}$. In $D = 3+1$ dimension the result reads

$$\begin{aligned} G_m(x-y) &= \theta\Big((x-y)^2\Big)\frac{(-i)m}{2^3\pi((x-y)^2-i\epsilon)^{1/2}}H_1^{(2)}\Big(m\sqrt{(x-y)^2-i\epsilon}\Big) \\ &\quad +\theta\Big(-(x-y)^2\Big)\frac{m}{(2\pi)^2(-(x-y)^2+i\epsilon)^{1/2}}K_1\Big(m\sqrt{-(x-y)^2+i\epsilon}\Big). \end{aligned} \tag{2.19}$$

2.1.2 The free fermionic propagator

Fermions are described by spinor fields ψ [3] with the Lagrangian density

$$\mathscr{L} = \overline{\psi}(i\partial_\mu\gamma^\mu - m)\psi \tag{2.20}$$

where $\overline{\psi} = \psi^\dagger\gamma^0$ and γ_μ are the Dirac gamma matrices that obey the relation

$$\{\gamma^\mu,\gamma^\nu\} := \gamma^\mu\gamma^\nu + \gamma^\nu\gamma^\mu = 2\eta^{\mu\nu} \tag{2.21}$$

These matrices are not unique. We stick to the convention of Peskin & Schroeder [3]. The gamma matrices in the chiral basis are

$$\gamma^\mu = \begin{pmatrix} 0 & \sigma^\mu \\ \overline{\sigma}^\mu & 0 \end{pmatrix}, \qquad \gamma^5 = \begin{pmatrix} -1 & 0 \\ 0 & 1 \end{pmatrix}, \qquad \sigma^\mu = (\mathbb{1}_{2\times2}, \boldsymbol{\sigma}), \qquad \overline{\sigma} = (\mathbb{1}_{2\times2}, -\boldsymbol{\sigma}), \tag{2.22}$$

where the Pauli matrices in the standard basis are

$$\sigma^1 = \begin{pmatrix} 0 & 1 \\ 1 & 0 \end{pmatrix}, \qquad \sigma^2 = \begin{pmatrix} 0 & -i \\ i & 0 \end{pmatrix}, \qquad \sigma^3 = \begin{pmatrix} 1 & 0 \\ 0 & -1 \end{pmatrix}. \tag{2.23}$$

The time-like γ_0 matrix is Hermitian, $\gamma_0^\dagger = \gamma_0$, and the space-like matrices γ_i for $i = 1,2,3$ are antihermitian, $\gamma_i^\dagger = -\gamma_i$.
Similar to Eq. 2.15 the fermionic Feynman propagator is

$$\begin{aligned} \langle 0|T\{\overline{\psi}(x_M)\psi(y_M)\}|0\rangle &= S_m(x_M - y_M) \\ &= \int\frac{d^4p}{(2\pi)^4}\frac{i(p_\mu\gamma^\mu+m)}{p^2-m^2+i\epsilon}e^{-ip_M(x_M-y_M)}. \end{aligned} \tag{2.24}$$

For a derivation we refer to the textbook by Srednicki [67]. From Eq. 2.24 we can immediately check that it is a Green's function of the Dirac Operator:

$$(-i\partial_\mu^{(x_M)}\gamma^\mu + m)S_m(x_M - y_M) = \delta(x_M - y_M) \tag{2.25}$$

and can be expressed through the scalar Feynman propagator, via the relation

$$S_m(x_M - y_M) = (i\partial_\mu^{(x_M)}\gamma^\mu + m)G_m(x_M - y_M). \tag{2.26}$$

For a general n-point correlator function we obtain

$$\langle 0|T\{\overline{\psi}(x_M^1)\psi(y_M^1)\dots\overline{\psi}(x_M^n)\psi(y_M^n)\}|0\rangle = \sum_{\sigma\in S_n} S_m(x_M^{\sigma(1)} - y_M^1)\dots S_m(x_M^{\sigma(n)} - y_M^n), \tag{2.27}$$

where S_n is the set of all possible permutations.

2.2 Wick rotation

In this section we want to describe the process connecting the observables calculated in Minkowski space to their counterpart in Euclidean spacetime. This process is called Wick rotation. In the physics literature [2, 3, 67] this is often written as a simple coordinate transformation

$$x^0 \to x_E^4 = -i\,x^0, \qquad x^j \to x_E^j = x^j \quad \text{for} \quad j = 1,2,3 \tag{2.28}$$

where we use the subscript E for the spacetime coordinates in euclidean space. This implies

$$x_\mu x^\mu = (x^{(0)})^2 - (x^{(1)})^2 - (x^{(2)})^2 - (x^{(3)})^2 = -(x_E^{(4)})^2 - (x_E^{(1)})^2 - (x_E^{(2)})^2 - (x_E^{(3)})^2 = -|\boldsymbol{x_E}|^2. \tag{2.29}$$

From the viewpoint of axiomatic quantum field theory, Wick rotation is an isometry between the Minkowski and Euclidean spacetime which are both embedded in a complex four dimensional manifold. The Osterwalder-Schrader theorem states the precise conditions under which this transformation is valid [70]. In the context of the Feynman propagator 2.13 the prescription of adding $+i\epsilon$ in the denominator corresponds to a specific choice of integration contour in the complex x_0 plane. The process of Wick rotation has to be performed in such a way that the contour is continuously transformed onto the axis of complex time, see Fig. 2.1a. The choice given in Eq. 2.28 satisfies this condition. However, the momentum coordinate needs to be rotated in the opposite direction,

$$p^0 \to p_E^4 = i\,p^0, \qquad p^j \to p_E^j = p^j \quad \text{for} \quad j = 1,2,3. \tag{2.30}$$

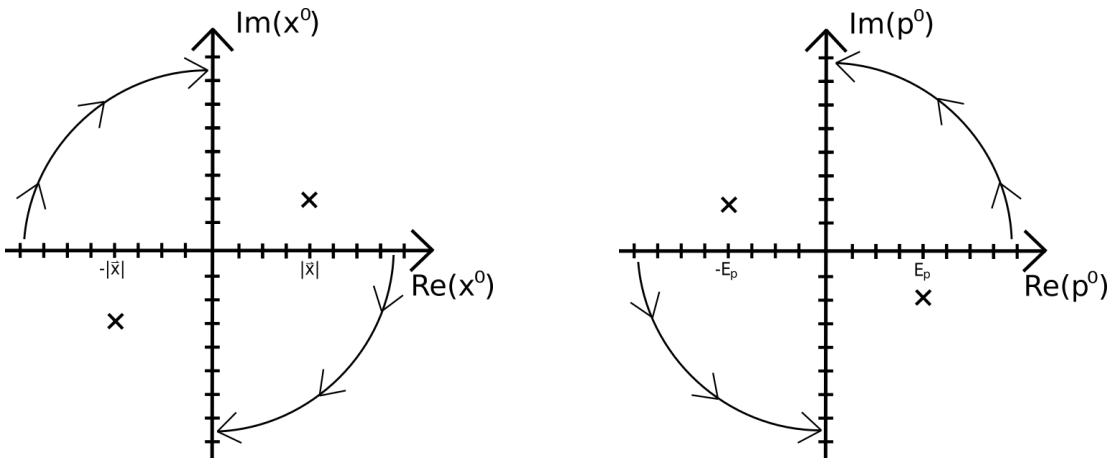

(a) x^0 in the complex plane **(b)** p^0 in the complex plane

Figure 2.1: Wick rotation in position (a) and momentum space (b). Singularities of the propagator are marked with an "x". This graphic is taken from Ref. [68].

2.2.1 The propagator in Euclidean space

Now, we are ready to evaluate the Euclidean form of the propagator. Recalling Eq. 2.13 and performing the Wick rotation,

$$\begin{aligned} G_m(x_E) &= i\int \frac{d^4p_E}{(2\pi)^4}\frac{i}{-p_E^2-m^2+i\epsilon}e^{-ip_E^4x_E^4+ip_E^1x_E^1+ip_E^2x_E^2+ip_E^3x_E^3} \\ &= \int \frac{d^4p_E}{(2\pi)^4}\frac{1}{p_E^2+m^2-i\epsilon}e^{ip_E\cdot x_E}, \end{aligned} \tag{2.31}$$

where we used the substitution $p_E^4 \to -p_E^4$ in the last step. A feature of this form is that the pole of the integrand is now located at $p_E^2 = -m^2$ and is not touched by the integration contour. So, the limit $\epsilon \to 0$ becomes trivial. In Euclidean space, one obtains for the propagator in $D = 2\lambda + 2$ dimensions, similar to the second term of Eq. 2.19 the result

$$G_m^\lambda(x_E) = \frac{m^\lambda}{(2\pi)^{\lambda+1}}\frac{K_\lambda(m|x_E|)}{|x_E|^\lambda}, \tag{2.32}$$

and for $D = 4$ we have

$$G_m(x_E) = \frac{m}{4\pi^2}\frac{K_1(m|x_E|)}{|x_E|}. \tag{2.33}$$

In the Euclidean formulation equation 2.17 reads:

$$(-\Delta^{(x_E)} + m^2)G_m^\lambda(x_E) = \delta^D(x_E), \tag{2.34}$$

where $\Delta^{(x_E)}$ is the D dimensional Laplacian Operator $\Delta^{(x_E)} = \sum_{j=1}^{D} \frac{\partial^2}{\partial (x_E^j)^2}$.
For the case of a massless scalar we can take the limit $m \to 0$. This yields

$$G_0^\lambda(x_E) = \frac{\Gamma(\lambda)}{4\pi^{\lambda+1}|x_E|^{2\lambda}}, \tag{2.35}$$

where $\Gamma(\lambda)$ is the Gamma function. For $D = 4$ this simplifies to

$$G_0(x_E) = \frac{1}{4\pi^2|x_E|^2}. \tag{2.36}$$

For the case of fermions we define the Euclidean γ matrices

$$\gamma^0 \to \gamma_E^0 = \gamma^0 \qquad \gamma^j \to \gamma_E^j = i\gamma^j \quad \text{for} \quad j = 1,2,3. \tag{2.37}$$

These Euclidean gamma matrices are all Hermitian and obey the anticommutation relation:

$$\{\gamma_E^\mu, \gamma_E^\nu\} := \gamma_E^\mu \gamma_E^\nu + \gamma_E^\nu \gamma_E^\mu = 2\delta^{\mu\nu}. \tag{2.38}$$

So, in the Euclidean formalism the fermionic propagator is a solution to the equation:

$$((x_E)_\mu \gamma_\mu + m) S_m(x_E) = \delta(x_E) \tag{2.39}$$

For a general spacetime dimension $D = 2\lambda + 2$ the result reads:

$$S_m^\lambda(x_E) = \frac{m^{\lambda+1}}{(2\pi)^{\lambda+1}} \Big((x_E)_\mu \gamma_\mu \frac{K_{\lambda+1}(m|x_E|)}{|x_E|^{\lambda+1}} + \frac{K_\lambda(m|x_E|)}{|x_E|^\lambda} \Big). \tag{2.40}$$

2.2.2 Euclidean path integral

The transformation described in section 2.2 can be applied to the very starting point of all our derivations, the generating functional 2.3. This defines the Euclidean generating functional

$$Z_E[\xi] = \int \mathscr{D}\Phi \exp\Big(- \int d^4 x_E (\mathscr{L} + \xi \hat{O}[\Phi(x_E)]) \Big). \tag{2.41}$$

$$= \int \mathscr{D}\Phi \exp\Big(- S_E[\Phi] + \int d^4 x_E \xi \hat{O}[\Phi(x_E)]) \Big) \tag{2.42}$$

This makes the connection with statistical mechanics immanent. The generating functional becomes a weighted integral with the Boltzmann factor $\exp(-S_E)$, which is real for a real action S_E. This can be utilized for Monte-Carlo methods and will be the key instrument for lattice QCD, which will be described in chapter 5.

In the following, we will only work in the Euclidean space formulation and thus drop the subscript E, $x := x_E$, $p := p_E$.

2.3 Scalar quantum electrodynamics

In this section we want to discuss an interacting field theory in the case of scalar quantum electrodynamics (sQED). The Lagrangian in Euclidean space is given by

$$\mathscr{L} = \frac{1}{4} F_{\mu\nu} F_{\mu\nu} + (D_\mu \phi)^\dagger (D_\mu \phi) + m^2 \phi^\dagger \phi, \tag{2.43}$$

where $D_\mu = \partial_\mu + ieA_\mu$ is the covariant derivative and $F_{\mu,\nu}$ is the electromagnetic field strength tensor defined as

$$F_{\mu\nu} = \partial_\mu A_\nu - \partial_\nu A_\mu, \tag{2.44}$$

m is the mass of the scalar particle, e is the electric charge of the scalar particle. The kinetic term can be expanded as:

$$(D_\mu \phi)^\dagger (D_\mu \phi) = (\partial_\mu \phi^\dagger - ieA_\mu \phi^\dagger)(\partial_\mu \phi + ieA_\mu \phi), \tag{2.45}$$

yielding a cubic interaction term $ieA_\mu((\partial_\mu \phi^\dagger)\phi - \phi^\dagger(\partial_\mu \phi))$ and a quartic interaction term $e^2 A_\mu A_\mu |\phi|^2$. If we apply a local $U(1)$ transformation to the scalar field,

$$\phi \to \phi e^{i\alpha(x)}, \qquad \phi^\dagger \to \phi^\dagger e^{-i\alpha(x)}, \tag{2.46}$$

the resulting additional terms due to the derivative ∂_μ acting on $\alpha(x)$ can be absorbed into a redefinition of the vector field

$$A_\mu \to A_\mu + \partial_\mu \alpha(x), \tag{2.47}$$

leaving the form of the Lagrangian, and thus the equations of motion, invariant. This is known as gauge invariance.

It is convenient to split the Lagrangian into three different parts

$$\mathscr{L} = \mathscr{L}_\phi + \mathscr{L}_A + \mathscr{L}_{\text{int}} \tag{2.48}$$

where $\mathscr{L}_\phi$ is the Lagrangian of the free complex scalar field, $\mathscr{L}_A$ the Lagrangian of the free photon and $\mathscr{L}_{\text{int}}$ the interaction term:

$$\mathscr{L}_\phi[\phi, \phi^\dagger] = (\partial_\mu \phi)^\dagger (\partial_\mu \phi) + m^2 |\phi|^2, \tag{2.49}$$

$$\mathscr{L}_A[A] = \frac{1}{4} F_{\mu\nu} F_{\mu\nu}, \tag{2.50}$$

$$\mathscr{L}_{\text{int}}[\phi, \phi^\dagger, A] = ieA_\mu((\partial_\mu \phi^\dagger)\phi - \phi^\dagger(\partial_\mu \phi)) + e^2 A_\mu A_\mu |\phi|^2. \tag{2.51}$$

To evaluate any Green's functions in the interacting theory with ground state $|\Omega\rangle$, which is different from the vacuum state $|0\rangle$, we first write down the Green's functions in the free theory. In section 2.1.1, we have already seen how to calculate correlation functions in the free theory by making use of the generating functional. When we only consider $\mathscr{L}_\phi[\phi,\phi^\dagger]$, the Feynman propagator for the scalar field in the free theory is derived similarly to Eq. 2.13,

$$\begin{aligned}\langle 0|T\{\phi(x)\phi^\dagger(y)\}|0\rangle &= G_m(x)\\ &= \frac{m}{4\pi^2}\frac{K_1(m|x-y|)}{|x-y|}.\end{aligned} \tag{2.52}$$

If we only consider the kinetic term for the vector boson $\mathscr{L}_A[A]$, we can derive the photon propagator in the free theory. However, the procedure described in section 2.1.1 can not simply be applied here. Gauge invariance of the photon leads to a divergence due to the fact that one is redundantly integrating over an infinite set of physical equivalent field configurations, resulting in a badly divergent integral [3]. Instead one can make use of the Fadeev-Popov procedure [3] to express a gauge fixing choice with the tunable parameter ξ. Following this procedure one obtains the photon propagator in Euclidean space

$$\langle 0|T\{A_\mu(x)A_\nu(y)\}|0\rangle = \int \frac{d^4p}{(2\pi)^4}\frac{e^{-ixp}}{p^2}\Big(\delta_{\mu\nu}-(1-\xi)\frac{p_\mu p_\nu}{p^2}\Big). \tag{2.53}$$

In Feynman gauge $\xi = 1$ the result in position space is simply given by

$$\langle 0|T\{A_\mu(x)A_\nu(y)\}|0\rangle = \delta_{\mu\nu}G_0(x) \tag{2.54}$$

$$= \frac{\delta_{\mu\nu}}{4\pi^2|x-y|^2}. \tag{2.55}$$

Now with the Green's functions of the free theory at hand, we can look at the interacting theory. The generating functional for any correlation function of the fields $[\phi,\phi^\dagger,A]$ is given by

$$Z[\xi,\xi',\alpha] = \int \mathscr{D}\phi\mathscr{D}\phi^\dagger\mathscr{D}A\exp\Big(-\int d^4x\mathscr{L}_\phi[\phi,\phi^\dagger]+\mathscr{L}_A[A]+\mathscr{L}_{\text{int}}[\phi,\phi^\dagger,A]+\xi\phi+\xi'\phi+\alpha_\mu A_\mu\Big). \tag{2.56}$$

Now, we can express all dependencies of the fields in the interaction Lagrangian by functional derivatives with respect to the corrresponding parameters ξ,ξ',α:

$$\begin{aligned}Z[\xi,\xi',\alpha] &= e^{\left(-\int d^4x\mathscr{L}_{\text{int}}\left[-\frac{\delta}{\delta\xi},-\frac{\delta}{\delta\xi'},-\frac{\delta}{\delta\alpha_\mu}\right]\right)}\int\mathscr{D}\phi\mathscr{D}\phi^\dagger\mathscr{D}A\exp\Big(-\int d^4x\mathscr{L}_\phi[\phi,\phi^\dagger]\\ &\qquad +\mathscr{L}_A[A]+\xi\phi+\xi'\phi+\alpha_\mu A_\mu\Big)\\ &= e^{\left(-\int d^4x\mathscr{L}_{\text{int}}\left[-\frac{\delta}{\delta\xi},-\frac{\delta}{\delta\xi'},-\frac{\delta}{\delta\alpha_\mu}\right]\right)}Z_0[\xi,\xi',\alpha]\end{aligned} \tag{2.57}$$

where $Z_0[\xi,\xi',\alpha]$ is the generating functional of the free theory. Making use of Eq. 2.14 this can be

rewritten as

$$Z_0[\xi,\xi',\alpha] = Z[0,0,0]\exp\Big[\frac{i}{2}\int d^4x d^4x'\xi(x)G_m(x-x')\xi'(x') + \alpha_\mu(x)\cdots\Big], \tag{2.58}$$

where we have not written the term for the photon propagator explicitly. One would need to apply the Fadeev-Popov procedure here as well, to obtain a meaningful photon propagator. The crucial point in Eq.2.57 is that we have expressed the generating functional of the interacting theory through functional derivatives acting on the generating functional of the free theory.

Expression 2.57 is well suited for applying perturbation theory. We can write down the Taylor expansion of the first exponential function of Eq. 2.57 in powers of e,

$$\begin{aligned} e^{\left(-\int d^4x \mathscr{L}_{\rm int}\left[-\frac{\delta}{\delta\xi},-\frac{\delta}{\delta\xi'},-\frac{\delta}{\delta\alpha_\mu}\right]\right)} &= \sum_{n=0}^{\infty}\frac{1}{n!}\Big[-e\int d^4x\frac{\delta}{\delta\alpha_\mu(x)}\Big(\frac{\delta}{\delta\xi(x)}\partial_\mu^{(x)}\frac{\delta}{\delta\xi'(x)} - \frac{\delta}{\delta\xi'(x)}\partial_\mu^{(x)}\frac{\delta}{\delta\xi(x)}\Big)\Big]^n \\ &= \sum_{j=0}^{\infty}\frac{1}{j!}\Big[e^2\int d^4x'\frac{\delta}{\delta\alpha_\mu(x')}\frac{\delta}{\delta\alpha_\mu(x')}\frac{\delta}{\delta\xi(x')}\frac{\delta}{\delta\xi'(x)}\Big]^j. \end{aligned} \tag{2.59}$$

Under the condition that the electromagnetic coupling e is small, the sums over n and j do converge. This means that up to a given order in e we can express Eq. 2.59 by a finite number of terms. For the total generating functional of the interacting theory, Eq. 2.57, we have to take into account that the functional derivatives in Eq.2.59 are acting on the free Lagrangian. We can now apply our master formula, Eq. 2.4, to obtain any correlation function of the fields ϕ, $\phi^\dagger$, A_μ up to a given order in e. Although this is challenging , it can be done in a purely systematic way by the use of Feynman diagrams.

2.3.1 Feynman rules in position space

Any correlation function $\langle\Omega|T\{\Phi_x(x)\Phi_y(y)(\ldots)\}|\Omega\rangle$, where Φ_x is any field ϕ, $\phi^\dagger$, A_μ evaluated at the source x, can be expressed in perturbation theory up to a given order in e as a sum of all amputated Feynman diagram with connected propagator lines between all sources $x, y, \ldots$ [67]. Each Feynman diagram is composed of simple building blocks [3].

1. The scalar propagator

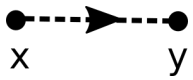

$$= \qquad G_m(x-y) \tag{2.60}$$

2. The photon propagator in Feynman gauge

$$= \qquad \delta_{\mu\nu}G_0(x-y) \tag{2.61}$$

3. The 3 Vertex

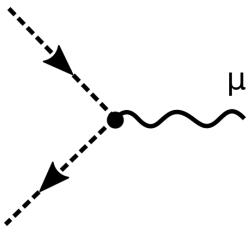

$$= \quad e\int d^4z([\partial_\mu^{(z)}]^{(\text{in})} + [\partial_\mu^{(z)}]^{(\text{out})}) \tag{2.62}$$

4. The 4 Vertex

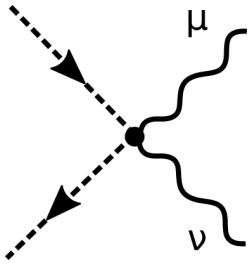

$$= \quad 2e^2\delta_{\mu\nu}\int d^4z \tag{2.63}$$

The expression $[\partial_\mu^{(z)}]^{(\text{in/out})}$ means that the derivative is only acting on the incoming/outgoing scalar propagator. When writing down the generating functional, Eq. 2.57, and using Eq. 2.59, this generates some equivalent terms. To account for that one needs to divide each Feynman diagram by a corresponding symmetry factor [3].

2.3.2 Renormalization

In Eq. 2.43 we have written down a Lagrangian for scalar QED by adding an interaction term to the Lagrangian of the free theory. From this we were able to calculate correlation functions of the interacting theory using Feynman diagrams. However, it turns out that for this naive Lagrangian the parameter for the mass does not mean the same thing as in the free case anymore. In the case of the free scalar field the pole of the Feynman propagator in Euclidean momentum space 2.13 is located at $p^2 = -m^2$. In the Källén-Lehmann spectral representation of the two-point function of a general QFT the complex poles on the euclidean space energy axis correspond to 1-particles states [3]. The mass of these states is exactly the value of the corresponding pole.

If we write down the two-point function of the interacting theory in terms of Feynman diagrams

$\langle\Omega|\phi(x)\phi^\dagger(y)|\Omega\rangle =$ 

(2.64)

the additional terms lead to a shift of the pole. So, the actual mass of the 1-particle state is different than the bare mass parameter that we used in the Lagrangian Eq. 2.43. This means that in an interacting field theory the scales of the theory, in our case the mass of the scalar particle, arise dynamically from the underlying interactions and cannot just be set in the bare Lagrangian 2.43. In order to

make a connection between the dynamic scale parameter and the experimental value for the mass of the scalar particle we need to make use of the process of renormalization. In fact, the contribution from loop-diagrams to the two-point function is formally infinite, but also in a theory where all loop contributions are finite, we still would need to renormalize [67]. The process of renormalization can be seen as a simple redefinition of the bare parameters of the Lagrangian in terms of new quantities that are now physically meaningful,

$$A_\mu^{\text{ren}} = \sqrt{Z_3} A_\mu, \quad \phi^{\text{ren}} = \sqrt{Z_2}\phi, \qquad e^{\text{ren}} = Z_e e, \qquad m^{\text{ren}} = Z_m m. \tag{2.65}$$

The renormalization coefficients Z_i have to be calculated from the dynamical interactions of the theory. Typically one writes $Z_i = 1 + \delta_i$. Introducing the δ_i terms in the Lagrangian leads to new interaction vertices with coupling coefficients proportional to δ_i [3]. These new terms are called counterterms. They need to be taken into account when writing down all Feynman diagrams to a given order in perturbation theory. For our example in Eq. 2.64 one would need to take a counterterm into account that renormalizes the one-loop contributions. Since these loop contributions are divergent one needs to choose a regularization scheme, such as dimensional regularization or Pauli-Villars regularization [3].

After calculating the loop contribution at a given order in perturbation theory one fixes the value of the δ_i coefficients of the counterterms by imposing physical constraints. A set of constraints is called renormalization scheme. There are different schemes used in the literature, for example the $\overline{MS}$, or the on-shell scheme [3]. Physical observables are independent of the renormalization scheme, but correlation functions may be scheme dependent. For a renormalizable theory, as it is for scalar QED, only a finite number of diagrams to each given order in the coupling constant need to be calculated in order to fully determine all renormalized correlation functions to that order.

2.4 Gegenbauer polynomial method

Most computational applications of perturbation theory rely on the momentum-space formulation of the Feynman rules, due to the simple form of the euclidean propagator $\frac{1}{p^2+m^2}$. Since the early formulations of QFT, tremendous achievements have been accomplished for the evaluation of loop diagrams in momentum-space. Nowadays, there are several computer tools for such calculation, for example the package FeynCalc [71]. As for calculations in coordinate-space, only little effort has been made in developing more advanced computational techniques. Here, one has to mention the early works of Chetyrkin, Kataev and Tkachov [72] and Kotikov [73], [74]. In their work they used the so called Gegenbauer polynomial method, which we want to review in this section.

The scalar propagator in $D = 2\lambda + 2$ dimensions, $G_m^\lambda(x-y)$, can be expressed as a series of orthog-

onal Gegenbauer polynomials $C_k^\lambda(\hat{x}\cdot\hat{y})$ [68]:

$$G_m^\lambda(x-y) = \sum_{k=0}^{\infty} \gamma_k^{\lambda,m}(|x|,|y|) C_k^\lambda(\hat{x}\cdot\hat{y}), \tag{2.66}$$

with coefficients depending only on the absolute value of x and y

$$\begin{aligned}\gamma_k^{\lambda,m}(|x|,|y|) &= \frac{\lambda+k}{\lambda S_{2\lambda+1}|x|^\lambda|y|^\lambda}\Big[\theta(|x|-|y|)I_{\lambda+k}(m|y|)K_{\lambda+k}(m|x|) \\ &\quad +\theta(|y|-|x|)K_{\lambda+k}(m|y|)I_{\lambda+k}(m|x|)\Big]\end{aligned} \tag{2.67}$$

where $\theta(|x|)$ is the Heaviside function. The coefficients $\gamma_k^{\lambda,m}(|x|,|y|)$ are continuous everywhere, but not differentiable at $|x|=|y|$. The Gegenbauer polynomials are defined by the generating functional

$$\frac{1}{(1-2ut+t^2)^\lambda} = \sum_{n=0} C_n^\lambda(u)\, t^n, \tag{2.68}$$

and obey the orthogonality relation

$$\int_{-1}^{1} du(1-u^2)^{\lambda-\frac{1}{2}} C_k^\lambda(u) C_l^\lambda(u) = \delta_{lk}\frac{\pi 2^{1-2\lambda}\Gamma(l+2\lambda)}{k!(k+\lambda)\Gamma(\lambda)^2}, \tag{2.69}$$

where $(1-u^2)^{\lambda-\frac{1}{2}}$ is a weight function. It can be shown that by rewriting this weight function in terms of the $D-1$ surface element of spherical coordinates in D dimensions and using Eq. 2.69 one obtains the relation for the $D-1$ dimensional angular integral

$$\int_{S^{D-1}} d\Omega_x^{D-1} C_k^\lambda(\hat{x}\cdot\hat{y}) C_l^\lambda(\hat{x}\cdot\hat{z}) = S_{D-1}\delta_{kl}\frac{\lambda}{\lambda+k} C_k^\lambda(\hat{y}\cdot\hat{z}), \tag{2.70}$$

where $d\Omega_x^{D-1}$ is the spherical surface element and S_{D-1} is the volume of the unit sphere

$$S_{D-1} := \int_{S^{D-1}} d\Omega_x^{D-1} = \frac{2\pi^{\frac{D}{2}}}{\Gamma(\frac{D}{2})}. \tag{2.71}$$

The Gegenbauer polynomial of arbitrary order n can be calculated using the recurrence relation

$$C_0^\lambda(x) = 1, \tag{2.72}$$

$$C_1^\lambda(x) = 2\lambda x, \tag{2.73}$$

$$C_n^\lambda(x) = \frac{1}{n}\Big[2x(\lambda+n-1)C_{n-1}^\lambda(x) - (2\lambda+n-2)C_{n-2}^\lambda(x)\Big]. \tag{2.74}$$

By making use of the orthogonality relation of the Gegenbauer polynomials 2.70, one can often easily simplify integrals of vertices connecting multiple propagators. In a theory with a vertex connecting

three propagators, such as spinor or scalar QED one typically encounters the integral

$$B(x,y) = \int d^D z G^{\lambda}_{m_1}(x-z) G^{\lambda}_{m_2}(y-z) G^{\lambda}_{m_3}(z). \tag{2.75}$$

By expressing the first and second propagator in terms of Gegenbauer polynomials we can simplify the angular integral

$$\begin{aligned} B(x,y) &= \sum_{k,l\geq 0} \int_z \gamma^{\lambda,m_1}_k(|x|,|z|)\gamma^{\lambda,m_2}_l(|y|,|z|) C^{\lambda}_k(\hat{x}\cdot\hat{z}) C^{\lambda}_l(\hat{y}\cdot\hat{z}) G_{m_3}(z) \\ &= \sum_{k\geq 0} C^{\lambda}_k(\hat{x}\cdot\hat{y}) \frac{\lambda}{\lambda+k} S_{D-1} \int_0^{\infty} d|z||z|^{2\lambda+1} \gamma^{\lambda,m_1}_k(|x|,|z|)\gamma^{\lambda,m_2}_k(|y|,|z|) G_{m_3}(z) \\ &= \sum_{k\geq 0} C_k(\hat{x}\cdot\hat{y})\beta_k(|x|,|y|). \end{aligned} \tag{2.76}$$

$B(x,y)$ can be written as an expansion in Gegenbauer polynomials with coefficients:

$$\begin{aligned} \beta_k(|x|,|y|) = \frac{(\lambda+k)m_3^{\lambda}}{(2\pi)^{\lambda+1}\lambda S_{D-1}|x|^{\lambda}|y|^{\lambda}} \Big[& \theta(|y|-|x|)\Big(I_{\lambda+k}(m_1|x|) I_{\lambda+k}(m_2|y|)\beta^{(1)}_k(|y|) \\ & + K_{\lambda+k}(m_1|x|)K_{\lambda+k}(m_2|y|)\beta^{(2)}_k(|x|) + I_{\lambda+k}(m_1|x|)K_{\lambda+k}(m_2|y|)\beta^{(3)}_k(m_1,m_2,|x|,|y|)\Big) \\ & + \theta(|x|-|y|)\Big(I_{\lambda+k}(m_1|x|) I_{\lambda+k}(m_2|y|)\beta^{(1)}_k(|x|) + K_{\lambda+k}(m_1|x|)K_{\lambda+k}(m_2|y|)\beta^{(2)}_k(|y|) \\ & + K_{\lambda+k}(m_1|x|) I_{\lambda+k}(m_2|y|)\beta^{(3)}_k(m_2,m_1,|y|,|x|)\Big)\Big], \end{aligned} \tag{2.77}$$

where one needs to evaluate the integrals

$$\beta^{(1)}_k(|u|) = \int_u^{\infty} d|z||z|^{-\lambda+1} K_{\lambda}(m_3|z|) K_{(\lambda+k)}(m_1|z|) K_{(\lambda+k)}(m_2|z|), \tag{2.78}$$

$$\beta^{(2)}_k(|u|) = \int_0^{u} d|z||z|^{-\lambda+1} K_{\lambda}(m_3|z|) I_{(\lambda+k)}(m_1|z|) I_{(\lambda+k)}(m_2|z|), \tag{2.79}$$

$$\beta^{(3)}_k(m_1,m_2,|u|,|v|) = \int_u^{v} d|z||z|^{-\lambda+1} K_{\lambda}(m_3|z|) K_{(\lambda+k)}(m_1|z|) I_{(\lambda+k)}(m_2|z|). \tag{2.80}$$

Here, we have only written the mass dependence explicitly in Eq. 2.80, where it is necessary in order to define Eq. 2.77 properly. For the full result of the four-dimensional integral in Eq. 2.75, one only needs to evaluate one dimensional integrals over Bessel functions. For our example, the result is finite in $D = 4$ dimensions for $|x| \neq |y|, |y| \neq 0, |x| \neq 0$. But, in general one needs to be cautious when evaluating loop integrals, because of occuring divergences. However, it can be shown that these divergences can be treated in a systematic way by using the ϵ expansion similar to the momentum-space case [68].

Lastly, we want to mention that certain classes of diagrams, such as sunrise diagrams are much easier to evaluate with coordinate-space methods [75], [76], especially in a theory that includes vertices that connect a large number of propagators.

3 Quantum chromo dynamics

In this chapter, we give a brief introduction to Quantum Chromodynamics (QCD), the theory of the strong interaction, describing the interactions between quarks and gluons. The chapter is based on the introductions to the topic by Peskin & Schroeder [3], Srednicki [67], Weinberg [2], Skads [77], Gattringer & Lang [78], Mangano [79]. The layout of this chapter is losely inspired by the PhD theses [80], [81] and [82].

3.1 SU(3)

The mathematical framework of QCD is built on the concept of non-Abelian gauge theory. In the case of scalar QED we have seen that the Lagrangian is invariant under a local U(1) transformation of the fields 2.46. For QCD the symmetry group is SU(3), which is a simply-connected eight-dimensional compact Lie group. This means that it is also a differentiable manifold, defined as

$$SU(3) := \left\{ \Omega \in GL(3,\mathbb{C}) \middle| \Omega^\dagger \Omega = \mathbb{1}, \quad \det(\Omega) = 1 \right\}. \tag{3.1}$$

The Lie group SU(3) gives rise to the Lie algebra $\mathfrak{su}(3)$, which can be understood as the tangent space of SU(3) at the identity [83]. The Lie algebra $\mathfrak{su}(3)$ is a vector-space together with the Lie bracket, which is an alternating bilinear map satisfying the Jacobi identitiy. A representation of $\mathfrak{su}(3)$ is given by the eight generators

$$T^a = \frac{1}{2}\lambda^a \qquad (a = 1,2,\dots 8), \tag{3.2}$$

where λ^a are the traceless hermitian Gell-Mann matrices

$$\lambda^1 = \begin{pmatrix} 0 & 1 & 0 \\ 1 & 0 & 0 \\ 0 & 0 & 0 \end{pmatrix}, \quad \lambda^2 = \begin{pmatrix} 0 & -i & 0 \\ i & 0 & 0 \\ 0 & 0 & 0 \end{pmatrix}, \quad \lambda^3 = \begin{pmatrix} 1 & 0 & 0 \\ 0 & -1 & 0 \\ 0 & 0 & 0 \end{pmatrix},$$

$$\lambda^4 = \begin{pmatrix} 0 & 0 & 1 \\ 0 & 0 & 0 \\ 1 & 0 & 0 \end{pmatrix}, \quad \lambda^5 = \begin{pmatrix} 0 & 0 & -i \\ 0 & 0 & 0 \\ i & 0 & 0 \end{pmatrix}, \quad \lambda^6 = \begin{pmatrix} 0 & 0 & 0 \\ 0 & 0 & 1 \\ 0 & 1 & 0 \end{pmatrix},$$

$$\lambda^7 = \begin{pmatrix} 0 & 0 & 0 \\ 0 & 0 & -i \\ 0 & i & 0 \end{pmatrix}, \quad \lambda^8 = \begin{pmatrix} \frac{1}{\sqrt{3}} & 0 & 0 \\ 0 & \frac{1}{\sqrt{3}} & 0 \\ 0 & 0 & -\frac{2}{\sqrt{3}} \end{pmatrix}.$$

Defining the commutator [.,.] as

$$[A, B] = AB - BA \tag{3.3}$$

these matrices satisfy the relations

$$[\lambda^a, \lambda^b] = 2if^{abc}\lambda^c \tag{3.4}$$

where f^{abc} are the structure constants of $\mathfrak{su}(3)$

$$f^{123} = 1 \tag{3.5}$$

$$f^{147} = -f^{156} = f^{246} = f^{257} = f^{345} = -f^{367} = \frac{1}{2} \tag{3.6}$$

$$f^{458} = f^{678} = \frac{\sqrt{3}}{2}, \tag{3.7}$$

The elements of the Lie algebra are connected to those of the Lie group via the exponential map. Every element of $SU(3)$ can be expressed through the generators of $\mathfrak{su}(3)$ by

$$\Omega(x) = \exp\left(i\theta^a(x)T^a\right). \tag{3.8}$$

where $\theta^a(x)$ are eight real valued functions depending on x.

3.2 QCD Lagrangian

The QCD Lagrangian contains the quark field. Since these are fermions, they are described by spinor fields ψ, which we introduced in section 2.1.2. These spinors have four Dirac components, which we do not write explicitly. With respect to the action of the SU(3) group, ψ_a transforms in the three-dimensional fundamental representation of SU(3). This means that they also carry a color index $a = (R, G, B)$[1]. The anti-fermion $\overline{\psi}_a$ transforms in the anti-fundamental representation which is not equivalent to the fundamental representation. We denote this by $\overline{\psi}_a$ carrying anti-color indices $a = (\overline{R}, \overline{G}, \overline{B})$[2] The transformation for the spinor and anti-spinor are

$$\psi_a(x) \to \Omega_{a,b}(x)\psi_b(x), \qquad \overline{\psi}_a(x) \to \overline{\psi}_b\Omega^\dagger_{b,a}(x). \tag{3.9}$$

[1] (red,green,blue)
[2] (anti-red,anti-green,anti-blue)

The interaction between quarks is governed by the eight ($a = 1,2,\ldots,8$) gluon fields [3] $\mathscr{A}_\mu^a$. We define $\mathscr{A}_\mu := \sum_{a=1}^{8} \mathscr{A}_\mu^a T^a$. These are massless vector bosons transforming in the adjoint representation of SU(3) according to

$$\mathscr{A}_\mu(x) \to \Omega(x)\mathscr{A}_\mu(x)\Omega^\dagger(x) + \frac{i}{g_s}(\partial_\mu\Omega(x))\Omega^\dagger(x), \tag{3.10}$$

where g_s is the strong coupling constant. One often expresses the strong coupling through $\alpha_s = \frac{g_s^2}{4\pi}$ analog to the electromagnetic finestructure constant $\alpha = \frac{e^2}{4\pi}$. The $SU(3)$ invariant QCD Lagrangian is given by

$$\mathscr{L}_{\text{QCD}} = \frac{1}{2}\text{Tr}(G_{\mu\nu}G_{\mu\nu}) + \sum_{f=u,d,s,c,b,t} \overline{\psi}_f(\gamma_\mu D_\mu + M_f)\psi_f, \tag{3.11}$$

where the field strength tensor $G_{\mu\nu}$ is defined by

$$G_{\mu\nu} = \partial_\mu\mathscr{A}_\nu - \partial_\nu\mathscr{A}_\mu + ig_s[\mathscr{A}_\mu, \mathscr{A}_\nu]. \tag{3.12}$$

This field strength tensor is analogous to the field strength tensor of the photon 2.44 except for the last term, which vanishes in case of an Abelian gauge theory. The covariant derivative is given by $D_\mu = \partial_\mu - ig_s\mathscr{A}_\mu^a T^a$, where T^a are the generators of $\mathfrak{su}(3)$ defined in Eq. 3.2. The sum in Eq. 3.11 takes into account all six different quark flavours $f = (u,d,s,c,b,t)$.

3.3 Chiral symmetry

In the case where the quarks are massless, there is an additional global symmetry [84] [85]

$$SU(N_f)_L \times SU(N_f)_R, \tag{3.13}$$

where N_f is the number of quark flavours. R and L denote the left-handed and right-handed component of the Dirac spinor. These can be obtained by using the projectors

$$\psi_L = \frac{\mathbb{1}-\gamma_5}{2}\psi, \qquad \psi_R = \frac{\mathbb{1}+\gamma_5}{2}\psi. \tag{3.14}$$

The massless Lagrangian is invariant under the chiral transformation

$$\psi_{R/L} \to \exp(i\theta_i\gamma_5\tilde{T}_i)\psi_{R/L}, \qquad \overline{\psi}_{R/L} \to \overline{\psi}_{R/L}\exp(-i\theta_i\gamma_5\tilde{T}_i), \tag{3.15}$$

where $\tilde{T}_i$ are the $N_f^2 - 1$ generators of $\mathfrak{su}(N_f)$. However, the ground state of massless QCD is not invariant under chiral transformation. This means that the $SU(N_f)_L \times SU(N_f)_R$ is spontaneously

[3] We write the gluon field with a caligraphic $\mathscr{A}_\mu$, so that we not confuse it with the photon A_μ

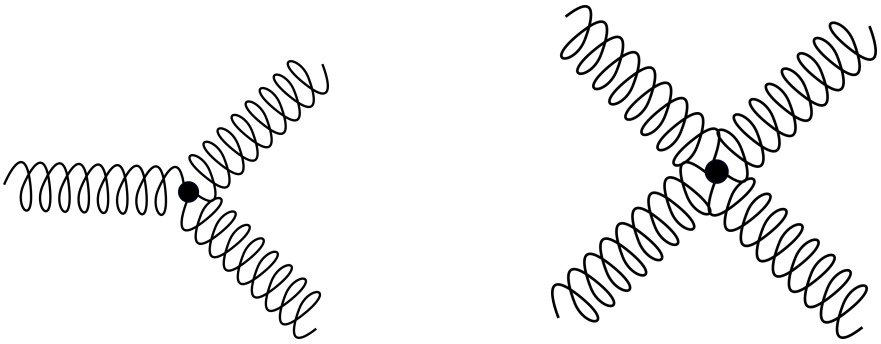

(a) 3-gluon vertex **(b)** 4-gluon vertex

Figure 3.1: Gluon self interaction vertices that appear in perturbative QCD 3.11

broken to $SU(N_f)_V$. Therefore not the left- and right-handed components, but only the transformation of the ψ vector in flavour space remains

$$\psi \to \exp(i\theta_i \tilde{T}_i)\psi, \qquad \overline{\psi} \to \overline{\psi}\exp(-i\theta_i \tilde{T}_i). \tag{3.16}$$

The spontanously broken chiral symmetry of the massless theory gives rise to N_f^2-1 Nambu-Goldstone bosons [84]. In the case of two flavours, up and down, these Goldstone bosons are the three pions π^+,π^-,π^0. However in nature the spontanously broken symmetry is explicitly broken by the quark masses. This gives rise to the pion masses. If we only consider the case of two flavours, up and down, with the same mass after spontanous symmetry breaking the remaining $SU(2)_V$ symmetry is called isospin symmetry. In nature the up and down quark mass are not too different in comparison to the typical hardonic scale. Therefore isospin symmetry is a good approximation [5] and one can in practice expand the Lagrangian around the difference of the quark masses $m_u - m_d$ and treat the resulting contributions as corrections to the isospin symmetry result.

There is also another global $U(1)_V$ symmetry that hold even in the case of massive quarks. This symmetry is associate with baryon number conservation. Lastly the Lagrangian is also invariant under a $U(1)_A$ transformation of the quark field. However, after quantization this symmetry is not apparent anymore [84] [5].

3.4 Perturbative QCD

In principle one can apply the formalism we have developed in section 2.3 to the QCD Lagrangian 3.11 and derive Feynman rules for quark and gluon propagators, as well as interaction vertices. However, applying the path integral quantization to a non-Abelian gauge theory requires adding Fadeev-Popov ghost fields [3]. These ghosts are not physical in the sense that they are not associated with in or outgoing particle states. But, they need to be taken into account when writing down Feynman diagrams in order to preserve unitarity. Another important difference to Abelian gauge theory is the

appearance of a gluon self interaction term in the form of a three-gluon and four-gluon vertex 3.1. Perturbation theory is only applicable to QCD at high energies because of the running coupling, which we will discuss in the next section 3.5. Since we are eventually interested in the computation of the muon anomalous magnetic moment, which receives large contributions from the low energy regime, we can not rely on perturbation theory.

3.5 Running coupling

In section 2.3.2 we have seen that the electromagnetic coupling needs to be renormalized in order to be a meaningful physical quantity. The same is also true for the strong coupling g_s or $\alpha_s := \frac{g_s^2}{4\pi}$. In the process of renormalization the coupling receives contributions that are dependent on the renormalization scale μ_r [86]. This means that the coupling is really a function of the scale parameter $\alpha_s(\mu_r^2)$ obeying the renormalization group equation

$$Q^2 \frac{\partial}{\partial Q^2} \frac{\alpha_s(Q^2)}{4\pi} = \beta(\alpha_s(Q^2)). \tag{3.17}$$

The β function in the ultraviolet (UV) region, i.e. for large Q^2, can be expressed as a series [86]

$$\beta(\alpha_s) = -\left(\frac{\alpha_s}{4\pi}\right)^2 \sum_{n=0} \left(\frac{\alpha_s}{4\pi}\right)^n \beta_n, \tag{3.18}$$

where the first term is given by [87]

$$\beta_0 = 11 - \frac{2}{3} N_f, \tag{3.19}$$

with the number of fermions N_f. The second term [88] is [89]

$$\beta_1 = 102 - \frac{38}{3} N_f. \tag{3.20}$$

The first two terms in this series are renormalization scheme independent. However, all other terms are scheme dependent [86]. The exact solution to Eq.3.17 is only known for $n = 0$

$$\alpha_s(Q^2) = \frac{4\pi}{\beta_0 \log(Q^2/\Lambda^2)}, \tag{3.21}$$

where Λ is a renormalization scheme dependent scale parameter. In the $\overline{\text{MS}}$-scheme it is $\Lambda \approx 0.34\text{GeV}$ for $N_f = 3$. This scale is associated with the phenomenon of confinement, which means that free quarks can not be observed in nature but they form bound states at energies $Q^2 > \Lambda^2$. The fact that the pion masses are smaller than Λ can be explained by the fact that they are pseudo-Goldstone bosons, which acquire mass through explicit chiral symmetry breaking due to the small quark masses. However, it is worth noting that there is yet no formal proof for quark confinement.

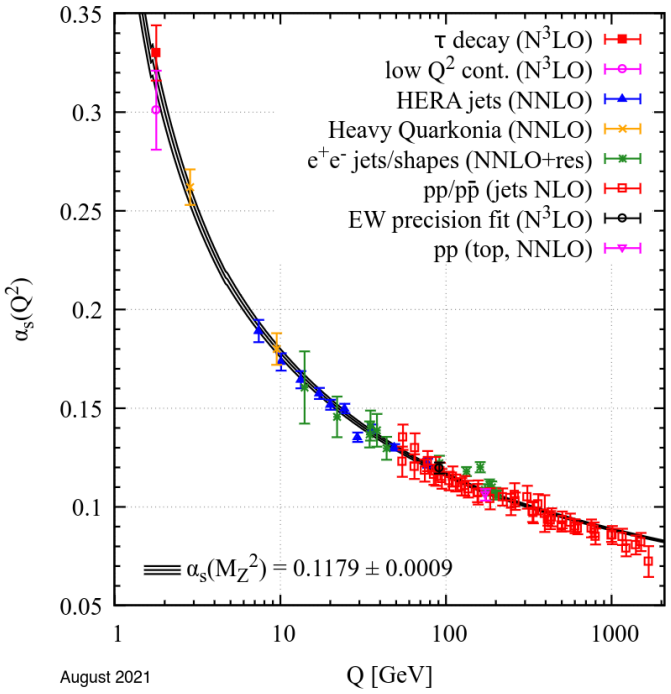

Figure 3.2: This figure displays the current experimental results for the strong coupling α_s taken from the Particle Data Group [90]

Eq. 3.21 also shows that in the limit $Q^2 - \Lambda^2 \to 0^+$ the coupling constant diverges. This also means that perturbation theory is not applicable in this regime, which is a completely different behaviour from the case of QED [3]. On the other hand in the limit $Q^2 \to \infty$ the coupling α_s vanishes and quarks are asymptotically free. This is also seen in experiments, see Fig. 3.2. The fact that the perturbative approach is not applicable for QCD in the small energy regime leads to many difficulties in the computation of hadronic contribution to observables, such as the hadronic vacuum polarization contribution to the anomalous magnetic moment of the muon, which we will discuss in chapter 6

3.6 QCD + QED

For many problems in hadron physics it is sufficient to consider QCD on its own to obtain results that agree with experiment. However, this can only be seen as an approximation, since in nature we can not "turn off" the other interactions. While contributions of the weak interaction enter only at high energies, at the typical electroweak scale $v \approx 246$ GeV [91], contributions due to QED effects are present at all scales. To describe these we would need to write down a Lagrangian containing QCD and QED

$$\mathscr{L}_{\text{QCD+QED}} = \frac{1}{2}\text{Tr}(G_{\mu\nu}G_{\mu\nu}) + \frac{1}{4}F_{\mu\nu}F_{\mu\nu} + \sum_{f=u,d,s,c,b,t} \overline{\psi}_f(\gamma_\mu \tilde{D}_\mu + M_f)\psi_f, \tag{3.22}$$

with the covariant derivative

$$\tilde{D}^f_{\mu\nu} = \partial_\mu - i g_s \mathscr{A}^a_\mu T^a - i e Q_f A_\mu, \tag{3.23}$$

where $F_{\mu\nu} = \partial_\mu A_\nu - \partial_\nu A_\mu$ is the field strength tensor for the photon and $Q_f = \text{diag}(2/3, -1/3, -1/3, 2/3, -1/3, 2/3)$ is the charge matrix representing the fraction of the electric charge e that the individual quarks carry, when we write the quarks in the order $f = (u, d, s, c, b, t)$. The Lagrangian 3.22 exhibits a local $SU(3)$ symmetry with respect to the color change and a local $U(1)$ symmetry with respect to electric charge. Defining the conserved vector current as [4]

$$j_\mu(x) = \frac{2}{3}\overline{u}(x)\gamma_\mu u(x) - \frac{1}{3}\overline{d}(x)\gamma_\mu d(x) - \frac{1}{3}\overline{s}(x)\gamma_\mu s(x) + \frac{2}{3}\overline{c}(x)\gamma_\mu c(x) - \frac{1}{3}\overline{b}(x)\gamma_\mu b(x) + \frac{2}{3}\overline{t}(x)\gamma_\mu t(x), \tag{3.24}$$

we can write Eq. 3.22 as

$$\mathscr{L}_{\text{QCD+QED}} = \mathscr{L}_{\text{QCD}} + \frac{1}{4}F_{\mu\nu}F_{\mu\nu} + j_\mu A_\mu. \tag{3.25}$$

In section 3.5 we have seen that QCD can not be treated perturbatively in the regime of small energies. However, looking back at Eq. 2.57 using the Lagrangian 3.25 we can split the interaction part into a QED part for which pertubation theory is applicable and a part that ecodes the non-perturbative interaction of QCD. This is especially useful for quantities where QCD enters only in photon loops like for the case of the anomalous magnetic moment of the muon. We can write down Feynman diagrams as an expansion in the electromagnetic coupling e, where non-perturbative QCD phenomema are depicted as *blobs* with n-points connecting to photon lines, see Fig 1.1a.

When the photon is treated as a background field, first used in [92] [93], i.e. the photon dynamics are neglected the Lagrangian reads

$$\mathscr{L}_{\text{QCD+bQED}} = \mathscr{L}_{\text{QCD}} + j_\mu A_\mu. \tag{3.26}$$

This looks similar to the Lagrangian inside the generating functional that we defined in Eq.5.2. We can now define the generating functional for QCD in the background of the photon field as

$$Z[A_\mu] = \int \Pi_{a,f} D\mathscr{A}^a_\mu D\psi_f D\overline{\psi}_f \exp\Big(-\int d^4x \mathscr{L}_{\text{QCD}} + j_\mu A_\mu\Big), \tag{3.27}$$

where a correlation function with n-points that connect to photon lines is defined as

$$\Big(-\frac{\delta}{\delta A_\mu(x_1)}\Big)\Big(-\frac{\delta}{\delta A_\nu(x_2)}\Big)\Big(\cdots\Big)\Big(-\frac{\delta}{\delta A_\sigma(x_n)}\Big)\log\Big((Z[A_\mu]\Big)\Big|_{A_\mu=0}. \tag{3.28}$$

this clearly neglects contributions of order e^2 due to internal photon loops. This frameworks allows

[4] we have written the quark field ψ_f with the corresponding letter $(u, d, \ldots)$

for a computation of the leading order QED contribution to the vector-vector correlator in QCD+QED while QCD can still be treated non-perturbatively

$$\langle j_\mu(x)\, j_\nu(y)\rangle_{QCD+bQED} = \langle\Big(-\frac{\delta}{\delta A_\mu(x)}\Big)\Big(-\frac{\delta}{\delta A_\nu(y)}\Big)\log\Big((Z[A_\mu]\Big)\Big|_{A_\mu=0}\rangle_{QCD}. \tag{3.29}$$

In chapter 6 we will see how the vector-vector correlator 3.29 is related to the computation of the hadronic vacuum polarization contribution to the anomalous magnetic moment of the muon.

When we consider the case of two mass degenerate flavours the QCD part of the Lagrangian in Eq. 3.26 is symmetry under a global $SU(2)_f$ transformation, we referred to this as isopin symmetry in section 3.3. The term $j_\mu A_\mu$ breaks this isospin symmetry due to fact that the quarks have different charges. It is convenient to define an isoscalar ($I=0$) part, that is invariant under isospin transformation and an isovector ($I=1$) part

$$j_\mu^{I=0}(x) = \frac{1}{6}\Big(\overline{u}(x)\gamma_\mu u(x) + \overline{d}(x)\gamma_\mu d(x)\Big), \tag{3.30}$$

$$j_\mu^{I=1}(x) = \frac{1}{2}\Big(\overline{u}(x)\gamma_\mu u(x) - \overline{d}(x)\gamma_\mu d(x)\Big), \tag{3.31}$$

which add up to the two flavour vector current

$$j_\mu(x) = j_\mu^{I=0}(x) + j_\mu^{I=1}(x). \tag{3.32}$$

4 Effective field theory

We want to start this chapter by stating Steven Weinberg's famous "Folk theorem":

"If one writes down the most general possible Lagrangian, including all terms consistent with assumed symmetry principles, and then calculates matrix elements with this Lagrangian to any given order of perturbation theory, the result will simply be the most general possible S-matrix consistent with perturbative unitarity, analyticity, cluster decomposition, and the assumed symmetry properties" [94].

The big problem with this statement is that the most general Lagrangian contains infinitely many parameters. But, if we would have a starting point in parameters space characterised by a finite number of parameters and an ordering principle for additional terms, one could use perturbation theory with respect to the given ordering parameter. The choice of a good starting point is dependent on the observable that one wants to calculate and the relevant energy scale. This can be seen as a reparametrization of the generating functional in terms of different field variables that are consistent with the given symmetry properties

$$Z[\xi] = \int D\Phi \exp\Big(-S[\Phi] - \int d^4x \xi \hat{O}[\Phi(x)]\Big) \approx \int D\tilde{\Phi} \exp\Big(-S[\tilde{\Phi}] - \int d^4x \xi \hat{O}[\tilde{\Phi}(x)]\Big) \tag{4.1}$$

where the $\approx$ is valid as long as we have a good choice of the new parameters $\tilde{\Phi}$. In practice this reparametrisation can be quite complicated. We are ultimatively interested in effective field theories for QCD in the small energy regime, where quarks can not be treated perturbatively. This is particularly interesting for investigating the hadronic contributions to the anomalous magnetic moment of the muon.

We start this chapter with a short introduction to the topic of chiral perturbation theory based on the work of Scherer [5] [95] and then turn to a phenomenological model originally motivated in the work of Jegerlehner & Nyffeler [96], which my collaborators and I used for our work in Ref. [97].

4.1 Chiral perturbation theory

Chiral perturbation theory (χPT) is an effective field theory for QCD that is built on the idea that one can describe the low energy spectrum of QCD by considering the approximate symmetries of the

Lagrangian 3.11. We have already discussed them in section 3.3. When examining the masses of the different quark flavours, we observe that they can be organized into two categories. The up, down and strange quarks have masses that are much smaller than the intrinsic scale of QCD, and the charm, bottom and top quarks have much higher masses [5]

$$\begin{pmatrix} m_u \approx 0.002GeV \\ m_d \approx 0.005GeV \\ m_s \approx 0.095GeV \end{pmatrix} \ll 1\text{GeV} \leq \begin{pmatrix} m_c \approx 1.2GeV \\ m_b \approx 4.18GeV \\ m_t \approx 173GeV \end{pmatrix}. \tag{4.2}$$

When one is interested in the regime below 1GeV, where the heavy quarks can not "go on-shell", it is therefore useful to consider only the three lightest quarks first.

We have already pointed out in section 3.3 that in the case of 3 massless quarks the spontaneously broken $SU(3)_R \times SU(3)_L$ symmetry gives rise to eight Goldstone bosons that acquire mass if the quarks are not massless. These Goldstone bosons can be identified with the meson octet of pions, kaons and the η-meson. We define the chiral limit as the limit where all quark masses are zero $m_f \to 0$. Our goal is to construct a Lagrangian that has the full $SU(3)_R \times SU(3)_L$symmetry in the chiral limit, but relies on the Goldstone bosons as the dynamical degrees of freedom. We define [5]

$$U(x) = \exp\Big(i\frac{\phi(x)}{F_0}\Big), \tag{4.3}$$

$$\phi(x) = \sum_{a=1}^{8} \lambda^a \phi^a(x) := \begin{pmatrix} \pi^0 + \frac{1}{\sqrt{3}}\eta_8 & \sqrt{2}\pi^+ & \sqrt{2}K^+ \\ \sqrt{2}\pi^- & -\pi^0 + \frac{1}{\sqrt{3}}\eta_8 & \sqrt{2}K^0 \\ \sqrt{2}K^- & \sqrt{2}\overline{K}^0 & -\frac{2}{\sqrt{3}}\eta_8 \end{pmatrix} \tag{4.4}$$

with the Gell-Mann matrices λ^a that we defined in section 3.1. We make use of Weinberg´s power counting scheme [98] that classifies operators with their mass dimension. Derivatives, for example, count as one mass dimension. The lowest order chiral effective Lagrangian reads [5]

$$\mathscr{L}_{\text{eff}} = -\frac{F_0^2}{4} Tr\Big((\partial_\mu U)(\partial_\mu U)^\dagger\Big) + \frac{F_0^2 B_0^2}{2} Tr\Big(MU^\dagger + UM^\dagger\Big), \tag{4.5}$$

where F_0 is a free parameter, that is later related to the pion decay constant. Since we are interested in the case where the quarks have masses, we define the mass matrix $M = \text{diag}(m_u, m_d, m_s)$. More general considerations can be found in the introductory work of Scherer [5]. The parameter B_0 is related to the chiral quark condensate (in the chiral limit)

$$B_0 = -\frac{1}{3F_0^2}\langle \overline{u}u + \overline{d}d + \overline{s}s\rangle, \tag{4.6}$$

and the meson masses in the isospin symmetric case ($m_u = m_d = m$) to leading order are given by

$$\begin{aligned} m_\pi^2 &= 2B_0 m, \\ m_K^2 &= B_0(m+m_s), \\ m_\eta^2 &= \frac{2}{3}B_0(m+2m_s). \end{aligned} \tag{4.7}$$

One can see that the meson masses satisfy the Gell-Mann-Okubo relation

$$4m_K^2 = 4B_0(m+m_s) = 2B_0(m+2m_s) + 2B_0 m = 3m_\eta^2 + m_\pi^2. \tag{4.8}$$

4.1.1 Coupling to the photon

If one wants to introduce interaction with the photon field A_μ in the chiral effective Lagrangian 4.5, this is only consistent with gauge invariance of the electromagnetic field when we exchange the partial derivative for covariant derivative

$$D_\mu U = \partial_\mu U - ieA_\mu. \tag{4.9}$$

If we now expand the exponential function in the definition of $U(x)$ and write only the first terms containing pions π^+, π^-, π^0 we see that the photon does not couple to the π^0 which we would naively expect,

$$\mathscr{L}_{\text{eff}} \supset -D_\mu\pi^+ D_\mu\pi^- - m_\pi^2\pi^+\pi^- - \partial_\mu\pi^0\partial_\mu\pi^0 - m_\pi^2\pi^0\pi^0 \tag{4.10}$$

This is exactly the toy model of scalar QED which we have discussed in section 2.3. So, to leading order in chiral perturbation theory, where the pions are treated as point particles, the results from scalar QED can be used for the calculation of scattering processes of the photon and the charged pions.

4.1.2 Wess-Zumino-Witten term

The processes $P \to \gamma\gamma$, where P is a pseudoscalar meson, arise from the odd-intrinstic parity part of the effective field theory [99]. At leading order they are accounted for by the Wess-Zumino-Witten term [100], [101]. The interaction vertex arising from this term is given by [102]

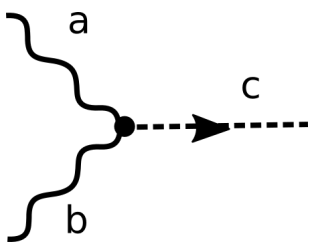

$$\propto \quad \text{str}(T^a T^b T^c) \int d^4x \phi^c \epsilon^{\mu\nu\rho\sigma} F^a_{\mu\nu} F^b_{\rho\sigma} \tag{4.11}$$

where str(...) denotes the supertrace [103], T^a are the $\mathfrak{su}(3)$ generators, ϕ^a are the meson fields and $F^a_{\mu\nu}$ is the field strength tensor for an external electromagnetic field.

4.1.3 $\eta - \eta'$ mixing

The full global symmetry of the QCD Lagrangian for three quark flavours is $U(N_f)_V \times U(N_f)_A$ on the classical level, which is broken down to $SU(3)_V \times U(1)_V$ [5], [99]. The spontaneously broken $SU(3)_A \times U(1)_A$ symmetry would naively give rise to 9 massless Goldstone bosons in the chiral limit. But, the $U(1)_A$ symmetry is broken by quantum effects [104] [105], [106]. This leads to the η' acquiring a mass even in the chiral limit. In order to describe the η' in the framework of χPT one needs an additional ordering parameter. In Ref. [99] and [107], the η' meson is studied in the context of a large N_c expansion. In this so called L$N_c\chi$PT a $SU(3)$ singlet η_1 is added to the effective field content in Eq. 4.4. The physical mass eigenstates η and η' for $m_u = m_d \neq m_s$ are linear combinations of the singlet η_1 and the octet η_8 characterized by the mixing angle θ

$$\begin{pmatrix} \eta \\ \eta' \end{pmatrix} = \begin{pmatrix} \cos(\theta) & -\sin(\theta) \\ \sin(\theta) & \cos(\theta) \end{pmatrix} \begin{pmatrix} \eta_1 \\ \eta_8 \end{pmatrix}. \tag{4.12}$$

In Ref. [107] the θ has been calculated to leading order and next-to-leading (NLO) order. The mixing angle at leading order, denoted by $\theta^{[0]}$ result is fully determined by the physical meson masses

$$\sin(2\theta^{[0]}) = -\frac{4\sqrt{2}(m_K^2 - m_\pi^2)(-4m_K^2 + 3m_{\eta'}^2 + m_\pi^2)}{3\Big[-8m_K^2(m_{\eta'}^2 + m_\pi^2) + 8m_K^4 + 3m_{\eta'}^2 + 2m_\pi^2 m_{\eta'}^2 + 3m_\pi^4\Big]}, \tag{4.13}$$

which yields $\theta^{[0]} = -19.6°$. At NLO it is necessary to determine several low energy constants in χPT. There are several different strategies in fitting these low energy constants [107], which give compatible results for the mixing angle at NLO $\theta^{[1]} = -(11.1 \pm 0.6)°$.

4.2 Sakurai theory

In this section we want to discuss a phenomenological approach to an EFT for QCD in the energy regime below 1 GeV. We want to investigate the model suggested by Jegerlehner and Safron [96] and first proposed by Sakurai [108]. This model is used for the determination of the finite-size effects in my work on the calculation of the intermediate window quantity, published in Ref. [97]. Therefore, there is some text overlap, with the published version. The Lagrangian for the Sakurai QFT reads

$$\mathscr{L}_{[Sak]} = \frac{1}{4}F_{\mu\nu}(A)^2 + \frac{1}{4}F_{\mu\nu}(\rho)^2 + \frac{1}{2}m_\rho^2\rho_\mu^2 + \frac{e}{2g_\gamma}F_{\mu\nu}(A)F_{\mu\nu}(\rho) + (D_\mu\pi)^\dagger(D_\mu\pi) + m_\pi^2\pi^\dagger\pi, \tag{4.14}$$

where the ρ resonance of the pion in described by a vector meson ρ_μ. We use the definition of the field strength tensor of a generic vector field X_μ

$$F_{\mu\nu}(X) = \partial_\mu X_\nu - \partial_\nu X_\mu. \tag{4.15}$$

This Lagrangian incorporates a kinetic mixing term $F_{\mu\nu}(A)F_{\mu\nu}(\rho)$ that couples the ρ directly to the photon field.

In the following, we want to discuss some features of the Sakurai QFT in detail, with special focus on its renormalization to one-loop, where we use dimensional regularisation. The number of spacetime dimensions is given by

$$D = 2\lambda + 2 = 4 - \varepsilon. \tag{4.16}$$

For the free propagator of the ρ meson, we obtain

$$G_{\mu\nu}(x) \equiv \langle \rho_\mu(x)\rho_\nu(0)\rangle = \int \frac{d^d k}{(2\pi)^d}\, e^{ikx}\, \frac{\delta_{\mu\nu} + k_\mu k_\nu / m_\rho^2}{k^2 + m_\rho^2} = \left(\delta_{\mu\nu} - \frac{1}{m_\rho^2}\partial_\mu\partial_\nu\right) G_{m_\rho}(x), \tag{4.17}$$

where $G_m(x)$ is the massive scalar propagator 2.32.

We begin by determining the couplings g and g_γ, working at tree-level. The kinematic mixing term between ρ and photon can be removed at the cost of generating a direct coupling of the ρ to electrons. For the determination of the couplings, it is useful to work in this new basis. We set

$$\beta = \frac{e}{g_\gamma} \tag{4.18}$$

and remove the kinetic mixing term by a field transformation,

$$\begin{pmatrix} A_\mu \\ \rho_\mu \end{pmatrix} = \begin{pmatrix} 1 & -\frac{\beta}{\sqrt{1-\beta^2}} \\ 0 & \frac{1}{\sqrt{1-\beta^2}} \end{pmatrix} \begin{pmatrix} \tilde{A}_\mu \\ \tilde{\rho}_\mu \end{pmatrix}. \tag{4.19}$$

The square-mass for the $\tilde{\rho}_\mu$ field is

$$\tilde{m}_\rho^2 = \frac{m_\rho^2}{1-\beta^2}. \tag{4.20}$$

The covariant derivative takes the form

$$D_\mu = \partial_\mu - ieA_\mu - ig\rho_\mu = \partial_\mu - ie\tilde{A}_\mu - i\tilde{g}\tilde{\rho}_\mu, \tag{4.21}$$

$$\tilde{g} = \frac{g - e\beta}{\sqrt{1-\beta^2}}. \tag{4.22}$$

Thus the Lagrangian can be written as

$$\mathscr{L}_E = \frac{1}{4}F_{\mu\nu}(\tilde{A})^2 + \frac{1}{4}F_{\mu\nu}(\tilde{\rho})^2 + \frac{1}{2}\tilde{m}_\rho^2\tilde{\rho}_\mu^2 + (D_\mu\pi)^\dagger(D_\mu\pi) + m_\pi^2\pi^\dagger\pi. \tag{4.23}$$

While the form of the Lagrangian is now simpler, in the new basis of fields the electromagnetic current of the electron couples not only to $\tilde{A}_\mu$, but also directly to $\tilde{\rho}_\mu$. Explicitly, the coupling to the electron reads

$$\mathscr{L}_E = \bar{e}((\partial_\mu - ieA_\mu)\gamma_\mu + m_e)e = \bar{e}((\partial_\mu - ie\tilde{A}_\mu + ie\frac{\beta}{\sqrt{1-\beta^2}}\tilde{\rho}_\mu)\gamma_\mu + m_e)e. \tag{4.24}$$

From here, one calculates the tree-level decay width for $\tilde{\rho} \to e^+e^-$ by standard QFT methods [3](similar to the calculation $Z^0 \to \bar{\ell}\ell$) and finds, neglecting the electron mass,

$$\Gamma_{e^+e^-} = \frac{1}{3}\alpha\frac{\beta^2}{1-\beta^2}\,\tilde{m}_\rho. \tag{4.25}$$

From the PDG [109], we set

$$\tilde{m}_\rho = 775.26(23)\,\text{MeV}, \qquad \Gamma_{e^+e^-} = (4.72\times10^{-5})\times 149.1\,\text{MeV} = 7.04\,\text{keV}, \tag{4.26}$$

and from here find

$$\beta = 0.0610, \qquad g_\gamma = \frac{\sqrt{4\pi\alpha}}{\epsilon} = 4.97. \tag{4.27}$$

From the value of β, one sees that one could have dropped the factor $1/\sqrt{1-\beta^2}$.

Similarly, the $\tilde{\rho}\pi\pi$ decay is driven at leading order by the interaction $\Delta\mathscr{L}_E = \tilde{g}\tilde{\rho}_\mu j_\mu$. Here, if p and q are respectively the final-state momenta of the π^+ and π^-, we have

$$i\mathscr{M}^{(\sigma)} = \tilde{g}\,\epsilon_\nu^{(\sigma)}(p^\nu - q^\nu), \tag{4.28}$$

and

$$\frac{1}{3}\sum_{\sigma=0,\pm}|\mathscr{M}^{(\sigma)}|^2 = \frac{2\tilde{g}^2}{3}(p\cdot q - m_\pi^2). \tag{4.29}$$

In the CM frame, where the norm of the pion spatial momentum is p_π, one obtains

$$\Gamma_{\pi^+\pi^-} = \frac{p_\pi}{8\pi m_\rho^2}\frac{1}{3}\sum_{\sigma=0,\pm}|\mathscr{M}^{(\sigma)}|^2 = \frac{\tilde{g}^2 p_\pi^3}{6\pi m_\rho^2}. \tag{4.30}$$

Setting this equal to the experimental value of 149.1 MeV, one extracts

$$\tilde{g} = 5.976, \qquad g = 5.984. \tag{4.31}$$

The values $(g_\gamma, g) = (4.97, 5.984)$ are now the renormalized couplings that we will use further on to make predictions in the Sakurai QFT. In section 7.2.2 we will use this theory to make predictions for the integrand of the hadronic vacuum polarization contribution a_μ^{hvp} coming from the charged pion channel. In section 8.3, we will use this theory to calculate finite-size effects that arise when calculating a_μ^{hvp} in a finite volume, which we will then use to correct the data calculated in lattice QCD in chapter 9.

5 Lattice QCD

This chapter serves as an introduction to the topic of lattice QCD. The lattice can be understood as a discretization of Euclidean spacetime in a finite box, with the goal to compute hadronic observables on a modern computer, by simulating QCD interactions. We will concentrate on the methods used by the Coordinated Lattice Simulations (CLS) initiative [110]. We follow the derivations of the introductory textbooks of Gattringer and Lang [78], Smit [111], Knechtli, Günther and Peardon [112]. The structure of this section is partly inspired by the PhD theses [80], [81] and [82].

5.1 Discretization of Euclidean spacetime

We start by defining the discretized finite volume spacetime as

$$\Lambda = \Big\{(n_1, n_2, n_3, n_4) \in \mathbb{N} \quad \Big| \quad n_1, n_2, n_3 = 0, 1, 2, \ldots, N_L - 1, \quad n_4 = 0, 1, 2, \ldots, N_T - 1\Big\}, \tag{5.1}$$

where N_L is the extend of the spatial dimensions (n_1, n_2, n_3) and N_T is the length of the euclidean time dimension (n_4) . In most simulations all three spatial dimensions are of equal length, while the time dimension is taken to be much longer. We also need to introduce the lattice spacing parameter a that is the minimal distance between two lattice points. This parameter serves as ultraviolet (UV) cutoff, since the maximal momentum on the lattice is $p = \frac{\pi}{a}$. The continuum limit is then defined as the limit $a \to 0$. We will see in section 5.5 that the lattice spacing parameter has the dimension of length. Simulations of QCD are typically performed at scales between $a \approx 0.04 - 0.15$ fm.

The physical volume of the box is given by $L^3 T = (aN_L)^3 (aN_T)$. Eventually, we want to obtain results in infinite volume. This means after performing a lattice simulation we need to take the limit $L \to \infty, T \to \infty$, where a is kept constant.

Because of the finite extent of the lattice, one needs to specify boundary conditions at the borders of the lattice. A natural choice is to consider periodic boundary conditions, i.e. the lattice fields are periodic functions $\psi(x + \hat{\mu}L) = \psi(x)$. All CLS ensembles have periodic boundary conditions in the spatial dimensions. For the time extent a large amount of ensembles have been generated with open boundary conditions in order minimize the effect of topological freezing [113]. A smaller amount has been generated, admitting also periodic boundary conditions in the time extend.

The generating functional for an arbitrary field Φ living on the lattice sites of the discretized

spacetime is simply obtained by replacing the integral over spacetime in Eq. 2.3 with a sum over all lattice sites

$$Z[\xi] = \int \mathscr{D}\Phi \exp\Big(- a^4 \sum_{n\in\Lambda} (\mathscr{L} + \xi \hat{O}[\Phi(n)])\Big). \tag{5.2}$$

In order to write down a kinetic term we need to define the lattice derivative

$$\partial_\mu \Phi(x) \to \frac{1}{2a}\Big(\Phi(x + a\hat{\mu}) - \Phi(x - a\hat{\mu})\Big), \tag{5.3}$$

where $\hat{\mu}$ is a vector in μ direction. Eq. 5.3 is the symmetrized version of the derivative. The advantage of the symmetric derivative is that cutoff effects are of order $O(a^2)$, as opposed to the $O(a)$ cutoff effects of the ordinary derivative $\frac{1}{a}(\Phi(x + a\hat{\mu}) - \Phi(x))$. This can easily be seen by Taylor expanding the function Φ.

5.2 Gauge invariance and link variables

Our goal is to write down a $SU(3)$ gauge theory on the discretized spacetime. For that purpose we assume that the discretized spacetime is embedded in the continuum, more precisely a principle bundle that is a cartesian product of R^4 and the $SU(3)$ gauge group equipped with a connection $\mathscr{A}$. The gauge transporter between two points x and y is defined as [78]

$$G(x, y) = P \exp\Big(i \int_{\mathscr{C}_{x,y}} \mathscr{A} \cdot ds\Big), \tag{5.4}$$

where $\mathscr{C}_{x,y}$ is a continuously connected curve from x to y and P denotes the path ordering. We define the lattice gauge link variable as

$$U_\mu(n) = \exp(i a \mathscr{A}^i_\mu(n) T^i), \tag{5.5}$$

where T^i are the generators of $\mathfrak{su}(3)$ defined in Eq. 3.2. This is an approximation of the gauge transporter $U_\mu(n) = G(n, n + \hat{\mu}) + O(a)$ connecting two neighbouring sides n and $n + \hat{\mu}$ on the lattice. Analogously, we can define the gauge link pointing in the negative direction as

$$U_{-\mu}(n) := U_\mu(n - \hat{\mu})^\dagger. \tag{5.6}$$

The gauge link transforms under a local $SU(3)$ transformation, which we defined in Eq. 3.1 as

$$U_\mu(n) \to \Omega(n) U_\mu(n) \Omega(n + \hat{\mu})^\dagger. \tag{5.7}$$

These gauge link variables are considered to be the fundamental degrees of freedom on the lattice. This also means that in the generating functional on the lattice we do not consider the Lie algebra

valued field A_μ but instead the gauge links U_μ that are elements of the Lie group.

5.2.1 Wilson gauge action

The gauge action can now be constructed as a functional with respect to the gauge links U_μ. To this end, we define the *plaquette* as the shortest, nontrivial closed loop on the lattice [78]

$$P_{\mu\nu}(n) := U_\mu(n)U_\nu(n+\hat{\mu})U_{-\mu}(n+\hat{\mu}+\hat{\nu})U_{-\nu}(n+\hat{\nu}). \tag{5.8}$$

This quantity is gauge invariant, due to the transformation properties of $U_\mu(n)$ in Eq. 5.7. The Wilson gauge action is a sum over all plaquettes, where only one orientation of each plaquette is counted

$$S_G[U] = \frac{2}{g^2}\sum_{n\in\Lambda}\sum_{1\le\mu<\nu\le 4}\mathrm{Re}\Big(\mathrm{Tr}\Big[\mathbb{1}-P_{\mu\nu}(n)\Big]\Big), \tag{5.9}$$

using the Baker-Campbell-Hausdorff rule and expanding in the lattice spacing a one can show that the plaquette can be written as [78]

$$\begin{aligned} P_{\mu\nu}(n) &= \exp\Big(ia^2(\partial_\mu\mathscr{A}_\nu - \partial_\nu\mathscr{A}_\mu + i[\mathscr{A}_\mu,\mathscr{A}_\nu]) + O(a^3)\Big) &(5.10)\\ &= \exp\Big(ia^2 G_{\mu\nu} + O(a^3)\Big), &(5.11)\end{aligned}$$

and therefore we obtain for Eq. 5.9

$$S_G[U] = \frac{a^4}{2g^2}\sum_{n\in\Lambda}\sum_{\mu,\nu=1}^{4} Tr\Big[G_{\mu\nu}G_{\mu\nu}\Big] + O(a^2). \tag{5.12}$$

So, in the naive continuum limit $a\to 0$ the first sum together with the a^4 term is replaced by the integral over $\int d^4x$ and we recover the continuum version of the $SU(3)$ gauge action.

5.2.2 Lüscher-Weisz gauge action

For the case of the lattice derivative 5.3 we have already seen that for different choices for the discretization of a continuum quantity, one approaches the continuum limit with a different power in the lattice spacing, e.g. $O(a)$ for the ordinary derivative and $O(a^2)$ for the symmetric derivatives. If we want to keep cutoff effects as small as possible, it is desirable to find discretizations of the continuum quantities with $O(a^n)$ effects, where we want n to be large. This process is known as *improvement*. The so called Symanzik improvement programme [114] [115] eliminates $O(a^2)$ effect in the Wilson action 5.9 by computing these effects at tree level, neglecting loop corrections and determining improvement coefficients that cancel the $O(a^2)$ terms accordingly. In order to do so, one defines the rectangle[1]

$$R_{\mu\nu}(n) = U_\mu(n)U_\mu(n+\hat{\mu})U_\nu(n+2\hat{\mu})U_\mu(n+\hat{\mu}+\hat{\nu})^\dagger U_\mu(n+\hat{\nu})^\dagger U_\nu(n)^\dagger. \tag{5.13}$$

[1] Here, we do not use the Einstein summation convention

The $O(a^2)$ tree level improved action by Lüscher and Weisz is then given by [116] [117]

$$S_G^{\text{imp}}[U] = \frac{a^4}{2g^2} \sum_{n\in\Lambda} \sum_{1\leq\mu<\nu\leq 4} c_0 Re\Big(Tr\Big[\mathbb{1} - P_{\mu\nu}(n)\Big]\Big) + c_1 Re\Big(Tr\Big[\mathbb{1} - R_{\mu\nu}(n) + \mathbb{1} - R_{\nu\mu}(n)\Big]\Big) \tag{5.14}$$

with coefficients $c_0 = 5/3$ and $c_1 = -\frac{1}{12}$. This action is implemented in the sofware package `openQCD` that is used by the CLS initiative.

5.3 Fermions on the lattice

Now that we have defined the pure gauge action on the lattice, we want to discuss the case of fermions in this section. The continuum action for a free spinor field ψ reads [78]

$$S_F^{0,\text{cont}}[\overline{\psi},\psi] = \int d^4x \overline{\psi}(x)(\gamma_\mu\partial_\mu + m)\psi(x). \tag{5.15}$$

We only focus on a single flavour in this section. Replacing the integral with a sum over lattice points and using the symmetric lattice derivative 5.3 we obtain the free fermion action on the lattice

$$S_F^0[\overline{\psi}\psi] = a^4 \sum_{n\in\Lambda} \overline{\psi}(n)\Big(\sum_{\mu=1}^{4} \frac{\psi(n+\hat{\mu}) - \psi(n-\hat{\mu})}{2a} + m\psi(n)\Big). \tag{5.16}$$

Our goal is to write down a gauge invariant expression for the fermion action. If we consider the transformation of the spinor $\psi(n)$ with $\Omega(n)$ an element of $SU(3)$

$$\psi(n) \to \Omega(n)\psi(n), \qquad \overline{\psi}(n) \to \overline{\psi}(n)\Omega^\dagger(n), \tag{5.17}$$

then a product, where one argument of the spinors is shifted by a finite difference μ transforms as

$$\overline{\psi}(n)\psi(n+\hat{\mu}) \to \overline{\psi}(n)\Omega^\dagger(n)\Omega(n+\hat{\mu})\psi(n+\hat{\mu}). \tag{5.18}$$

So, the finite shift by $n+\hat{\mu}$ in the argument of Ω would break gauge invariance. If we instead insert the gauge link $U_\mu(n)$ defined in Eq. 5.5, we have

$$\begin{aligned} \overline{\psi}(n)U_\mu(n)\psi(n+\hat{\mu}) &\to \overline{\psi}(n)\Omega^\dagger(n)\Omega(n)U_\mu(n)\Omega(n+\hat{\mu})^\dagger\Omega(n+\hat{\mu})\psi(n+\hat{\mu}) &(5.19)\\ &= \overline{\psi}(n)U_\mu(n)\psi(n+\hat{\mu}). &(5.20)\end{aligned}$$

So, if we just attach the gauge link to the $\psi(n+\hat{\mu})$ and $\psi(n-\hat{\mu})$ in the free fermion action 5.16, we can make the action gauge invariant. We define the forward covariant derivative $\overrightarrow{D}_\mu$ and backward

covariant derivative $\overleftarrow{D}_\mu$ on the lattice as

$$\overrightarrow{D}_\mu \psi(n) = \frac{U_\mu(n)\psi(n+\hat{\mu}) - \psi(n)}{a}, \tag{5.21}$$

$$\overleftarrow{D}_\mu \psi(n) = \frac{\psi(n) - U_{-\mu}(n)\psi(n-\hat{\mu})}{a}. \tag{5.22}$$

The gauge invariant fermion action on the lattice then reads

$$S_F[\overline{\psi}\psi] = a^4 \sum_{n\in\Lambda} \overline{\psi}(n)\Big(\sum_{\mu=1}^{4} \gamma_\mu \frac{\overrightarrow{D}_\mu + \overleftarrow{D}_\mu}{2} + m\Big)\psi(n). \tag{5.23}$$

This is the so-called naive fermion action on the lattice. We can furthermore define the naive Dirac operator D as

$$D\psi(n) = \Big(\frac{1}{2}\sum_{\mu=1}^{4} \gamma_\mu(\overrightarrow{D}_\mu + \overleftarrow{D}_\mu) + m\Big)\psi(n). \tag{5.24}$$

This Dirac operator has the property of γ^5-hermiticity

$$D = \gamma^5 D^\dagger \gamma^5, \tag{5.25}$$

which is very useful for practical purposes since the hermitian conjugated Dirac operator $D^\dagger$ does not need to be calculated separately, but can instead be obtained using Eq. 5.25. Next, we want to look at the naive Dirac operator in the continuum limit. For the case of free fermions, $U_\mu = \mathbb{1}$, the Dirac operator in momentum space yields

$$\tilde{D}(p) = m\mathbb{1} + \frac{i}{a}\sum_{\mu=1}^{4} \gamma_\mu \sin(p_\mu a). \tag{5.26}$$

Therefore, we can obtain the fermionic propagator by inverting Eq. 5.26 [78]

$$\tilde{D}(p)^{-1} = \frac{m\mathbb{1} - i\,a^{-1}\sum_\mu \gamma_\mu \sin(p_\mu a)}{m^2 + a^{-2}\sum_\mu \sin(p_\mu a)^2}. \tag{5.27}$$

It is straightforward to show that the continuum propagator is recovered in the limit $a \to 0$

$$\lim_{a\to 0} \tilde{D}(p)^{-1} = \frac{m - i\gamma_\mu p_\mu}{m^2 + p^2}. \tag{5.28}$$

However, the lattice propagator has a different pole structure. If we look at the massless case $m = 0$ for simplicity, there is the correct pole at $p^2 = 0$. But, in addition to that there are 15 other poles in the

first Brillouin-zone [78], at

$$p = \Big\{(\pi/a,0,0,0), \quad (0,\pi/a,0,0), \quad (\pi/a,\pi/a,0,0),\dots\Big\}. \tag{5.29}$$

This is referred to as the *fermion doubling problem*. There are several attempts to solve this problem by choosing a different discretization of the fermion action. However, the Nielsen-Ninomiya-Theorem [118], [119] states that it is not possible to define an essentially local Dirac operator on the lattice that ensures that the right continuum limit is obtained for $a \to 0$ and that is invariant under continuous chiral transformations [120].

5.3.1 Wilson-Dirac fermions

The are different approaches in dealing with the problem of fermion doublers that we encountered in section 5.3. Here, we want to discuss the formulation first proposed by Wilson [121]. By adding an additional term $-\frac{a}{2}\overleftarrow{D}_\mu\overrightarrow{D}_\mu$ to the naive Dirac operator, we define the Wilson-Dirac operator D_W

$$D_W\psi(n) := \Big(\frac{1}{2}\sum_{\mu=1}^{4}(\gamma_\mu(\overrightarrow{D}_\mu + \overleftarrow{D}_\mu) - a\overleftarrow{D}_\mu\overrightarrow{D}_\mu) + m\Big)\psi(n). \tag{5.30}$$

The momentum space Wilson-Dirac operator is then given by

$$\tilde{D}_W(p) = m\mathbb{1} + \frac{i}{a}\sum_{\mu=1}^{4}\gamma_\mu \sin(p_\mu a) + \mathbb{1}\frac{1}{a}\sum_{\mu=1}^{4}(1-\cos(p_\mu a)). \tag{5.31}$$

Again, for the massless case the real pole at $p = (0,0,0,0)$ is preserved, but all other poles obtain a mass term proportional to $1/a$. For small a these doublers become very heavy and effectively decouple from the theory. A downside of this approach is that the additional term breaks chiral symmetry. In addition to that, the continuum limit is approached at $O(a)$ instead of $O(a^2)$ for the naive Dirac operator. But, the property of γ^5-hermiticity 5.25 is still valid for the Wilson-Dirac operator [78].

5.3.2 Improvement of the fermion action

The downside of having $O(a)$ lattice artifacts for the Wilson-Dirac operator can be overcome by adding a dimension 5 operator to the fermion action. The so called clover term initially proposed by Sheikholeslami and Wohlert [122] reads

$$S_{\text{clover}}[U,\overline{\psi},\psi] = a^5 c_{SW}\sum_{n\in\Lambda}\overline{\psi}(n)\frac{i}{4}\sigma_{\mu\nu}\hat{F}_{\mu\nu}(n)\psi(n) \tag{5.32}$$

with

$$\hat{F}_{\mu\nu}(n) = \frac{1}{8a^2}\Big(Q_{\mu\nu}(n) - Q_{\nu\mu}(n)\Big), \tag{5.33}$$

where $Q_{\mu\nu}$ is the sum of 4 plaquettes, resembling the form of a clover leaf around the lattice site n [78]:

$$Q_{\mu\nu}(n) = P_{\mu\nu}(n) + P_{\nu,-\mu}(n) + P_{-\mu,-\nu}(n) + P_{-\nu,\mu}(n) \tag{5.34}$$

The coefficient c_{SW} on the CLS ensemble with $N_f = 2+1$ [2] has been determined in Ref. [123]. The improved fermion action for Wilson-Dirac fermions reads

$$S_F^{\text{imp}}[\overline{\psi},\psi] = a^4 \sum_{n\in\Lambda} \overline{\psi}(n) D_W \psi(n) + a^5 c_{SW} \sum_{n\in\Lambda} \overline{\psi}(n) \frac{i}{4} \sigma_{\mu\nu} \hat{F}_{\mu\nu}(n) \psi(n). \tag{5.35}$$

For different fermion flavours we simply write

$$S_F^{\text{imp}}[\overline{\psi},\psi] = a^4 \sum_f \sum_{n\in\Lambda} \overline{\psi}(n) D_f \psi(n), \tag{5.36}$$

where D_f contains the Wilson-Dirac operator and the clover term. There are also several other ways to deal with fermions on the lattice, such as staggered fermions [124], [125], domain wall fermions [126], [127] and twisted mass fermions [128], [129], [130] [3].

5.4 Numerical methods for lattice QCD

The fermion action defined in Eq. 5.35 together with the pure gauge action 5.14 describe the dynamics of the gauge links $U_\mu(n)$ and fermion fields $\psi(n)$. In order to compute observables, we make use of the partition function for an Euclidean action that we defined in Eq. 2.41.

$$Z = \int D[U] D[\overline{\psi},\psi] \exp\Big(- S_G^{\text{imp}}[U] - S_F^{\text{imp}}[U,\overline{\psi},\psi] \Big). \tag{5.37}$$

The expectation value of an operator $\hat{O}$ is then given by

$$\langle \hat{O} \rangle = \frac{1}{Z} \int D[U] D[\overline{\psi},\psi] \exp\Big(- S_G^{\text{imp}}[U] - S_F^{\text{imp}}[U,\overline{\psi},\psi] \Big) O[U,\overline{\psi},\psi]. \tag{5.38}$$

So far, we did not specify the measure $D[U]D[\overline{\psi},\psi]$, since for the sake of perturbation theory we could simply use the trick described in Eq. 2.14 to obtain the Green´s function of the theory. For lattice QCD, we want to make explicit use of the path integral formalism as a quantization scheme. The product measure

$$D[\overline{\psi},\psi] = \prod_{n\in\Lambda} \prod_{f,\alpha,c} d\psi_f(n)^\alpha_c \, d\overline{\psi}_f(n)^\alpha_c, \tag{5.39}$$

[2] 2 mass degenerate light quarks and 1 strange quark

[3] This is not a comprehensive list, we just want to mention some reviews here

where the f are all quark flavours, c is the color index and α the Dirac index, and

$$D[U] = \prod_{n\in\Lambda}\prod_{\mu=1}^{4} dU_\mu(n), \tag{5.40}$$

are performed on all configurations of classical fields $U_\mu, \overline{\psi}, \psi$ [78]. The spinor fields need to be implemented as *Grassmann numbers*, in order to satisfy the correct spin-statistics as fermions.

The measure for a single gauge link $dU_\mu(n)$ is the so-called Haar measure, which is well known in the literature [78]. This measure is invariant under the action of the $SU(3)$ group

$$dU = d(UV) = d(VU), \qquad \text{for } V \in SU(3), \tag{5.41}$$

and normalized

$$\int dU = 1. \tag{5.42}$$

The integral over fermion fields can be written as a determinant over the Wilson-Dirac operator [78]

$$Z = \int D[U] \exp\Big(-S_G^{\text{imp}}[U]\Big) \prod_f \det(D_f). \tag{5.43}$$

In the following, we drop the superscript "imp" for simplicity.

5.4.1 Monte Carlo sampling

Correlation functions of fermionic fields can then be expressed using the generating functional

$$Z[\xi,\overline{\xi}] = \int D[U] \exp\Big(-S_G[U]\Big) \prod_f \det(D_f) \exp\Big(\sum_f \xi_f \psi_f + \overline{\psi}_f \overline{\xi}_f\Big) \tag{5.44}$$

For the expectation value we get

$$\begin{aligned}
\langle\Omega|T\{\overline{\psi}_{f_1}(x_1)\psi_{f_2}(x_2)\cdots\}|\Omega\rangle &= \frac{1}{Z}\Big(-\frac{\delta}{\delta\overline{\xi}_{f_1}(x_1)}\Big)\Big(-\frac{\delta}{\delta\xi_{f_2}(x_2)}\Big)\Big(\ldots\Big) Z[\xi,\overline{\xi}]\Big|_{\overline{\xi}_{f_1},\xi_{f_2},\cdots=0} \\
&= \frac{1}{Z}\int D[U]\exp\Big(-S_G^{\text{imp}}[U]\Big)\prod_f \det(D_f) \\
&\qquad \Big(\frac{\delta}{\delta\overline{\xi}_{f_1}(x_1)}\Big)\Big(\frac{\delta}{\delta\xi_{f_2}(x_2)}\Big)\Big(\ldots\Big)\exp\Big(\sum_f \overline{\xi}_f D_f^{-1}[U]\xi_f\Big)\Big|_{\overline{\xi}_{f_1},\xi_{f_2},\cdots=0}.
\end{aligned} \tag{5.45}$$

Here, we have used the trick that we have already explained in Eq. 2.11 to rewrite the exponential of a bilinear of two fields in terms of the inverse of the Dirac operator. This is the key equation for the computation of observables in lattice QCD. The integral over all possible configurations of the gauge link can be estimated by a Monte Carlo simulation using importance sampling. The gauge links are

sampled according to a probability density function

$$dP[U] = \frac{\exp(-S_G[U])}{Z} D[U] \prod_f \det(D_f). \tag{5.46}$$

The expectation value can then be estimated by an average over different gauge configurations U_i ($i = 1, 2, \dots N$),

$$\langle \Omega | T\{\overline{\psi}_{f_1}(x_1)\psi_{f_2}(x_2)\cdots\}|\Omega\rangle \approx \frac{1}{N}\sum_{i=1}^{N}\Big(\frac{\delta}{\delta\overline{\xi}_{f_1}(x_1)}\Big)\Big(\frac{\delta}{\delta\xi_{f_2}(x_2)}\Big)\Big(\dots\Big)\exp\Big(\sum_f \overline{\xi}_f D_f^{-1}[U_i]\xi_f\Big)\Big|_{\overline{\xi}_{f_1},\xi_{f_2},\dots=0}, \tag{5.47}$$

where the inverse of the Dirac operator D_f^{-1} is evaluated on each gauge configuration. The statistical error of this result scales with $O(\frac{1}{\sqrt{N}})$ according to the central limit theorem. With Eq. 5.47 general n-point functions of fermionic operators can be evaluated. This is also true for observables containing combinations of Dirac matrices γ_μ such as the electromagnetic vector current, e.g. for the up quark

$$\begin{aligned}\langle \Omega | T\{\overline{u}(x_1)\gamma_\mu u(x_1)\overline{u}(x_2)\gamma_\nu u(x_2)\}|\Omega\rangle \quad \approx \quad & \frac{1}{N}\sum_{i=1}^{N}\Big(-Tr\Big[D_u^{-1}(U_i;x_1,x_2)\gamma_\mu D_u^{-1}(U_i;x_2,x_1)\gamma_\nu\Big] \\ & + Tr\Big[D_u^{-1}(U_i;x_1,x_1)\gamma_\mu\Big]Tr\Big[D_u^{-1}(U_i;x_2,x_2)\gamma_\nu\Big]\Big).\end{aligned} \tag{5.48}$$

In practice, it can be challenging to compute the inverse of the Dirac operator D_f^{-1}, since its dimension scales with the lattice volume V. It is not feasible to compute the all-to-all propagator from every lattice point x_1 to every other point x_2 since this scales with V^2. The one-to-all propagator on the other hand, can be evaluated even for large lattices, e.g. $N_L = 96$, on modern supercomputers. A trick for computing Eq. 5.48 is to exploit the γ_5 hermiticity to express the propagator from x_2 to x_1 through

$$D_u^{-1}(U_i;x_2,x_1) = \gamma_5 D_u^{-1}(U_i;x_1,x_2)^\dagger \gamma_5 \tag{5.49}$$

such that one only needs to compute $D_u^{-1}(U_i;x_1,x_2)$.

5.4.2 Markov chains

A major challenge for numerical calculations in lattice QCD is to find a set of gauge configurations that are distributed in accordance with the Boltzmann weight defined in Eq.5.46. This can be achieved by use of the Markov process [78]. We start from an arbitrary gauge configuration U_0 and generate subsequent configurations

$$U_0 \to U_1 \to U_2 \to \dots, \tag{5.50}$$

where we define the simulation time $\tau = 1, 2, 3$ as the index of each subsequent gauge configuration. To this end, we define the probability for a transition from configuration U to U' as $T(U', U)$. The

equilibrium is reached, when the equation of balance is satisfied [78]

$$\sum_U T(U',U)dP[U] = \sum_U T(U,U')dP[U'] \tag{5.51}$$

To achieve this, we impose the even stronger equation of detailed balance on the transition probability

$$T(U',U)dP[U] = T(U,U')dP[U'] \tag{5.52}$$

for each update of the gauge configuration U to the new configuration U'. With this constraint the equilibrium is eventually reached. This process is called thermalization. In practice it is not trivial to determine when the equilibrium is reached. For this purpose one typically computes observables such as the topological charge [78] and monitors their behaviour in relation to the simulation time τ.

However, there are two crucial requirements for the Markov process that one needs to pay attention to. The probability distribution has to be real and non-negative. Working in the Euclidean-space formulation the Boltzmann factor $\exp(-S_G[U])$ is real. One can easily show that the fermion determinant is also strictly real,

$$\det(D_f^\dagger) = \det(\gamma_5 D \gamma_5) = \det(D) \tag{5.53}$$

However, it is not generally true that the weight distribution is non-negative. The CLS ensembles are generated for degenerate up and down quark flavours, thus preserving isospin symmetry. We will refer to them as *light* (l) quarks. Thus, we have

$$\det(D_u)\det(D_d) = \det(D_l)\det(D_l) = \det(D_l D_l^\dagger) \geq 0. \tag{5.54}$$

But, for the strange quark there is no mechanism preventing $\det(D_s)$ to have negative eigenvalues. We will address this issue in section 5.4.5. On the CLS ensembles that we use in this thesis, only the light and strange quark determinants are taken into account.

Note that one can still make a measurement of the Dirac operator according to Eq. 5.47 using the parameters of the heavier quarks, such as the charm. This is the so called partially quenched approximation, in reminiscence of the fully quenched approximation of the weight distribution which refers to setting all quark determinants to $\det(D_f) = 1$.

As a side remark, the case of a non-strictly positive weight distribution also occurs, when a chemical potential μ for quarks is introduced. This famously known as the *sign problem* [131], [132], [133].

5.4.3 Hybrid Monte Carlo

In this section, we want to discuss the Hybrid Monte Carlo (HMC) algorithm [134] that is used for the generation of gauge configurations with dynamical fermions. The first step is to rewrite the fermion determinant as a Gaussian functional integral over bosonic fields that we call *pseudo-fermions* ϕ and

$\phi^\dagger$, according to Ref. [135]. For a non-negative fermion the determinant is given by

$$\det\left(D_f D_f^\dagger\right) \propto \int D[\phi] D[\phi^\dagger] \exp\left(-\phi^\dagger (D_f D_f^\dagger)^{-1} \phi\right). \tag{5.55}$$

We do not need to know the exact constant of proportionality since this would divide out with the factor $\frac{1}{Z}$. In the next step we introduce auxiliary momentum fields $\pi_\mu(n,\tau)$ which depend on the lattice coordinate n and the simulation time τ. These fields are elements of the Lie algebra $\mathfrak{su}(3)$

$$\pi_\mu(n,\tau) = \pi_\mu^i(n,\tau)\lambda^i, \tag{5.56}$$

where λ are the generators of $\mathfrak{su}(3)$, which we defined previously in Eq. 3.2. The elements π_μ^i are the conjugate momenta of the gauge fields $A_\mu^i(n,\tau)$ for a given parameter of the simulation time τ. If we now introduce the conjugate momenta in the partition function as

$$Z = \int D[U] D[\phi,\phi^\dagger] D[\pi,\pi^\dagger] \exp\left(-\frac{1}{2}\sum_n Tr[\pi_\mu \pi_\mu^\dagger] - S_G[U] - \phi^\dagger \left(D_f D_f^\dagger\right)^{-1} \phi\right), \tag{5.57}$$

an expectation value computed with this partition function

$$\langle\Omega|O|\Omega\rangle = \frac{\int D[U] D[\phi,\phi^\dagger] D[\pi,\pi^\dagger] O[U] \exp\left(-\frac{1}{2}\sum_n Tr[\pi_\mu \pi_\mu^\dagger] - S_G[U] - \phi^\dagger \left(D_f D_f^\dagger\right)^{-1} \phi\right)}{\int D[U] D[\phi,\phi^\dagger] D[\pi,\pi^\dagger] \exp\left(-\frac{1}{2}\sum_n Tr[\pi_\mu \pi_\mu^\dagger] - S_G[U] - \phi^\dagger \left(D_f D_f^\dagger\right)^{-1} \phi\right)} \tag{5.58}$$

is identical to an expectation value computed according to the partition function in Eq. 5.44. But, we can recognize the Hamiltonian of the microcanonical ensemble [78]

$$H[\pi,U] = \frac{1}{2}\sum_n Tr[\pi_\mu \pi_\mu^\dagger] + S_G[U] + \phi^\dagger \left(D_f D_f^\dagger\right)^{-1} \phi. \tag{5.59}$$

For this Hamiltonian the equations of motion in simulation time τ are given by the molecular dynamics equations

$$\frac{d\pi_\mu(n,\tau)}{d\tau} = -\frac{d(S_G[U] + \phi^\dagger \left(D_f D_f^\dagger\right)^{-1} \phi)}{dA_\mu^i(n,\tau)}, \qquad \frac{dA_\mu^i(n,\tau)}{d\tau} = \pi_\mu^i(n,\tau). \tag{5.60}$$

By using the definition of the gauge link 5.5 we obtain a differential equation for the gauge field on every lattice site for a given simulation time

$$\frac{dU_\mu(n,\tau)}{d\tau} = i\pi_\mu(n,\tau) U_\mu(n,\tau) \tag{5.61}$$

Integrating this differential equation for $U_\mu(n,\tau)$ numerically will generate a new field configuration, while evolving in simulation time. To this end, we start with a random distributed auxiliary complex field χ that is sampled randomly according to a Gaussian distribution $\exp(-\chi^\dagger\chi)$. The

pseudo-fermions are then given by

$$\phi = D_f \chi. \tag{5.62}$$

We then compute the conjugate momenta π_μ for a start configuration U_μ according to a Gaussian distribution $\exp(-Tr[\pi^\dagger \pi])$. Afterwards, we need to evolve U_μ and π with respect to the simulation time τ, thus generating a new candidate gauge configuration U'_μ and conjugate momenta π'. There are many algorithms to achieve this. The CLS ensembles are generated with the Omelyn, Mryglod and Folk (OMF) integrator [136]. But, one could also use other integrators such as the leapfrog algorithm [78]. These methods only need to fullfill the following two properties [78]. The area of the integration measure $D[U]D[\pi,\pi^\dagger]$ needs to be preserved and the trajectory needs to be reversible, i.e. $T(\pi', U'|\pi, U) = T(-\pi, U|-\pi', U')$.

For a perfect new solve of the molecular dynamics equation, the new gauge configuration U'_μ would be a valid successor of the gauge configuration U_μ in the Markov chain. However, the numerical integration introduces an error. To mitigate this problem, the last step of the HMC is an accept-reject step. The new gauge configuration is accepted if a random number $r \in [0,1)$ is smaller than the acceptance probability

$$r < T(U'_\mu, \pi'_\mu | U_\mu, \pi_\mu) = \min\Big(1, \frac{\exp(-H[U', \pi', \phi, \phi^\dagger])}{\exp(-H[U, \pi, \phi, \phi^\dagger])}\Big). \tag{5.63}$$

This last step is called *Metropolis step*. It guarantees that the equation of detailed balance 5.52 is fulfilled and we will eventually reach thermal equilibrium. At this point, gauge configurations are stored and used to compute the expectation value of observables according to 5.47.

5.4.4 Twisted mass reweighting

For two mass degenerate light quarks the fermion determinant $\det(D_l^\dagger D_l)$ fulfills the property of non-negativity required for the HMC algorithm. However, in practice the Dirac operator can have eigenvalues that are zero or smaller than the quark mass, which results in surfaces in configuration space that the HMC algorithm can not cross [137]. This leads to instabilities in the process of generating gauge configuration. A solution proposed by Lüscher and Palombi [138] suggests the introduction of a small twisted-mass parameter μ in the fermion determinant for the light quarks

$$\det(D_l^\dagger D_l) \to \det\Big(\frac{D_l^\dagger D_l + \mu^2}{D_l^\dagger D_l + 2\mu^2}\Big). \tag{5.64}$$

For the computation of an observable O one needs to compensate for this twisted-mass by reweighting the measurement of the observable

$$\langle O \rangle = \frac{\langle OW \rangle_\mu}{\langle W \rangle_\mu}, \tag{5.65}$$

where $\langle\rangle_\mu$ denotes the expectation value computed with the action with the twisted mass. The reweighting factor

$$W = \det\Big(\frac{D_l^\dagger D_l (D_l^\dagger D_l + 2\mu^2)}{(D_l^\dagger D_l + \mu^2)}\Big) \tag{5.66}$$

is evaluated stochastically on each gauge configuration.

5.4.5 Rational approximation for the strange determinant

Since the strange quark determinant has no mass degenerate counterpart, we can not simply write down a term like $\det(D^\dagger D)$ for it. But instead, one can use a rational approximation R of the square root of the Dirac operator $R = \sqrt{D^\dagger D}$ to write the strange determinant as

$$\det(D_s) = W_s \det(R^{-1}), \tag{5.67}$$

where Zolotorev's optimal parameters for that approximation can be found in Ref. [137]. W_s is the strange reweighting factor $W_s = \det(D_s R)$ that needs to be compensated for by reweighting the expectation value of an observable similar to Eq. 5.65.

5.5 Scale setting

Results of calculations on the lattice are always dimensionless quantities, such as ratios between different physical observables [78]. In order to compare these results for experiments one needs to relate these results to a physical scale. To this end, one needs to determine a value for the lattice spacing a in physical units, which can then be used to convert a calculated dimensionless mass aM to the physical value M. This procedure is known as *scale setting*. There are different methods for determining this scale parameter. We want to discuss the Wilson flow, which is used to define the parameter t_0 which is often used to parametrize the scale setting quantities.

5.5.1 Wilson flow

The Wilson flow introduces a new parameter [139], which is called the flow time t. This is not to be confused with the actual euclidean time coordinate x_4. We introduce the flow $B_\mu(t,x)$ that is given by the continuum gauge field evolve in flow time as governed by the equations

$$\frac{\partial B_\mu}{\partial t} = D_\nu G_{\nu\mu}(B), \qquad B_\mu(0,x) = A_\mu(x), \tag{5.68}$$

$$G_{\mu\nu}(B) = \partial_\mu B_\nu - \partial_\nu B_\mu + [B_\mu, B_\nu], \quad D_\mu = \partial_\mu + [B_\mu, .]. \tag{5.69}$$

The associated flow for the gauge link on the lattice, the Wilson flow, $V_\mu(t,x)$ is then defined by the equations

$$\frac{\partial V_\mu(t,x)}{\partial t} = -g_0^2\{\partial_{x,\mu} S_G[V]\}V_\mu(t,x), \qquad V_0(x,\mu) = U_\mu(0,x) \tag{5.70}$$

in which $\partial_{x,\mu}$ stands for the natural $\mathfrak{su}(3)$-valued differential operator with respect to the link variable $V_\mu(t,x)$ [139] and $S_G[V]$ is the Wilson gauge action defined in Eq. 5.9, but with the gauge link U_μ replaced by V_μ in the plaquette.

If we consider the continuum observable $E = \frac{1}{4}G_{\mu\nu}(B)G_{\mu\nu}(B)$ then asymptotic freedom implies that the combination $t^2\langle E\rangle$ goes to zero in the limit $t \to 0$. We define the reference scale t_0 with the condition

$$\left\{t^2\langle E\rangle\right\}_{t=t_0} = 0.3. \tag{5.71}$$

5.5.2 Choice of parameters

In order to relate a physical scale to the observables computed in lattice QCD, we need to define a set of scale setting quantities. We want to relate the physical value for these quantities with the result of the lattice calculation. The CLS ensembles that we use for our calculation are generated in isospin symmetric QCD, which means that the up and down quark are implemented with the same mass and effects from QED are not taken into account. But, since these effects are present in the 'real' world, one can not relate the isospin symmetric calculation to the true physical point, but rather a reference point that is very close to the physical point. This results in a very subtle ambiguity in the result computed from different lattice groups if they do not use the same reference point.

In total, we need to pick three physical observables as scale setting quantities. It is preferable to choose quantities that fulfill some specific properties: The observable should be easy to calculate on the lattice with small statistical error. It should be a quantity that is accessible to direct measurement in an experiment with high precision. The effects of isospin breaking should be as small as possible. In practice it is not easy to find three observables with these properties.

Two reliable observables are the pion and kaon mass m_π and m_K. These quantities are relatively easy to compute on the lattice [110] and are experimentally well determined. We define the pion and kaon mass for the physical point in the isospin symmetric theory similar to Ref. [23] as

$$m_\pi = 134.9768(5)\text{MeV}, \qquad m_K = 495.011(10)\text{MeV}. \tag{5.72}$$

But, we still need a third observable for defining the lattice scale a. A first strategy to determine the scale for new ensembles can be to use the reference scale in flow time defined in Eq.5.71 as first applied for the $N_f = 2+1$ CLS ensembles in Ref. [110]. This quantity is not accessible to the experiment but can be obtained from another lattice simulation. However, it is dependent on the

particular number of flavours of dynamical quarks used in the simulation. One finds $\sqrt{8t_o} = 0.4341(33)$ fm for two-flavour QCD with Wilson fermions [140]. We will adopt the strategy proposed in Ref. [110] to use the combination of the pion and kaon decay constants.

$$f_{K\pi} = \frac{2}{3}\Big(f_K + \frac{1}{2}f_\pi\Big). \tag{5.73}$$

To perform a chiral extrapolation, we need to define a chiral trajectory in the (m_l, m_s) plane. To this end, we define the dimensionless parameters

$$\phi_2 = 8t_0 m_\pi^2, \qquad \phi_4 = 8t_0(m_K^2 + \frac{1}{2}m_\pi^2), \tag{5.74}$$

where we use the value of t_0 as an intermediate scale. In this work, we will only use the CLS ensembles that are on the line of $\mathrm{Tr}M_q = 2m_l + m_s = \text{const}$. By using Eq. 4.7 we see that ϕ_4 is then constant to leading order in χPT. For determining the lattice space an iterative ansatz is used in Ref. [110]. First one starts with a generic value for t_0. Then one calculates the result for $\sqrt{8t_0}f_{K\pi}$ on each ensemble. This value is extrapolated to the physical point in the (ϕ_2, ϕ_4) plane which we denote by $(\sqrt{8t_0}f_{K\pi})_{\text{phys}}$. Now, we can take the ratio

$$\frac{(\sqrt{8t_0}f_{K\pi})_{\text{phys}}}{(f_{K\pi})_{\text{exp}}}, \tag{5.75}$$

where $(f_{K\pi})_{\text{exp}}$ is the experimental input. The resulting ratio has to be equal to the initial guess for $\sqrt{8t_0}$. If that is not the case the steps are repeated with a different initial guess, eventually reaching the correct ratio. The study in Ref. [110] found

$$(\sqrt{8t_0})_{\text{phys}} = 0.415(4)(2)\text{fm}. \tag{5.76}$$

A more recent work by RQCD in 2022 [141], which relies not on $f_{K\pi}$ but on the Ξ baryon mass, found the value $(\sqrt{8t_0})_{\text{phys}} = 0.4098(19)(25)$fm. To determine the lattice spacing a for a given value of the bare coupling β one can calculate $\frac{t}{a^2}$ on each ensemble that was generated with that value of β and extrapolate to the physical point $(t_0)_{\text{phys}}$.

5.6 Data analysis

The computation of observables in lattice QCD according to Eq. 5.47 is a stochastic process. This involves performing N measurements of an observable x on a set of statistically indepentent gauge configurations. We denote a measurement of the observable with x_i for $i = 1, 2, \ldots, N$. The average

$$\overline{x} = \frac{1}{N}\sum_i^N x_i \tag{5.77}$$

yields a stochastic estimate of the true expectation value $\langle x \rangle$ that we are interested in [142] [78]. Estimating the true expectation value using the stochastic estimator $\overline{x}$ leads to a statistical error that we need to quantify in order to make a meaningfull physical prediction. In principle, this can be done by performing N independent determinations of the estimator $\overline{x}$. However, in practice this is costly, as one needs to make N^2 measurements. Instead, one relies on resampling techniques such as the Jackknife or Bootstrap method [78] [142].

5.6.1 Estimation of uncertainties using the Jackknife procedure

The Jackknife method is a technique which generates N different stochastic estimator $\overline{x}_j$ from the N original measurements. A Jackknife set on which the estimator $\overline{x}_j$ is calculated is constructed by removing the jth measurement from the original sample. On this subset of the original data we calculate the mean

$$\overline{x}_j = \frac{1}{N-1} \sum_{i=1, i\neq j}^{N} x_i. \tag{5.78}$$

This way we obtain N different estimators $\overline{x}_j$ with $j = 1, 2, \ldots N$. The standard deviation can then be calculated using the squared difference between the estimators calculated on the Jackknife sets with the estimator $\overline{x}$ calculated on the full dataset.

$$\sigma^2_{\overline{x}} = \frac{N-1}{N} \sum_{j=1}^{N} (\overline{x} - \overline{x}_j)^2. \tag{5.79}$$

The result for the observable is then given by $\overline{x} \pm \sigma_{\overline{x}}$ [78]. However, this can introduce a bias, which can be corrected by computing the average of all means on the Jackknife subsets

$$\tilde{x} = \frac{1}{N} \sum_{j=1}^{N} \overline{x}_j. \tag{5.80}$$

The bias corrected estimator is then given by [142]

$$\overline{x} - (N-1)^{-1}(\tilde{x} - \overline{x}). \tag{5.81}$$

5.6.2 Fitting

For most practical cases it is not sufficient to determine the expectation value on a single gauge ensemble, but instead one needs to compute the quantity on many ensembles and perform a fit in order to obtain the desired physical observable. This is the case if one wants to perform a continuum extrapolation. Also in many cases, one only has access to unphysical pion masses. The result at physical pion mass can then be obtained by performing a fit along a trajectory of results computed with different pion masses. In these scenarios one often relies on the method of χ^2-fitting [78]. For

a given set of measurements y_i, y_i', where each measurement is taken in for the parameter x_i, x_i' respectively, in which one wants to extrapolate or interpolate the result, one defines the quantity

$$\chi^2 = \sum_i^N (y_i - f(x_i, \boldsymbol{A}))\mathrm{Cov}^{-1}(x_i, x_i')(y_i' - f(x_i', \boldsymbol{A})), \tag{5.82}$$

where $\mathrm{Cov}(x_i, x_i')$ is the covariance matrix of the parameters and $f(x, \boldsymbol{A})$ is the hypothesis function depending on multiple fit parameters $\boldsymbol{A} = (A_1, A_2, \ldots)^T$. This function models the dependence of the measurements y_i with respect to the parameters x_i. The analytic form of $f(x, \boldsymbol{A})$ is often guided by some additonal knowledge about the dependance of y_i with respect to x_i. This can be drawn for example from prediction from chiral perturbation theory in the case of a fit to different pion masses. If one neglects the correlation betwen the diffent data points that are used Eq. 5.83 simplifies to

$$\chi^2 = \sum_i^N \frac{(y_i - f(x_i, \boldsymbol{A}))^2}{\sigma_i^2}, \tag{5.83}$$

where σ_i is the standard deviation of the i measurement.

The model parameters $\boldsymbol{A}$ are obtained from minimizing χ^2 with respect to $\boldsymbol{A}$. In many cases it is useful to define the reduced χ^2

$$\chi^2/\mathrm{DOF} = \frac{\chi^2}{N - M}, \tag{5.84}$$

where N is the number of measurements and M is the number of fit parameters A_i. $N - M$ is the total number of degrees of freedom (DOF). If χ^2/DOF is not of order unitiy, the data is not well described by the model. For $\chi^2/\mathrm{DOF} >> 1$ and $\chi^2/\mathrm{DOF} << 1$ the model is not capable of describing the correlation in the data accurately. Especially a value of $\chi^2/\mathrm{DOF} << 1$ is a clear sign of overfitting. This can easily happen if one chooses a model with too many fit parameters. But, this can also happen, when one estimates the uncertainties σ_i^2 for the individual data much larger than the true uncertainty.

5.6.3 Model averaging

In most cases where one wants to fit a model to a given dataset, the true function describing the correlation in the data is not known. There might be several hypothesis functions $f(x_i, \boldsymbol{A})$ that are equally well motivated with similar χ^2, or one wants to test how much the result changes if one only uses subsets of the data. An example in lattice QCD is the continuum limit. There, one often wants to check how stable the fit is against leaving out data computed at typically the coarser lattice spacings, to ensure that one can trust the continuum extrapolation.

In these cases, one can make use of the procedure of model averaging. In these cases one performs multiple fits with different hypothesis functions that can depend on a different number of parameters to different subsets of the data. The different fits are weighted according to an information criterion,

such aus the Akaike Information Criterion (AIC) [143] [144].

$$w_i = \frac{1}{N}\exp\Big[-\frac{1}{2}(\chi^2 + 2k - 2n)\Big], \tag{5.85}$$

where k is the number of fit parameters and n is the number of data points that are included. N is chosen such that the sum of all weights adds up to one. One can then compute the model average for each of the results for the extrapolated quantity O_i computed from the individual fits by

$$\overline{O} = \sum_i w_i O_i \tag{5.86}$$

and the uncertainty as

$$(\sigma^2)_{\text{av}} = \sum_i w_i (\sigma^2)_{O_i}. \tag{5.87}$$

Often one adds to that the additional uncertainty coming from the model averaging as the variance of the different results from each fit,

$$(\sigma^2)_{\text{AIC}} = \sum_i w_i (O_i - \overline{O})^2 \tag{5.88}$$

such that $(\sigma^2)_{\text{total}} = (\sigma^2)_{\text{av}} + (\sigma^2)_{\text{AIC}}$.

6 Hadronic vacuum polarization contribution to $(g-2)_\mu$

Now, that we have established the basics in the previous chapters, we want to focus on the calculation of the hadronic vacuum polarization contribution to the anomalous magnetic moment of the muon a_μ. In the theory community this quantity is of main interest because it generates the largest part of the uncertainty of the theory prediction for a_μ. We will first take a look at the dispersive approach [20, 30–40, 50–53, 55–62], which was used to obtain the result given in the White Paper [17]. Then we will review the common method for calculating a_μ^{hvp} in lattice QCD, the so called time-momentum representation [21, 22, 41–49, 54, 63] . Lastly, we will look at different partial contributions to a_μ^{hvp} defined by euclidean time windows to disentangle the different systematic uncertainties of lattice calculations.

6.1 The dispersive approach

The dispersive approach is based on unitarity and analyticity of the scattering matrix. The leading-order (LO) contribution to the HVP contribution is written as an integral over the total cross section of a virtual photon decaying into hadrons

$$a_\mu^{HVP,LO} = \frac{\alpha^2}{3\pi^2}\int_{m_\pi^2}^{\infty} ds \frac{K(s)}{s} R(s), \qquad R(s) = \frac{\sigma^0\left(e^+e^- \to \text{hadrons}(+\gamma)\right)}{4\pi\alpha^2/(3s)}, \tag{6.1}$$

where the denominator of the R-ratio is the tree-level cross section $\sigma^0(e^+e^- \to \mu^+\mu^-)$, see figure 6.1 The kernel function is given by

$$K(s) = \frac{x^2}{2}(2-x^2) + \frac{(1+x^2)(1+x)^2}{x^2}\left(\log(1+x) - x + \frac{x^2}{2}\right) + \frac{1+x}{1-x}x^2\log(x), \tag{6.2}$$

where $x = \frac{1-\beta}{1+\beta}$ and $\beta = \sqrt{1-4m_\mu^2/s}$. σ^0 denotes the bare cross section, where effects of the vacuum polarization have to be excluded. This is to ensure that these effects are not double counted in the next-to-leading order (NLO) contribution [17]. It is worth mentioning that the kernel function $\frac{K(s)}{s}$ is large for small s. Therefore $a_\mu^{HVP,LO}$ receives large contributions from the small energy regime. To

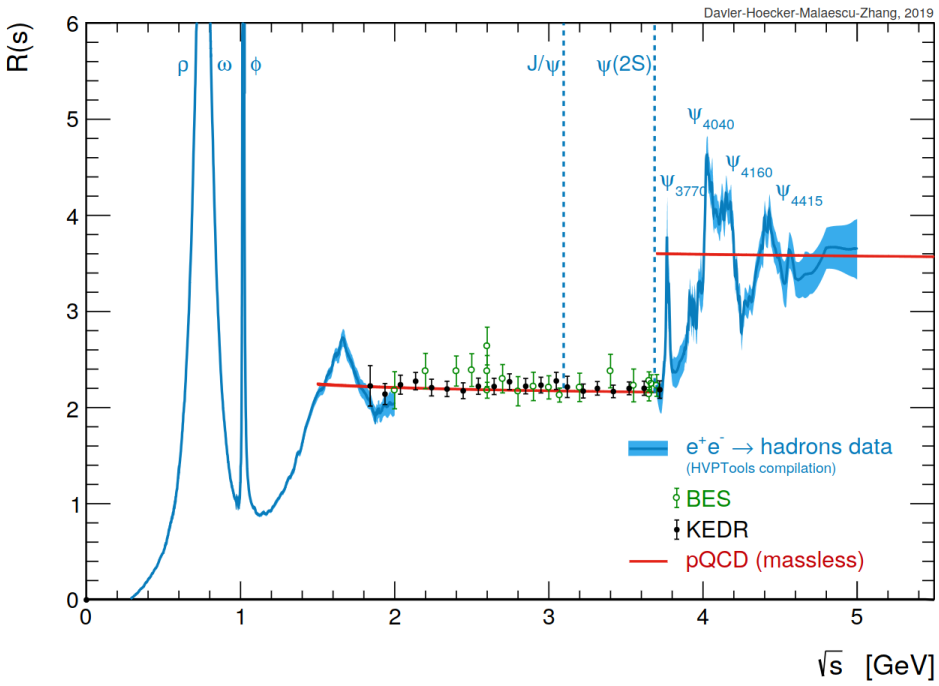

Figure 6.1: The total e^+e^- cross section R ratio, defined in Eq. 6.1 as a function of the energy $\sqrt{s}$ taken from Ref. [34]

obtain $\sigma^0(e^+e^- \to \text{hadrons}(+\gamma))$ the data of several experiments measuring different decay channels and energy regions have to be combined. A detailed analysis of this is provided in Refs. [34, 35, 38, 39]. The most important channel is the $e^+e^- \to \pi^+\pi^-$ channel, which amounts to almost 2/3 of the total $a_\mu^{HVP,LO}$ contribution. This channel has been measured with high precision in the energy region $0.6GeV < \sqrt{s} < 0.88GeV$ by various experiments. However, these experiments do not fully agree within the claimed uncertainties. Especially the long-standing tension between the KLOE and BABAR experiments limited the precision of the theory White Paper in 2020 [17]. A more recent measurement in 2023 with the CMD-3 detector [145] shows an even larger tension with all the previous experiments, with a discrepancy of $> 5\sigma$ to the measurement from the KLOE experiment [31]. Taking the result from CMD-3 only would significantly reduce the tension between the standard model result for the total anomalous magnetic between experimental measurement [33]. However, one can not simply ignore all previous measurements. But, this issue needs to be understood by the physics community to reliably use the data from e^+e^- scattering experiments for data-driven evaluations.

6.2 The hadronic vacuum polarization from lattice QCD

Lattice QCD provides an alternative approach to determine the hadronic vacuum polarization contribution from first principles. The primary observable that can be calculated on the lattice is the

correlator

$$G_{\mu\nu}(x) = \langle j_\mu(x)\, j_\nu(0)\rangle \tag{6.3}$$

of the quark electromagnetic vector current

$$j_\mu = \frac{2}{3}\bar{u}\gamma_\mu u - \frac{1}{3}\bar{d}\gamma_\mu d - \frac{1}{3}\bar{s}\gamma_\mu s + \frac{2}{3}\bar{c}\gamma_\mu c - \frac{1}{3}\bar{b}\gamma_\mu b + \frac{2}{3}\bar{t}\gamma_\mu t. \tag{6.4}$$

The vacuum polarization tensor is given by the Fourier transform of the vector correlator

$$\Pi_{\mu\nu}(Q) = \int d^4x e^{iQ\cdot x} G_{\mu\nu}(x) = (Q_\mu Q_\nu - \delta_{\mu\nu}Q^2)\Pi(Q^2). \tag{6.5}$$

The hadronic vacuum polarization contribution can be obtained from the integral [18]

$$a_\mu^{\text{hvp}} = \left(\frac{\alpha}{\pi}\right)^2 \int_0^\infty dQ^2\, \mathcal{K}(Q^2)\, \overline{\Pi}(Q^2), \tag{6.6}$$

with the subtracted vacuum polarization $\overline{\Pi}(Q^2) = \Pi(Q^2) - \Pi(0)$ and the kernel function

$$\mathcal{K}(Q^2) = \frac{1}{2m_\mu^2}\frac{(v-1)^3}{2v(v+1)}, \quad v = \sqrt{1+4\frac{m_\mu^2}{Q^2}}. \tag{6.7}$$

By rewriting the subtracted vacuum polarization in Eq.6.6 as

$$\overline{\Pi}(Q^2) = \frac{4\pi^2}{Q^2}\int_0^\infty \mathcal{G}(t)\left[Q^2t^2 - 4\left(\sin\left(0.5Qt\right)\right)^2\right]dt. \tag{6.8}$$

Making use of the spatially summed correlator projected onto vanishing spatial momentum

$$\mathcal{G}(t) = -1/3 \sum_{i=1,2,3}\int d^3x\, G_{ii}(t,\boldsymbol{x}), \tag{6.9}$$

and interchanging the integrals, we obtain the time-momentum representation (TMR), first derived in Ref. [146]

$$a_\mu^{\text{hvp}} = \left(\frac{\alpha}{\pi}\right)^2 \int_0^\infty dt\, f(t,m_\mu)\mathcal{G}(t). \tag{6.10}$$

In Eq. 6.10 the hadronic vacuum polarization contribution is given by an integral over Euclidean time weighted with a QED kernel [147]

$$f(t,m_\mu) = \frac{2\pi^2}{m_\mu^2}\left(-2 + 8\gamma_E + \frac{4}{\hat{t}^2} + \hat{t}^2 - \frac{8K_1(2\hat{t})}{\hat{t}} + 8\ln(\hat{t}) + G_{1,3}^{2,1}\left(\hat{t}^2\Big|_{0,1,\frac{1}{2}}^{\frac{3}{2}}\right)\right), \tag{6.11}$$

with $\hat{t} = m_\mu t$. The vector-vector correlator 6.3 is calculated on the lattice by making use of Eq. 5.47. In Eq. 5.48 we have already seen the result if one only takes into account the up quark contribution. Likewise, it is possible to look at the contribution from different quark species, by adjusting the mass

that enters the inverse of the Dirac operator. Eq. 5.48 also shows that there are two possible Wick contractions. We define the quark-connected contribution of flavour f as

$$\mathcal{G}_f(t) = -\frac{1}{N}\sum_{i=1}^{N} -\mathrm{Tr}\Big[D_u^{-1}(U_i;x_1,x_2)\gamma_\mu D_u^{-1}(U_i;x_2,x_1)\gamma_\nu\Big] \tag{6.12}$$

and the quark-disconnected contribution as

$$\mathcal{G}_{\mathrm{disc},ff'}(t) = \frac{1}{N}\sum_{i=1}^{N} \mathrm{Tr}\Big[D_u^{-1}(U_i;x_1,x_1)\gamma_\mu\Big]\mathrm{Tr}\Big[D_u^{-1}(U_i;x_2,x_2)\gamma_\nu\Big], \tag{6.13}$$

where the average is taken over all gauge configurations. Although the two valence quark loops for the quark flavours f and f' in Eq. 6.13 are not connected, evaluating them on a gauge field background gives rise to gluon interactions between the valence quark loops.

The total contribution to the spatially summed vector correlator can now be written as

$$\mathcal{G}(t) = \frac{4}{9}\mathcal{G}_u(t) + \frac{1}{9}\mathcal{G}_d(t) + \frac{1}{9}\mathcal{G}_s(t) + \frac{4}{9}\mathcal{G}_c(t) + \frac{1}{9}\mathcal{G}_b(t) + \frac{4}{9}\mathcal{G}_t(t) + \mathcal{G}_{\mathrm{disc}}(t), \tag{6.14}$$

where $\mathcal{G}_{\mathrm{disc}}(t)$ contains all disconnected contributions. In isospin symmetric QCD, with $m_l = m_u = m_d$ one commonly defines the isovector

$$\mathcal{G}^{I=1}(t) = \frac{1}{2}\mathcal{G}_l(t) \tag{6.15}$$

and isoscalar contributions

$$\mathcal{G}^{I=0}(t) = \frac{1}{18}\mathcal{G}_l(t) + \frac{1}{9}\mathcal{G}_s(t) + \frac{4}{9}\mathcal{G}_c(t) + \frac{1}{9}\mathcal{G}_b(t) + \frac{4}{9}\mathcal{G}_t(t) + \mathcal{G}_{\mathrm{disc}}(t). \tag{6.16}$$

The contribution of the top quark to a_μ^{hvp} can be safely neglected at the current level of uncertainties, due to it's heavy mass [18]. In recent years, many lattice results for a_μ^{hvp} have been published. A few collaborations also computed all contributions [21, 22, 41–49, 54, 63]. But, so far only one group has claimed sub-percent precision [21] [22]. On the lattice there a several challenges that one needs to take into account when calculating a_μ^{hvp}:

1. The vector-vector correlator 6.3 is affected by a signal to noise problem for large Euclidean times.

2. The finite extent of the lattice leads to potentially large finite-volume effects that need to be understood in order to reconstruct the infinite volume result.

3. Since lattice calculations are performed at fixed lattice spacings, one needs to do several calculations at multiple lattice spacings and take the continuum limit.

4. Some lattice calculations are performed at unphysically large pion masses to save computational

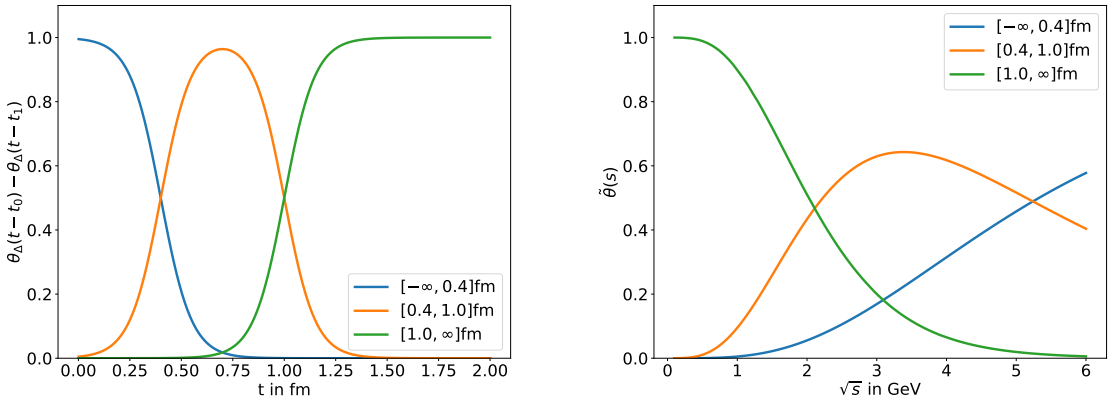

(a) Weight functions in Euclidean time for the short-, intermediate- and long-distance window defined in Eq. 6.18. **(b)** Weight functions for the dispersive representation defined in Eq. 6.20.

cost. For these calculations, one needs to extrapolate the result to the physical point.

6.3 Euclidean time windows in the HVP contribution

To break down the challenge of computing a_μ^{hvp} on the lattice into simpler sub-tasks, the so-called window quantities were first introduced in Ref. [148]

$$a_\mu^{\text{hvp}} = a_\mu^{SD} + a_\mu^{ID} + a_\mu^{LD}, \tag{6.17}$$

where the euclidean-time kernel $f(t)$ of Eq. 6.10 is multiplied with a weight function

$$f_{\text{W}}(t, m_\mu) = \Big[\theta_\Delta(t-t_0) - \theta_\Delta(t-t_1)\Big] f(t, m_\mu) \tag{6.18}$$

with the smooth heaviside theta function $\theta_\Delta(t) = \frac{1}{2}(1+\tanh(\frac{t}{\Delta}))$. The standard choice for the intermediate window is $\Delta = 0.15$ fm, $(t_0^{ID}, t_1^{ID}) = (0.4, 1.0)$ fm. Choosing the same Δ value for short-distance and long-distance window and $(t_0^{SD}, t_1^{SD}) = (-\infty, 0.4)$ fm, $(t_0^{LD}, t_1^{LD}) = (1.0, \infty)$ fm, Eq. 6.17 is satisfied. The different weight functions are shown in Fig.6.2b.

The three window quantities are all still affected by lattice artifacts, but the dominant source of error is different for the three different regions. For the short-distance region, the problem of cutoff effects due to the finite lattice spacing is the dominant source of error, while in the long-distance window the signal to noise problem and the finite-size effects are more severe. In the intermediate distance window the problematic regions are suppressed, promoting a_μ^{ID} to be an excellent benchmark quantity for the comparison between different lattice collaborations and a first step in computing the total contribution to a_μ^{hvp} on the lattice with sub-percent precision.

On the other hand, it is straightforward to obtain a dispersive representation of a_μ^{ID} similar to Eq.

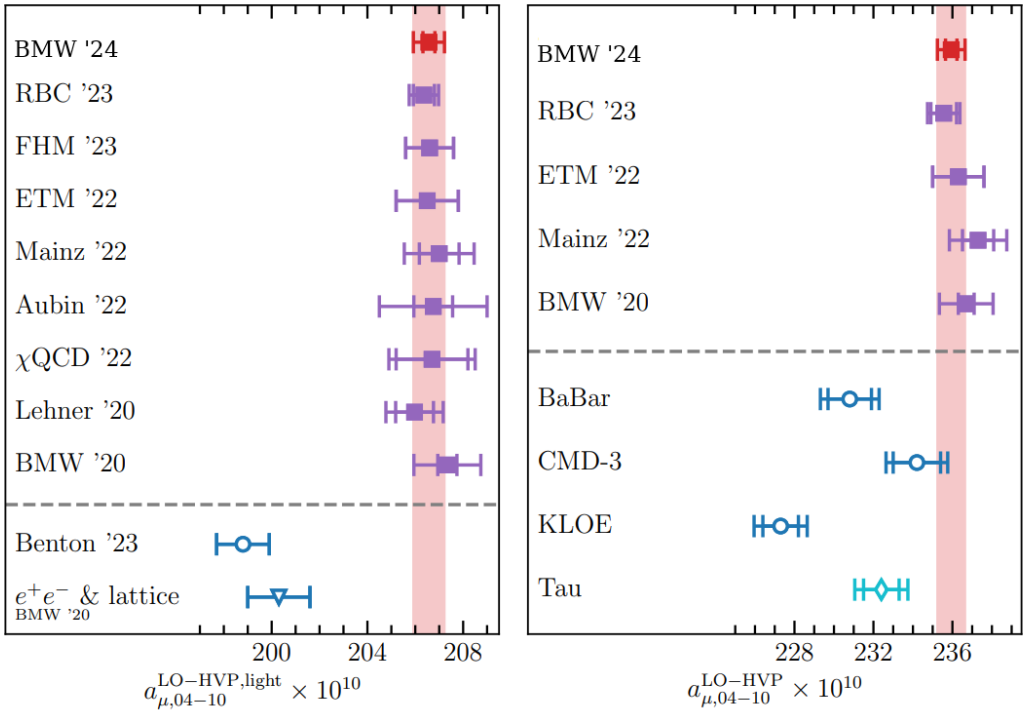

Figure 6.3: Comparison between different results for the light quark-connected contribution (left) and full contribution to the intermediate distance window taken from Ref. [22]. Above the dashed line are results calculated from the lattice and the blue dots are results evaluated with the dispersive approach.

6.1 using

$$a_\mu^{ID} = \frac{\alpha^2}{3\pi^2}\int_{m_\pi^2}^{\infty} ds \frac{K(s)}{s} R(s)\tilde{\theta}(s) \tag{6.19}$$

where

$$\tilde{\theta}(s) = \frac{s^{3/2}}{8m_\mu^2 K(s)}\int_0^\infty dt\Big[\theta_\Delta(t-t_0)-\theta_\Delta(t-t_1)\Big]e^{-t\sqrt{s}}\int_0^\infty ds' w\Big(\frac{s'}{m_\mu^2}\Big)\Big(t^2-\frac{4}{s'}\Big(\sin(t\sqrt{s'}/2)\Big)^2\Big) \tag{6.20}$$

and $w(r) = \frac{(r+2-\sqrt{r(r+4)})^2}{\sqrt{r(r+4)}}$. The dispersive integral 6.19 uses the same experimental data as the leading order HVP contribution 6.1 and can therefore be used as a crosscheck between the dispersive approach and lattice QCD. A detailed analysis of different euclidean time windows is carried out in Ref. [32]. There are several results on the dominant light-connected contribution, see Fig. 6.3 (left) [21–29], which all agree fully within error. Additionally there are 5 results that include the contribution from all quark flavours and also disconnected diagrams to the intermediate window quantity [21–25]. These results also agree perfectly, see see Fig. 6.3 (right). However, one can clearly see a large deviation between the results from lattice QCD and the computations using the dispersive approach.

7 Covariant coordinate-space representation

The covariant coordinate-space (CCS) representation, first derived in Ref. [149], gives an alternative way for computing a_μ^{hvp} on the lattice. Here, we want to introduce the reader to this framework as well as give some example calculations. So far, nearly all lattice results for a_μ^{hvp} [21, 22, 41–49, 54, 63] rely on the time-momentum representation (TMR) given in Eq. 6.10. In the spirit of Feynman's quote from the very beginning of this thesis, we investigate the CCS representation as an alternative approach to the problem. This serves furthermore as a check if Lorentz invariance is correctly restored by the continuum limit in the TMR method, since there the calculation is performed at $\boldsymbol{p} = 0$. On the other hand, we will see that the CCS representation offers additional flexibility in tuning the kernel function to allow for further optimization.

We also expect the master-field approach [150, 151] to benefit from the CCS representation. There only one gauge configuration is generated on a very large lattice. Measurements of a correlation function are taken on a large number of four dimensional spacetime chunks distributed on the masterfield. In the CCS formulation one can simply do a calculation in coordinate space on these chunks and does not need to transform to momentum-space.

We will first derive the CCS representation for a general quantity that depends on the vacuum polarization function $\Pi(Q^2)$ and look at different examples including a_μ^{hvp}. We will then examine some tests of the method using an effective field theory approach.

7.1 Derivation

The covariant coordinate-space (CCS) representation [149] can be derived for a general Lorentz-scalar quantity ϕ that can be obtained from the integral

$$\phi[g] = \int_0^\infty dQ^2 \mathscr{A}(Q^2) g(Q^2). \tag{7.1}$$

for any weight function $g(Q^2)$. The Adler function $\mathscr{A}(Q^2)$ is defined as

$$\mathscr{A}(Q^2) = Q^2 \frac{d}{dQ^2}\Pi(Q^2) \tag{7.2}$$

By reinterpreting the integral in Eq. 7.1 as a four dimensional integral and following the derivation given in Ref. [149], one can write

$$\phi[g] = \int d^4x\, H_{\mu\nu}(x)\, G_{\mu\nu}(x)\,, \qquad G_{\mu\nu}(x) = \langle j_\mu(x)\, j_\nu(0)\rangle, \tag{7.3}$$

with the tensor

$$H_{\mu\nu}(x) = -\delta_{\mu\nu}\mathscr{H}_1(|x|) + \frac{x_\mu x_\nu}{|x|^2}\mathscr{H}_2(|x|). \tag{7.4}$$

We will refer to this as the *CCS kernel* in the following. The kernel functions $\mathscr{H}_1(|x|)$ and $\mathscr{H}_2(|x|)$ are obtained from

$$\mathscr{H}_i(|x|) = \frac{2}{3}\int_0^\infty dQ^2 \frac{h_i(|Q||x|)}{Q^2} g(Q^2) \tag{7.5}$$

with

$$h_1(z) = \frac{3}{8} + \frac{1}{2}J_0(z) - \frac{5}{2}\frac{J_1(z)}{z} + 3\frac{J_2(z)}{z^2}, \tag{7.6}$$

$$h_2(z) = \frac{1}{2z^3}\Big(z(z^2-24)J_0(z) - 8(z^2-6)J_1(z)\Big) \tag{7.7}$$

where $J_n(z)$ is the Bessel function of the first kind. The CCS representation Eq. 7.8 seems more complicated than Eq. 7.1. But, after contracting the Lorentz indices of the kernel $H_{\mu\nu}(x)$ with $G_{\mu\nu}(x)$, the integrand is only a function of $|x|$

$$\phi[g] = 2\pi^2 \int_0^\infty d|x||x|^3\, H_{\mu\nu}(x)\, G_{\mu\nu}(x). \tag{7.8}$$

7.1.1 Non-transverse kernels

One can add a total derivative $\partial_\mu(x_\nu f(|x|))$ to the kernel function which by partial integration can be transferred to the vector-vector correlator. Due to current conservation ($\partial_\mu j_\mu(x)$), the derivative acting on the vector-vector correlator vanishes $\partial_\mu G_{\mu\nu}(x) = 0$. For all the observables we are interested in the following, the surface-term of the partial integration vanishes likewise. This results in an ambiguity in the definition of $H_{\mu\nu}$ in the integral 7.8 in the continuum and infinite volume that we can gain advantage from. By adding a term $\partial_\mu(x_\nu(\mathscr{H}_1(|x|) - \mathscr{H}_2(|x|))$ to $H_{\mu\nu}$ one obtains the traceless ('TL') kernel

$$H^{\mathrm{TL}}_{\mu\nu}(x) = \left(-\delta_{\mu\nu} + 4\frac{x_\mu x_\nu}{|x|^2}\right)\mathscr{H}_2(|x|). \tag{7.9}$$

It is straightforward to obtain a kernel that is only proportional to $x_\mu x_\nu$,

$$H^{\mathrm{XX}}_{\mu\nu}(x) = \frac{x_\mu x_\nu}{|x|^2}\Big(\mathscr{H}_2(|x|) + |x|\frac{d}{d|x|}\mathscr{H}_1(|x|)\Big). \tag{7.10}$$

We will refer to this as the 'XX' kernel regardless of the explicit variable name of the argument. These choices first appeared in Ref. [152]. For completeness, we will denote the original transverse ('TV') kernel as

$$H^{\mathrm{TV}}_{\mu\nu}(x) = -\delta_{\mu\nu}\mathscr{H}_1(|x|) + \frac{x_\mu x_\nu}{|x|^2}\mathscr{H}_2(|x|) \tag{7.11}$$

Since each kernel gives the same result in the continuum and infinite volume, we will often just write

$$H_{\mu\nu}(x) = -\delta_{\mu\nu}\mathscr{H}_1(|x|) + \frac{x_\mu x_\nu}{|x|^2}\mathscr{H}_2(|x|) \tag{7.12}$$

for a generic CCS kernel, if the derivation does not depend on the use of a specific kernel.

7.1.2 Subtracted vacuum polarization

As a first example, we want to consider the case of the subtracted vacuum polarization

$$\overline{\Pi}(Q^2_{\mathrm{ref}}) = \Pi(Q^2_{\mathrm{ref}}) - \Pi(0). \tag{7.13}$$

Using the definition 7.2 and integrating over Q^2 the subtracted vacuum polarization can be written as

$$\overline{\Pi}(Q^2_{\mathrm{ref}}) = \int_0^\infty dQ^2\, g^{\Pi}(Q^2_{\mathrm{ref}})\mathscr{A}(Q^2) \tag{7.14}$$

with

$$g^{\Pi}(Q^2_{\mathrm{ref}}) = \frac{1}{Q^2}\theta(Q^2_{\mathrm{ref}} - Q^2), \tag{7.15}$$

where $\theta(Q^2)$ is the heaviside function. Making use of Eq. 7.5, we obtain the weight functions

$$\mathscr{H}_i(|x|) = x^2 f_i^{\Pi}(|Q||x|) \tag{7.16}$$

$$\begin{aligned} f_1^{\Pi}(z) \quad = \quad & \frac{z^2}{4608}\Big\{24\,{}_2F_3\Big(1,2;2,3,3;-\frac{z^2}{4}\Big) - 20\,{}_2F_3\Big(1,2;2,3,4;-\frac{z^2}{4}\Big) \\ & +3\,{}_2F_3\Big(1,2;2,3,5;-\frac{z^2}{4}\Big)\Big\}, \end{aligned} \tag{7.17}$$

$$f_2^{\Pi}(z) = \frac{z^2}{1152}\Big\{6\,{}_2F_3\Big(1,2;2,3,3;-\frac{z^2}{4}\Big) - 8\,{}_2F_3\Big(1,2;2,3,4;-\frac{z^2}{4}\Big) + 4\,{}_2F_3\Big(1,2;2,4,4;-\frac{z^2}{4}\Big) - {}_2F_3\Big(1,2;2,4,5;-\frac{z^2}{4}\Big)\Big\}, \tag{7.18}$$

where ${}_2F_3$ is the hypergeometric function.

7.1.3 Kernel functions for $a_\mu^{\rm hvp}$

The hadronic vacuum polarization contribution to a_μ in terms of the Adler function can be easily obtained by using partial integration in Eq. 6.6. It is given by

$$a_\mu^{\rm hvp} = \Big(\frac{\alpha}{\pi}\Big)^2 \int_0^\infty \frac{dQ^2}{Q^2} 2\pi^2 \Big(\frac{m_\mu y(|Q|)}{Q}\Big)^4 \mathscr{A}(Q^2(y)) \tag{7.19}$$

where

$$Q^2(y) = \frac{y^2 m_\mu^2}{1-y}, \qquad y(|Q|) = \frac{2|Q|}{|Q| + \sqrt{4m_\mu^2 + Q^2}}. \tag{7.20}$$

Therefore we have

$$g^a(Q^2) = 2\alpha^2 \frac{(m_\mu y(|Q|))^4}{Q^6}. \tag{7.21}$$

The functions $\mathscr{H}_1(|x|)$ and $\mathscr{H}_2(|x|)$ are analytically known and read

$$\mathscr{H}_i(|x|) = \frac{8\alpha^2}{3m_\mu^2} f_i(m_\mu|x|), \tag{7.22}$$

with

$$f_2(z) = \frac{1}{8\sqrt{\pi}z^4}\left[G_{2,4}^{2,2}\left(z^2\Big|_{4,5,1,1}^{\frac{7}{2},4}\right) - G_{2,4}^{2,2}\left(z^2\Big|_{4,5,0,2}^{\frac{7}{2},4}\right)\right] \tag{7.23}$$

and

$$f_1(z) = f_2(z) - \frac{3}{16\sqrt{\pi}}\left[G_{3,5}^{2,3}\left(z^2\Big|_{2,3,-2,0,0}^{1,\frac{3}{2},2}\right) - G_{3,5}^{2,3}\left(z^2\Big|_{2,3,-1,-1,0}^{1,\frac{3}{2},2}\right)\right]. \tag{7.24}$$

Here, $G_{c,d}^{a,b}$ is the Meijer's G function [149]. So, the hadronic vacuum polarization contribution to the anomalous magnetic moment of the muon in the CCS representation is simply given by

$$a_\mu^{\rm hvp} = 2\pi^2 \int_0^\infty d|x||x|^3\, H_{\mu\nu}(x)\, G_{\mu\nu}(x). \tag{7.25}$$

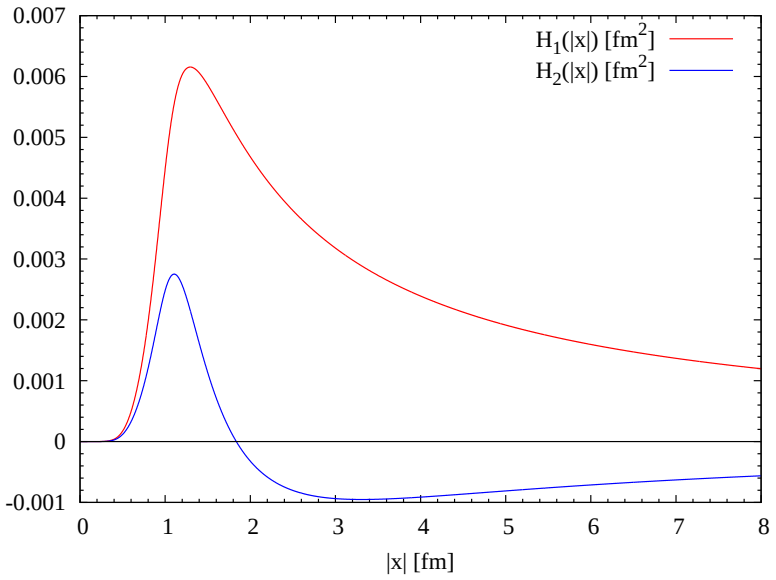

Figure 7.1: The weight functions for obtaining the intermediate window a_μ^W (defined by $t_0 = 0.4$ fm, $t_1 = 1.0$ fm, $\Delta = 0.15$ fm) in the CCS method taken from Ref. [97].

for a generic kernel 7.12.

7.1.4 Intermediate window observable

In this section we want to show how to derive the CCS kernel functions for the intermediate window quantity defined in section 6.3. We start from the expression

$$a_\mu^{ID} = \int_0^\infty dt\, f_W(t)\, G(t). \tag{7.26}$$

We need to write this in terms of the Adler function $\mathscr{A}(Q^2) = Q^2 \frac{d}{dQ^2}\Pi(Q^2)$. In Eq. 6.5 we project onto the Lorentz scalar part and invert the Fourier transform in time to express the spatially summed correlator as

$$G(t) \overset{t\neq 0}{=} \int_{-\infty}^{\infty} \frac{dQ}{2\pi}\, Q^2\, [\Pi(Q^2) - \Pi(0)]\, e^{iQt}. \tag{7.27}$$

Now using the definition on the Adler function 7.2 we can express the subtracted vacuum polarization as

$$\Pi(Q^2) - \Pi(0) = \int_0^{Q^2} \frac{ds}{s}\, \mathscr{A}(s) \tag{7.28}$$

and integrating by parts over Q (i.e. $e^{iQt} = \frac{d}{dQ}\frac{e^{iQt}}{it}$) in Eq. (7.27),

$$G(t) = \frac{1}{\pi}\int_0^\infty \frac{dQ^2}{Q^2}\, \mathscr{A}(Q^2)\, \frac{d^2}{dt^2}\left(\frac{\sin(Qt)}{t}\right). \tag{7.29}$$

Inserting expression (7.29) for the correlator $G(t)$ in Eq. 7.26, one finds

$$a_\mu^W = \int_0^\infty dQ^2\, \mathscr{A}(Q^2)\, g_W(Q^2), \tag{7.30}$$

with

$$g_W(Q^2) = \frac{1}{\pi Q^2} \int_0^\infty dt\, f_W(t)\, \frac{d^2}{dt^2}\left(\frac{\sin(|Q|t)}{t}\right). \tag{7.31}$$

Again, we can make use of Eq. 7.5 to obtain the weight functions for the intermediate window quantity

$$\begin{aligned} \mathscr{H}_i(|x|) &= \frac{2}{3}\int_0^\infty \frac{dQ^2}{Q^2}\, h_i(|Q||x|)\, g_W(Q^2) & (7.32)\\ &= \frac{2}{3\pi}\int_0^\infty dt\, f_W(t)\, \frac{d^2}{dt^2}\left[\frac{1}{t}\int_0^\infty \frac{dQ^2}{Q^4}\, h_i(|Q||x|)\, \sin(|Q|t)\right]. & (7.33) \end{aligned}$$

One finds, with $r = |x|$,

$$\begin{aligned} \frac{1}{t}\int_0^\infty \frac{dQ^2}{Q^4}\, h_1(|Q||x|)\, \sin(|Q|t) &= \frac{\theta(r-t)}{120}\Big(\frac{\sqrt{r^2-t^2}\left(32r^4+11r^2t^2+2t^4\right)}{r^4} \\ &\qquad -45t\arccos(t/r)\Big), & (7.34)\\ \frac{1}{t}\int_0^\infty \frac{dQ^2}{Q^4}\, h_2(|Q||x|)\, \sin(|Q|t) &= \theta(r-t)\frac{\left(r^2-t^2\right)^{5/2}}{15r^4}. & (7.35) \end{aligned}$$

In the second derivatives, needed in Eq. (7.33), the terms proportional to $\delta(t-r)$ or its derivative do not contribute to the $\mathscr{H}_i$, as long as $f_W(t)$ is smooth. One then finds

$$\begin{aligned} \mathscr{H}_1(|x|) &= \frac{2}{9\pi r^4}\int_0^r dt\, \sqrt{r^2-t^2}\left(2r^2+t^2\right) f_W(t), & (7.36)\\ \mathscr{H}_2(|x|) &= \frac{2}{9\pi r^4}\int_0^r dt\, \sqrt{r^2-t^2}\left(4t^2-r^2\right) f_W(t). & (7.37) \end{aligned}$$

It is worth noting that if $f_W(t)$ practically vanishes beyond a distances t_1, then for $|x| \gg t_1$,

$$\begin{aligned} \mathscr{H}_1(|x|) &\simeq \frac{4}{9\pi|x|}\int_0^\infty dt\, f_W(t), & (7.38)\\ \mathscr{H}_2(|x|) &\simeq \frac{-2}{9\pi|x|}\int_0^\infty dt\, f_W(t). & (7.39) \end{aligned}$$

Therefore, these weight functions have a long tail, unlike $f_W(t)$. Still, the $1/|x|$ behaviour amounts to a suppression compared to the weight functions for $a_\mu^{\rm hvp}$, which grow like x^2 at large $|x|$. In the specific case of the 'window quantity', numerical integration of Eqs. (7.36–7.37) yields the weight functions displayed in Fig. 7.1.

7.2 Tests of the CCS representation

A simple test for validating the CCS method is to calculate the leading order QED contribution to the vacuum polarization contribution to $(g-2)_\mu$ [68]. The QED Lagrangian is given by

$$\mathscr{L}_{QED} = \frac{1}{4}F_{\mu\nu}F_{\mu\nu} + \overline{\psi}(\gamma_\mu\partial_\mu + m)\psi + ieA_\mu j_\mu \tag{7.40}$$

with the electromagnetic vector current $j_\mu(x) = \overline{\psi}(x)\gamma_\mu\psi(x)$. We can simply use the method described in section 2.3, to obtain the leading order contribution to the vector-vector correlator

$$\begin{aligned}\langle j_\mu(x)\, j_\nu(y)\rangle &= -\mathrm{Tr}\Big[S_m(x)\gamma_\mu S_m(-x)\gamma_\nu\Big] \\ &= 4\big(2\hat{x}_\mu\hat{x}_\nu - \delta_{\mu\nu}\big)(G'_m(x))^2 - 4\delta_{\mu\nu}m^2(G_m(x))^2,\end{aligned} \tag{7.41}$$

where $S_m(x)$ is the fermionic propagator 2.24 and $G_m(x)$ is the scalar propagator 2.15. to the correlator of two electromagnetic vector currents. By inserting this into Eq. 7.8 and using the weight functions from Eq. 7.22, one can perform the radial integral numerically and verify that the result matches the known result from the literature for $m = m_\mu$ [18]

$$a_\mu^{VP(1)} = \Big(\frac{119}{36} - \frac{\pi^2}{3}\Big)\frac{\alpha^2}{\pi^2}. \tag{7.42}$$

In practice this result can serve as a check for the correct implementation of the CCS kernel in a lattice QCD code.

7.2.1 Vacuum polarization at high energies

In this section, we want to look at the shape of the integrand of Eq. 7.1 for the different kernels for the case of the subtracted vacuum polarization. For the calculation of the hadronic contribution to the running of the electromagnetic coupling one typically relies on lattice QCD for the small energy region and use perturbative QCD for high energies [153]. Here, we want to look at a reference energy $Q^1_{\mathrm{ref}} = 5$ GeV and $Q^1_{\mathrm{ref}} = 7$ GeV, where one can apply perturbation theory. We define the observable

$$\Pi\Big(Q^2_{\mathrm{ref}}\Big) - \Pi\Big(Q^2_{\mathrm{ref}}/4\Big). \tag{7.43}$$

In contrast to the subtracted vacuum polarization defined in Eq. 7.13, this quantity is not affected by non-perturbative effects from the $\Pi(0)$ term if one chooses Q^2_{ref} to be large.

The leading order contribution to the vector-vector correlator for mass degenerate up and down quarks is simply given by the fermion loop calculated in Eq.7.41 with the correct charge factor 5/9 for the light quarks and a factor $N_c = 3$ (number of colors).

$$\langle j_\mu(x)\, j_\nu(y)\rangle_{\text{quark-loop}} = \frac{5}{9}N_c\Big[4\big(2\hat{x}_\mu\hat{x}_\nu - \delta_{\mu\nu}\big)(G'_m(x))^2 - 4\delta_{\mu\nu}m^2(G_m(x))^2\Big], \tag{7.44}$$

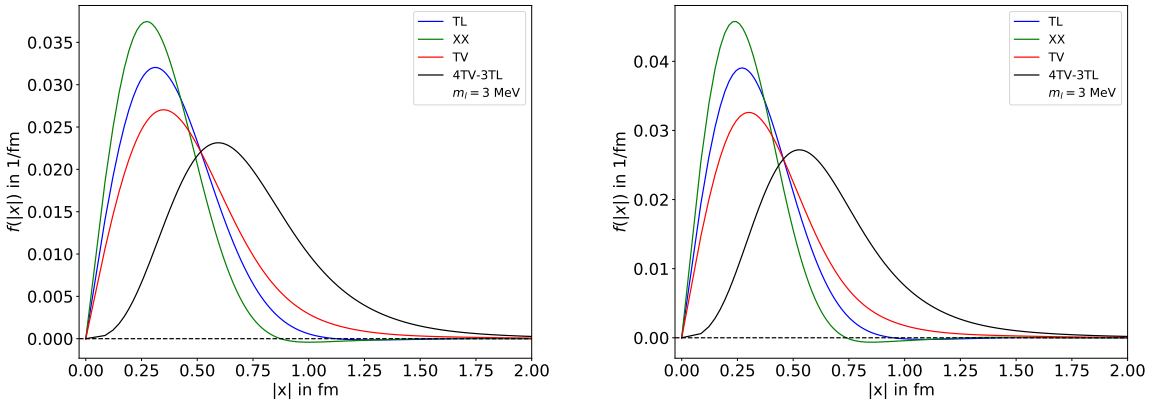

(a) $Q^2 = 5\ \mathrm{GeV}^2$ **(b)** $Q^2 = 7\ \mathrm{GeV}^2$

Figure 7.2: Plot of the integrand of Eq. 7.45 for two different values of Q^2 and four different kernel functions

where m is the mass of the light quarks. In the CCS representation this quantity is now given by

$$\begin{aligned} \Pi\left(Q^2_{\mathrm{ref}}\right) - \Pi\left(\frac{Q^2_{\mathrm{ref}}}{4}\right) &= \int d^4x H_{\mu\nu}(x) \langle j_\mu(0)\, j_\nu(x)\rangle_{\text{quark-loop}} \\ &= \int d|x| f(|x|), \end{aligned} \tag{7.45}$$

with

$$\mathscr{H}_i(|x|) = x^2\left(f_i^{\Pi}(|Q_{\mathrm{ref}}||x|) - f_i^{\Pi}(|Q_{\mathrm{ref}}||x|/2)\right). \tag{7.46}$$

A comparison between the integrand in Eq. 7.45 between the 'TL' 7.9, 'XX' 7.10 and 'TV' 7.11 kernel is shown in figure 7.2. We see that the peak of the integrand for three different kernels is slightly shifted, but more importantly the 'TV' kernel is more long-ranged than the 'TL', which is itself more long ranged than the 'XX' kernel.

If one computes this quantity on the lattice, one needs to have a good resolution of the integrand. For typical lattice spacings between $a = 0.04 - 0.1$ fm it might be more advantagous to choose a kernel that is more long-ranged. It is also possible to tune the kernel by choosing a new kernel that is a linear combination of the others, in order to 'stretch' out the integrand even further. This is for example the case if one computes the integrand with the new kernel

$$H^{4TV-3TL}_{\mu\nu}(x) = 4H^{TV}_{\mu\nu}(x) - 3H^{TL}_{\mu\nu}(x) \tag{7.47}$$

as shown in figure 7.2. This flexibility is a feature of the CCS method, which is not present in the TMR method 6.10. The particular choice of a kernel is dependent on the observable one wants to compute. As lattice calculations suffer from cutoff effects in the infrared (IR) and finite-volume effects

in the ultraviolet (UV) regime a naive approach for finding the optimal kernel is to make sure that the dominant part of the integrand is in the region where the lattice data is most precise.

7.2.2 Sakurai theory prediction for a_μ^{hvp}

For the hadronic contribution to the anomalous magnetic moment of the muon we can not rely on perturbation theory, since the kernel in Eq. 6.6 is peaked in the small energy regime. It is nevertheless possible to get an estimate for the shape of the integrand in the CCS method by making use of the Sakurai effective field theory, which we introduced in section 4.2. To this end, we want to treat the photon field $A_\mu(x)$ as a background field, thus neglecting higher order QED corrections and assume that the Sakurai theory 4.14 is an effective description of QCD for the physics of the light (up and down) quarks below 1 GeV. For now, we do not take into account the strange quark and the heavy quarks. Since the Lagrangian in Eq. 4.14 does not contain the η and π^0, we will constrain ourselves to the isovector ($I = 1$) channel. The isovector contribution to the vector current for the light quarks is given by

$$j_\mu^{(I=1)}(x) = \frac{1}{2}(\overline{u}(x)\gamma_\mu u(x) - \overline{d}(x)\gamma_\mu d(x)). \tag{7.48}$$

If we now assume that the photon is a background field coupled to the isovector part of the vector current, we can use Eq. 3.29

$$\langle j_\mu^{(I=1)}(x)\, j_\nu^{(I=1)}(y)\rangle_{QCD+bQED} = \langle\Big(-\frac{\delta}{\delta A_\mu(x)}\Big)\Big(-\frac{\delta}{\delta A_\nu(y)}\Big)\log\Big((Z[A]^{(I=1)}_{QCD+bQED}\Big)\Big|_{B_\mu=0}\rangle_{QCD}, \tag{7.49}$$

where the partition function for QCD with the photon as a background field is given by

$$Z[A]^{(I=1)}_{QCD+bQED} = \int D[\Phi_{QCD}]\exp\Big(-S_{QCD}[\Phi_{QCD}] - \int d^4x\, j_\mu^{(I=1)}(x)A_\mu(x)\Big), \tag{7.50}$$

where we do not write the field content of QCD explicitly. Assuming now that

$$Z[A]^{(I=1)}_{QCD+bQED} \approx Z[A]_{\text{Sak}} \tag{7.51}$$

holds with

$$Z[A]^{(I=1)}_{\text{Sak}} = \int D[\Phi_{\text{Sak}}]\exp\Big(-\int d^4x\,\mathscr{L}_{\text{Sak}}[\Phi_{\text{Sak}}, A]\Big), \tag{7.52}$$

where the Sakurai QFT Lagrangian is given in Eq. 4.14 and does already include the interaction of the pions and the ρ meson with the photon field. Eq. 7.51 can be seen as a reparametrisation of the gluon and quark degrees of freedom to the pions and ρ meson, where the photon field stays fixed. This is certainly not a derivation, but rather a phenomenological model motivated by the fact that hadronic contribution to $(g-2)_\mu$ in the dispersive approach 6.1 is dominated by the $\pi^+\pi^-$ channel with the ρ

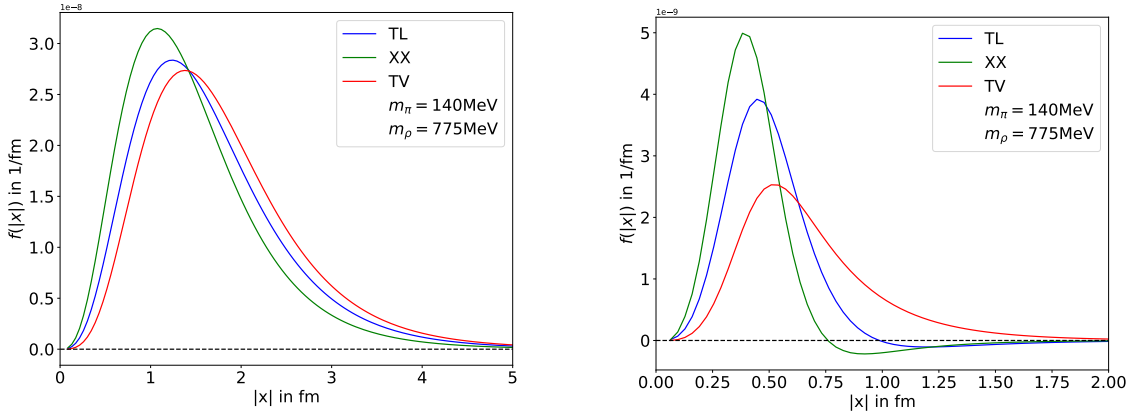

(a) Integrand for a_μ^{hvp}

(b) Integrand for a_μ^{ID}

Figure 7.3: Plot of the integrand of Eq. 7.64 for the three different kernels at approximately physical values for the pion and rho mass. For (a) we use the kernel functions derived in section 7.1.3 to compute the integrand for the contribution to a_μ^{hvp} and in (b) we use the kernel functions from section 7.1.4 to compute the integrand for the intermediate window observable a_μ^{ID}.

meson being the lowest lying vector meson resonance showing up in the $\pi^+\pi^- \to \rho$ channel [18]. We therefore do not assume the $\approx$ to be valid for all observables, but reasonably well motivated for the case of a_μ^{hvp}.

Since the photon degree of freedom is unchanged, we expect the quantity

$$J_{\mu\nu}(x,y) = \langle \left(-\frac{\delta}{\delta A_\mu(x)}\right)\left(-\frac{\delta}{\delta A_\nu(y)}\right) \log\left((Z[A]_{\text{Sak}}\right)\Big|_{A_\mu=0} \rangle \tag{7.53}$$

to be a good approximation for $\langle j_\mu^{(I=1)}(x)\, j_\nu^{(I=1)}(y)\rangle_{QCD+bQED}$ in case Eq. 7.51 holds. We note

$$\frac{\delta S_{\text{Sak}}}{\delta A_\mu(x)} = \frac{e}{g_\gamma}\partial_\alpha F_{\mu\alpha}(\rho) - ie\left(\pi\partial_\mu\pi^* - \pi^*\partial_\mu\pi\right) + 2eg\rho_\mu\pi^*\pi + 2e^2 A_\mu\pi^*\pi. \tag{7.54}$$

It is useful to introduce the vector current of charged pions in scalar QED

$$j_\mu^{sQED} = -i\left(\pi\partial_\mu\pi^* - \pi^*\partial_\mu\pi\right). \tag{7.55}$$

Then we have

$$\begin{aligned} J_{\mu\nu}(x,y) &= \left\langle \frac{\delta S}{\delta A_\mu(x)}\frac{\delta S}{\delta A_\nu(y)}\right\rangle_{\text{conn}} - \left\langle \frac{\delta^2 S}{\partial A_\mu(x)\partial A_\nu(y)}\right\rangle\Big|_{A=0} \qquad (7.56)\\ &= e^2\left\langle \left(j_\mu + \frac{1}{g_\gamma}\partial_\alpha F_{\mu\alpha}(\rho) + 2g\rho_\mu\pi^*\pi\right)_x \left(j_\nu + \frac{1}{g_\gamma}\partial_\beta F_{\nu\beta}(\rho) + 2g\rho_\nu\pi^*\pi\right)_y \right\rangle \\ &\quad -2e^2\delta_{\mu\nu}\delta(x-y)\langle\pi^*\pi\rangle, \qquad (7.57) \end{aligned}$$

where the expectation value is now in the theory without the field A_μ. Evaluating the expectation value to order g^0, counting g_γ/g to be O(1), yields [97]

$$\begin{aligned}\frac{1}{e^2}\,J_{\mu\nu}(x,y) \quad = \quad & \frac{m_\rho^2(m_\rho^2+2\delta m_\rho^2)}{g_\gamma^2}G_{\mu\nu}(x-y)+\frac{1}{g_\gamma^2}\Big(\partial_\mu\partial_\nu-(\triangle+m_\rho^2)\delta_{\mu\nu}\Big)\delta(x-y)\\ & +\Big(1-\frac{g}{g_\gamma}\Big)^2\Big(\langle j_\mu^{\rm sQED}(x)\,j_\nu^{\rm sQED}(y)\rangle_{\rm sQED}-2\delta_{\mu\nu}\delta(x-y)G_{m_\pi}(0)\Big)\\ & +2m_\rho^2(\partial_\mu\partial_\nu-\delta_{\mu\nu}\triangle)\int\frac{d^dk}{(2\pi)^d}\frac{e^{ik(x-y)}}{k^2+m_\rho^2}\Big(\frac{g}{g_\gamma}(1-\frac{g}{g_\gamma})\Pi(k^2)-\frac{\delta g_\gamma^{-1}}{g_\gamma}+\frac{Z_3-1}{g_\gamma^2}\Big)\\ & +\frac{1}{g_\gamma^2}(\partial_\mu\partial_\nu-\delta_{\mu\nu}\triangle)m_\rho^4\int\frac{d^dk}{(2\pi)^d}\frac{e^{ik(x-y)}}{(k^2+m_\rho^2)^2}\,(g^2\Pi(k^2)-(Z_3-1))\\ & -\frac{\delta m_\rho^2}{g_\gamma^2}\Big(\delta_{\mu\nu}\delta(x-y)+\int_k\frac{e^{ik(x-y)}}{(k^2+m_\rho^2)^2}(\delta_{\mu\nu}m_\rho^4+k_\mu k_\nu(2m_\rho^2+k^2))\Big)\\ & +\Big(\frac{2}{g_\gamma}\delta\frac{1}{g_\gamma}-\frac{Z_3-1}{g_\gamma^2}\Big)\Big(\partial_\mu\partial_\nu-\triangle\delta_{\mu\nu}\Big)\delta(x-y)\,,\end{aligned} \tag{7.58}$$

where in dimensional regularization we have

$$G_{\mu\nu}(x)\equiv\langle\rho_\mu(x)\rho_\nu(0)\rangle=\int\frac{d^dk}{(2\pi)^d}\,e^{ikx}\,\frac{\delta_{\mu\nu}+k_\mu k_\nu/m_\rho^2}{k^2+m_\rho^2}=\left(\delta_{\mu\nu}-\frac{1}{m_\rho^2}\partial_\mu\partial_\nu\right)G_{m_\rho}(x). \tag{7.59}$$

and

$$\Pi(k^2)=-\frac{1}{(4\pi)^{d/2}}\Gamma(2-\tfrac{d}{2})\int_0^1 dx\frac{(1-2x)^2}{(x(1-x)k^2+m^2)^{2-d/2}}, \tag{7.60}$$

The renormalization coefficients Z_3 , δ_m and $\delta\frac{1}{g_\gamma}$ are determined to one-loop order by

$$\delta m_\rho^2=m_\rho^2\,g^2\left(k^2\frac{d}{dk^2}\mathrm{Re}\,\Pi(k^2)\right)_{k^2=-m_\rho^2}, \tag{7.61}$$

and the wave-function renormalization

$$Z_3-1=g^2\Big(1+k^2\frac{d}{dk^2}\Big)\,\mathrm{Re}\,\Pi(k^2)\Big|_{k^2=-m_\rho^2}. \tag{7.62}$$

$$\delta\frac{1}{g_\gamma}=g\,\mathrm{Re}\,\Pi(-m_\rho^2). \tag{7.63}$$

Details of the derivation can be found in the appendix of Ref. [97]. In the following we want to calculate the contribution to the HVP contribution using the correlator 7.58

$$a_\mu^{\rm hvp}=\int d^4H_{\mu\nu}(x)J_{\mu\nu}(x,0) \tag{7.64}$$

and compare again the 'TV', 'TL' and 'XX' kernel. The weight functions $f_1(x)$ and $f_2(x)$ defined in 7.23,

7.24 are regular at the origin [149] with

$$\lim_{x\to 0}\frac{f_1(x)}{x^4}=\frac{7}{9216},\qquad \lim_{x\to 0}\frac{f_2(x)}{x^4}=\frac{1}{2304} \tag{7.65}$$

Therefore, we do not need to care about the delta function in Eq. 7.58. Our goal is now to write down Eq. 7.58 in a form that is easy to evaluate numerically. We define

$$J_{\mu\nu}(x,y)=J^{sQED}_{\mu\nu}(x,y)+J^{\rho}_{\mu\nu}(x,y)+J^{(1)}_{\mu\nu}(x,y)+J^{(2)}_{\mu\nu}(x,y)+J^{\delta}_{\mu\nu}(x,y) \tag{7.66}$$

where $J^{sQED}_{\mu\nu}(x,y)$contains the expectation value of the scalar QED vector-vector correlator evaluated without the ρ meson

$$\begin{aligned} J^{sQED}_{\mu\nu}(x,0) &= \Big(1-\frac{g}{g_\gamma}\Big)^2\langle j^{\rm sQED}_\mu(x)\, j^{\rm sQED}_\nu(0)\rangle_{\rm sQED} \\ &= 2\Big(1-\frac{g}{g_\gamma}\Big)^2\Big(\partial_\mu G_{m_\pi}(x)\partial_\nu G_{m_\pi}(x)-G_{m_\pi}(x)\partial_\mu\partial_\nu G_{m_\pi}(x)\Big) \qquad (7.67)\\ &= \frac{m_\pi^6}{2^3\pi^4}\Big[\delta_{\mu\nu}\Big(\frac{K_2(m_\pi|x|)K_1(m_\pi|x|)}{(m_\pi|x|)^3}\Big) \\ &\quad +\frac{x_\mu x_\nu}{|x|^2}\Big(-\frac{K_1(m_\pi|x|)^2}{(m_\pi|x|)^2}-4\frac{K_2(m_\pi|x|)K_1(m_\pi|x|)}{(m_\pi|x|)^3}+\frac{K_2(m_\pi|x|)^2}{(m_\pi|x|)^2}\Big)\Big] \qquad (7.68)\end{aligned}$$

where $K_n(x)$ is the modified Bessel function of the second kind. We define

$$\begin{aligned} J^{\rho}_{\mu\nu}(x,0) &= \frac{m_\rho^2(m_\rho^2+2\delta m_\rho^2)}{g_\gamma}G_{\mu\nu}(x)-\frac{\delta m_\rho^2}{g_\gamma^2}\Big(\delta_{\mu\nu}m_\rho^4-\partial_\mu\partial_\nu(2m_\rho^2-\partial_\rho\partial_\rho\Big)G_\rho(x) \\ &= \frac{m_\rho^2}{g_\gamma^2}\Big(m_\rho^2+2\delta m_\rho^2+m_\rho^2\delta m_\rho^2\frac{\partial}{\partial m_\rho^2}\Big)G_{\mu\nu}(x), \qquad (7.69)\end{aligned}$$

$$J^{(1)}_{\mu\nu}(x,0)=2m_\rho^2(\partial_\mu\partial_\nu-\delta_{\mu\nu}\partial_\rho\partial_\rho)\int\frac{d^Dk}{(2\pi)^D}\frac{e^{ixk}}{k^2+m_\rho^2}\Big(\frac{g}{g_\gamma}(1-\frac{g}{g_\gamma})\Pi(k^2)-\frac{\delta\frac{1}{g_\gamma}}{g_\gamma}+\frac{Z_3-1}{g_\gamma^2}\Big), \tag{7.70}$$

$$J^{(2)}_{\mu\nu}(x,0)=\Big(\frac{g}{g_\gamma}\Big)^2m_\rho^4(\partial_\mu\partial_\nu-\delta_{\mu\nu}\partial_\rho\partial_\rho)\int\frac{d^Dk}{(2\pi)^D}\frac{e^{ixk}}{(k^2+m_\rho^2)^2}\Big(\Pi(k^2)-\frac{Z_3-1}{g^2}\Big) \tag{7.71}$$

and $J^{\delta}_{\mu\nu}(x,0)$ as the part containing all δ functions, which we do not need explicitly. In order to calculate the integrals over k, we use the representation of the scalar QED vacuum polarization in terms of the spectral function

$$\Pi(k^2)-\Pi(0)=k^2\int_0^\infty ds\,\frac{\rho_{\rm sQED}(s)}{s(s+k^2)}, \tag{7.72}$$

with

$$\begin{aligned}\rho_{\mathrm{sQED}}(s) &= -\frac{1}{\pi}\mathrm{Im}\Pi(s)\\ &= \frac{1}{48\pi^2}(1-4\frac{m_\pi^2}{s})^{3/2}\theta(s-4m_\pi^2).\end{aligned} \tag{7.73}$$

We can furthermore write

$$\begin{aligned}\int\frac{d^4k}{(2\pi)^4}\frac{e^{ixk}}{(k^2+m_\rho^2)}\Big(\Pi(k^2)-\Pi(0)\Big) &= \int_0^\infty ds\frac{\rho_{\mathrm{sQED}}(s)}{s}\int\frac{d^4k}{(2\pi)^4}\frac{k^2e^{ixk}}{(k^2+m_\rho^2)(s+k^2)}\\ &= \int_0^\infty\frac{\rho_{\mathrm{sQED}}(s)}{s(m_\rho^2-s)}\Big[m_\rho^2G_{m_\rho}(x)-sG_{\sqrt{s}}(x)\Big],\end{aligned} \tag{7.74}$$

where we have set $D=4$ since $\Pi(k^2)-\Pi(0)$ is UV finite. The necessary renormalization coefficients Z_3, δ_m and $\delta\frac{1}{g_\gamma}$ can all be written as combinations of

$$\begin{aligned}\xi_1 &= \mathrm{Re}\Big(\Pi(0)-\Pi(Q^2)\Big)|_{Q^2=-m_\rho^2}\\ &= \Pi(0)-\frac{Z_3-1}{g^2}\\ &= -\frac{1}{(4\pi)^2}\Big(\frac{8(-3+z)}{9z}-\mathrm{Re}\Big[\frac{2(\sqrt{4-z})^3}{3z^{3/2}}\mathrm{Artanh}\Big(\frac{\sqrt{z}}{\sqrt{4-z}}\Big)\Big]\Big),\end{aligned} \tag{7.75}$$

and

$$\begin{aligned}\xi_2 &= Q^2\frac{d}{dQ^2}\Pi(Q^2)|_{Q^2=-m_\rho^2}\\ &= \frac{1}{4^2\pi^2 3z}\Big(-12+z+12\mathrm{Re}\Big[\sqrt{4z^{-1}-1}\Big(\arcsin(\sqrt{z}/2)\Big)^*\Big],\end{aligned} \tag{7.76}$$

where $z=\frac{m_\rho^2}{m_\pi^2}$ and $(.)^*$ denotes the complex conjugate. Inserting now Eq. 7.74, 7.75 and into Eq. 7.70 and 7.71 yields

$$\begin{aligned}J_{\mu\nu}^{(1)}(x,0) &= 2m_\rho^2(\partial_\mu\partial_\nu-\delta_{\mu\nu}\partial_\rho\partial_\rho)\Big[\frac{g}{g_\gamma}\Big(1-\frac{g}{g_\gamma}\Big)\int_0^\infty ds\frac{\rho_{\mathrm{sQED}}(s)}{s(m_\rho^2-s)}\Big[m_\rho^2G_{m_\rho}(x)-sG_{\sqrt{s}}(x)\Big]\\ &\quad+\Big(\frac{g}{g_\gamma}\Big(1-\frac{g}{g_\gamma}\Big)\xi_1+\frac{g^2}{g_\gamma^2}\xi_2\Big)G_{m_\rho}(x)\Big],\end{aligned} \tag{7.77}$$

$$J_{\mu\nu}^{(2)}(x,0)=\Big(\frac{g}{g_\gamma}\Big)^2m_\rho^4(\partial_\mu\partial_\nu-\delta_{\mu\nu}\partial_\rho\partial_\rho)\Big(-\frac{\partial}{\partial m_\rho^2}\Big)\Big[\int_0^\infty ds\frac{\rho_{\mathrm{sQED}}(s)}{s(m_\rho^2-s)}\Big[m_\rho^2G_{m_\rho}(x)-sG_{\sqrt{s}}(x)\Big]+\xi_1G_{m_\rho}(x)\Big]. \tag{7.78}$$

So, we have expressed the full vector-vector correlator $J_{\mu\nu}(x,0)$ in the Sakurai QFT through combinations and one dimensional integrals over Bessel functions, which are numerically stable to compute.

Table 7.1: Predictions of the Sakurai QFT for different Euclidean time windows defined by Eq. (6.18) with $\Delta = 0.15$ fm and the corresponding values for t_1 and t_0. m_π and m_ρ in the Lagrangian are set to their physical values and $(g, g_\gamma) = (5.984, 4.97)$. The precision requirement for the numerical integration is set below the displayed digits. All numbers in the table are in units of 10^{-10}. The uncertainties quoted for the values from Ref. [32] result from all sources of error added in quadrature.

$[t_0, t_1]$	Sakurai QFT	Ref. [32]
[0, 0.1] fm	0.66	0.83(1)
[0.1, 0.4] fm	14.05	12.89(12)
[0.4, 0.7] fm	53.03	51.02(45)
[0.7, 1.0] fm	87.59	87.28(72)
[1.0, 1.3] fm	94.05	95.31(73)
[1.3, 1.6] fm	79.64	80.88(58)
[1.6, ∞] fm	165.81	166.08(106)
total	494.83	494.30(355)

We choose approximate physical parameters $m_\pi = 140$ MeV and $m_\rho = 775$ MeV. With the expression for $J_{\mu\nu}(x, 0)$ at hand, we can calculate the integral in Eq. 7.64. We do so for the case of the hadronic contribution to a_μ and also for the window observable 7.26 for different euclidean time windows. The results for the integral are given in table 7.1. We also depict the integrand for three different kernels in figure 7.3. The results for the different euclidean time windows show remarkable agreement with the contribution from the $\pi\pi$ channel obtained in the dispersive framework [32]. This fosters our assumption that the $\pi\pi$ scattering amplitude is well described by our phenomenological model. However, one should not draw the naive conclusion that this agreement confirms the correctness of the results for a_μ^{hvp} obtained in the dispersive framework. To make a stronger statement about this, one would need to carefully examine the systematic uncertainties of our model, such as higher order electromagnetic corrections and also next-to-leading order contributions in g and g_γ, as well as the uncertainties in tuning the parameters of the model.

8 Finite-size effects in the CCS method

We want to take at look at the finite-size effects that arise in lattice calculations with the CCS method. There is is some text overlap with the work published in Ref. [97], where we used the prediction of the finite-size effects from the Sakurai QFT to correct our lattice results.

The finite-size effects (FSEs) on the electromagnetic correlator come dominantly from the two-pion intermediate states, which belong to the isovector channel. In the context of the TMR method, a number of different approaches have been considered to estimate the FSEs. Perhaps the most straightforward way to estimate FSEs is to rely on Chiral Perturbation Theory (ChPT) in a finite box. The role of the ρ-meson, which contributes very strongly to the HVP at intermediate distances, however only enters at higher orders [48]. Alternatively, one can use phenomenological models, e.g. Ref. [96], to include the effects of the ρ [21]. Finite-size effects in the tail of the TMR correlator can also be computed based on the pion electric form factor in the timelike region, which can be obtained from auxiliary lattice calculations [47, 147, 154, 155]. Finally, the first terms of a systematic asymptotic expansion are given in Refs. [156, 157], where the finites-size correction to a_μ^{hvp} are related to a pion-photon Compton scattering amplitude.

In our approach with the CCS method, where the position-space vector-vector correlator is needed, a new aspect in the study of volume effects comes from the Lorentz structure of the correlator as a symmetric rank-2 tensor under the breaking of the O(4)-symmetry into that of a subgroup of the hypercubic group H(4), or the octahedral group O_h if the time extent is taken to be infinite. In addition, it is not straightforward to generalize the approach of Refs. [156, 157] or of Ref. [154]: as the correlator used in the CCS method is a position-space object, the whole range of center-of-mass momenta must be considered.

In the first part of this chapter we want to develop a method for estimating the FSE of the vector-vector correlator for the case of point-like pions, i.e. scalar QED in the box. We will crosscheck this method with results computed using the TMR method. We will then turn to a more sophisticated approach by utilizing the Sakurai QFT 4.2 as a more realistic model for the two pion channel.

8.1 FSE with point-like pions

We want to consider a scalar particle in the finite box $x \in [0,L]^3 \times [0,T]$, where L is length of the spatial dimensions and T is the time extend. In a typical lattice calculation T is taken to be much larger than L, so finite size effects in the temporal dimension can be neglected in most cases. The truncation in position space leads to a discrete spectrum of momenta $p \in \left(\frac{2\pi}{L}\mathbb{Z}\right)^3 \times \left(\frac{2\pi}{T}\mathbb{Z}\right)$. The infinite volume propagator in position space 2.31, which can be expressed as an integral over momenta, becomes a sum over the discretized momenta

$$\begin{aligned} G_m(x) &= \int \frac{d^4p}{(2\pi)^4} \frac{1}{p^2+m^2} e^{ip\cdot x} \\ &\to \sum_{p\in\left(\frac{2\pi}{L}\mathbb{Z}\right)^3\times\left(\frac{2\pi}{T}\mathbb{Z}\right)} \frac{1}{p^2+m^2} e^{ip\cdot x} = G_m^{(FV)}(x). \end{aligned} \tag{8.1}$$

By making use of Poisson summation formula, one can express the finite volume (FV) propagator $G_m^{(FV)}(x)$ as a sum over the infinite volume propagators where the argument is shifted by multiples of the spatial and temporal extent

$$G_m^{(FV)}(x) = \sum_{n\in\mathbb{Z}^4} \int \frac{d^4p}{(2\pi)^4} \frac{1}{p^2+m^2} e^{ip\cdot(x+\hat{e}_1 n_1 L+\hat{e}_2 n_2 L+\hat{e}_3 n_3 L+\hat{e}_3 n_4 T)} \tag{8.2}$$

$$= \sum_{n\in\mathbb{Z}^4} G_m(y)\Big|_{\substack{y_{1,2,3}=x_{1,2,3}+n_{1,2,3}L,\\ y_4=x_4+n_4T}} \tag{8.3}$$

For simplicity we will set $T = L$ in the following, since the generalization for arbitrary T is straightforward. Starting from the vector-vector correlator in scalar QED in infinite volume 7.67

$$\langle j_\mu^{\text{sQED}}(x) j_\nu^{\text{sQED}}(0)\rangle_{\text{sQED}} = 2\Big(\partial_\mu G_{m_\pi}(x)\partial_\nu G_{m_\pi}(x) - G_{m_\pi}(x)\partial_\mu\partial_\nu G_{m_\pi}(x)\Big) \tag{8.4}$$

$$= \int \frac{d^4k}{(2\pi)^4}\frac{d^4p}{(2\pi)^4} \frac{(-p-k)_\mu(-p-k)_\nu}{(p^2+m_\pi^2)(k^2+m_\pi^2)} e^{-i(p-k)x} \tag{8.5}$$

We can again obtain the finite volume version by replacing the integrals with sums

$$\langle j_\mu^{\text{sQED}}(x) j_\nu^{\text{sQED}}(0)\rangle_{\text{sQED}}^{(FV)} = \sum_{p,k\in\left(\frac{2\pi}{L}\mathbb{Z}\right)^4} \frac{(-p-k)_\mu(-p-k)_\nu}{(p^2+m^2)(k^2+m^2)} e^{-i(p-k)x} \tag{8.6}$$

$$= \sum_{n,q\in\mathbb{Z}^4} \Big(2\partial_\mu^{(y)}\partial_\nu^{(z)} - \partial_\mu^{(y)}\partial_\nu^{(y)} - \partial_\mu^{(z)}\partial_\nu^{(z)}\Big) G_m(y)G_m(z)\Big|_{y=x+nL,z=x+qL}. \tag{8.7}$$

We obtain a sum over two winding numbers n and k. Since the two sums factorize, this can be written as

$$\langle j_\mu(x) j_\nu(0)\rangle_{\text{sQED}}^{(FV)} = \frac{m^6}{2^4\pi^4}\Big[-2F_{\mu\nu}^1(x)F^4(x) - 8F_{\mu\nu}^2(x)F^4(x) + 2F_\mu^3(x)F_\nu^3(x) + \delta_{\mu\nu}2F^4(x)F^5(x)\Big], \tag{8.8}$$

where the functions $F^{(i)}(x)$ only involve one winding number.

$$F^1_{\mu\nu}(x) = \sum_{n\in\mathbb{Z}^4} y_\mu y_\nu \frac{K_1(m|y|)}{m|y|^3}\Big|_{y=x+nL}, \qquad F^2_{\mu\nu}(x) = \sum_{n\in\mathbb{Z}^4} y_\mu y_\nu \frac{K_2(m|y|)}{m^2|y|^4}\Big|_{y=x+nL}, \tag{8.9}$$

$$F^3_{\mu}(x) = \sum_{n\in\mathbb{Z}^4} y_\mu \frac{K_2(m|y|)}{m|y|^2}\Big|_{y=x+nL}, \qquad F^4(x) = \sum_{n\in\mathbb{Z}^4} \frac{K_1(m|y|)}{m|y|}\Big|_{y=x+nL}. \tag{8.10}$$

$$F^5(x) = \sum_{n\in\mathbb{Z}^4} \frac{K_2(m|y|)}{(m|y|)^2}\Big|_{y=x+nL} \tag{8.11}$$

Eq. 8.8 can now be used to calculate the correlator for a given vector x in the finite volume. The finite size effect (FSE) is simply given by

$$\langle j^{\mathrm{sQED}}_\mu(x)\, j^{\mathrm{sQED}}_\nu(0)\rangle^{(FSE)}_{\mathrm{sQED}} = \langle j^{\mathrm{sQED}}_\mu(x)\, j^{\mathrm{sQED}}_\nu(0)\rangle_{\mathrm{sQED}} - \langle j^{\mathrm{sQED}}_\mu(x)\, j^{\mathrm{sQED}}_\nu(0)\rangle^{(FV)}_{\mathrm{sQED}}. \tag{8.12}$$

We will refer to Eq. 8.8 as the *double winding expansion* in the following.

8.2 Crosscheck with the TMR method

In order to crosscheck the double winding expansion for the finite size effect computed in scalar QED, we compute the spatially summed correlator $G(t)$ 6.9 from the vector-vector correlator for the FSE 8.12. We compare this to $G(t)$ obtained from two traditional methods used in Ref. [147]. There, one uses the representation of $G(t)$ as a sum of energy eigenstates

$$G(t,L) - G(t,\infty) = \frac{1}{3}\Big[\frac{1}{L^3}\sum_{\boldsymbol{k}\in\left(\frac{2\pi}{L}\mathbb{Z}\right)^3} - \int\frac{d^3k}{(2\pi)^3}\Big]\frac{\boldsymbol{k}^2}{\boldsymbol{k}^2+m^2}e^{-2t\sqrt{\boldsymbol{k}^2+m^2}}, \tag{8.13}$$

for the large t regime. For the small t regime a series in a single winding number is used

$$\begin{aligned} G(t,L) - G(t,\infty) \quad = \quad & \frac{m^4 t}{3\pi^2}\sum_{\boldsymbol{n}\in\mathbb{Z}^3}\Big[\frac{K_2(m\sqrt{L^2\boldsymbol{n}^2+4t^2}}{m^2(L^2\boldsymbol{n}^2+4t^2)} \\ & -\frac{1}{mL|\boldsymbol{n}|}\int_1^\infty dy K_0(my\sqrt{L^2\boldsymbol{n}^2+4t^2})\sinh(mL|\boldsymbol{n}|(y-1). \end{aligned} \tag{8.14}$$

This single winding number expansion can be derived starting from Eq. 8.6 and performing the integral over the spatical components analytically. However, for the case of the CCS method, where we need $\langle j^{\mathrm{sQED}}_\mu(x)\, j^{\mathrm{sQED}}_\nu(0)\rangle^{(FSE)}_{\mathrm{sQED}}$ the double winding number expansion does not collapse to a sum over a single winding number.

In order to calculate the series in Eqs8.9 to 8.11 numerically, we need to truncate the sum over all winding numbers. In the sum we include all winding numbers with 1-norm less or equal than

Table 8.1: Comparison between the double and single winding expansion and the energy eigenstate series representation, for $m_\pi L = 4$ for the contribution for the finite volume effects of the $G(t)$ for a given value of the euclidean time t in 10^{-12} . The single winding expansion is summed until $|\boldsymbol{n}|_1 = 4$. The energy eigenstate series representation is summed until $|\boldsymbol{k}|_1 = 30\frac{2\pi}{L}$, where ($|\boldsymbol{n}|_1 = |n_1| + |n_2| + |n_3|$). The values for the double winding expansion are for a maxmimum winding number of $w_{max} = 4$

t	Double Wind. Exp.	Single Wind. Exp.	Energy Eigenstate Series
4	6.80825	6.80304	6.81066
5	10.8123	10.8009	10.8168
6	14.1296	14.1088	14.1367
7	16.0812	16.0479	16.091
8	16.5199	16.4717	16.5324
9	15.6932	15.6287	15.7082
10	14.0246	13.9437	14.0415

$|\boldsymbol{n}|_1, \leq w_{max}$. For the comparison we assume the time dimension to be infinite and $m_\pi L = 4$. We compare the FSE to the correlator for given values of the euclidean time t in table 8.1. We see, that all three methods are in good agreement in the intermediate regime, if enough terms in the double winding expansion are included.

8.3 FSE in the Sakurai QFT

After the calculation of the vector vector correlator for point-like pions in scalar QED, we want to turn to the more realistic model of the Sakurai QFT 4.2. We have already derived the Sakurai QFT analog to the QCD vector-vector correlator $J^{(\infty)}_{\mu,\nu}(x)$, given in Eq. 7.66, where we denote the quantity in infinite volume by $^{(\infty)}$. In order to simplify the calculation for the FSE, we assume $g = g_\gamma$ in the following. We furthermore neglect terms, that are suppressed by $e^{-m_\rho L/2}$, since the contribution of such terms is very small in comparison to the leading FV effect that is only suppressed by a factor $e^{-m_\pi L}$. Then the only term contributing to the FSE is

$$J^{(2,L)}_{\mu\nu}(x) = \frac{m_\rho^4}{V} \sum_k e^{ikx} \frac{\overline{\Pi}^{(L)}_{\mu\nu}(k)}{(k^2 + m_\rho^2)^2}, \tag{8.15}$$

where $\overline{\Pi}^{(L)}_{\mu\nu}(k)$ is the finite-volume renormalized vacuum polarization tensor, where the renormalization is always performed in infinite volume. It is useful to decompose the latter into its infinite-volume counterpart, plus a remainder,

$$\overline{\Pi}^{(L)}_{\mu\nu}(k) = (\delta_{\mu\nu}k^2 - k_\mu k_\nu)(\Pi(k^2) - (Z_3 - 1)/g^2) + \Delta\Pi^{(L)}_{\mu\nu}(k), \tag{8.16}$$

because the remainder is ultraviolet finite. By making use of the Poisson resummation trick 8.2 again, we can then write

$$J_{\mu\nu}^{FSE}(x) = J_{\mu\nu}^{(2,L)}(x) - J_{\mu\nu}^{(2,\infty)}(x) \quad = \quad \sum_{n\in\mathbb{Z}^4\setminus\{0\}} J_{\mu\nu}^{(2,\infty)}(x+nL) + \sum_{n\in\mathbb{Z}^4} J_{\mu\nu}^{(3,L)}(x+nL) \tag{8.17}$$

with

$$J_{\mu\nu}^{(3,L)}(w) = \int \frac{d^4k}{(2\pi)^4} e^{ikw} \frac{m_\rho^4}{(k^2+m_\rho^2)^2} \Delta\Pi_{\mu\nu}^{(L)}(k). \tag{8.18}$$

The first term appearing in the sum in Eq. 8.17 is precisely the infinite volume result for $J_{\mu\nu}^{(2,L)}(x)$ given in Eq. 7.71, which has to be evaluated with the argument $x+nL$ for all winding numbers $n \in \mathbb{Z}^4$. The term given in Eq. 8.18 is more complicated. We note that

$$\Delta\Pi_{\mu\nu}^{(L)}(k) = \sum_{\nu\neq 0} \int \frac{d^4q}{(2\pi)^4} e^{iLq\cdot\nu} \frac{-(k+2q)_\mu(k+2q)_\nu + 2\delta_{\mu\nu}((k+q)^2+m_\pi^2)}{((k+q)^2+m_\pi^2)(q^2+m_\pi^2)}. \tag{8.19}$$

One finds, using a Feynman parameter α,

$$\Delta\Pi_{\mu\nu}^{(L)}(k) \quad = \quad \sum_{\nu\neq 0} \Delta\Pi_{\mu\nu}^{(L)}(k, y = L\nu), \tag{8.20}$$

$$\begin{aligned} \Delta\Pi_{\mu\nu}^{(L)}(k,y) \quad &= \quad \{-(k+2q)_\mu(k+2q)_\nu + 2\delta_{\mu\nu}((k+q)^2+m_\pi^2)\}_{q=-i\nabla_y} \\ &\quad \cdot \frac{1}{8\pi^2} \int_0^1 d\alpha\, e^{-i\alpha k\cdot y} K_0(\sqrt{\alpha(1-\alpha)k^2+m_\pi^2}|y|). \end{aligned} \tag{8.21}$$

Inserting Eq .8.20 into Eq. 8.18 together with Eq. 8.17 one can write the second term as a double winding expansion

$$J_{\mu\nu}^{FSE}(x) = \sum_{n\in\mathbb{Z}^4\setminus\{0\}} J_{\mu\nu}^{(2,\infty)}(x+nL) + \sum_{\substack{n\in\mathbb{Z}^4, \\ \nu\in\mathbb{Z}^4\setminus\{0\}}} J_{\mu\nu}^{(4)}(x+nL,\nu L) \tag{8.22}$$

with

$$\begin{aligned} J_{\mu\nu}^{(4)}(w,y) \quad &= \quad \{-(k+2q)_\mu(k+2q)_\nu + 2\delta_{\mu\nu}((k+q)^2+m_\pi^2)\}\Big|_{q=-i\nabla_y, k=-i\nabla_w} \\ &\quad \int \frac{d^4k}{(2\pi)^4} e^{ikw} \frac{m_\rho^4}{(k^2+m_\rho^2)^2} \cdot \frac{1}{8\pi^2} \int_0^1 d\alpha\, e^{-i\alpha k\cdot y} K_0(\sqrt{\alpha(1-\alpha)k^2+m_\pi^2}|y|). \end{aligned} \tag{8.23}$$

These integrals in Eq. 8.23 can be simplified even further. However, this calculation is rather technical. We give the details in the appendixA.2. For the numerical implementation of $J_{\mu\nu}^{(4)}(w,y)$ we finally use Eq. A.8.

We can now use Eq. 8.22 for the calculation of the FSE in the Sakurai QFT. The sum over winding numbers ($n \in \mathbb{Z}^4\setminus\{0\}$) and ($\nu \in \mathbb{Z}^4$) converges very fast, because of the asymptotic behaviour of the

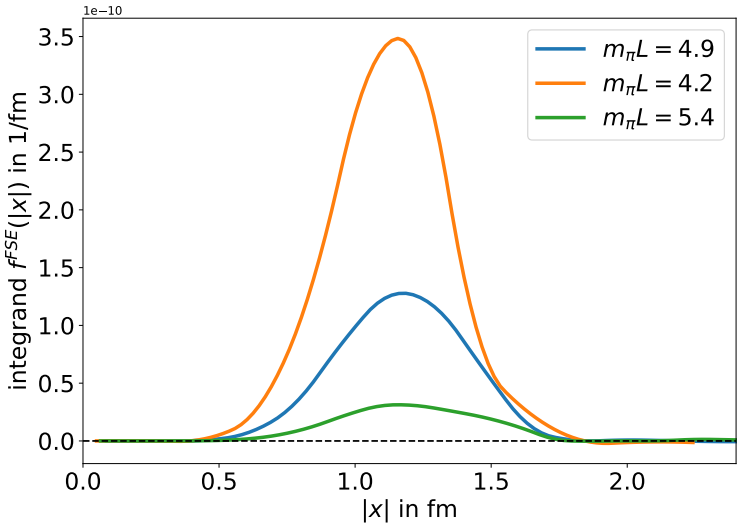

Figure 8.1: Integrand for the finite-size correction for the intermediate window quantity 8.25 computed in the Sakurai theory for several values of $m_\pi L$. These values correspond to three of the ensembles used in the study of the intermediate window quantity in chapter 9. We tune the ρ mass to be the same as the one calculated on these specific ensembles.

individual terms proportional to $\exp(-m_\pi L|n|)$ for large $|x|$. We calculate winding number up to $|n|+|\nu|=2$. To this end, we compute the contracted quantity quantities

$$J_1^{FSE}(x) = x_\mu x_\nu J_{\mu\nu}^{FSE}(x), \qquad J_2^{FSE}(x) = \delta_{\mu\nu} J_{\mu\nu}^{FSE}(x) \tag{8.24}$$

stochastically for several values of $|x|$.

In chapter 9 we apply the method described here, to correct the lattice data for the computation of the intermediate window quantity for several ensembles. Here, we want to present the integrand for the 'TL' kernel 7.9 for three different values of $m_\pi L = (4.2, 4.9, 5.4)$ which correspond to the ensembles 9.1 that are used in the analysis in chapter 9. We use the pion mass calculated on these ensembles 9.1 and the rho mass calculated in a previous study for the Gounaris-Sakurai parametrization of the pion electric form factor [47]. The result for the FSE on the integrand

$$\int d^4x H_{\mu\nu}^W(x) J_{\mu\nu}^{FSE}(x) = \int d|x| f^{FSE}(|x|) \tag{8.25}$$

is depicted in Fig. 8.1.

9 The window quantity in the CCS representation in lattice QCD

Here, we want to recall our work on the intermediate distance window quantity, already presented in Ref. [97]. This chapter has substantial text overlap with the published paper [97]. We will start with explaining the lattice basic lattice setup used to compute the window observable and then apply the finite-size correction, which we already introduced in chapter 8. We conclude with a comparison to the time-momentum representation and an extrapolation to the continuum result at the reference point $(m_\pi, m_K) = (350, 450)$ MeV. We will stick to the notation of Ref. [97] for the intermediate window observable $a_\mu^{\mathrm{W}} := a_\mu^{ID}$.

9.1 Lattice setup

We apply the CCS method to five different $N_f = 2+1$ flavor gauge ensembles generated by the Coordinated Lattice Simulations consortium [137] at a pion mass around 350 MeV. These ensembles have been generated with the O(a)-improved Wilson-clover fermion action and tree-level O(a^2) improved Lüscher-Weisz gauge action. The detailed information about the used ensembles can be found in Tab. 9.1. In this work, our goal is to provide a cross-check for the calculation carried out in the conventional TMR method [23], restricting ourselves to the (strongly dominant) quark-connected contributions in the $f = u, d, s$ sector.

To control the discretization effects, in this work, we consider both the local (L) and the conserved (C) version of the vector current on the lattice

$$j_\mu^{(\mathrm{L})}(x) = \bar{\psi}(x)\gamma_\mu \mathcal{Q}\psi(x)\,, \tag{9.1}$$

and

$$j_\mu^{(\mathrm{C})}(x) = \tfrac{1}{2}\Big(j_\mu^{(\mathrm{N})}(x) + j_\mu^{(\mathrm{N})}(x - a\hat{\mu})\Big), \tag{9.2}$$

$$j_\mu^{(\mathrm{N})}(x) = \frac{1}{2}\Big[\bar{\psi}(x + a\hat{\mu})(1+\gamma_\mu)U_\mu^\dagger(x)\mathcal{Q}\psi(x) - \bar{\psi}(x)(1-\gamma_\mu)U_\mu(x)\mathcal{Q}\psi(x + a\hat{\mu})\Big], \tag{9.3}$$

where $U_\mu(x)$ is the gauge link and $\mathcal{Q}$ is a generic quark charge matrix acting in flavor space. Starting

from the Noether current $j_\mu^{(\mathrm{N})}$, we have defined the site-centered current $j_\mu^{(\mathrm{C})}$, which obeys the on-shell conservation equation $\sum_{\mu=0}^{3}\partial_\mu^* j_\mu^{(\mathrm{C})}=0$, where ∂_μ^* is the lattice backward derivative.

In practice, to handle the O(a) lattice artifacts, we substitute the lattice vector currents with their improved counterparts[1] [158]

$$j_\mu^{(\alpha),\mathrm{I}}(x)=j_\mu^{(\alpha)}(x)+ac_V^{(\alpha)}\partial_\nu T_{\mu\nu}(x),\qquad \text{for}\quad \alpha=\mathrm{L},\mathrm{C}, \tag{9.4}$$

where the local tensor current is defined by $T_{\mu\nu}\equiv-\frac{1}{2}\bar\psi(x)[\gamma_\mu,\gamma_\nu]\mathscr{Q}\psi(x)$ and $c_V^{(\alpha)}$ is an improvement coefficient. For $c_V^{(\alpha)}$, we use the interpolating formulae Eq. (46.a) and Eq. (46.b) of Ref. [159], consistently with the treatment of Ref. [23]. For both flavor combinations considered here, the renormalization is multiplicative,

$$j_\mu^{(\mathrm{L}),\mathrm{R}}(x)=\hat Z_{\mathrm{V}}^{(\mathrm{L})}\,j_\mu^{(\mathrm{L}),\mathrm{I}}(x). \tag{9.5}$$

In the case of the local isovector current, corresponding to $\mathscr{Q}=\mathrm{diag}(\frac{1}{2},-\frac{1}{2},0)$, the renormalization factor is given by

$$\hat Z_{\mathrm{V}}^{(\mathrm{L})}=Z_V(g_0)\Big[1+3\bar b_V^{\mathrm{eff}}am_{\mathrm{q}}^{\mathrm{av}}+b_V am_{\mathrm{q},l}\Big], \tag{9.6}$$

where the parameters Z_V, $\bar b_V^{\mathrm{eff}}$ and b_V are obtained from the Padé fits Eqs. (44.a,b,c) of Ref. [159]. The average quark mass $m_{\mathrm{q}}^{\mathrm{av}}$ and the mass of the quark of flavour f, $m_{\mathrm{q},f}$, are taken from the same reference. The conserved vector current does not need to be renormalized, thus we have $\hat Z_{\mathrm{V}}^{(\mathrm{C})}=1$. This treatment of the renormalization and improvement coefficients corresponds to Set 1 in the calculation of the window observable of the Mainz group [23].

The strange current, since we consider only the connected contribution to its two-point function, must be defined within a partially quenched theory. For instance, adding a fourth, purely 'valence' quark s' mass-degenerate with s, the flavor structure corresponds to $\mathscr{Q}=\mathrm{diag}(0,0,\frac{1}{3\sqrt{2}},-\frac{1}{3\sqrt{2}})$. The corresponding renormalization factor can be written in the form

$$\hat Z_{\mathrm{V}}^{(\mathrm{L})}=Z_V(g_0)\Big[1+3\bar b_V^{\mathrm{eff}}am_{\mathrm{q}}^{\mathrm{av}}+b_V am_{\mathrm{q},s}+b_V^{\mathrm{pq}}(am_{\mathrm{q}}^{\mathrm{av}}-am_{\mathrm{q},s})\Big]. \tag{9.7}$$

It contains an additional term with a coefficient b_V^{pq} (of order g_0^4 in perturbation theory) representing a sea-quark effect. Both for the latter reason and the fact that we work quite close to the $SU(3)_{\mathrm{f}}$ point $am_{\mathrm{q}}^{\mathrm{av}}=am_{\mathrm{q},s}$, we neglect this additional term.

We give some further details for the implementation in the following subsections. Although the expressions are given for the case where both currents are local, the generalization to the cases with conserved currents should be straightforward.

[1] Eq. (9.4) is valid for the flavor non-singlet combinations considered here.

Table 9.1: Overview of the used ensembles. The lattice spacings are determined in Ref. [110] and the pion and kaon masses are taken from Ref. [23]. Open boundary conditions are employed for all of the listed ensembles. For the ensemble N203, two replica have been included in the analysis. To exploit translational invariance to reduce statistical fluctuations, all contracted correlators [Eqs. (9.11,9.12,9.15)] have been computed at L different choices of origin situated at $(n, n, n, T/2)$.

Id	β	$L^3 \times T$	a [fm]	m_π [MeV]	m_K [MeV]	$m_\pi L$	L [fm]	#confs light/strange
U102	3.4	$24^3 \times 96$	0.08636	353(4)	438(4)	3.7	2.1	200/0
H102		$32^3 \times 96$				4.9	2.8	240/120
S400	3.46	$32^3 \times 128$	0.07634	350(4)	440(4)	4.2	2.4	240/120
N203	3.55	$48^3 \times 128$	0.06426	346(4)	442(5)	5.4	3.1	$90 \times 2/90 \times 2$
N302	3.7	$48^3 \times 128$	0.04981	346(4)	450(5)	4.2	2.4	240/120

9.1.1 Contracted correlators

Eq. (7.26), can be conveniently written as

$$a_\mu^{\mathrm{W}} = \int_0^\infty dr\, f(r), \quad f(r) \equiv r^3 \Big[-\widetilde{\mathscr{K}}_1(r) G_1(r) + \frac{1}{r^2} \widetilde{\mathscr{K}}_2(r) G_2(r) \Big], \tag{9.8}$$

where

$$G_1(r) = \int_{\mathbb{S}^3} d\Omega_x\, G_{\mu\nu}(x) \delta_{\mu\nu}, \tag{9.9}$$

$$G_2(r) = \int_{\mathbb{S}^3} d\Omega_x\, G_{\mu\nu}(x) x_\mu x_\nu, \tag{9.10}$$

with $r \equiv |x|$, $\hat{x} \equiv x/|x|$ and $\mathbb{S}^3$ is the measure of the three-sphere. The functions G_1 and G_2 will be referred to as the *contracted correlators* and f as the *integrand*.

In infinite volume, the integrand transforms as a scalar under O(4)-transformations. In particular, it is expected to decay exponentially with the separation r at large distances due to the behavior of the vector-current two-point correlator. For our lattice calculation, where the O(4)-symmetry is broken, the contracted correlators need to be sampled by points which are spread around on the same shell as evenly as possible to restore the rotational symmetry. This in part motivates our choice for saving the following quantities on each given distance r on the lattice for the quark-connected contribution of a_μ^{W}

$$\widehat{G}_1^{\mathrm{conn.}}(r) = -\mathrm{Tr}\{\mathscr{Q}^2\} \sum_{x \in \Lambda, |x|=r} \Re\,\mathrm{Tr}[S(x,0)\gamma_\mu S(0,x)\gamma_\mu], \tag{9.11}$$

$$\widehat{G}_2^{\mathrm{conn.}}(r) = -\mathrm{Tr}\{\mathscr{Q}^2\} \sum_{x \in \Lambda, |x|=r} \Re\,\mathrm{Tr}[S(x,0)\not{x} S(0,x)\not{x}], \tag{9.12}$$

where Λ denotes the set of all points on the lattice and $S(x,0)$ is a quark propagator with point-source at 0. Note that, in this convention, we have $\widehat{G}_i^{\mathrm{conn.}}(r) \to r^3 G_i(r)$ in the continuum and infinite-volume limit. Another advantage of such choice is the re-usability of the data for other quantities for which the weight functions of the CCS kernel are known; it suffices to substitute the weight functions $\widetilde{\mathscr{K}}_1$

and $\widetilde{\mathscr{H}_2}$ in the master formula Eq. (9.8) with the desired one in such a case.

For the $O(a)$-improvement of the discretized lattice vector current Eq. (9.4), there is another quantity which has to be taken into account due to the tensor current. Starting with the O(a)-improved vector-current given Eq. (9.4), one can keep the explicit coefficient ac_V fixed and substitute the vector- and tensor-currents by their continuum and infinite-volume limit counterparts. Plugging it into the original infinite-volume vector-current two-point correlator, Eq. (9.8) is then modified to, up to O(a^2)-terms,

$$\tilde{a}_\mu^{\mathrm{W}}(a) = \int d^4x \left\{ H_{\mu\nu}(x) G_{\mu\nu}(x) + ac_V \Big[\langle j_\mu(x) T_{\nu\alpha}(0)\rangle - \langle T_{\mu\alpha}(x) j_\nu(0)\rangle \Big] \partial_\alpha H_{\mu\nu}(x) \right\}, \tag{9.13}$$

where we have performed an integration-by-part to get the second term on the right-hand side. The second term in the curly bracket can be seen as a lattice artifact as it vanishes at the $a \to 0$ limit at fixed c_V, where a_μ^{W} is recovered. Exploiting the Lorentz symmetry as done previously, we can consider it as a convolution of the correlation function in the square-bracket as

$$ac_V \int_0^\infty dr\, r\, \widetilde{\mathscr{H}_3}(r) G_3(r)\,, \tag{9.14}$$

where

$$G_3(r) = \int_{\mathbb{S}^3} d\Omega_x\, x_\alpha \Big[-\langle j_\mu(x) T_{\mu\alpha}(0)\rangle + \langle T_{\mu\alpha}(x) j_\mu(0)\rangle \Big], \tag{9.15}$$

$$\widetilde{\mathscr{H}_3}(r) = \widetilde{\mathscr{H}_2}(r) + r\widetilde{\mathscr{H}_1'}(r)\,. \tag{9.16}$$

This observation facilitates the numerical computation as the same propagators required for the calculation of the previously-mentioned contracted correlators can be reused and leads to the quantity to be computed on the lattice

$$\widehat{G}_3^{\mathrm{conn.}}(r^2) = -\mathrm{Tr}\{\mathscr{Q}^2\} \sum_{x\in\Lambda,\,|x|=r} \Re\,\mathrm{Tr}[S(x,0)\gamma_\mu S(0,x)(\not{x}\gamma_\mu - \gamma_\mu \not{x})]\,. \tag{9.17}$$

9.1.2 Summation schemes

Because of the periodicity in the spatial directions on the lattice, the spatial separation in each direction is mapped to $x_k \in [-L/2, L/2]$ in infinite-volume spacetime. This means that, in total, one can sample up to $r = L$ on a lattice with $T \geq L$. However, the CCS formulation consists in treating the lattice points shell-by-shell with fixed r across the hypercube, following the radial direction; in the $r > L/2$ region, the corresponding shell on the hypercube is not faithfully sampled anymore. Upon taking the continuum and infinite-volume limit, the summations in the lattice-summed contracted correlators $\widehat{G}_i$ run over the three-sphere $\mathbb{S}^3$. As the summands become O(4)-invariant objects in this limit, it suffices to evaluate them at a given point and multiply by the $\mathbb{S}^3$-measure to get the answer. However, on a finite lattice, this simplified procedure is exposed to both discretization and finite-volume effects. This is better illustrated with Fig. 9.1: when going beyond $r = L/2$ in the radial

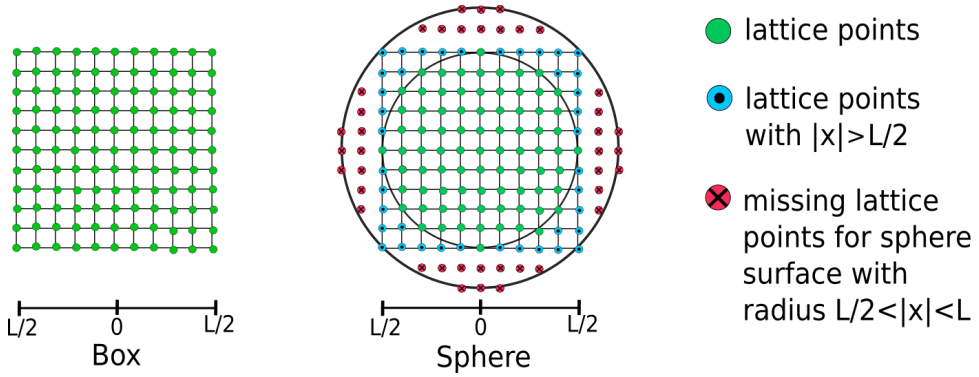

Figure 9.1: Visualization of the domain of integration on a hypercube of size L. The Details of the integration procedure are provided in Sect. 9.1.2

direction, the hypersphere only intersects with a subset of points on the entire shell of the hypercube submerged in infinite-volume spacetime.

In order to control the finite-volume effects, we propose the following summation scheme for our lattice data. We correct for these missing points by a multiplicative factor given by:

$$c(r,L) = \frac{r_4((r/a)^2)}{n_{\text{avail}}(r^2,L)}, \quad \text{with} \quad r_4(n) = 8 \sum_{d\,|\,n,\ 4\nmid d} d \tag{9.18}$$

being the number of ways to represent n as the sum of four squares and $n_{\text{avail}}(r^2,L)$ is the number of available points on the lattice, which can easily be counted. The sum in Eq. (9.18) runs over all divisors d of the integer number n, where 4 is not a divisor of d itself. This is known as Jacobi's four-square theorem. A proof is given for example in Ref. [160]. Note that, in this definition, $c(r,L) = 1$ for all $r \leq L/2$. This summation scheme allows one to sample the contribution from the portion of a hypersphere cut out by the box as described by the red points on the right panel of Fig. 9.1. As a consequence, our lattice version of the master formula for a_μ^{W} reads:

$$a_\mu^{\text{W,lat.}} = a^4 \sum_{r=0}^{L} c(r,L) f^{\text{lat.}}(r), \tag{9.19}$$

where the lattice integrand is defined as

$$f^{\text{lat.}}(r) \equiv -\widetilde{\mathscr{H}}_1(r)\widehat{G}_1^{\text{conn.}}(r) + \frac{1}{r^2}\widetilde{\mathscr{H}}_2(r)\widehat{G}_2^{\text{conn.}}(r) + \frac{ac_V}{r^2}\widetilde{\mathscr{H}}_3(r)\widehat{G}_3^{\text{conn.}}(r). \tag{9.20}$$

The results for the ensembles given in Tab. 9.1 calculated with this scheme are collected in Tab. 9.3. Finally, as commented earlier, we could also have computed the lattice-summed correlators $\widehat{G}_i$'s by starting from the continuum expression (9.8), which is based on 4d spherical coordinates, and implementing it in one particular direction on the lattice. The result should agree with the summation scheme of Eq. (9.19) after a proper continuum and infinite-volume extrapolation. In general, the two

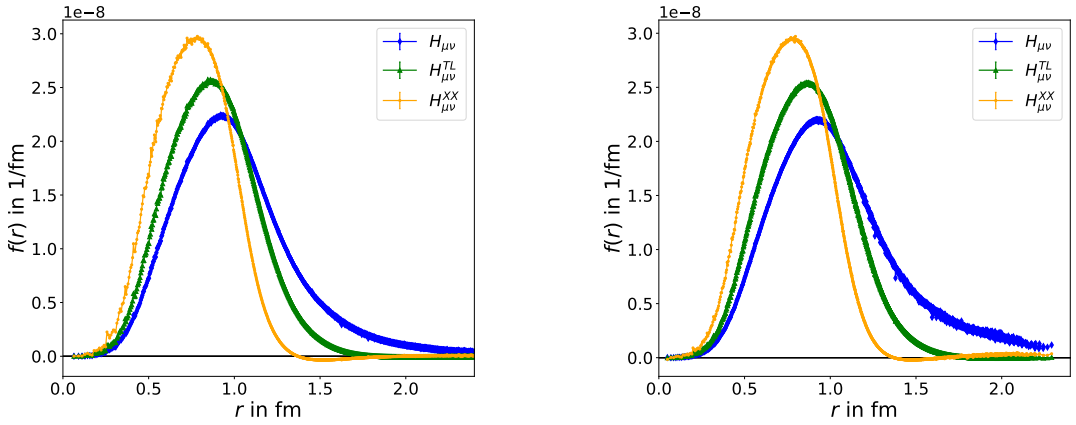

(a) N203 (L=3.1fm)

(b) N302 (L=2.4fm)

Figure 9.2: Comparison of the integrand of Eq. (9.8) for different kernels [Eqs. (7.11,7.9,7.10)], for two different ensembles for the conserved-local discretization.

approaches introduce a different scaling toward to continuum limit. We have explicitly verified in the present case that the difference between these two treatments of the lattice data is much smaller than the statistical error of the data.

9.2 Numerical results

In this section, we discuss the numerical results for a_μ^{W} from our lattice simulations, which are based on the traceless kernel $H_{\mu\nu}^{\mathrm{TL}}$ and on the finite-size corrections detailed in chapter 8. We first compare the results from each individual ensemble to what has been obtained in the previous Mainz publication based on the TMR [23]. Then, we correct for the mistuning of the pion mass to shift to the reference pion mass of 350 MeV and kaon mass of 450 MeV prior to extrapolating the data to the continuum limit.

9.2.1 Comparison of the prediction from the Sakurai QFT with the lattice results

In Fig. 9.3, we display the integrand of Eq. 9.19 for one ensemble (N203) and the prediction from the Sakurai QFT 7.64 in infinite volume for the pion mass of $m_\pi = 346$ MeV and two different values for the mass of the ρ. One of these is the ρ mass computed in [47] and the other one is approximately the physical value. For the ρ mass computed on the same ensemble, we see a very good agreement in the long-distance part of the integrand, although the lattice calculation is performed at finite lattice spacing. This observation makes us confident that the finite-size effects which come predominantly from the long-distance region can be accurately described with the Sakurai QFT.

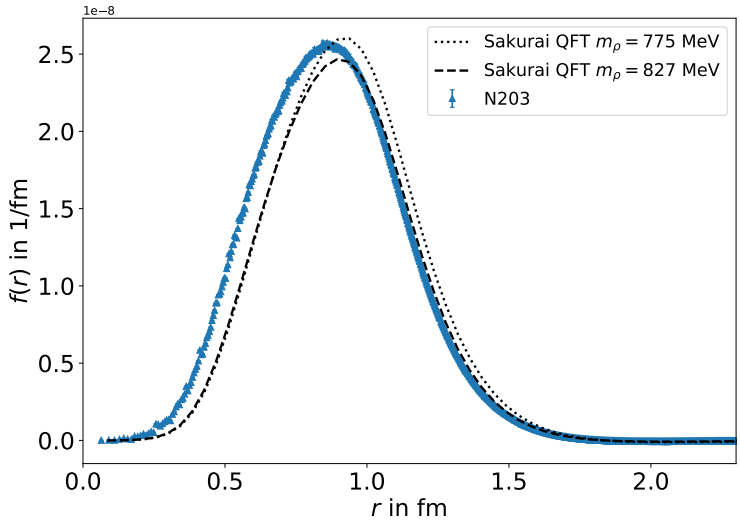

Figure 9.3: Comparison between the integrand from the ensemble N203 for the conserved-local discretization of the vector current and the prediction of the Sakurai QFT for the corresponding m_π and m_ρ. The correction for the wrap-around-the-world pion has been applied to the lattice data.

9.2.2 Finite-size-effect correction of the data

We neglect the effects of having a finite temporal extent, as $m_\pi T$ is large for the ensembles included in this calculation. In the CCS method, one has to correct for the FSEs coming from two sources. The first one is the truncation of the integrand of Eq. (9.8) at $r_{\text{max}} = L/2$ because of the finite lattice size. The resulting missing contribution could be large if the integrand is long-ranged. Selected raw lattice results obtained with different kernels are displayed in Fig. 9.2. We see that the widths of the integrand are very different according to the kernel used. For the kernels $H^{\text{TL}}_{\mu\nu}$ and $H^{\text{XX}}_{\mu\nu}$, the integrals to get a_μ^{hvp} saturate more rapidly than in the case of the original, un-subtracted kernel $H_{\mu\nu}$; the FSE corrections due to the truncation are thus much smaller for the first two.

The second source of FSEs is the wrap-around-the-world effect related to the discretized momenta in a finite, periodic box. We estimate this effect by directly comparing the correlators computed in finite- and infinite-volume Sakurai QFT [Eq. (8.17)]. The finite-volume part of the latter is to be done following the same summation schemes described in Sect. 9.1.2 for different spacetime regions to match the lattice QCD calculation. As ultimately, the relevant quantities for the calculation of a_μ^{W} are the contracted correlators [Eqs. (9.9,9.10)], we compute the contracted finite-volume correlators at a distance $|x| = r$ by sampling them at several points x equally-distributed on the same hypersphere in order to reduce the computational cost.

The numerical error of this sampling procedure is quantified based on the variation of the correction when increasing the density of the sampled points. With our setup, we estimate the wrap-around-the-world effect to be controlled at the 10%-level. An additional uncertainty comes from the

fact that the winding expansion Eq. (8.17) is truncated at a given order. Our choice is to truncate at $\|n\|_2^2 = 4$ and $\|n\|_2^2 + \|v\|_2^2 = 3$ in the first and the second sum in Eq. (8.17) respectively. An estimate of the upper bound for the truncation error is given by the highest-order kept term. This error is added in quadrature to the uncertainty of the sampling procedure, which gives the total numerical error of the calculation. The FSE corrections computed according to the procedure described above are summarized in Tab. 9.2.

To get an idea of the size of the systematic error associated with the use of the Sakurai QFT, we also compute the same quantity in leading-order ChPT, where the photon-two-pions coupling is described by scalar QED. There are significant relative differences between the estimates, though the order of magnitude remains the same. Thus we decide to quote 25% of the total FSE correction as a modelling error, which we add in quadrature to the numerical error discussed in the previous paragraph.

9.2.3 Comparison of the prediction for the finite-size error between the Sakurai QFT and lattice data

Although in Fig. 9.2, the shorter-range $H_{\mu\nu}^{\mathrm{XX}}$ might appear to be beneficial in terms of its noise-to-signal ratio, we still prefer the $H_{\mu\nu}^{\mathrm{TL}}$ kernel in this study for two reasons. First, on coarser ensembles, the integrand exhibits noticeable oscillations at short distances, which indicates that the discretization effect due to the breaking of the O(4)-symmetry might be less well handled by performing the angular average over the available lattice points. This effect can be observed in the comparison between the data from a coarser (N203) and finer (N302) ensemble plotted in Fig. 9.2. The second reason for preferring the TL-kernel is that, even though the tail is strongly suppressed, the Sakurai theory still predicts non-negligible contributions in this region, if the box size is not big enough. On the left panel of Fig. 9.4, we show a zoomed-in version of the tail of the integrand of H102 with the TL-kernel. With this choice of kernel, the integrand is very well described by the Sakurai QFT. On the other hand, with the quality of our data, using the XX-kernel in this region gives a noisy result consistent with zero, making it hard to really conclude if the model describes the long distance behavior of the integrand correctly. Therefore, we deem it most appropriate to opt for the traceless kernel $H_{\mu\nu}^{\mathrm{TL}}$ in our calculation for a_μ^{W}, as the FSE due to the truncation seems to be better controlled. However, one should not exclude the possibility that the shorter ranged XX-kernel might become a better choice, if only fine enough ensembles are included in the continuum extrapolation, with well-resolved tails of the integrand.

In order to test to what extent our FSE correction procedure works, we compare the difference between the integrand data computed with H102 and U102, differing only in their spatial length L, to the Sakurai QFT prediction at the corresponding volumes, as shown on the right panel of Fig. 9.4. For this study, we set m_ρ for U102 to be the same as that of H102, as only the latter is available from Ref. [47]. The error on the lattice data is obtained by adding the statistical errors from each individual ensemble in quadrature. Although the fluctuations on the lattice data are large compared to the central values, the prediction from the Sakurai QFT seems to follow the trend very nicely and gives

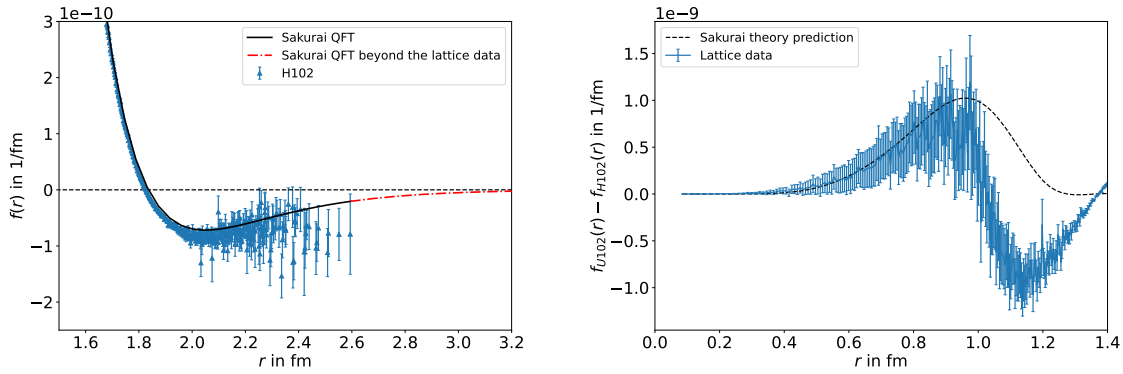

Figure 9.4: Left: Plot of the lattice data from H102 and the prediction of the Sakurai QFT for the tail of the integrand. The red curve is used to calculate the correction for truncating the integrand. Right: Comparison of the difference between the ensembles U102 and H102 and the prediction from the Sakurai QFT.

the right order of magnitude up to about $r = 0.8$ fm, where the integrand from the Sakurai QFT peaks. However, beyond this region, the Sakurai QFT is no longer in good agreement with the lattice data. Beside a possible mistuning in m_ρ for U102, another reason for this discrepancy might be that, as we approach or go beyond the half of the linear box size (1.05 fm for U102), the convergence of the winding expansion Eq. (8.17) is not sufficiently good for such a small box. As the summation scheme for the region beyond $r = 1.05$ fm requires one to sample the two boxes in different ways for geometrical reasons, a more careful discussion of the validity of the Sakurai QFT would be needed, especially on smaller boxes where the sensitivity of the model at short distances becomes critical.

The study described above suggests that the Sakurai QFT is able to effectively model the FSE due to the wrap-around-the-world effect of the pion up to medium values of r, but this effect might become too large to control with smaller boxes. Moreover, the correction needed to reconstruct the tail is sizeable for a small box like U102, leading to a less predictive result. For these reasons, the ensemble U102 is not included in the final analysis of this work.

Table 9.2: Results for the corrections for the finite-size effect of discretized momenta calculated in the Sakurai QFT and scalar QED and truncation of the integrand calculated in the Sakurai QFT. See the text in Sect. 9.2.2 for details. All values are in units of 10^{-10}. To get the FSE correction for N302 with the TL-kernel for example, we have FSE $= -1.693 - 1.104 = -2.797$ for the central value with an uncertainty of $\sigma_{\text{FSE}} = \sqrt{0.533^2 + (0.25 \cdot 2.797)^2} = 0.879$

		Wrap-around-the-world correction						Trunc. cor.
		Sakurai QFT			Scalar QED			Sakurai QFT
Id	L [fm]	$H_{\mu\nu}$	$H^{\text{TL}}_{\mu\nu}$	$H^{\text{XX}}_{\mu\nu}$	$H_{\mu\nu}$	$H^{\text{TL}}_{\mu\nu}$	$H^{\text{XX}}_{\mu\nu}$	$H^{\text{TL}}_{\mu\nu}$
U102	2.1	-3.859(455)	-2.834 (962)	-5.805(1865)	1.023(320)	-6.62(155)	-10.099(177)	-1.511
H102	2.8	-0.990(103)	-0.759(208)	-1.243(308)	0.419(9)	-1.424(10)	-1.577(8)	-0.584
S400	2.4	-2.047(255)	-1.479(429)	-2.677(719)	0.705(28)	-3.075(38)	-3.897(35)	-1.654
N203	3.1	0.114(26)	-0.200(21)	-0.259(49)	0.266(30)	-0.747(40)	-0.744(31)	-0.200
N302	2.4	-2.396(310)	-1.693(533)	-3.130(894)	0.714(163)	-3.611(51)	-4.712(48)	-1.104

Table 9.3: Comparison between the results for the isovector and strange connected contribution obtained in the CCS method using spherical integration and the results of the Mainz group [23] using the TMR method. Finite size corrections are applied to the isovector contribution for both methods. The results for U102 are not included in the final analysis. All values are in units of 10^{-10}.

	CCS method $H_{\mu\nu}^{\mathrm{TL}}$ kernel				TMR method			
	isovector		strange		isovector		strange	
Id	(LL)	(CL)	(LL)	(CL)	(LL)	(CL)	(LL)	(CL)
U102	174.26(191)	164.78(190)	—	—	—	—	—	—
H102	177.83(92)	168.66(90)	35.66(19)	33.54(19)	178.54(52)	179.75(52)	35.66(12)	35.90(11)
S400	175.21(96)	167.57(94)	34.90(20)	33.15(20)	173.82(69)	174.49(68)	34.402(86)	34.548(82)
N203	173.25(89)	167.60(88)	34.11(14)	32.83(13)	173.75(43)	174.11(43)	34.225(90)	34.283(89)
N302	169.08(96)	165.39(95)	33.31(17)	32.46(17)	167.77(87)	167.84(87)	32.427(83)	32.444(82)

9.2.4 Comparison to the time-momentum representation result

The ensemble-by-ensemble results for the isovector and strange contributions are displayed in table 9.3. Recall that two discretizations of the current-current correlator, namely the local-local (LL) and the conserved-local (CL), have been used to check for discretization effects (cf. Sect. 9.1). Due to the different discretization schemes, the results from this study based on the CCS method do not necessarily agree with those obtained with the TMR method. For the strange-quark contribution, the results obtained from both methods agree with each other quite well. Note that we do not apply any FSE correction to the strange data, as they receive contributions from the kaon loop at the leading order in ChPT, which is far more suppressed at large distances due to the higher mass of the kaon. In the isovector channel, we observe a good agreement between the CCS and the TMR methods for the local-local data on the larger ensembles H102 and N203. For the smaller ensembles S400 and N302 the agreement for the local-local discretization is slightly worse. When we look at the strange data, the agreement on the smaller ensembles is better. This could be a sign that the worse agreement in the isovector channel for S400 and N302 is due to finite-size effects, because these effects are much smaller for the strange channel. On the contrary, for the conserved-local data we see a different behaviour, when we compare the individual ensembles: our results with the CCS method lie below the TMR values. This fact is a hint that the results for the conserved-local discretization show a much flatter gradient as the continuum limit is approached, since in both methods, the O(a)-improvement has been implemented. This behaviour is illustrated in Fig. 9.5, when we later perform the continuum extrapolation at the common reference point.

9.2.5 Shift to a common reference point

The chosen ensembles from table 9.1 are not exactly at the same pion and kaon mass. Although these masses are not very different, we want to shift the results for each ensemble to a common reference point in the (m_π, m_K)-phase-space. We define this reference point to be at $m_\pi = 350$ MeV and $m_K = 450$ MeV. For this task, we use one of the best global fits from the calculation of the Mainz

group in the TMR method [23]. For the isovector contribution the fit has the following form

$$\begin{aligned}(a_\mu^{\mathrm{W}})_{I=1}(a,\phi_2,\phi_4) = \quad & p_0 + p_1(\phi_2-\phi_{2,\mathrm{phys}}) + p_2(\log(\phi_2)-\log(\phi_{2,\mathrm{phys}})) \\ & + p_3(\phi_4-\phi_{4,\mathrm{phys}}) + p_4 a^2\,,\end{aligned} \tag{9.21}$$

and for the strange contribution we have

$$\begin{aligned}(a_\mu^{\mathrm{W}})_{\mathrm{strange}}(a,\phi_2,\phi_4) = \quad & p_0 + p_1(\phi_2-\phi_{2,\mathrm{phys}}) + p_2(\phi_2-\phi_{2,\mathrm{phys}}) \\ & + p_3(\phi_4-\phi_{4,\mathrm{phys}}) + p_4 a^2\,.\end{aligned} \tag{9.22}$$

The fit parameters p_i and the associated covariance matrices are taken from the calculation done in Ref. [23]. In the above, a is the lattice spacing, $\phi_2 \equiv 8t_0 m_\pi^2$ and $\phi_4 \equiv 8t_0(m_K^2 + \frac{1}{2}m_\pi^2)$ are the dimensionless parameters defined with the gradient flow time t_0 [139]. With this fit form we calculate the differences between the result at the reference point and the result at the pion and kaon mass of the specific ensemble. This difference is independent of the lattice spacing of the given ensemble. The errors are calculated from the covariance matrices of the fits and the results of this calculation are given in tab. 9.4. We then apply these differences as a correction to the results on each ensemble in the CCS method. We used the TMR fit for the same current discretization (LL, CL) to correct the corresponding CCS data. However, we see that there is only a very small difference between the shifts for the LL and CL discretization calculated in the TMR method.

Again, 25% of the correction is assigned for the systematic uncertainty for this procedure. Since the chosen ensembles are very close to the chosen reference point, the systematic errors from shifting to that reference point are very small.

Table 9.4: Corrections to the reference point $m_\pi = 350$ MeV $m_K = 450$ MeV determined using calculations based on the TMR method. All values are in units of 10^{-10}

	isovector		strange	
Id	(LL)	(CL)	(LL)	(CL)
H102	0.11(4)	0.12(4)	-0.5(1)	-0.49(1)
S400	-0.07(2)	-0.06(2)	-0.27(1)	-0.26(1)
N203	-0.74(5)	-0.72(5)	-0.21(1)	-0.2(1)
N302	-0.63(1)	-0.62(1)	0.22(0)	0.22(0)

9.2.6 Continuum extrapolation

After we applied the corrections to account for the mistuning of the pion masses to the reference point, we perform an extrapolation to the continuum with a linear fit in a^2

$$f_1(a,\alpha_1,\beta_1) = \alpha_1 + \beta_1 a^2\,. \tag{9.23}$$

This is depicted in Fig. 9.5 and the results of the continuum extrapolation are displayed in Tab. 9.5.

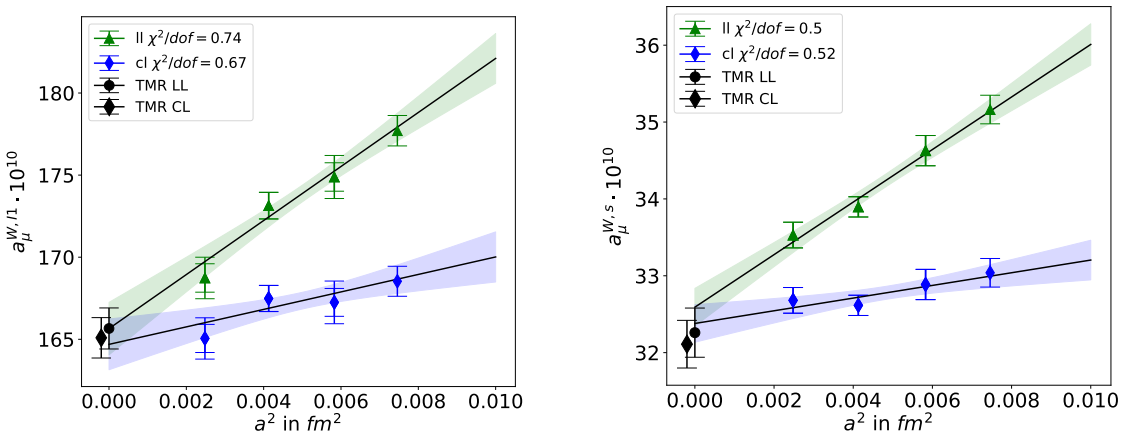

(a) Isovector contribution

(b) Strange contribution

Figure 9.5: Continuum extrapolation at the reference point $m_\pi = 350$ MeV and $m_K = 450$ MeV using the TL-kernel. The results from the TMR method are both at $a = 0$. They are separated slightly for a better visibility. The isovector contribution is corrected for finite-size effects. For the strange contribution no finite-size correction is applied. The smaller error bar is only the statistical error, the larger is the total error. The systematic error on N203 and H102 in the isovector contribution is almost not visible. For the strange contribution the uncertainty on each ensemble is highly dominated by the statistical error, as the systematic error from the shift to the reference point is not visible.

Table 9.5: Results of the continuum extrapolation from the CCS method and the TMR method with statistical uncertainties. The results of the TMR method are obtained from the fits in Eqs. (9.21) and (9.22). All values are in units of 10^{-10}.

	isovector		strange	
Id	(LL)	(CL)	(LL)	(CL)
$H_{\mu\nu}^{\mathrm{TL}}$	165.75(158)	164.69(156)	32.61(24)	32.38(23)
TMR [23]	165.66(125)	165.09(123)	32.26(32)	32.11(31)

Since the O(a)-improvement procedure is fully implemented, O(a) artifacts are expected to be absent in the continuum extrapolation. However, higher order terms, such as a^3, $a^2\log(a)$ and $a^2/\log(a)$ could also be non-negligible. This leads to a systematic error of the extrapolation. In order to obtain an estimate of this uncertainty, we perform several additional fits. For each of the fits, we allow one of these terms to be non zero. This makes us consider the following additional three-parameter fit-ansätze

$$f_2(a,\alpha_2,\beta_2,\gamma_2) = \alpha_2 + \beta_2 a^2 + \gamma_2 a^3, \tag{9.24}$$

$$f_3(a,\alpha_3,\beta_3,\gamma_3) = \alpha_3 + \beta_3 a^2 + \gamma_3 a^2 \log(a), \tag{9.25}$$

$$f_4(a,\alpha_4,\beta_4,\gamma_4) = \alpha_4 + \beta_4 a^2 + \gamma_4 \frac{a^2}{\log(a)}. \tag{9.26}$$

These fit ansätze leave only one degree of freedom with our available data. Hence, over-fitting could potentially be an issue. We observe a large cancellation between the term multiplying β_i and the one

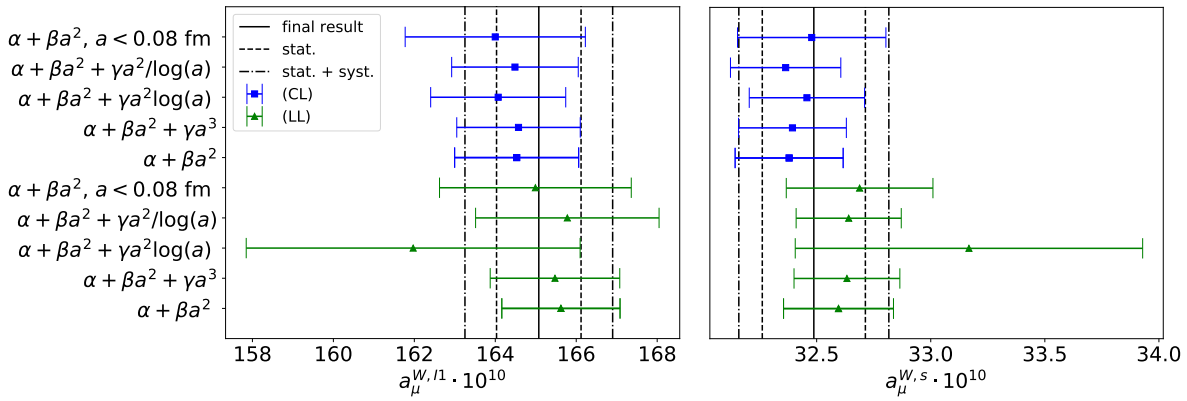

(a) Isovector contribution

(b) Strange contribution

Figure 9.6: Comparison of the different fit-ansätze for the continuum extrapolation at the reference point $m_\pi = 350$ MeV and $m_K = 450$ MeV using the TL-kernel. The root-mean-square deviation of all the different fits is calculated and gives the systematic uncertainty of the continuum extrapolation.

multiplying γ_i. Lacking guidance from additional data points, we introduce Gaussian priors to constrain the highest order terms in a, γ_i, in the ansätze Eqs. (9.24-9.26) to be in similar size as the best-fit coefficient β_1 from Eq. (9.23). Additionally, to probe the sensitivity of the linear fit f_1 to the range in lattice spacing of the data, we also perform the fit with the coarsest lattice spacing left out. We apply this procedure to the LL and CL data independently, resulting in 10 different fits. To get an estimate of the systematic error of the fitting procedure, we calculate the root-mean-squared deviation of the individual fit results in the continuum limit y_i from their average $\bar{y}$, $\Delta y_{\mathrm{RMS}} \equiv \left(\sum_{i=1}^{N} (y_i - \bar{y})^2 / N\right)^{1/2}$. The results for a_μ^{W} from the different fits are shown in Fig. 9.6. We see that the extrapolations for the conserved and the local current are in good agreement. Furthermore, the continuum values at the reference point are consistent with the calculation with the TMR method.

For our final estimate for the isovector and the strange-quark contribution to a_μ^{W} with the CCS method at the reference point of $m_\pi = 350$ MeV and $m_K = 450$ MeV, we quote the result from a constant fit to the LL and CL outcomes under the fit-ansatz f_1:

$$a_\mu^{\mathrm{W,I1}} = 165.17(1.57)_{\mathrm{stat}}(0.99)_{\mathrm{syst}} \times 10^{-10}, \tag{9.27}$$

$$a_\mu^{\mathrm{W,s}} = 32.49(0.22)_{\mathrm{stat}}(0.23)_{\mathrm{syst}} \times 10^{-10}. \tag{9.28}$$

9.3 Conclusion

In this study, we have extended the Covariant Coordinate Space method first proposed in Ref. [149] to the window quantity for the anomalous magnetic moment of the muon. Due to the stark geometric difference to the Time-Momentum Representation, this alternative approach provides a valuable

cross-check for the existing window quantity results from Lattice QCD. We provide values for the intermediate window quantity in the isovector channel and for the strange quark-connected contribution at $m_\pi = 350$ MeV and $m_K = 450$ MeV. With an appropriate finite-size effect correction scheme and a careful scrutiny of the discretization effects, we obtain $a_\mu^{\mathrm{W}} = 165.17(186) \times 10^{-10}$ for the isovector contribution and $a_\mu^{\mathrm{W}} = 32.49(32) \times 10^{-10}$ for the strange quark-connected contribution, where the statistical and systematic errors have been added in quadrature, confirming the results of the calculation of the Mainz group using the TMR method [23]. This study strengthens the tension between the lattice calculations and the dispersive approach on the window quantity.

One advantage of the CCS method is the freedom to modify the weight of the correlator computed at different regions without changing the final summed answer. This might turn out to be useful especially if one wants to adjust the shape of the lattice integrand to mitigate statistically noisy contributions. Future applications might involve different weight functions for different Euclidean time windows to optimize the integrand for minimal lattice artifacts and statistical noise. Furthermore, we have demonstrated how to correct for the finite-size effects in the CCS method based on an effective field theory approach. A strong motivation for this strategy is the non-trivial symmetric rank-two tensor structure of the coordinate-space correlator required by the formalism. A simple ρ-γ mixing model advocated by Jegerlehner and Szafron [96] successfully captures the long-distance contribution to a_μ^{W} in the CCS representation. The expected a^2-scaling that our data shows after the finite-size correction based on this model is encouraging and suggests that the same model might also be utilized as a guideline for further optimizations with the CCS method. This is of special interest for the calculation of the full Hadronic Vacuum Polarization to a_μ, whose integrand is much longer-ranged than a_μ^{W}. The technical details appended to this paper might be useful while computing other coordinate-space observables with similar integrable divergences in momentum-space.

The present calculation can be easily carried over to calculations of other lattice observables such as the full Hadronic Vacuum Polarization contribution to a_μ or the running of the QED coupling. For these observables, it might be of interest to combine the CCS method with master field simulations [161]. These simulations are performed over very large lattices, thus finite-size effects are expected to be highly suppressed. In particular, we expect that this framework is the best suited for studying the quark-disconnected contribution, which has been omitted in this work. It might be possible to get a more precise determination of this contribution with a short-ranged CCS kernel to filter out the noisy region for lattice calculations.

10 QED Corrections to the hadronic vacuum polarization contribution

Lattice QCD calculations of the hadronic vacuum polarizaton (HVP) contribution to the anomalous magnetic moment of the muon are typically performed in isospin symmetric QCD. As the theory effort for the evaluation of the HVP contributions aims for sub-percent precision, it is strictly necessary to include effects from QED and those that arise because of the mass difference between up and down quark. These so called *isospin breaking* effects can be treated as corrections added to the isospin symmetric result. The effects due to the mass difference can be expressed perturbatively in $m_u - m_d$. Effects from QED can be split from the QCD interactions according to section 3.6. The former can then be treated perturbatively as an expansion in the fine structure constant $\alpha = \frac{e^2}{4\pi}$. We only want to focus on corrections from QED effects in the following work.

There are different strategies for evaluating QCD+QED effects on the lattice, which need to regularize the infrared IR divergences of the photon propagator. A common framework is called QED_L, where the zero modes of the photon field are removed by setting $A_\mu(x_0, \boldsymbol{k} = 0) = 0$ on all time slices x_0 [162]. Another option is to introduce a small photon mass which also regularizes the divergence of the photon propagator at zero, which is referred to as QED_m [163]. In this chapter we want to look at the so called QED_∞ scheme [164, 165], which treats QED in the continuum and infinite volume, using the continuum expression for the scalar propagator $G_0(x)$ in Euclidean space, see section 2.1.1. IR divergences can then be removed by regularizing the integrals one needs to compute at the point $x = 0$.

A more severe issue for the calculation of QED corrections to the HVP is the occurrence of ultraviolet (UV) divergences, which requires renormalization. This is connected to the fact that one needs to set another scale associated with the effects of QED in a measurable physical observable, for example the mass splitting of the kaon. In this chapter, we want to look at the coordinate-space framework proposed in Ref. [166] for the calculation of the $O(\alpha)$ effects, which introduces a Pauli-Villars regulator for the photon propagator for the treatment of UV divergences. The definition of the disconnected contribution was already presented in the proceedings [167].

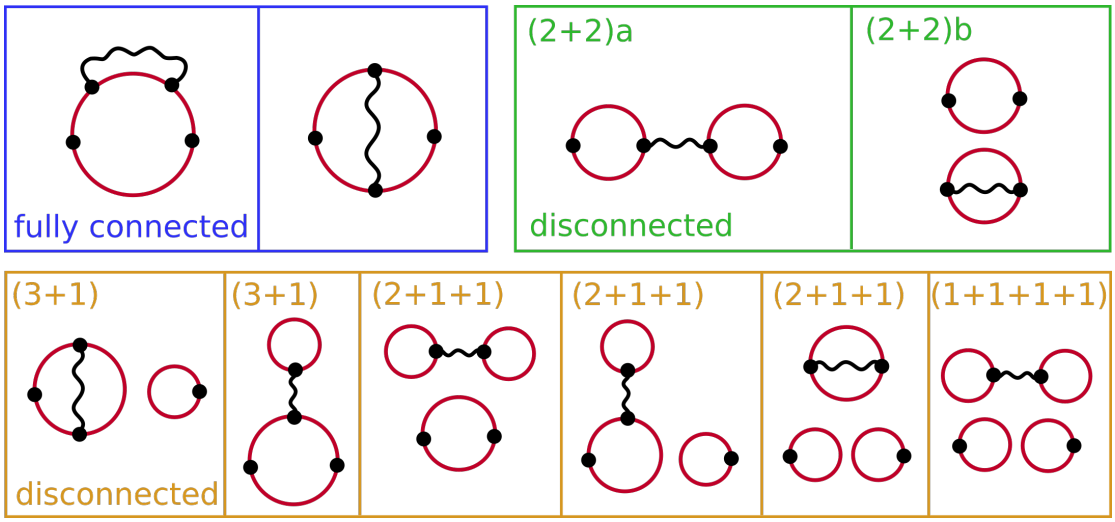

Figure 10.1: Diagrams that contribute to $\langle j_\mu(z)\, j_\nu(y)\, j_\rho(x)\, j_\sigma(0)\rangle_{QCD}$. We categorize the relevant diagrams according to the number of vector currents (black dots) that are connected by valence quark propagators (red-lines).

10.1 QED corrections to the HVP in the CCS representation

In our approach, the QCD four-point function in Eq. 10.2 is calculated in isospin symmetric QCD on the lattice, while the photon is treated in the continuum similar to the Mainz group's calculation of the hadronic light-by-light (HLbL) scattering [102, 168]. However, the HLbL contribution is UV-finite, whereas for the QED corrections to the HVP, we need to deal with the UV divergences. To this end, we introduce a Pauli-Villars regularized photon propagator [165]

$$\Big[G_0(y-x)\Big]_\Lambda = \frac{1}{4\pi^2|y-x|^2} - \frac{\Lambda K_1(\Lambda|y-x|)}{4\pi^2|y-x|}. \tag{10.1}$$

The vector-vector correlator at NLO in α is the given by

$$\begin{aligned}\langle j_\mu(z)\, j_\sigma(0)\rangle \;=\; & \langle j_\mu(z)\, j_\sigma(0)\rangle_{QCD} - 2\pi\alpha \int_{x,y} \delta_{\nu\rho}\Big[G_0(y-x)\Big]_\Lambda \langle j_\mu(z)\, j_\nu(y)\, j_\rho(x)\, j_\sigma(0)\rangle_{QCD} \\ & + \text{counterterms} + O(\alpha^2),\end{aligned} \tag{10.2}$$

where $\delta_{\nu\rho}G_0(x)$ is the photon propagator in Feynman gauge and $\langle j_\mu(z)\, j_\nu(y)\, j_\rho(x)\, j_\sigma(0)\rangle_{QCD}$ is the four-point function evaluated in QCD. Inserting Eq. 10.2 into the definition of a_μ^{hvp} in the CCS representation 7.25 we define the NLO contribution from the QED corrections as

$$a_\mu^{\text{hvp,NLO}} = -2\pi\alpha \int_{x,y,z} H_{\mu\sigma}(z)\delta_{\nu\rho}\Big[G_0(y-x)\Big]_\Lambda \langle j_\mu(z)\, j_\nu(y)\, j_\rho(x)\, j_\sigma(0)\rangle_{QCD}. \tag{10.3}$$

After taking into account the counterterms, the limit $\Lambda \to \infty$ can be taken. Another method to obtain the proper QCD+QED result is to calculate the subtracted piece with the massive photon propagator

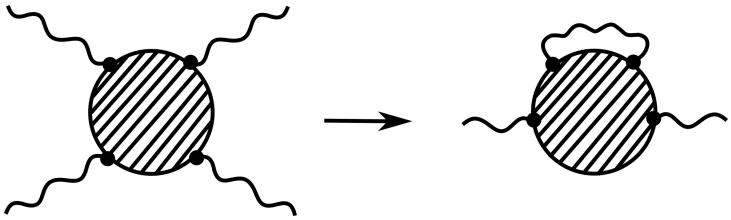

Figure 10.2: Cottingham-like formula for QCD LbL amplitude.

with mass Λ on the lattice using the QED$_m$ scheme. In this way one avoids power-law finite volume effects that can occur when putting the massless photon propagator on the lattice [162].

10.2 Connection to the hadronic light-by-light amplitude

In this section, we want to point out the connection between the hadronic light-by-light (HLbL) amplitude and the QED corrections to the HVP. To establish the connection we look at the HLbL scattering amplitude in momentum space with Minkowski signature $\mathcal{M}^{\mu_1\mu_2\mu_3\mu_4}(q_1,q_2,q_3,q_4)$. The forward kinematics correspond to $q_1 = q_3 \equiv k$ and $q_2 = q_4 \equiv q$, see Fig. 10.2. Contracting the photon-line 1 with 3, we obtain a contribution to the vacuum polarization tensor:

$$\Pi_{4\text{pt}}^{\mu_2\mu_4}(q^2,\Lambda) = -\frac{1}{2}\int \frac{d^4k}{(2\pi)^4}\left[\frac{-ig_{\mu_1\mu_3}}{k^2+i0^+}\right]_\Lambda \mathcal{M}^{\mu_1\mu_2\mu_3\mu_4}(k,q)\,, \tag{10.4}$$

whith the Pauli-Villars regularized photon propagator in momentum space

$$\left[\frac{1}{k^2}\right]_\Lambda = \frac{1}{k^2} - \frac{1}{k^2+\Lambda^2} \tag{10.5}$$

Due to gauge invariance, the VP tensor has the following general form,

$$\Pi^{\mu\nu}(q) = \Pi(q^2)(q^2 g^{\mu\nu} - q^\mu q^\nu), \tag{10.6}$$

and hence its scalar part can be expressed as:

$$\Pi_{4\text{pt}}(q^2,\Lambda) = -\frac{1}{6q^2}\int \frac{d^4k}{(2\pi)^4}\left[\frac{-i}{k^2+i0^+}\right]_\Lambda \mathcal{M}(k,q)\,, \tag{10.7}$$

where

$$\mathcal{M} \equiv g_{\mu_1\mu_3}g_{\mu_2\mu_4}\mathcal{M}^{\mu_1\mu_2\mu_3\mu_4}(k,q)\,, \tag{10.8}$$

is the traced LbL amplitude. The latter is a scalar function of three invariants: k^2, q^2, and $\nu \equiv k\cdot q$. It is even in ν and symmetric under the interchange of k and q. We shall write it as $\mathcal{M}(\nu,K^2,Q^2)$, where $K^2 = -k^2$ and $Q^2 = -q^2$ will further be assumed to be positive, i.e., the photons are spacelike.

By making use of the dispersion relation for $\mathscr{M}(\nu, K^2, Q^2)$ [165] one obtains the Cottingham formula analogue:

$$\Pi_{4\mathrm{pt}}(Q^2,\Lambda) = -\frac{1}{6Q^4(2\pi)^3}\int_0^\infty dK^2\left[\frac{1}{K^2}\right]_\Lambda \int_0^{K^2Q^2} d\nu^2\left(\frac{K^2Q^2}{\nu^2}-1\right)^{1/2}\mathscr{M}(\nu,K^2,Q^2), \tag{10.9}$$

which can be inserted into Eq. 6.6 in order to obtain the HVP contribution to a_μ.

10.3 Connected contribution to the QCD four-point function

In the following, we want to consider the case of two mass-degenerate light quarks and one strange quark with the electromagnetic vector current in the continuum

$$j_\mu(x) = \frac{2}{3}(\bar{u}\gamma_\mu u)(x) - \frac{1}{3}(\bar{d}\gamma_\mu d)(x) - \frac{1}{3}(\bar{s}\gamma_\mu s)(x). \tag{10.10}$$

For the evaluation of the four point function in lattice QCD one typically writes down all Wick contractions between the valence quarks and performs an average over the gauge configurations according to Eq. 5.47. These Wick contractions are depicted in figure 10.1, where the red lines indicate that one needs to evaluate the inverse of the Dirac operator sitting between the connected vertices. We call this *valence quark propagator*. The "wiggled" line depicts the photon propagator. We categorize the relevant diagrams according to the number of vertices that are connected by valence quark propagators.

Evaluating Eq. 5.47 for the case of four local vector currents, we obtain for the fully connected contributions

$$\begin{aligned}\langle j_\mu(z)j_\nu(y)j_\rho(x)j_\sigma(0)\rangle_{QCD}^{\mathrm{con}} = {}& \frac{17}{81}\mathscr{Z}_V^{(l)}\Big(\widetilde{\Pi}^{4a,l}_{\mu\nu\rho\sigma}(x,y,z,0)+\widetilde{\Pi}^{4b,l}_{\nu\rho\mu\sigma}(y,z,x,0)+\widetilde{\Pi}^{4c,l}_{\nu\mu\rho\sigma}(y,x,z,0)\Big)\\ &+\frac{1}{81}\mathscr{Z}_V^{(s)}\Big(\widetilde{\Pi}^{4a,s}_{\mu\nu\rho\sigma}(x,y,z,0)+\widetilde{\Pi}^{4b,s}_{\nu\rho\mu\sigma}(y,z,x,0)+\widetilde{\Pi}^{4c,s}_{\nu\mu\rho\sigma}(y,x,z,0)\Big),\end{aligned} \tag{10.11}$$

where $\mathscr{Z}_V^{(f)}$ is the renormalization coefficient for the vector currents of the light ($f=l$) and strange ($f=s$) quarks and

$$\widetilde{\Pi}^{4a,f}_{\mu\nu\rho\sigma}(x,y,z,0) = -2\mathrm{Re}\,\langle\mathrm{Tr}\big[D_f^{-1}(0,x)\gamma_\mu D_f^{-1}(x,y)\gamma_\nu D_f^{-1}(y,z)\gamma_\rho D_f^{-1}(z,0)\gamma_\sigma\big]\rangle_U, \tag{10.12}$$

$$\widetilde{\Pi}^{4b,f}_{\nu\rho\mu\sigma}(y,z,x,0) = -2\mathrm{Re}\,\langle\mathrm{Tr}\big[D_f^{-1}(0,y)\gamma_\nu D_f^{-1}(y,z)\gamma_\rho D_f^{-1}(z,x)\gamma_\mu D_f^{-1}(x,0)\gamma_\sigma\big]\rangle_U, \tag{10.13}$$

$$\widetilde{\Pi}^{4c,f}_{\nu\mu\rho\sigma}(y,x,z,0) = -2\mathrm{Re}\,\langle\mathrm{Tr}\big[D_f^{-1}(0,y)\gamma_\nu D_f^{-1}(y,x)\gamma_\mu D_f^{-1}(x,z)\gamma_\rho D_f^{-1}(z,0)\gamma_\sigma\big]\rangle_U, \tag{10.14}$$

where $\langle \ldots \rangle_U$ denotes the average over gauge configurations and D_f^{-1} is the inverse of the Dirac operator 5.30 for a given flavour f evaluated on the lattice. Contracting now y and x with the photon propagator (a) and (c) are identical. Inserting Eq. 10.11 into Eq. 10.3 yields

$$\begin{aligned} a_\mu^{\text{con}} &= -4\alpha\pi^3 \int d|z||z|^3 \int_{y,x} H_{\mu\sigma}(z)\Big[G_0(y-x)\Big]_\Lambda \Big[\frac{17}{81}\mathcal{Z}_V^{(l)}\Big(2\widetilde{\Pi}^{4a,l}_{\mu\nu\nu\sigma}(x,y,z,0)+\widetilde{\Pi}^{4b,l}_{\nu\nu\mu\sigma}(y,z,x,0)\Big) \\ &\quad \frac{1}{81}\mathcal{Z}_V^{(s)}\Big(2\widetilde{\Pi}^{4a,s}_{\mu\nu\nu\sigma}(x,y,z,0)+\widetilde{\Pi}^{4b,s}_{\nu\nu\mu\sigma}(y,z,x,0)\Big)\Big]. \end{aligned} \tag{10.15}$$

10.4 Disconnected contribution

All diagrams containing a self-contracted propagator contribute with a factor proportional to the charge of the quark in the self-contracted loop. Due to the property $\sum_{f=u,d,s} Q_f = 0$ these contributions cancel at the $SU(3)$ flavour symmetric point where all three quarks have equal mass $m_s = m_l$. This means that these diagrams are suppressed with a factor proportional to the difference between the strange and the light quark masses. This is seen also in the calculation of the HLbL contribution to a_μ [168], where the contribution of the diagrams at the bottom of figure 10.1 can be neglected. The $(2+2)$ diagrams on the other hand do contribute significantly to a_μ^{HLbL}. So, it is expected that for the QED corrections to the HVP these contributions are also relevant.

For the diagrams of the $(2+2)$ topology, each of the valence quark loops can either be a light or a strange quark, so there are in principle 4 combinations of light and strange quark loops: (ll), (ls), (sl), (ss). For the total $(2+2)$ vector correlator, we have

$$\begin{aligned} \langle j_\mu(z) j_\nu(y) j_\rho(x) j_\sigma(0)\rangle_{QCD}^{(2+2)} &= \frac{25}{81}\mathcal{Z}_V^{(ll)}\Big(\widetilde{\Pi}^{(2+2)a,ll}_{\mu\nu\rho\sigma}(x,y,z)+\widetilde{\Pi}^{(2+2)b,ll}_{\mu\nu\rho\sigma}(x,y,z)+\widetilde{\Pi}^{(2+2)c,ll}_{\mu\nu\rho\sigma}(x,y,z)\Big) \\ &+\frac{5}{81}\mathcal{Z}_V^{(ls)}\Big(\widetilde{\Pi}^{(2+2)a,ls}_{\mu\nu\rho\sigma}(x,y,z)+\widetilde{\Pi}^{(2+2)b,ls}_{\mu\nu\rho\sigma}(x,y,z)+\widetilde{\Pi}^{(2+2)c,ls}_{\mu\nu\rho\sigma}(x,y,z)\Big) \\ &+\frac{5}{81}\mathcal{Z}_V^{(sl)}\Big(\widetilde{\Pi}^{(2+2)a,sl}_{\mu\nu\rho\sigma}(x,y,z)+\widetilde{\Pi}^{(2+2)b,sl}_{\mu\nu\rho\sigma}(x,y,z)+\widetilde{\Pi}^{(2+2)c,sl}_{\mu\nu\rho\sigma}(x,y,z)\Big) \\ &+\frac{1}{81}\mathcal{Z}_V^{(ss)}\Big(\widetilde{\Pi}^{(2+2)a,ss}_{\mu\nu\rho\sigma}(x,y,z)+\widetilde{\Pi}^{(2+2)b,ss}_{\mu\nu\rho\sigma}(x,y,z)+\widetilde{\Pi}^{(2+2)c,ss}_{\mu\nu\rho\sigma}(x,y,z)\Big), \end{aligned} \tag{10.16}$$

where again $\mathcal{Z}^{(ff')}$ is a renormalization coefficients and

$$\widetilde{\Pi}^{(2+2)a,ff'}_{\mu\nu\rho\sigma}(x,y,z) = \langle \hat{\Pi}^f_{\mu\nu}(z,x)\hat{\Pi}^{f'}_{\rho\sigma}(y,0)\rangle_U, \tag{10.17}$$

$$\widetilde{\Pi}^{(2+2)b,ff'}_{\mu\nu\rho\sigma}(x,y,z) = \langle \hat{\Pi}^f_{\mu\sigma}(z,0)\hat{\Pi}^{f'}_{\rho\nu}(y,x)\rangle_U, \tag{10.18}$$

$$\widetilde{\Pi}^{(2+2)c,ff'}_{\mu\nu\rho\sigma}(x,y,z) = \langle \hat{\Pi}^f_{\mu\rho}(z,y)\hat{\Pi}^{f'}_{\nu\sigma}(x,0)\rangle_U, \tag{10.19}$$

where the two-point correlation function for the local vector current is given by

$$\Pi^f_{\mu\nu}(x,y) = -\mathrm{Re}\Big(\mathrm{Tr}\Big[D_f^{-1}(y,x)\gamma_\mu D_f^{-1}(x,y)\gamma_\nu\Big]\Big). \tag{10.20}$$

The vacuum expectation value needs to be subtracted in order to avoid double counting of the contribution where the two QCD 'blobs' are not interconnected,

$$\hat{\Pi}^f_{\mu\nu}(x,y) = \Pi^f_{\mu\nu}(x,y) - \langle\Pi^f_{\mu\nu}(x,y)\rangle_U. \tag{10.21}$$

Again the (a) und (c) contractions are identical, when the vertices x and y are contracted with the photon propagator. Inserting Eqs. 10.16 into Eq. 10.3. the integrals over y and z factorize and the final integral over x only depends on its norm $|x|$. In the continuum and infinite-volume limit the $(2+2)$ contributions to $a_\mu^{HVP,NLO}$ now take the form

$$a_\mu^{(2+2)a,ff'} = -8\pi^3\alpha C^{(ff')}\mathcal{Z}_V^{(ff')}\int_0^\infty d|x||x|^3\Big[\langle I^{(2,f)}_{\rho\sigma}(x)I^{(3,f')}_{\sigma\rho}(x)\rangle_U - \langle I^{(2,f)}_{\rho\sigma}(x)\rangle_U\langle I^{(3,f')}_{\sigma\rho}(x)\rangle_U\Big], \tag{10.22}$$

$$a_\mu^{(2+2)b,ff'} = -4\pi^3\alpha C^{(ff')}\mathcal{Z}_V^{(ff')}\int_0^\infty d|x||x|^3\Big[\langle I^{(1,f)}(x)I^{(4,f')}\rangle_U - \langle I^{(1,f)}(x)\rangle_U\langle I^{(4,f')}\rangle_U\Big], \tag{10.23}$$

with the four integrals [167]

$$I^{(1,f)}(x) = \int_z \Big[G_0(x-z)\Big]_\Lambda \Pi^f_{\nu\nu}(x,z), \tag{10.24}$$

$$I^{(2,f)}_{\rho\sigma}(x) = \int_y \Big[G_0(x-y)\Big]_\Lambda \Pi^f_{\rho\sigma}(y,0), \tag{10.25}$$

$$I^{(3,f)}_{\sigma\rho}(x) = \int_z H_{\nu\sigma}(z)\Pi^f_{\nu\rho}(z,x), \tag{10.26}$$

$$I^{(4,f)} = \int_y H_{\mu\sigma}(y)\Pi^f_{\mu\sigma}(y,0), \tag{10.27}$$

where the chargefactors are $C^{(ll)} = \frac{25}{81}$, $C^{(ls)} = C^{(sl)} = \frac{5}{81}$ and $C^{(ss)} = \frac{1}{81}$. In the total result the (ls) and (sl) contributions are equivalent, since the ordering of the quark loops does not matter. For the numerical implementation of the integrals 10.25 and 10.26 this can be a crosscheck. In the definition of $a_\mu^{(2+2)a,ff'}$ 10.22 we have absorbed the contribution from the contractions (c) 10.19 resulting in a factor of 2. It is worth noting that although we are calculating a four-point function in QCD, the $(2+2)$ contribution can be evaluated only by computation of correlated two-point functions $\Pi^f_{\mu\nu}(x,y)$, that depend on two lattice coordinates. We call the coordinate at x the *source* and y the *sink*. In order to calculate the integrand of Eq. 10.22 or Eq. 10.23 for a given point $|x|$, using the definition of

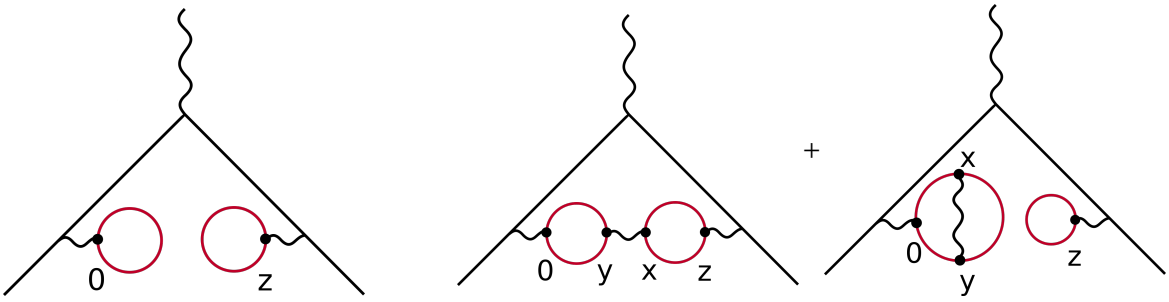

(a) Leading order disconnected contribution **(b)** QED corrections to the disconnected contribution

the two-point function 10.20 one only needs to calculate the one-to-all propagator for one source at the origin and another source at the lattice point x. However, in practice one wants to take several measurements for different origins to increase the statistics.

We also want to point out that the VEV of Eq. 10.27 $\langle I^{(4,f)}\rangle_U$ is exactly the leading order HVP contribution to a_μ. So, the $a_\mu^{(2+2)b}$ contribution can be seen as reweighting of the leading order contribution with a QED effect in the sea-quark loop.

The diagram $a_\mu^{(2+2)a}$ on the other hand is precisely the QED correction of the leading order disconnected contribution, see figure 10.3b. The leading order disconnected diagram is suppressed due to the fact that each quark contributes proportional to its charge factor, so at the $SU(3)$ flavour symmetric point the diagram vanishes. The photon propagator connecting the quark loops in the $(2+2)a$ diagram however, lifts this double $SU(3)$ flavour suppression. Therefore, it is expected that this QED correction is quite large relative to the leading order disconnected. An important aspect that we want to stress here, is that the $(2+2)a$ contribution is UV-finite. This can be seen by writing down an expression in partially quenched QCD that corresponds to this specific diagram [102]

$$\delta_{\mu\nu}\Big[G_0(x-y)\Big]_\Lambda \langle \overline{u}(0)\gamma_\sigma d(0)\overline{d}(y)\gamma_\mu u(y)\overline{s}(x)\gamma_\nu r(x)\overline{r}(z)\gamma_\lambda s(z)\rangle \tag{10.28}$$

with quenched flavours s and r. Using Wick's theorem on this expression generates precisely the contraction that corresponds to the $(2+2)a$ topology. Now, we want to look at the case where x is close to y, but both are not zero. The operator product expansion of the operator $\overline{d}(y)\gamma_\mu u(y)\overline{s}(x)\gamma_\nu r(x)$ needs to contain four quark flavours and therefore the lowest dimension effective operator one can write down for this is of mass dimension six. We especially obtain the term

$$\overline{d}(y)\gamma_\mu u(y)\overline{s}(x)\gamma_\nu r(x) \quad \overset{x\to y}{\sim} \quad \Big(\overline{d}(x)\gamma_\mu u(x)\overline{s}(x)\gamma_\nu r(x)\Big)c(|x|)+\ldots \tag{10.29}$$

with Wilson coefficient $c(|x|)$. From dimensional analysis this Wilson coefficient needs to be constant or can have a $\log(|x|)$ dependence, but nothing else. This behaviour is not sufficient to cause a

divergence when integrating over x. The case where $x \to y \to 0$ is more subtle. If we express x and y as

$$x \to \lambda x, \qquad y \to \lambda y, \tag{10.30}$$

with the parameter λ carrying the dimension of inverse mass, we want to look at the limit $\lambda \to 0$. In the OPE of the operator $\overline{u}(0)\gamma_\sigma d(0)\overline{d}(y)\gamma_\mu u(y)\overline{s}(x)\gamma_\nu r(x)$ two quark flavours can be reduced to two propagators resulting in a $\frac{1}{\lambda^6}$ behaviour as $\lambda \to 0$. From the photon propagator we get another factor $\frac{1}{\lambda^2}$. Taking the integral measure with λ^8 one would still expect a logarithmic divergence in the case where the two valence quark loops are not connected by gluons. However, when we only take into account the case where the valance quark loops are connected with gluon lines, there is an additional factor of the strong coupling $(\alpha_s(1/\lambda))^2$ entering. The strong coupling behaves asymptotically as $(\alpha_s(1/\lambda))^2 \sim \log(1/\lambda)^2$, which is just enough to make the result UV-finite. The fact that we subtract the vacuum expectation value in Eq. 10.21 ensures exactly that the two hadronic blobs are still connected by gluon lines. Without the subtraction, one would see the logarithmic divergence of the result for $x \to y \to 0$.

11 Computing the (2+2)a disconnected contribution

In this final chapter, we want to present the details of the lattice QCD calculation of the QED corrections of the $(2+2)a$ topology that we introduced in chapter 10, see figure 10.1. The formalism we use for this calculation as well as the method to obtain the lattice result on one ensemble was already pointed out in Ref. [167]. There is some minor text overlap with this source.

In our calculation, the photon propagator is treated in the continuum. Since this diagram is UV-finite, see section 10.4, the continuum limit $a \to 0$ exists and the result can in principle be used as a bechmark quantity, to compare different lattice calculations, if the same reference point for the physical point in isospin symmetric QCD is chosen. In section 11.1 we will discuss the lattice setup that we use and in section 11.2 we analyse the finite-size effects. In section 11.3 we will see how one can describe the data from lattice QCD by using a phenomenological model. We will then use this model to approximate the tail of the integrand 11.5 and to estimate the chiral dependence for the extrapolation to the physical point 11.6.

11.1 Lattice setup

To evaluate the $(2+2)a$ diagram, we rely on the coordinate-space formalism defined in Eq. 10.22. We calculate the integrals $I^{(2,f)}_{\rho\sigma}(x)$ and $I^{(3,f)}_{\sigma\rho}(x)$ defined in Eq. 10.25, 10.26 for several points x. This allows us to display the integrand of Eq. 10.22 as a function of $|x|$. The two-point function 10.20 is calculated on seven ensembles generated by the CLS consortium with parameters given in Table 9.1. The simulation is performed with $N_f = 2+1$ dynamical flavors of non-perturbatively $O(a)$ improved Wilson quarks and tree-level $O(a^2)$ improved Lüscher-Weisz gauge action. We only calculate the two-point functions for the light quark propagators, with the exception of the ensemble N451, where we also compute the strange quark two-point function. In Eq. 10.20 the one-to-all propagator is calculated for fixed source positions that are placed along the diagonal $(n,n,n,N_T/2)$ for $n = \{0,1,\ldots,N_L\}$ on each ensemble. In our position-space approach the two-point function for $I^{(2,f)}_{\rho\sigma}(x)$ needs to be evaluated at the origin, whereas the two-point function for $I^{(3,f)}_{\sigma\rho}(x)$ needs to be calculated at a position x. The absolute difference between the origin and x is exactly the value of $|x|$ where the integrand with

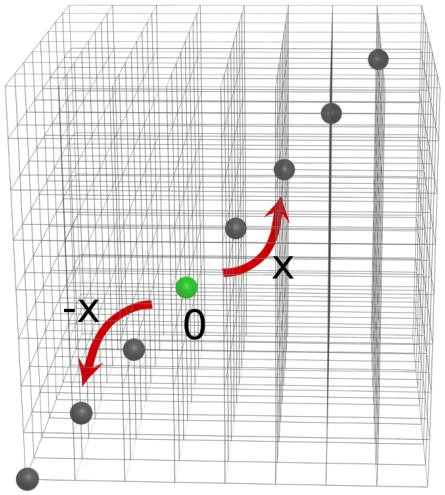

Figure 11.1: Illustration of the positioning of the point sources on the lattice according to the explanation in section 11.1.

respect to the final integration parameter is sampled, see figure 11.1. After evaluating the average over gauge configurations, the definition of the origin in the final result Eq. 10.22 is ambiguous. To increase the statistics, the above procedure is repeated for each of the N_L source positions used as the origin and averaging over all measurements. Using periodicity of the spatial dimensions and the fact that the measurement for $-x$ and x is equivalent in the result for the integrand $f(|x|)$ we obtain in total $2N_L$ measurements for each value of $|x|$.

The integrals in Eq. 10.25, 10.26 are calculated as a sum over all lattice points using the simpson rule and results for different positions of the origin and different x are stored. The gauge average is calculated according to Eq. 10.22, where we evaluate the error using the Jackknife procedure 5.6.1. The correlated result for $\langle I^{(2)}_{\rho\sigma}(x) I^{(3)}_{\sigma\rho}(x)\rangle_U$ as well as the subtraction of the VEV $\langle I^{(2)}_{\rho\sigma}(x)\rangle_U \langle I^{(3)}_{\sigma\rho}(x)\rangle_U$ is done on every Jackknife sample. We observe that the relative size of the quantity after subtraction of the VEV compared to the unsubtracted quantity can be $\sim 1\% - 5\%$ for small values of $|x|$ which can be challenging, when the calculation is performed with low numerical accuracy.

We choose to calculate $I^{(3)}_{\sigma\rho}(x)$ for the 'XX' and 'TL' kernel defined in 7.10 and 7.9. After the integration over z the results for $I^{(3)}_{\sigma\rho}(x)$ calculated with either one of the kernels differ only by lattice artifacts, so comparing both kernels serves as a consistency check. Since we know that the $(2+2)a$ contribution is UV finite we can drop the Pauli-Villars regulator in the photon-propagator, effectively sending $\Lambda \to \infty$. But in order to obtain a numerical result, one needs to choose an additional regularization of the photon propagator in Eq. 10.25 for the point where $x = y$. The photon propagator is numerically

Table 11.1: This table shows the parameters of the ensembles used in the analysis generated by the CLS consortium. The lattice spacing, the pion and kaon is determined in Ref. [169], [141].

Id	β	$N_L^3 \times N_T$	a [fm]	m_π [MeV]	m_K [MeV]	$m_\pi L$	L [fm]	#confs light/strange
C101	3.4	$48^3 \times 96$	0.0849(9)	222(3)	478(5)	4.6	4.1	200/0
N451	3.46	$48^3 \times 128$	0.0751(8)	291(4)	468(5)	5.3	3.6	200 /200
D450		$64^3 \times 128$		219(3)	483(5)	5.3	4.8	200/0
H200	3.55	$32^3 \times 96$	0.0635(6)	423(5)	423(5)	4.4	2.0	200/0
N202		$48^3 \times 128$		418(5)	418(5)	6.5	3.0	200/0
N203		$48^3 \times 128$		349(4)	447(5)	5.4	3.0	200/0
E250		$96^3 \times 192$		132(2)	495(6)	4.1	6.1	200
E300	3.7	$96^3 \times 192$	0.0491(5)	177(2)	497(6)	4.2	4.7	200/0

implemented as

$$G_0(x-y) = \begin{cases} \frac{1}{4\pi^2|\lambda a|^2}, & |x-y| = 0 \\ \frac{1}{4\pi^2|x-y|^2}, & \text{else} \end{cases}, \tag{11.1}$$

where a is the lattice spacing. We choose to work with $\lambda = 0.5$. Additionally we performed calculations for $\lambda = \{0.25, 0.5, 0.75\}$ on the ensemble N203, where no significant change in the result was visible.

For the calculation of the two-point functions, we use the vector current in the conserved discretization 9.3 at the origin and at x. The local discretization 9.1 of the vector current is used at the vertices y and z. The renormalization coefficient in Eq. 10.22 is then given by $\mathcal{Z}_V = (\hat{Z}_V^{(L)})^2 (\hat{Z}_V^{(C)})^2$, where $\hat{Z}^{(C)} = 1$ and $\hat{Z}^{(L)}$ is obtained from Eq. 9.6.

11.2 Finite-size effects of the different kernels

In order to study the finite size effects of our calculation, we compare the integrand of Eq. 10.22 between the ensembles N202 and H200. Both have been generated at the $SU(3)$ flavour symmetric point with the same value of β. However, H200 is significantly smaller with $m_\pi L = 4.4$ compared to $m_\pi L = 6.5$ for N202. Figure 11.2 shows this comparison for the 'TL' and 'XX' kernel. We observe that for the 'TL' kernel the results computed on the smaller ensemble H200 are in complete agreement with the results calculated on N202 up to $x_m < 1$fm which is half the size of the spatial dimension of H200. Effects due to the finite-size only become visible for $x_m > 1$fm. For the XX kernel however, the finite-size effects become significant at $x_m > 0.75$ fm. We therefore choose to work with the 'TL' kernel in our analysis. In addition to that the 'TL' kernels shows smaller statistical error for each of the data points. The preference for the 'TL' kernel is furthermore in accordance with our analysis of the leading order intermediate window observable in chapter 9. The analogy to this computation can be seen from the fact that the integral in Eq. 10.26 that one has to compute to obtain Eq. 10.22 is very similar to the leading order HVP contribution to a_μ, but with different combination of Lorentz indices.

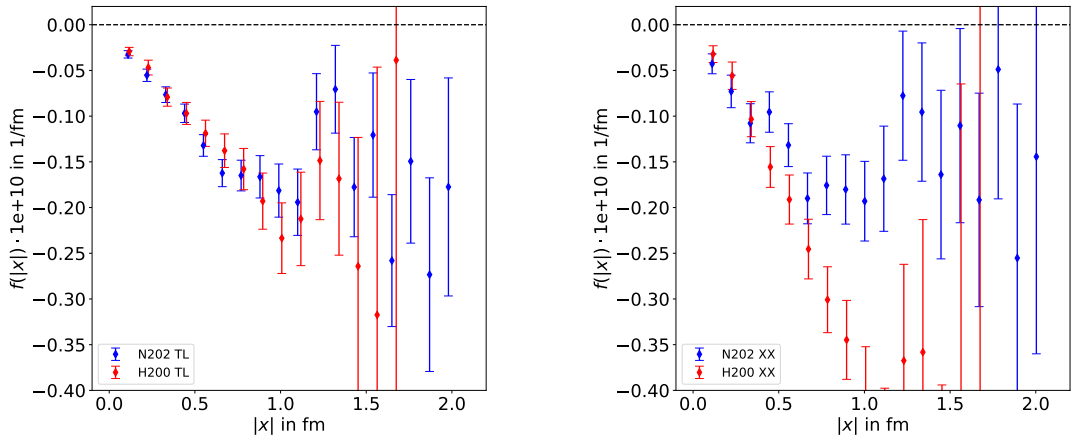

(a) 'TL' kernel

(b) 'XX' kernel

Figure 11.2: Comparison of the integrand of Eq. 10.22, including all prefactors, for the ensembles H200 ($m_\pi L = 4.4$) and N202 ($m_\pi L = 6.5$) for the 'TL' kernel (left) and the 'XX' kernel (right), defined in Eqs. 7.10 and 7.9

Here, we want to mention that one has additional freedom in the treatment of the integral in Eq. 10.26. One could for example explore different summation schemes related to the scheme proposed 9.1.2 to suppress finite-size effects. However, in this analysis we perform a simple sum over all lattice points.

We also want to point out that one has additional freedom in adding a total derivative in the definition of the integral 10.25

$$\tilde{I}^2_{\rho\sigma}(x) = \int_y \left(\delta_{\alpha\rho}\left[G_0(x-y)\right]_\Lambda + \partial^{(y)}_\alpha\left(y_\rho f(|y|)\right)\right)\hat{\Pi}_{\alpha\sigma}(y,0), \tag{11.2}$$

for an arbitrary function $f(|x|)$. The additional term does not change the contribution in the continuum and infinite volume, because of the conservation of the vector current at the vertex y. This could potentially allow for more optimization.

11.3 Phenomenological description

In section 9.2.1, we saw that the lattice data could be approximated by using an effective field theory (EFT) approach. Although one does not expect the EFT to give precise results for the lattice calculation, one can still use these as a guideline and as a consistency check for the results computed in lattice QCD.

Here, we want to work out a phenomenological description of the $(2+2)a$ contribution 10.22. For this, we look at the light meson contributions at order $O(\alpha^3)$ in the fine structure constant. We compute the contribution of the pseudoscalar mesons π^0, η and η' as well as the $\pi^+\pi^-$-loop. We use the matching factor from chiral perturbation theory worked out for calculation of the HLbL

contribution [168] to calculate how much the hadronic contributions contribute to the (2+2)a diagram. For the pseudoscalar meson exchange (PME) we integrate out the vertices y and z keeping the value for the final integration variable $|x|$ fixed [167], so that the integrand calculated for the PME can be directly compared to the integrand of Eq. 10.22 computed in lattice QCD. This phenomenological model is then used for two purposes. First, to reconstruct the tail of the integrand of Eq. 10.22, where hadronic contributions dominate. Secondly, to determine the chiral dependence of the result and therefore to constrain the fit to the physical point.

11.3.1 The π^0 exchange contribution

In order to determine the contribution of the π^0 to the HVP at NLO 10.3 we can use the formula for the vacuum polarization given in Ref. [166]

$$\Pi_{4\mathrm{pt}}(q^2,\Lambda) = \frac{-e^4}{16\pi^2|q|}\int_0^\infty d|k||k|^4\Big[\frac{1}{k^2}\Big]_\Lambda \mathscr{F}(-q^2,-k^2)^2\, Z^{m_\pi}_{|q|,|k|}\Big(1-\tfrac{1}{3}(Z^{m_\pi}_{|q|,|k|})^2\Big), \tag{11.3}$$

where the Pauli-Villars regularization in momentum space is simply given by

$$\Big[\frac{1}{k^2}\Big]_\Lambda = \frac{1}{k^2}-\frac{1}{k^2+\Lambda^2}. \tag{11.4}$$

Here, we have

$$Z^m_{|q|,|k|} = \frac{1}{2|q||k|}\Big(q^2+k^2+m^2-\sqrt{(q^2+k^2+m^2)^2-4q^2k^2}\Big). \tag{11.5}$$

Now, we insert the subtracted vacuum polarization $\Pi_{4\mathrm{pt}}(q^2,\Lambda)-\Pi_{4\mathrm{pt}}(0,\Lambda)$ into Eq. 6.6 to obtain the contribution to a_μ. The result is finite in the limit $\Lambda\to\infty$. For a VMD form factor

$$\mathscr{F}(-q_1^2,-q_2^2) = \frac{\mathscr{F}_{\pi^0\gamma^*\gamma^*}(0,0)}{(1+q_1^2/m_V^2)(1+q_2^2/m_V^2)}, \tag{11.6}$$

and using $\mathscr{F}(0,0)=(4\pi^2 f_\pi)^{-1}$ for the PDG values $f_\pi = 92.4\,\mathrm{MeV}$, $m_V = 0.77549\,\mathrm{GeV}$, and the physical π^0 mass one obtains

$$a_\mu^{\pi^0} = 0.370\times 10^{-10}. \tag{11.7}$$

However, we want to go a step further and calculate the integrand of Eq. 10.3 in position space [167], where the vertices y and z are integrated out

$$a_\mu^{\pi^0} = \int_0^\infty d|x| f(|x|), \tag{11.8}$$

calculated from the coordinate space vector correlator for the π^0 exchange

$$\langle j_\sigma(z)\, j_\mu(y)\, j_\nu(x)\, j_\lambda(0)\rangle^{\pi^0} = \int_{q,k,p} e^{i(p\cdot z+q\cdot x+k\cdot y)}\Pi_{\sigma\mu\nu\lambda}(p,q,k). \tag{11.9}$$

Starting from the momentum space polarization tensor $\Pi_{\sigma\mu\nu\lambda}(p,q,k)$ given in Ref. [170]. Substituting Eq. 11.9 for the four-point vector-correlator in Eq. 10.3 we obtain for the integrand

$$\begin{aligned} f(|x|) &= -\frac{e^2}{2}2\pi^2|x|^3\frac{1}{(2\pi)^{12}}\int_{z,x} H_{\sigma\lambda}(z)\delta_{\mu\nu}\Big[G_0(x-y)\Big]_\Lambda \int_{q,k,p} e^{i(p\cdot z+q\cdot x+k\cdot y)}\Pi_{\sigma\mu\nu\lambda}(p,q,k) \\ &= -\frac{e^2}{2}2\pi^2|x|^3\frac{1}{(2\pi)^{12}}\int_k e^{ik\cdot y}\Big[\frac{1}{k^2}\Big]_\Lambda \int_p \tilde{H}_{\sigma\lambda}(p)\int_q e^{iq\cdot y}\,\Pi_{\sigma\mu\mu\lambda}(p,q,k), \end{aligned} \tag{11.10}$$

where the Fourier transform of the CCS kernel is

$$\tilde{H}_{\sigma\lambda}(p) = \int_z H_{\sigma\lambda}(z)\, e^{ip\cdot z}. \tag{11.11}$$

Using the definition of $g(p^2)$ in Ref. [149] we find

$$\tilde{H}_{\sigma\lambda}(p) = \frac{\delta_{\sigma\lambda}(2\pi)^4}{3\pi^2}\Big[\Big(3+p^2\frac{d}{dp^2}\Big)\Big(\frac{g(p^2)}{|p|^4}\Big) - 2\alpha^2\frac{\delta^{(1)}(|p|)}{|p|^5}\Big] + p_\lambda p_\sigma \ldots \tag{11.12}$$

with

$$g(p^2) = 2\alpha^2\frac{m_\mu^4}{p^6}y(|p|)^4, \qquad y(|p|) = \frac{2|p|}{|p|+\sqrt{4m_\mu^2+p^2}}, \tag{11.13}$$

where the terms proportional to $p_\lambda p_\sigma$ do not contribute to $f(|y|)$, owing to the transversality property $p_\sigma\Pi_{\sigma\mu\mu\lambda}(p,q,k)=0$. We write

$$\tilde{H}_{\sigma\lambda}(p) = \delta_{\sigma\lambda}\tilde{h}(p^2) + p_\lambda p_\sigma \ldots \tag{11.14}$$

As a check of Eq. 11.12 we can rewrite Eq. 11.8 as

$$a_\mu^{\mathrm{hvp},e^2} = \frac{-3}{2^3\pi^2}\int_0^\infty d|p||p|^5\tilde{h}(p^2)\Pi_{4\mathrm{pt}}(p^2,\Lambda) \tag{11.15}$$

with

$$\Pi_{4\mathrm{pt}}(p^2,\Lambda) = -\frac{e^2}{2}\frac{1}{(2\pi)^8}\int_{x,y,z}\int_k e^{ik\cdot y}\Big[\frac{1}{k^2}\Big]_\Lambda\int_q e^{iq\cdot y}\,\Pi_{\sigma\mu\mu\lambda}(p,q,k). \tag{11.16}$$

We can compare this to the familiar definition for a_μ^{hvp} in Eq. 6.6

$$a_\mu^{\mathrm{hvp},e^2} = \int_0^\infty dp^2\frac{d}{dp^2}\Big(p^2g(p^2)\Big)\overline{\Pi}_{4\mathrm{pt}}(p^2,\Lambda). \tag{11.17}$$

In order for $\Big(p^2g(p^2)\Big)$ to match the kernel in Eq. 6.6 the the $\delta^{(1)}(|p|)$ term in Eq. 11.12 is strictly

necessary for the subtraction of the vaccuum polarization at $p^2 = 0$. The details for the calculation of $f(|x|)$ can be found in appendix A.3. For the implementation we use the final result A.37. The result for the π^0 exchange is finite even for $\Lambda \to \infty$.

11.3.2 Model parameters and $\eta - \eta'$ mixing

The derivation in section 11.3.1 for the π^0 exchange is characterized by three dimensionful quantities: The pion mass m_π, the vector meson mass $m_{V,\pi}$ and the normalization of the transition form factor $\mathscr{F}(0,0)$ of the π^0 decaying into two virtual photons. We will denote $F_\pi := \mathscr{F}_{\pi^0\gamma^*\gamma^*}(0,0)$. The same derivation can be applied for the η and η' meson, for which we only need to change the model parameters. For the η we define $(m_\eta, m_{V,\eta}, F_\eta)$ and for η' the three parameters $(m_{\eta'}, m_{V,\eta'}, F_{\eta'})$. In total we have 9 parameters for the pseudoscalar meson contributions. The masses of the three pseudoscalar mesons have been determined on the CLS ensembles we use, for the pion mass we determination in Ref. [169], [141]. The masses of the η and η' meson have been determined in Ref. [171]. The normalization of the pion transition formfactor F_π and the VMD mass of the pion are obtained from a fit to the data from Ref. [47], where the fit is restricted to the single virtual case. This was done for the work in Ref. [102]. In order to get a better understanding of the other parameters, we take into account the prediction from large N_C chiral perturbation theory (L$N_c\chi$PT) [107], [99]. In L$N_c\chi$PT the η and η' are linear combinations of the η_8 field in the octet and the singlet field η_1, characterized by the mixing angle θ, see section 4.1.3. The normalization of the transition form factors for the π, η and η' have been worked out to NLO in χPT in Ref. [99] in terms of several low energy constants that have to be determined from experimental values. For this work, we will only use the leading order results

$$F_\pi^{LO} = \frac{1}{4\pi^2 f_\pi}, \tag{11.18}$$

$$F_\eta^{LO} = \frac{1}{4\sqrt{3}\pi^2 f_\pi}\left[\cos(\theta^{[0]}) - 2\sqrt{2}\sin(\theta^{[0]})\right], \tag{11.19}$$

$$F_{\eta'}^{LO} = \frac{1}{4\sqrt{3}\pi^2 f_\pi}\left[\sin(\theta^{[0]}) + 2\sqrt{2}\cos(\theta^{[0]})\right]. \tag{11.20}$$

In order to compare lattice results to the pseudoscalar meson exchange, we need to define a chiral trajectory from the $SU(3)$ symmetric point to the physical point in terms of the 9 parameters of the model. At the $SU(3)$ flavour symmetric point the mixing angle vanishes $\theta = 0$ and we have

$$F_\eta^{LO,SU(3)} = \frac{F_\pi^{LO,SU(3)}}{\sqrt{3}}, \qquad F_{\eta'}^{LO,SU(3)} = \frac{2\sqrt{2}F_\pi^{LO,SU(3)}}{\sqrt{3}}. \tag{11.21}$$

Table 11.2: The parameters, which define the chiral trajectory on the lattice ensembles from table 11.1 the pion mass is determined in Ref. [169], [141]. The masses for η and η' are obtained from Ref. [171]. The other parameters are calculated from the procedure described in section 11.3.2.

Id	H200/N202	N203	N451	C101/D450	E300	E250/physical
m_π [MeV]	423(5)/418(5)	349(4)	291(4)	222(3)/219(3)	177(2)	132(2)/134.9768(5)
$m_{V,\pi}$ [MeV]	952(15)	916(12)	869(15)	812(5)	785(4)	775.26(25)
F_π [1/GeV]	0.227(5)	0.238(5)	0.249(5)	0.264(4)	0.269(3)	0.272(3)
m_η [MeV]	423(5)/418(5)	487(6)	531(5)	523(9)	547.862(18)	547.862(18)
$m_{V,\eta}$ [MeV]	952(15)	894(15)	852(18)	807(24)	784(28)	774(29)
F_η [1/GeV]	0.131(2)	0.178(4)	0.212(4)	0.248(5)	0.26(6)	0.275(5)
$m_{\eta'}$ [MeV]	1028(136)	876(159)	941(113)	980(76)	957.78 (6)	957.78 (6)
$m_{V,\eta'}$ [MeV]	1036(28)	978(21)	936(20)	891(24)	869(27)	859(28)
$F_{\eta'}$ [1/GeV]	0.371(8)	0.362(6)	0.355(5)	0.348(5)	0.345(5)	0.343(5)

For η the relation holds also for NLO $F_\eta^{NLO,SU(3)} = \frac{F_\pi^{NLO,SU(3)}}{\sqrt{3}}$ [99]. At the physical point one can extract the normalization of the transition form factor using the decay with of the pseudoscalar meson into two photons

$$\Gamma(p \to \gamma\gamma) = \frac{\pi\alpha^2 m_p^3}{4}|F_p|^2 \tag{11.22}$$

where $p = \pi^0, \eta, \eta'$ and the value for $\Gamma(p \to \gamma\gamma)$ taken from the PDG [90] . The effective m_V mass for the η and η' mesons have determined at the physical point by using a fit to the CLEO data [172] giving

$$m_{V,\eta}^{phys} = 774 \pm 29 MeV, \qquad m_{V,\eta'}^{phys} = 859 \pm 28 MeV \tag{11.23}$$

We also know that the η meson and the π^0 are degenerate at the $SU(3)$ symmetric point, which means that also the VMD masses for both mesons will be the same $m_{V,\pi}^{SU(3)} = m_{V,\eta}^{SU(3)}$. For the ensembles that lie between the physical point and the $SU(3)$ symmetric point we interpolate the parameter F_η, $F_{\eta'}$ and $m_{V,\pi}$ between the physical and the $SU(3)$ symmetric point in the variable $\xi = m_K^2 - m_\pi^2$. For the VMD mass of the η' where we do not know the value at the $SU(3)$ symmetric point, we assume the same slope as for the $m_{V,\eta}$. For the mixing angle we apply two different methods:

1. We use Eq. 4.13 with the given meson masses on each ensemble.
2. We extrapolate $\sin(\theta^{[1]})$ between $\theta^{SU(3)} = 0°$ at the $SU(3)$ symmetric point and the NLO result for the mixing angle $\theta^{[1],phys} = -11.1(6)°$ [107].

The parameters for each ensemble are given in table 11.3. Due to the large uncertainty of the η' mass the mixing angles computed with method 1 show also large uncertainties. Additionally we see that the difference of the leading order computation with Eq. 4.13 and the NLO result from Ref. [107] is quite substantial.

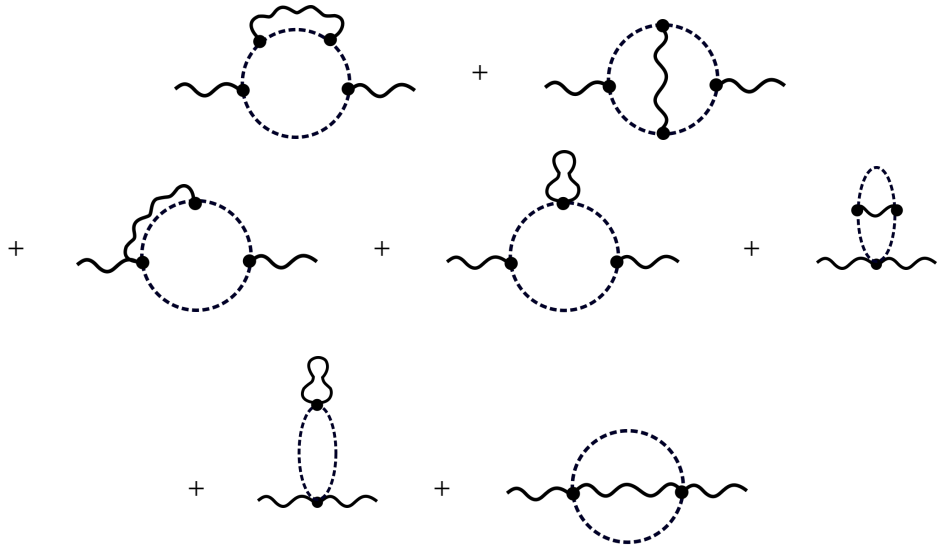

Figure 11.3: Diagrams for the charged pion loop contributing at $O(\alpha)$ with two remaining vertices in position space.

11.3.3 Charged pion loop

For the computation of the charged pion loop, we make use of Eq. 10.9 inserted into Eq. 6.6. The light-by-light scattering amplitude is calculated in scalar QED similar to section 3 of Ref. [165], where all diagrams of order α^2, including the tadpoles, are taken into account. For the $\pi\pi\gamma$ vertex a VMD form factor $F(Q^2) = \frac{m_V^2}{Q^2+m_V^2}$ is implemented such that the Lagrangian is gauge invariant. With the VMD form factor the result for $a_\mu^{NLO,\pi^+\pi^-}$ is UV-finite, without taking into account any counter terms. Without the VMD form factor the result in pure scalar QED is divergent. However, this can be regulararized by using a doubly-subtracted Pauli-Villars regularized photon propagator [165]

$$\frac{1}{k^2} - \frac{1}{1-\zeta}\left[\frac{1}{k^2+\zeta\Lambda^2} - \frac{\zeta}{k^2+\Lambda^2}\right] \tag{11.24}$$

with $\zeta \in (0,1)$. This results in the same asymptotic behaviour as with VMD form factors on each of the vertices that the photon propagator is attached to.

The only two parameters of the model for the charged pion loop are the pion mass m_π and the VMD mass m_V. We use the parameters for the neutral pion from table 11.2 and do not take into account effects from the pion mass splitting due to isospin breaking effects. Along the chiral trajectory in the range 120 MeV $< m_\pi <$ 450 MeV, the result for the charged pion loop contribution to the HVP at $O(\alpha^3)$ shows a very simple behaviour proportional to the pion mass, $a_\mu^{NLO,\pi^+\pi^-} \propto m_\pi^{-3}$, which is shown in Fig. 11.5. This means that starting from the $SU(3)$ flavour symmetric point and going down

to the physical point one sees a huge enhancement of the charged pion loop contribution compared to the pseudoscalar meson exchange contribution. This is quite different from what is observed in the HLbL contribution [168] for which the pseudoscalar exchange gives the dominant part and the charged pion loop is a rather small contribution.

11.3.4 Matching coefficients for the $(2+2)a$ topology

Eq. 11.8 for the pseudoscalar meson exchange gives the total contribution to the HVP at NLO 10.3. The contribution to the individual diagrams in Fig. 10.1 can be worked out by simply multiplying this contribution with an appropriate factor, which we will call *matching coefficient*. In this section, we want to work out the matching coefficients for the π^0, η and η' contribution as well as the charged pion loop, based on the derivation worked out in the appendix of Ref. [168], which relies on χPT 4.1.

The $(2+2)$ diagrams on the level of the four-point function matches the t-channel diagram for the pseudoscalar meson exchange, depicted in Fig.11.4. From this we see that the π^0 exchange does not contribute to the $(2+2)b$ diagram, because the self contracted photon loop results in a Kronecker delta multiplying the Wess-Zumino-Witten interaction term, which vanishes, because of the anti-symmetry of the term. The π^0 diagram that matches the $(2+2)a$ topology is precisely the one computed from the polarization tensor A.24 in appendix A.3. This diagram is also the only one contributing to the fully connected (4)-l contribution. In the case of $n_f = 2+1$ quark flavours, we have to distinguish between the light-light (ll), light-strange (ls) and strange-strange (ss) component of the $(2+2)a$ diagram. For the case of the π^0 only the ll receives a contribution. We can use the coefficients c_P in table X of Ref. [168] to compute the matching coefficients of the π^0 by multiplying with the corresponding quark charge factor and dividing by the normalization factor, where P stands for π^0, η or η'.

$$a_\mu^{(2+2)a-ll,\pi^0} = \left(2\frac{25}{81}c_\pi^{ll}\right)\left(2c_\pi^{ll}\frac{25}{81} + 2\frac{17}{81}(c_\pi^{(4)-l} + d_\pi^{(4)-l})\right)^{-1} a_\mu^{\pi^0} = -\frac{25}{9}a_\mu^{\pi^0} \tag{11.25}$$

where the factor 2 arises from the fact that there are 2 possible contractions of the photon propagator which give the same topology.

The case of the η and η' is more complicated. Neither of them contribute to the (4l) diagram. They instead split among the (ll), (ls),(sl) and (ss) component of the $(2+2)a$ diagram

$$a_\mu^{(2+2)a-ll,(\eta,\eta')} = \left(2\frac{25}{81}c_{(\eta,\eta')}^{ll}\right)\left(2c_{(\eta,\eta')}^{ll}\frac{25}{81} + 2\frac{5}{81}c_{(\eta,\eta')}^{ls} + 2\frac{1}{81}c_{(\eta,\eta')}^{ss}\right)^{-1} a_\mu^{(\eta,\eta')}, \tag{11.26}$$

$$\begin{aligned} a_\mu^{(2+2)a-ls,(\eta,\eta')} &= \left(2\frac{5}{81}\frac{c_{(\eta,\eta')}^{ls}}{2}\right)\left(2c_{(\eta,\eta')}^{ll}\frac{25}{81} + 2\frac{5}{81}c_{(\eta,\eta')}^{ls} + 2\frac{1}{81}c_{(\eta,\eta')}^{ss}\right)^{-1} a_\mu^{(\eta,\eta')} && (11.27)\\ &= a_\mu^{(2+2)a-sl,(\eta,\eta')}, && (11.28)\end{aligned}$$

$$a_\mu^{(2+2)a-ss,(\eta,\eta')} = \left(2\frac{1}{81}c_{(\eta,\eta')}^{ss}\right)\left(2c_{(\eta,\eta')}^{ll}\frac{25}{81} + 2\frac{5}{81}c_{(\eta,\eta')}^{ls} + 2\frac{1}{81}c_{(\eta,\eta')}^{ss}\right)^{-1} a_\mu^{(\eta,\eta')}, \tag{11.29}$$

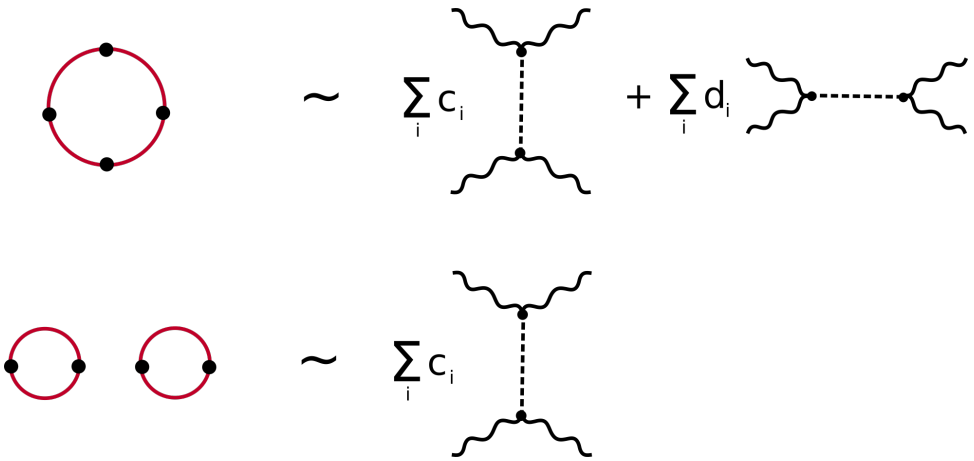

Figure 11.4: Diagram matching between the QCD valence quark connected Wick contracted on the left and the pseudoscalar meson exchange on the right

where coefficients for the (ls) and the (sl) are identical. In the normalization they are already symmetrized. Since η and η' receive contributions from the octet state as well as the singlet state depending on the mixing angle θ, see section 4.1.3, the matching coefficients are also dependent on the mixing angle. We will focus on the $SU(3)$ flavour symetric point at first, where the η is a true octet state and degenerate with the π^0 and the kaon, and the η' is a true singlet state. For this case we can obtain the coefficients for η from table X of Ref. [168]. We have $c_\eta^{ll} = \frac{1}{3}$, $c_\eta^{ls} = -\frac{4}{3}$ and $c_\eta^{ss} = \frac{4}{3}$ and thus the matching coefficients are

$$a_\mu^{(2+2)a-ll,\eta} = \frac{25}{9} a_\mu^\eta, \quad a_\mu^{(2+2)a-ls,\eta} = -\frac{1}{2}\frac{20}{9} a_\mu^\eta, \quad a_\mu^{(2+2)a-ss,\eta} = \frac{4}{9} a_\mu^\eta. \qquad (SU(3) \text{ sym. point}) \quad (11.30)$$

The singlet state splits equally among the three components proportional to charge factor, thus we have

$$a_\mu^{(2+2)a-ll,\eta'} = \frac{25}{36} a_\mu^{\eta'}, \quad a_\mu^{(2+2)a-ls,\eta'} = \frac{1}{2}\frac{10}{36} a_\mu^{\eta'}, \quad a_\mu^{(2+2)a-ss,\eta'} = \frac{1}{36} a_\mu^{\eta'}. \quad (SU(3) \text{ sym. point}) \quad (11.31)$$

The (ll) and (ls) components of the $(2+2)a$ contribution at the $SU(3)$ symmetric point in terms of the pseudoscalar meson exchange are given by

$$a_\mu^{(2+2)a-ll,PME} = -\frac{25}{9} a_\mu^{\pi^0} + \frac{25}{9} a_\mu^\eta + \frac{25}{36} a_\mu^{\eta'}, \qquad (SU(3) \text{ sym. point}) \qquad (11.32)$$

$$a_\mu^{(2+2)a-ls,PME} = \frac{1}{2}\Big(-\frac{20}{9} a_\mu^\eta + \frac{5}{18} a_\mu^{\eta'} \Big), \qquad (SU(3) \text{ sym. point}) \qquad (11.33)$$

In the (ss) channel an additional $s\bar{s}$ meson appears in the derivation in Ref. [168]. We can not map this to a physical state. We will therefore only focus on the (ll) and (ls) components. For all other points on the chiral trajectory we use the coefficients in the appendix 3b from Ref. [168] where the

Table 11.3: The mixing angles and matching coefficients for the η and η' meson in Eq. 11.35 along the chiral trajectory. The superscript $^{[0]}$ denotes leading order in χPT and indicates that the angle is evaluated with Eq. 4.13, while $^{[1]}$ denotes next-to-leading order and is interpolated between the SU(3) flavour symmetric point and the physical result from Ref. [107]. The coefficients $\hat{c}$ are computed using the procedure described in section 11.3.4.

Id	H200/N202	N203	N451	C101/D450	E300	E250/physical
m_π [MeV]	423(5)/418(5)	349(4)	291(4)	222(3)/219(3)	177(2)	132(2)/134.9768(5)
$\theta^{[0]}$ [°]	0	-7.2(3.7)	-10.8(3.6)	-14.7(3.2)	-18.5(6)	-19.7
$\theta^{[1]}$ [°]	0	-3.6(3)	-6.3(4)	-9.1(5)	-10.4(6)	-11.1(6)
$\hat{c}_\eta^{(ll)}$	25/9	2.27(1.49)	2.43(69)	2.14(12)	2.24(6)	2.19(3)
$\hat{c}_{\eta'}^{(ll)}$	25/36	0.51(20)	0.47(14)	0.42(11)	0.30(4)	0.28(3)
$\hat{c}_\eta^{(ls)}$	-20/9	-1.15(58)	-1.21(21)	-0.67(9)	-0.75(5)	-0.71(2)
$\hat{c}_{\eta'}^{(ls)}$	10/36	0.22(9)	-0.67(9)	0.25(4)	0.29(1)	0.30(1)

parameters ΔM^2, $\Delta \mathring{M}^2_{\eta'}$, $\delta \bar{m}^2$ and Λ are determined by the four meson masses m_π, m_K, m_η, $m_{\eta'}$ and the mixing angle θ. The calculated matching coefficients for both strategies for the mixing angle, which we propose in section 11.3.2 are given in table 11.3.

For the matching coefficient for the charged pion loop, we make use of the derivation in the appendix of Ref. [168]. All different Wick contractions one needs to calculate for the charged pion loop contribute equally to the $(2+2)$ diagrams with coefficient 1. Multiplying this with the quark charge factor in QCD 25/81 and 2 for the two possible contractions with the photon propagator for the $(2+2)a$ contribution we obtain the matching coefficient for the charged pion loop

$$a_\mu^{(2+2)a-ll,\pi^+\pi^-} = \frac{50}{81} a_\mu^{\pi^+\pi^-}. \tag{11.34}$$

Our full model prediction for the $(2+2)a-ll$ contribution is obtained by

$$\begin{aligned} a_\mu^{(2+2)a-ll,\text{model}} &= -\frac{25}{9} a_\mu^{\pi^0}(m_\pi, m_{V,\pi}, F_\pi) + \hat{c}_\eta^{(ll)}((m_\pi, m_K, m_\eta, m_{\eta'}, \theta)) a_\mu^{\eta}(m_\eta, m_{V,\eta}, F_\eta) \\ &\quad + \hat{c}_{\eta'}^{(ll)}((m_\pi, m_K, m_\eta, m_{\eta'}, \theta)) a_\mu^{\eta'}(m_{\eta'}, m_{V,\eta'}, F_{\eta'}) + \frac{50}{81} a_\mu^{\pi^+\pi^-}(m_\pi, m_{V,\pi}), \end{aligned} \tag{11.35}$$

where the parameters for the model are given in table 11.2 and the matching coefficients for the η and η' are given in table 11.3. We plot the dependence of Eq. 11.35 on m_π along our chiral trajectory in Fig. 11.5.

We see that the combined result for the pseudoscalar meson exchange is almost flat along the chiral trajectory. However, the charged pion-loop increases with $\propto m_\pi^{-3}$ when approaching the physical point. We expect this behaviour to show up in the results computed in lattice QCD. So, for a determination of $a_\mu^{(2+2)a-ll}$ at the physical point it is essential to include ensembles close to the physical point in order to control the chiral extrapolation. An important point we want to stress here is

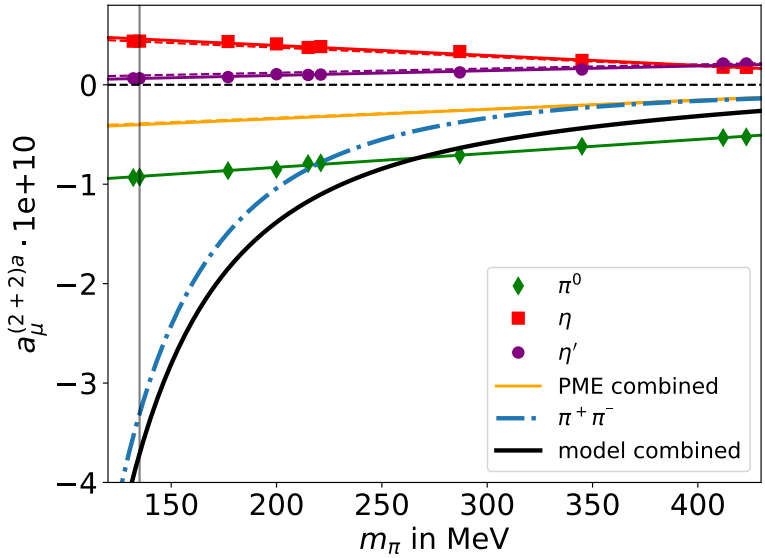

Figure 11.5: Plot of the chiral dependance of the the different contributions of the model from Eq. 11.35 $a_\mu^{(2+2)a-ll}$ including the matching coefficients for the individual contributions. The combination of π^0,η and η' is depicted in yellow as 'PME combined'. For the η and η' we display the result computed with the mixing angle for the two strategies described in section 11.3.2. The result with the mixing angle computed with strategy 1 is depicted with a dashed line, which is barely visible behind the solid line for the result computed with strategy 2. The black line gives the combined result for all contributions 11.35. The grey vertical line lies at the physical mass of the neutral pion $m_{\pi^0} = 134.9768(5)$.

that the physical point for the charged pion-loop and the pseudoscalar meson exchange do not lie on the same point on the x axis, since the mass of the charged pion is higher that the mass of the neutral pion $m_\pi^\pm = 139.57018(35)$ [109]. But, since we are only interested in the asymptotic behaviour when approaching the physical point, this is not a problem for our analysis. We also want to stress the fact that the the contribution from the pion is not expected to predict the full result for the light-connected contribution from QCD. It is only expected to account for a large part of the result as in the case of the leading order HVP contribution, where the result from the Sakurai QFT gives approximately 5/6 of the total light-connected result 7.2.2.

11.4 Light-strange and strange-strange component

Here, we want to look at the light-strange (ls), strange-light (sl) and strange-strange (ss) component of the $(2+2)a$ contribution 10.22. We have computed these on one the ensemble N451, on which the pion mass and kaon masses are $m_\pi = 291(4)$ MeV and $m_K = 468(5)$, see Fig. 11.6a. At the $SU(3)$ flavour symmetric point the only difference between the (ll), (ls), (sl) and (ss) component is that they contribute with a different charge factor $C^{(ls)} = C^{(sl)} = \frac{5}{81}$ and $C^{(ss)} = \frac{1}{81}$. But, following the chiral trajectory to the physical point the contribution with a strange valence quark loop without charge

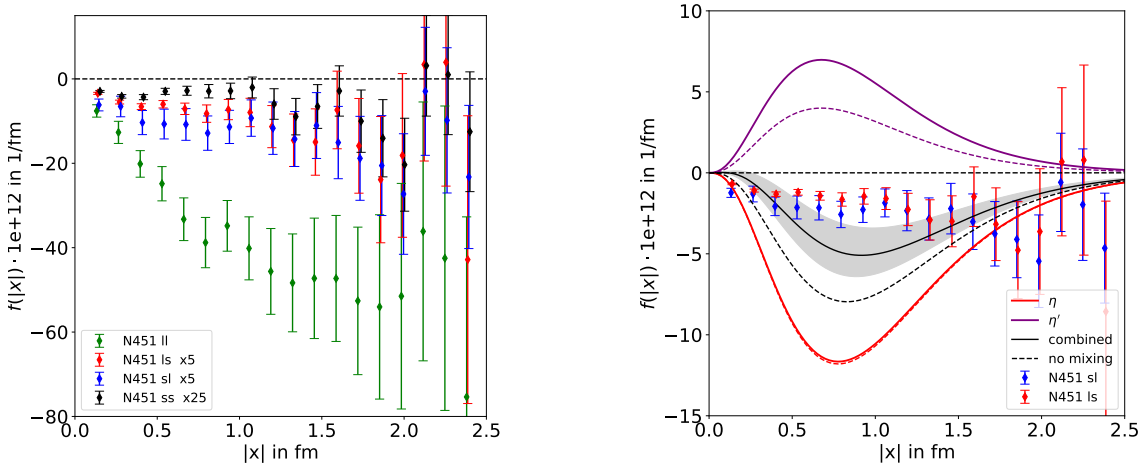

(a) **(b)**

Figure 11.6: (a) Comparison of the integrand of Eq. 10.22, including all prefactors, for the (ll), (ls), (sl) and (ss) component on the ensemble N451. (b) Model prediction for the (ls) and (sl) contribution, where the mixing angle $\theta = 6.47°$. The integrand for the η and η' contribution is obtained from Eq. A.37. The uncertainty of the model is dominated by the error of the charge factors 11.27 due to uncertainties of the meson masses.

factor gets smaller relative to the (ll) contribution as the difference $m_K^2 - m_\pi^2$ increases. In Fig. 11.6a we see that, if one scales al the component to have the same charge factor as the (ll) component, the latter is significantly larger on the ensemble N451 with a pion mass of $m_\pi = 291(5)$ MeV. We can also confirm that the (ls) and (sl) component agree within error. However, the (ls) component, where the integral $I^{(2)}$ 10.25 is calculated with the light-quark two-point function and the integral $I^{(3)}$ 10.26 is calculated with the strange-quark two-point function, has smaller statistical uncertainties in the small $|x|$ regime. We also examine the prediction of the pseudoscalar meson exchange for the (ls) and (sl) component. These components receive only contributions from the η, η' and the charged kaon loop. We neglect the effect of the charged kaon loop in the following.

In Fig. 11.6b we display the integrand of the prediction for the η and η' contribution calculated with Eq. A.37 and matching coefficients 11.27 calculated with a mixing angle $\theta = -6.37°$. We see a strong cancellation between both contributions. This cancellation and the fact that the matching coefficients for the (ls) and (sl) component are sensitive to the uncertainties of m_η and m_K, we see a relatively large uncertainty of the model prediction. Within this error-band the model prediction agrees with the lattice data. For the (ll) component the uncertainty of the model prediction is much smaller due to the fact that the π^0 is the dominant contribution. We also observe that if one assumes the matching coefficients to be the same as on the $SU(3)$ symmetric point 11.33 the agreement between the model

Table 11.4: Results on the ensemble N451 for contribution to $a_\mu^{(2+2)a}$ 10.22, where the lattice results are integrated up to $|x| = 2.5$ fm and prediction of the $\eta+\eta'$ contribution. The results for all components are multiplied with the corresponding charge factors and given in units of 10^{-10}.

	(ll)	(ls)	(sl)	(ss)	$\eta+\eta'$ (ls)
$a_\mu^{(2+2)a}$	-0.891(154)	-0.045(21)	-0.060(15)	-0.005(2)	-0.064(21)

and the lattice data is worse.

11.5 Approximation of the tail

Looking at the result for the integrand 10.22 computed on the lattice, we see that the tail is strongly affected by noise. In order to reduce the uncertainty coming from the long-distance behaviour of the integrand, we suggest the following strategy: We compute the integral in Eq. 10.22 with the lattice data on each ensemble up to a value of $|x| = |x|_{\text{cut}}$, where the uncertainty is calculated with the Jackknife procedure 5.6.1. For $|x| > |x|_{\text{cut}}$, we estimate the tail of the integrand using an ansatz motivated by phenomenology. This ansatz takes into account the π^0, η and η' contribution and the charged pion loop at $O(\alpha^2)$, described in section 11.3. For the pseudoscalar meson exchange, we know the form of the integrand with respect to the x vertex exactly, see Eq. A.37. Analogous to Eq. 11.35, we obtain for the integrand

$$\begin{aligned} f^{PME}(|x|) &= -\frac{25}{9} f^{\pi^0}(|x|)(m_\pi, m_{V,\pi}, F_\pi) + \hat{c}_\eta^{(ll)}(m_\pi, m_K, m_\eta, m_{\eta'}, \theta) f^{\eta}(|x|)(m_\eta, m_{V,\eta}, F_\eta) \\ &\quad + \hat{c}_{\eta'}^{(ll)}(m_\pi, m_K, m_\eta, m_{\eta'}, \theta) f^{\eta'}(|x|)(m_{\eta'}, m_{V,\eta'}, F_{\eta'}). \end{aligned} \tag{11.36}$$

For the charged pion loop, we use the following ansatz

$$f^{\pi^+\pi^-}(|x|) = A|x|^n e^{-2m_\pi|x|}. \tag{11.37}$$

This is motivated by the asymptotic behaviour of the pion propagator

$$G_{m_\pi}(x) \sim \frac{m_\pi}{4\pi^2} \frac{\exp(-m_\pi x)}{x^{\frac{3}{2}}}, \qquad \text{for} \quad x \to \infty, \tag{11.38}$$

which follows directly from Eq. 2.33. In the calculation of the large $|x|$ regime of the integrand for the charged pion loop, there are two propagators for which the argument gets large. With this argument, the exponential function in Eq. 11.37 is needed to obtain the right asymptotics. The integrand calculated in the model is then given by

$$f^{\text{model}}(|x|) = f^{PME}(|x|) + f^{\pi^+\pi^-}(|x|). \tag{11.39}$$

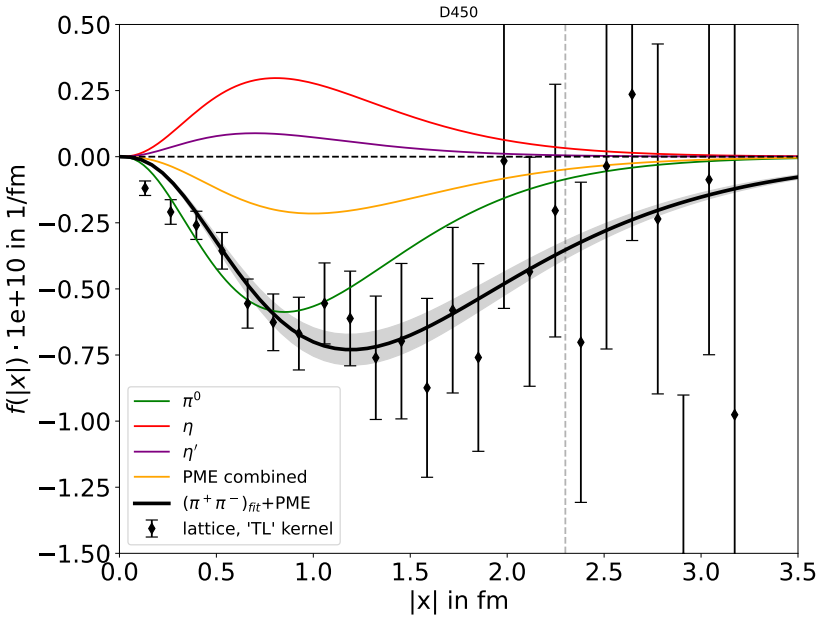

Figure 11.7: Plot of the integrand of Eq.10.22, including all prefactors, calculated on the ensemble D450 11.1 (black data points). We also show the prediction for the integrand from the pseudoscalar meson exchange described in section 11.3.1 with the correct matching factors calculated with the method described in section 11.3.4. The combined result from π^0, η and η' is shown in yellow. The black solid line corresponds to the fit that is used for approximating the tail described in section 11.5. The vertical dashed line gives the value of $|x|$ from which we use the fit to obtain the contribution from the tail.

On each individual ensemble we take the model parameters for the PME from table 11.2 and the matching coefficient $-25/9$ for the π^0 and the coefficients from table 11.3 for the η and η' meson. To determine the prefactor A and the exponent n for the charged pion loop 11.37, we perform a fit of the total model prediction Eq. 11.39 to the lattice data. The prefactor A is fitted on each ensemble individually and the exponent n in Eq. 11.37 is fitted globally, constraining it to be the same on all ensembles. In this method we obtain $n = 2.60(10)$. The lattice data on D450 as well as the model prediction is depicted in Fig. 11.7. The contribution to the integral Eq. 10.22 for $|x| > |x|_{\text{cut}}$ is now calculated with the model 11.39. The uncertainty of the tail contribution is taken conservatively to be 100% of the integral value of the tail. The cut is perfomed at $|x|_{\text{cut}} = L/2$ motivated from the fact that up to this point we do not see any finite-size effects for the traceless kernel, see Fig. 11.2.

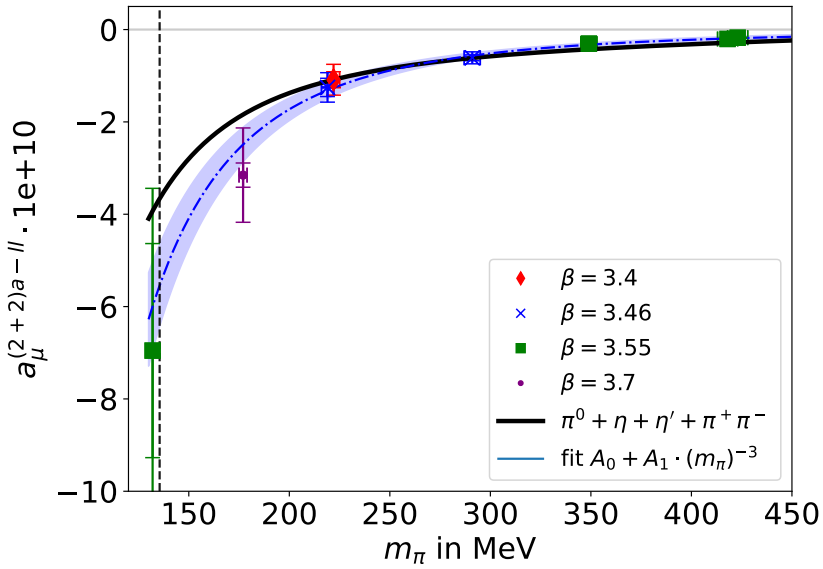

Figure 11.8: Plot of the results computed on the different lattice ensembles and a fit (blue line) of the chiral dependance 11.40 for $g(m_\pi) = 0$. The shown fit is associated with the highest AIC weight. We also plot the prediction from the model 11.35 (black solid line). The inner errorbar of the lattice data points gives only the statistical uncertainty, the outer errorbar includes the uncertainty from approximating the tail of the integrand.

11.6 Extrapolation to the physical point

For the extrapolation to the physical point on the chiral trajectory, we perform a fit of the individual results computed on each ensemble. For the fit, we choose the following ansatz

$$a_\mu^{(2+2)a-ll}(m_\pi) = A_0 + A_1 m_\pi^{-3} + A_2 g(m_\pi). \tag{11.40}$$

This anatz is again inspired by the phenomenological model of the $(2+2)a$ contribution in therms of the pseudoscalar mesons π^0, η, η' and the charged pion loop $\pi^+\pi^-$, given in Eq. 11.35. From this, we know that the dominant behaviour when approaching the physical point is given by the $\pi^+\pi^-$ contribution, which is proportional to $a_\mu^{(2+2)a,\pi^+\pi^-} \propto m_\pi^{-3}$ in the region $m_\pi^{\text{phys}} \leq m_\pi \leq m_\pi^{SU(3)}$. We perform fits of the coefficients A_0, A_1, A_2 for several functions $g(m_\pi)$, including different combinations of polynomials and logarithmic terms in m_π that are subdominant compared m_π^{-3} when aproaching the physical point. We also take into account different subsets of ensembles for several cuts in the pion mass m_{cut}. We use the Akaike Information criterion (AIC) to compute weights for each fit 5.6.3

$$w_i = \frac{1}{N}\exp\Big[-\frac{1}{2}(\chi^2 + 2k - 2n)\Big] \tag{11.41}$$

where k is the number of fit parameters and n is the number of data points that are included. N is chosen, such that the sum of all weights adds up to one. In all fits that we perform, we see a tendency

Table 11.5: Results for each ensembles with the method to approximate the tail discussed in section 11.5, for only the lattice data integrated up to $|x| = L$ and the results from the model. We only give the central value of the result from the model, since the model is only seen as a guideline and the results given in the third row do not enter in the final estimate for $a_\mu^{(2+2)a-ll)}$

Id	$a_\mu^{(2+2)a-ll}$ [model tail]	$a_\mu^{(2+2)a-ll}$ [only lattice]	$a_\mu^{(2+2)a-ll,\text{model}}$
H200	$-0.16(0.04)_{\text{stat}}(0.12)_{\text{tail}}$	$-0.24(0.1)_{\text{stat}}$	-0.28
N202	$-0.21(0.02)_{\text{stat}}(0.04)_{\text{tail}}$	$-0.26(0.03)_{\text{stat}}$	-0.29
N203	$-0.32(0.03)_{\text{stat}}(0.06)_{\text{tail}}$	$-0.35(0.06)_{\text{stat}}$	-0.43
N451	$-0.59(0.05)_{\text{stat}}(0.15)_{\text{tail}}$	$-0.85(0.13)_{\text{stat}}$	-0.62
C101	$-1.06(0.17)_{\text{stat}}(0.26)_{\text{tail}}$	$-1.2(0.36)_{\text{stat}}$	-1.09
D450	$-1.28(0.20)_{\text{stat}}(0.27)_{\text{tail}}$	$-1.49(0.41)_{\text{stat}}$	-1.12
E300	$-3.1(0.29)_{\text{stat}}(0.79)_{\text{tail}}$	$-3.78(0.56)_{\text{stat}}$	-1.84
E250	$-6.69(2.32)_{\text{stat}}(2.38)_{\text{tail}}$	$-9.5(4.9)_{\text{stat}}$	-3.93

of overfitting, since the $\frac{\chi^2}{k}$ is often significantly smaller than one for the fits with three fit parameters. The AIC assigns a relatively small weight to the fits that tend to overfit, so we expect it to be a good criterion in our case. We display the best fit, which only has two parameters, in Fig. 11.8.

The result for the model average is obtained by averaging the results for each fit multiplied with the assigned AIC weight

$$\overline{O} = \sum_i w_i O_i. \tag{11.42}$$

The uncertainty associated with the chiral extrapolation is calculated by the variance of the weighted fit results

$$(\sigma^2)_{\text{extr}} = \sum_i w_i (O_i - \overline{O})^2. \tag{11.43}$$

The uncertainty that is obtained from the fit is composed of the uncertainty associated with the tail approximation and the statistical uncertainty. In order to obtain each uncertainty individually, we perform another chiral fit, where we set the statistical uncertainty to zero and assume the relation for the results computed on each ensemble

$$(\sigma^2) = (\sigma^2)_{\text{stat}} + (\sigma^2)_{\text{tail}}. \tag{11.44}$$

We do not observe a lattice spacing dependence in the computed results within the given uncertainties. So, we can not perform an extrapolation to the continuum at this point. It is expected that the uncertainty associated with the continuum extrapolation is small compared to the other uncertainties. At this point, we do not correct for finite-size effects. The comparison between H200 and N202 in section 11.2, shows no significant finite-size effects for these ensembles, when one chooses the 'TL' kernel, so we also expect the uncertainty associated with the finite lattice size to be subdominant.

11.7 Discussion of the results

From the model average 11.42 for the light-light component of the $(2+2)a$ contribution, defined in Eq. 10.22 we obtain the result

$$a_\mu^{(2+2)a-ll} = \Big(-5.68 \pm (0.72)_{\text{stat}} \pm (0.12)_{\text{extr}} \pm (1.16)_{\text{tail}} \Big) 10^{-10}, \tag{11.45}$$

which is in agreement with the result computed by the RBC collaboration for this individual diagram on one lattice ensemble $a_\mu^{(2+2)a-ll} = -6.9(2.9)$ [148]. The relatively large size of this QED correction, being about 1% of the leading order HVP, can be explained by the very large contribution of the charged-pion loop and the fact that the insertion of the photon propagator lifts the $SU(3)$ flavour suppression. This fosters the statement that for a sub-percent determination of the HVP contribution from lattice QCD, having good control over the isospin breaking corrections is important. Because of the very steep increase of the charged-pion loop contribution when approaching the physical point, it is essential to perform the lattice calculation of the QED corrections at pion masses close to the physical point. A result from the BMW collaboration [21, 22] gives a value for the QED corrections to the disconnected contribution, see Fig. 10.3b, which is significantly smaller. One can not directly compare this number to 11.45, but one can expect that there is a large cancellation between the two contributing diagrams.

It is now desirable to compute also the other QED corrections from Fig. 10.1, starting with the fully-connected and the $(2+2)b$ contribution. For the latter, we already defined the master integral 10.23 from which one can obtain the result using the same technique as discussed in section 11.1. But, here one also needs to renormalize the divergence by imposing a renormalization scheme. Eventually one wants to match the lattice calculation to the 'real' world by including QED effects in the scale setting.

12 Conclusion

In this thesis, we have presented several calculations in the context of the anomalous magnetic moment of the muon that utilize coordinate-space methods. We have shown that the covariant coordinate-space (CCS) representation of the hadronic vacuum polarization (HVP) contribution to $(g-2)_\mu$ gives compatible results to the traditionally used time-momentum representation, see chapter 9, while the CCS representation offers additional flexibility in tuning the kernel function and the domain of integration. As the derivation for the CCS representation can be achieved for arbitrary observable 7 that can be derived from the vacuum polarization, we expect other precision calculations to benefit from the CCS representation as well. Some examples are the short-distance or long-distance $(g-2)_\mu$ window quantity, the hadronic contribution to the running of the electromagnetic coupling or the weak mixing angle. Here, one has to point out that the CCS method might have very different cut-off effects from traditional methods, as we have seen in this work for the intermediate distance window 9. These could potentially be varied by tuning the CCS kernel function in order to get even better control over lattice artifacts.

We have furthermore derived a new method for calculating finite-size corrections in the CCS representation 8, by utilizing the Sakurai QFT as a phenomenological model for the pion-photon interaction, which incorporates the ρ resonance. As this model predicts the two-pion channel with surprising accuracy, one can think of further applications of this model in the context of hadronic contributions to the vacuum polarization. It is also straightforward, to make use of this model for estimating finite-size effects in the TMR method.

Additionally, we have performed a calculation of a UV-finite QED correction to the HVP contribution at the physical point 11. These corrections are typically very costly to compute, but necessary in order to achieve sub-percent precision for a result for a_μ^{hvp} from lattice QCD.

In these calculations it is not possible to compare results for individual diagrams between different collaborations. However, the $(2+2)a$ diagram is an exception, since it is UV-finite even in isospin symmetric QCD. It can therefore serve as benchmark quantity, like the intermediate window quantity. A concensus on the result for this partial contribution would be a valuable crosscheck of different lattice calculations.

By comparing this diagram to the phenomenological model including the π^0, η η' exchange and $\pi^+\pi^-$ loop, one can learn important aspects of the underlying physics that can also be used in order

to understand the other diagrams, from Fig. 10.1.

From a more general viewpoint, we have utilized many techniques that rely on the coordinate-space representation, such as the Gegenbauer polynomial method. We have demonstrated that these methods are crucial in supporting lattice calculations by making use of effective theories.

We believe that there are many more applications of the methods used in this thesis. In the spirit of Feynmans quote from the very beginning of this thesis, it can be very beneficial to search for alternative formulations in order to simplify a given physics problem. Especially in the realm of lattice QCD, where enormous computational ressources are utilized in order to simulate the strong interaction, a more elegant formulation of amaster integral for the computation of a physical observable can often save a large amount of computing power and time. As field operators on the lattice are defined in coordinate-space, the CCS representation gives a more natural approach on defining these observables, as we have shown for the case of the muon $(g-2)$.

A Appendix

A.1 Acknowledgements

I want to thank my supervisor for sharing his knowledge and insight with me throughout the studies for my PhD. I furthermore want to thank my colleagues in Mainz for all helpful discussions along the way. Calculations for this project were partly performed on the HPC clusters “Mogon II” and ”Mogon NHR” at JGU Mainz. I am grateful to my colleagues in the CLS initiative for sharing ensembles. Our programs use the deflated SAP+GCR solver from the openQCD package [173], as well as the QDP++ library [174]. The measurement codes were developed based on the C++ library `wit`.

A.2 Calculation of the finite size effects for the Sakurai theory

Here, we want to work out the calculation of the integrals in Eq. 8.23 given by

$$\begin{aligned} J^{(4)}_{\mu\nu}(w,y) &= \{-(k+2q)_\mu(k+2q)_\nu + 2\delta_{\mu\nu}((k+q)^2+m_\pi^2)\}\Big|_{q=-i\nabla_y,k=-i\nabla_w} \\ &\int \frac{d^4k}{(2\pi)^4} e^{ikw} \frac{m_\rho^4}{(k^2+m_\rho^2)^2} \cdot \frac{1}{8\pi^2} \int_0^1 d\alpha\, e^{-i\alpha k\cdot y} K_0(\sqrt{\alpha(1-\alpha)k^2+m_\pi^2}|y|) \end{aligned} \tag{A.1}$$

The d^4k integral can be reduced to a one-dimensional integral by making use of the Gegenbauer polynomial expansion 2.4 of the exponential function [68]

$$\exp(ix\cdot p) = \sum_{k=0}^{\infty} \Gamma(\lambda) i^k (k+\lambda) J_{\lambda+k}(|x||p|)| \left(\frac{2}{|x||p|}\right)^\lambda C_k^\lambda(\hat{x}\cdot\hat{p}) \tag{A.2}$$

where $\hat{x} = \frac{x}{|x|}$, and $C_k^\lambda(\hat{x}\cdot\hat{p})$ is the k Gegenbauer polynomial 2.4 and $J_n(x)$ is the Bessel function of the first kind of order n. With this, we obtain

$$\begin{aligned} J^{(4)}_{\mu\nu}(w,y) &= \frac{m_\rho^4}{32\pi^4} \cdot \{-(k+2q)_\mu(k+2q)_\nu + 2\delta_{\mu\nu}((k+q)^2+m_\pi^2)\}\Big|_{q=-i\nabla_y,k=-i\nabla_w} \\ &\int_0^1 \frac{d\alpha}{|w-\alpha y|} \int_0^\infty dk\, \frac{k^2}{(k^2+m_\rho^2)^2} J_1(k|w-\alpha y|)\, K_0(\sqrt{\alpha(1-\alpha)k^2+m_\pi^2}|y|). \end{aligned} \tag{A.3}$$

Without the $(k^2+m_\rho^2)^{-2}$ factor, the k integral could be performed,

$$\begin{aligned}&\frac{1}{|x-\alpha y|}\int_0^\infty dk\, k^2\, J_1(k|w-\alpha y|)\, K_0(\sqrt{\alpha(1-\alpha)k^2+m_\pi^2}|y|) \\ &= \frac{m_\pi^2}{\alpha(1-\alpha)}\,\frac{K_2(\frac{m_\pi}{\sqrt{\alpha(1-\alpha)}}\sqrt{\alpha(y^2-2w\cdot y)+w^2})}{\alpha(y^2-2w\cdot y)+w^2}.\end{aligned} \tag{A.4}$$

Using this result, the integral that is actually required, which we denote by $\mathscr{G}_1(\alpha,w,y)$ can be brought into the following, non-oscillatory form,

$$\begin{aligned}\mathscr{G}_1(\alpha,w,y) &= \frac{1}{|w-\alpha y|}\int_0^\infty dk\,\frac{k^2}{(k^2+m_\rho^2)^2}\, J_1(k|w-\alpha y|)\, K_0(\sqrt{\alpha(1-\alpha)k^2+m_\pi^2}|y|) \\ &= -\frac{\partial}{\partial m_\rho^2}2\pi^2\frac{m_\pi^2}{\alpha(1-\alpha)}\int_0^\infty dz\, z^3\gamma_0^{(m_\rho)}(|w-\alpha y|,z)\frac{K_2(\frac{m_\pi}{\sqrt{\alpha(1-\alpha)}}\sqrt{z^2+\alpha(1-\alpha)y^2})}{z^2+\alpha(1-\alpha)y^2},\end{aligned} \tag{A.5}$$

where $\gamma_n^{(m)}(|x|,|u|)$ is defined in Eq. 2.67. It is possible to simplify Eq. A.5 even further by reinterpreting it as a convolution of two scalar propagators

$$\mathscr{G}_1(\alpha,w,y) = \frac{\partial}{\partial m_\rho^2}\frac{2\pi^2}{m_\alpha^2\alpha(1-\alpha)}\frac{1}{|\tilde{y}|}\frac{d}{d|\tilde{y}|}\Big|_{\tilde{y}=y}\int d^4z G_{m_\rho}\Big(z-(w-\alpha y)\Big)G_{m_\alpha}\Big(\sqrt{z^2+\alpha(1-\alpha)\tilde{y}^2}\Big) \tag{A.6}$$

where $m_\alpha = \frac{m_\pi}{\sqrt{\alpha(1-\alpha)}}$. Using Eq. A.23, we can then write

$$\begin{aligned}\mathscr{G}_1(\alpha,w,y) &= \frac{1}{2^3\pi^2}\frac{\partial}{\partial m_\rho^2}\frac{2\pi^2}{m_\alpha^2\alpha(1-\alpha)}\frac{1}{|\tilde{y}|}\frac{d}{d|\tilde{y}|}\Big|_{\tilde{y}=y} \\ &\quad \int_0^1 d\beta K_0\Big(\sqrt{\Big(m_\rho^2\beta+(1-\beta)m_\alpha^2\Big)\Big((w-\alpha y)^2+\frac{\alpha(1-\alpha)\tilde{y}^2}{1-\beta}\Big)}\Big)\end{aligned} \tag{A.7}$$

which is now an just an integral of over one Bessel function. The final result for $J_{\mu\nu}^{(4)}(w,y)$ is then given by two one dimensional integrals over two Feynman parameters α,β with derivatives acting on a single Bessel function

$$\begin{aligned}J_{\mu\nu}^{(4)}(w,y) &= \frac{m_\rho^4}{32\pi^4}\cdot\{-(k+2q)_\mu(k+2q)_\nu+2\delta_{\mu\nu}((k+q)^2+m_\pi^2)\}\Big|_{q=-i\nabla_y,k=-i\nabla_w} \\ &\quad \frac{1}{4}\frac{\partial}{\partial m_\rho^2}\frac{1}{|\tilde{y}|}\frac{d}{d|\tilde{y}|}\Big|_{\tilde{y}=y}\int_0^1 d\alpha\frac{1}{m_\alpha^2\alpha(1-\alpha)} \\ &\quad \int_0^1 d\beta K_0\Big(\sqrt{\Big(m_\rho^2\beta+(1-\beta)m_\alpha^2\Big)\Big((w-\alpha y)^2+\frac{\alpha(1-\alpha)\tilde{y}^2}{1-\beta}\Big)}\Big)\end{aligned} \tag{A.8}$$

A.2.1 Projection onto higher dimensional scalar propagators

In this section we want to evaluate the integral

$$\int d^4 z G^1_{m_1}(z-x) G^1_{m_2}(\sqrt{z^2+v^2}) \tag{A.9}$$

We define the D dimensional vector $\overset{\text{D}}{x} = (x_1, x_2, \ldots, x_D)^T$. We further drop the index above the variable for $D = 4$, i.e. $\overset{4}{x} = x$. Let us first recall the definition of the scalar propagator in euclidean coordinate space in $D = 2\lambda + 2$ spacetime dimension 2.32

$$G^\lambda_m(\overset{\text{D}}{x}) = \int \frac{d^D p}{(2\pi)^D} \frac{e^{-i\overset{\text{D}}{p}\cdot\overset{\text{D}}{x}}}{(\overset{\text{D}}{p})^2 + m^2} = \frac{m^\lambda}{(2\pi)^{\lambda+1}} \frac{K_\lambda(m|\overset{\text{D}}{x}|)}{|\overset{\text{D}}{x}|^\lambda} \tag{A.10}$$

where for the massless case, we have

$$G^\lambda_m(\overset{\text{D}}{x}) = \frac{\Gamma(\lambda)}{4\pi^{\lambda+1}|\overset{\text{D}}{x}|^{2\lambda}} \tag{A.11}$$

If we write down the equation for the $\lambda' = \lambda + \frac{1}{2}$ with $m = 0$ we make the observertation that the $D+1$ dimensional massless scalar propagator is the Fourier transform of the D dimensional scalar propagator with mass p_{D+1}

$$\begin{aligned} G_0^{\lambda+\frac{1}{2}}(\overset{\text{D+1}}{x}) &= \int \frac{dp_{D+1}}{(2\pi)} \int \frac{d^D p}{(2\pi)^D} \frac{e^{-i\overset{\text{D+1}}{p}\cdot\overset{\text{D+1}}{x}}}{(\overset{\text{D}}{p})^2 + p^2_{D+1}} && \text{(A.12)} \\ &= \int \frac{dp_{D+1}}{(2\pi)} e^{-ip_{D+1}\cdot x_{D+1}} G^\lambda_{p_{D+1}}(\overset{\text{D}}{x}) && \text{(A.13)} \end{aligned}$$

and the inverse respectively

$$G^\lambda_{p_{D+1}}(\overset{\text{D}}{x}) = \int dx_{D+1} e^{ip_{D+1}x_{D+1}} G_0^{\lambda+\frac{1}{2}}(\overset{\text{D+1}}{x}) \tag{A.14}$$

We can furthermore express the massive scalar propagator in $D = 4 \Rightarrow \lambda = 1$ via the six dimensional propagator

$$G^1_m(\overset{4}{x}) = \int dx_5 e^{ix_5 m} \int dx_6 G^2_0(\overset{6}{x}) \tag{A.15}$$

We also note the identity

$$\int d^4 z e^{izp} G^1_m(\sqrt{z^2+v^2}) = 4\pi^2 G^1_v(\sqrt{p^2+m^2}) \tag{A.16}$$

Now let us now come back to expression. A.9. We start by performing a Fourier transformation of the first propagator

$$\int d^4z G^1_{m_1}(z-x)G^1_{m_2}(\sqrt{z^2+v^2}) = \int \frac{d^4p}{(2\pi)^4}\frac{e^{ixp}}{p^2+m_1^2}\int d^4z e^{izp}G^1_{m_2}(\sqrt{z^2+v^2}) \quad (A.17)$$

$$= \int \frac{d^4p}{(2\pi)^4}\frac{e^{ixp}}{p^2+m_1^2}4\pi^2 G^1_v(\sqrt{p^2+m^2}) \quad (A.18)$$

where we have used Eq. A.16 in the second step. Now we use Eq. A.15 to write

$$\int \frac{d^4p}{(2\pi)^4}\frac{e^{ixp}}{p^2+m_1^2}4\pi^2 G^1_v(\sqrt{p^2+m_2^2}) = 4\pi^2\int \frac{d^4p}{(2\pi)^4}\frac{e^{ixp}}{p^2+m_1^2}\int dp_5 e^{ip_5 v}\int dp_6 G^2_0(\sqrt{(\overset{6}{p})^2+m_2^2})$$

$$= (2\pi)^4\int \frac{d^6p}{(2\pi)^6}\frac{e^{i\overset{6}{x}\overset{6}{p}}}{p^2+m_1^2}G^2_0(\sqrt{(\overset{6}{p})^2+m_2^2})\Big|_{x_6=0,x_5=v} \quad (A.19)$$

$$= \frac{(2\pi)^4}{4\pi^3}\int \frac{d^6p}{(2\pi)^6}\frac{e^{i\overset{6}{x}\overset{6}{p}}}{p^2+m_1^2}\frac{1}{((\overset{6}{p})^2+m_2^2)^2}\Big|_{x_6=0,x_5=v} \quad (A.20)$$

$$= 4\pi\Big(-\frac{\partial}{\partial m_2^2}\Big)\int_0^1\frac{d\beta}{1-\beta}\int\frac{d^6p}{(2\pi)^6}\frac{e^{i\overset{6}{x}\overset{6}{p}}}{(p^2+\Delta^2)^2}\Big|_{x_6=0,x_5=\frac{v}{\sqrt{1-\beta}}} \quad (A.21)$$

$$= 4\pi\Big(-\frac{\partial}{\partial m_2^2}\Big)\Big(-\frac{\partial}{\partial\Delta^2}\Big)\int_0^1\frac{d\beta}{1-\beta}G^2_\Delta(\overset{6}{x})\Big|_{x_6=0,x_5=\frac{v}{\sqrt{1-\beta}}} \quad (A.22)$$

where $\Delta^2=\beta m_1^2+(1-\beta)m_2^2$. Performing the mass derivatives and simplifying we obtain the result

$$\int d^4z G^1_{m_1}(z-x)G^1_{m_2}(\sqrt{z^2+v^2}) = \frac{1}{2^3\pi^2}\int_0^1 d\beta K_0\Big(\sqrt{(m_1^2\beta+(1-\beta)m_2^2)(x^2+\frac{v^2}{1-\beta})}\Big) \quad (A.23)$$

which can be easily numerically verified.

A.3 Calculating the integrand for the pseudoscalar meson exchange

From the vacuum polarization tensor from Ref. [170] for the π^0 exchange, we have

$$\Pi_{\sigma\mu\mu\lambda}(p,q,k) = \epsilon_{\sigma\mu\alpha\beta}\epsilon_{\mu\lambda\gamma\delta}\,p_\alpha\Big(\frac{\mathscr{F}(-p^2,-k^2)\,\mathscr{F}(-q^2,-(p+k+q)^2)}{(p+k)^2+m_\pi^2}\,k_\beta\,q_\gamma(p+k)_\delta$$
$$+\frac{\mathscr{F}(-p^2,-q^2)\,\mathscr{F}(-k^2,-(p+k+q)^2)}{(p+q)^2+m_\pi^2}\,q_\beta\,k_\gamma(p+q)_\delta\Big). \quad (A.24)$$

Given that the contributing part of $\tilde{H}_{\sigma\lambda}(p)=\delta_{\sigma\lambda}\tilde{h}(p^2)+p_\sigma p_\lambda\ldots$ is proportional to $\delta_{\sigma\lambda}$, we can simplify the Lorentz structure,

$$\delta_{\sigma\lambda}\epsilon_{\sigma\mu\alpha\beta}\epsilon_{\mu\lambda\gamma\delta} = -\epsilon_{\sigma\mu\alpha\beta}\epsilon_{\sigma\mu\gamma\delta} = -2(\delta_{\alpha\gamma}\delta_{\beta\delta}-\delta_{\alpha\delta}\delta_{\beta\gamma}) \quad (A.25)$$

Thus

$$\begin{aligned}\Pi_{\sigma\mu\mu\sigma}(p,q,k) &= -2\Big(\frac{\mathscr{F}(-p^2,-k^2)\,\mathscr{F}(-q^2,-(p+k+q)^2)}{(p+k)^2+m_\pi^2}\\ &\quad ((p\cdot q)(k\cdot(p+k))-(p\cdot(p+k))(k\cdot q))\\ &\quad +\frac{\mathscr{F}(-p^2,-q^2)\,\mathscr{F}(-k^2,-(p+k+q)^2)}{(p+q)^2+m_\pi^2}\\ &\quad ((p\cdot k)(q\cdot(p+q))-(p\cdot(p+q))(q\cdot k))\Big)\\ &= \Pi^{(1)}_{\sigma\mu\mu\sigma}(p,q,k)+\Pi^{(1)}_{\sigma\mu\mu\sigma}(p,k,q), \qquad \text{(A.26)}\\ \Pi^{(1)}_{\sigma\mu\mu\sigma}(p,q,k) &\equiv -2\frac{\mathscr{F}(-p^2,-k^2)\,\mathscr{F}(-q^2,-(p+k+q)^2)}{(p+k)^2+m_\pi^2}\\ &\quad ((p\cdot q)(k\cdot(p+k))-(p\cdot(p+k))(k\cdot q)). \qquad \text{(A.27)}\end{aligned}$$

Clearly, the second term is equal to the first term with k and q interchanged. Therefore, call the first term $\Pi^{(1)}_{\sigma\mu\mu\sigma}(p,q,k)$ and write

$$f(|x|) = -\frac{e^2}{2}2\pi^2|x|^3\frac{1}{(2\pi)^{12}}\int_p \tilde{h}(p^2)\int_{k,q} e^{i(k+q)\cdot x}\Big[\frac{1}{k^2}+\frac{1}{q^2}\Big]_\Lambda \Pi^{(1)}_{\sigma\mu\mu\sigma}(p,q,k). \qquad \text{(A.28)}$$

Set

$$\mathscr{F}(-p^2,-k^2) = \frac{c_\pi}{(p^2+m_V^2)(k^2+m_V^2)} \qquad \text{(A.29)}$$

to the VMD form. Then

$$\Big[\frac{1}{k^2}\Big]_\Lambda\int_q e^{iq\cdot x}\Pi^{(1)}_{\sigma\mu\mu\sigma}(p,q,k) = \Big[\frac{1}{k^2}\Big]_\Lambda\frac{(-2c_\pi)\mathscr{F}(-p^2,-k^2)}{(p+k)^2+m_\pi^2} \qquad \text{(A.30)}$$

$$((p\cdot q)(k\cdot(p+k))-(p\cdot(p+k))(k\cdot q))_{q=-i\nabla_x}\underbrace{\int_q\frac{e^{iq\cdot x}}{(q^2+m_V^2)((p+q+k)^2+m_V^2)}}_{=L(m_V,m_V;p+k,x)}$$

$$\int_k\frac{e^{ik\cdot z}}{k^2+\Lambda^2}\int_q e^{iq\cdot x}\Pi^{(1)}_{\sigma\mu\mu\sigma}(p,q,k) = \frac{(-2c_\pi^2)}{p^2+m_V^2}((p\cdot q)(k\cdot(p+k))-(p\cdot(p+k))(k\cdot q))^{k=-i\nabla_z}_{q=-i\nabla_x}$$
$$\int_k\frac{e^{ik\cdot z}}{[k^2+\Lambda^2][(p+k)^2+m_\pi^2][k^2+m_V^2]}L(m_V,m_V;p+k,x), \qquad \text{(A.31)}$$

$$
\begin{aligned}
&\int_k \frac{e^{ik\cdot z}}{[k^2+\Lambda^2][(p+k)^2+m_\pi^2][k^2+m_V^2]} L(m_V,m_V;p+k,x) \\
&= \frac{1}{\Lambda^2-m_V^2}\int_k \Big(\frac{1}{k^2+M_V^2}-\frac{1}{k^2+\Lambda^2}\Big)\frac{e^{ik\cdot z}}{(p+k)^2+m_\pi^2} L(m_V,m_V;p+k,x) \\
&= \frac{(8\pi^2)^{-1}}{\Lambda^2-m_V^2}\int_k \Big(\frac{1}{k^2+M_V^2}-\frac{1}{k^2+\Lambda^2}\Big)\frac{e^{ik\cdot z}}{(p+k)^2+m_\pi^2} \\
&\int_0^1 d\alpha\, e^{-i\alpha(p+k)\cdot x} K_0\Big(|x|\sqrt{\alpha(1-\alpha)(p+k)^2+m_V^2}\Big) \\
&\overset{k\to k-p}{=} \frac{e^{-ip\cdot z}}{4(\Lambda^2-m_V^2)}\int_0^1 d\alpha \int_0^\infty d|k||k|^3 \frac{1}{k^2+m_\pi^2}\, K_0\Big(|x|\sqrt{\alpha(1-\alpha)k^2+m_V^2}\Big) \\
&\Big\langle e^{ik\cdot(z-\alpha x)}\Big(\frac{1}{(k-p)^2+m_V^2}-\frac{1}{(k-p)^2+\Lambda^2}\Big)\Big\rangle_{\hat k} \\
&= \frac{e^{-ip\cdot z}}{4(\Lambda^2-m_V^2)}\int_0^1 d\alpha \int_0^\infty d|k||k|^3 \frac{1}{k^2+m_\pi^2}\, K_0\Big(|x|\sqrt{\alpha(1-\alpha)k^2+m_V^2}\Big) \\
&\frac{2}{|k||p|}\sum_{n=0}^\infty i^n \frac{J_{n+1}(|k||z-\alpha x|)}{|k||z-\alpha x|}\Big(Z^{(m_V)\ n+1}_{|k|,|p|}-Z^{(\Lambda)\ n+1}_{|k|,|p|}\Big) C_n^{(1)}(\hat p\cdot\widehat{z-\alpha x})
\end{aligned}
\tag{A.32}
$$

Performing the angular integral over $\hat p$:

$$
2\pi^2\Big\langle \int_k \frac{e^{ik\cdot z}}{[k^2+\Lambda^2][(p+k)^2+m_\pi^2][k^2+m_V^2]} L(m_V,m_V;p+k,x)\Big\rangle_{\hat p} \tag{A.33}
$$

$$
\begin{aligned}
&= \frac{2\pi^2}{2|p|(\Lambda^2-m_V^2)}\int_0^1 \frac{d\alpha}{|z-\alpha x|}\int_0^\infty d|k|\,\frac{|k|}{k^2+m_\pi^2}\, K_0\Big(|x|\sqrt{\alpha(1-\alpha)k^2+m_V^2}\Big) \\
&\sum_{n=0}^\infty i^n J_{n+1}(|k||z-\alpha x|)\Big(Z^{(m_V)\ n+1}_{|k|,|p|}-Z^{(\Lambda)\ n+1}_{|k|,|p|}\Big)\Big\langle e^{-ip\cdot w} C_n^{(1)}(\hat p\cdot\widehat{z-\alpha x})\Big\rangle_{\hat p}\Big|_{w=z}
\end{aligned}
\tag{A.34}
$$

$$
\begin{aligned}
&= \frac{2\pi^2}{2|p|(\Lambda^2-m_V^2)}\int_0^1 \frac{d\alpha}{|z-\alpha x|}\int_0^\infty d|k|\,\frac{|k|}{k^2+m_\pi^2}\, K_0\Big(|x|\sqrt{\alpha(1-\alpha)k^2+m_V^2}\Big) \\
&\sum_{n=0}^\infty i^n J_{n+1}(|k||z-\alpha x|)\Big(Z^{(m_V)\ n+1}_{|k|,|p|}-Z^{(\Lambda)\ n+1}_{|k|,|p|}\Big) 2(-i)^n \frac{J_{n+1}(|p||w|)}{|p||w|} C_n^{(1)}(\hat w\cdot\widehat{z-\alpha x})\Big|_{w=z} \\
&= \frac{2\pi^2}{p^2|w|(\Lambda^2-m_V^2)}\int_0^1 \frac{d\alpha}{|z-\alpha x|}\int_0^\infty d|k|\,\frac{|k|}{k^2+m_\pi^2}\, K_0\Big(|x|\sqrt{\alpha(1-\alpha)k^2+m_V^2}\Big) \\
&\sum_{n=0}^\infty \Big(Z^{(m_V)\ n+1}_{|k|,|p|}-Z^{(\Lambda)\ n+1}_{|k|,|p|}\Big) J_{n+1}(|k||z-\alpha x|)\, J_{n+1}(|p||w|)\, C_n^{(1)}(\hat w\cdot\widehat{z-\alpha x})\Big|_{w=z}
\end{aligned}
$$

Thus, finally,

$$
\begin{aligned}
f^{(1)}(|x|) = &-\frac{e^2}{2} 2\pi^2 |x|^3 \frac{1}{(2\pi)^8} \frac{-4\pi^2 c_\pi^2}{\Lambda^2 - m_V^2} ((p\cdot q)(k\cdot(p+k)) - (p\cdot(p+k))(k\cdot q))^{k=-i\nabla_z, p=i\nabla_w}_{q=-i\nabla_x} \\
&\int_0^\infty d|p| \frac{|p|\,\tilde{h}(p^2)}{p^2+m_V^2} \int_0^1 \frac{d\alpha}{|z-\alpha x|} \int_0^\infty d|k| \frac{|k|}{k^2+m_\pi^2} K_0\Big(|x|\sqrt{\alpha(1-\alpha)k^2+m_V^2}\Big) \\
&\frac{1}{|w|} \sum_{n=0}^{\infty} \Big(Z^{(m_V)\ n+1}_{|k|,|p|} - Z^{(\Lambda)\ n+1}_{|k|,|p|} \Big) J_{n+1}(|k||z-\alpha x|)\, J_{n+1}(|p||w|)\, C_n^{(1)}(\hat{w}\cdot\widehat{z-\alpha x}) \Big|_{w=z} \Big|_{z=x}.
\end{aligned}
\tag{A.35}
$$

The notation $\nabla_z \nabla_w(.)\Big|_{w=z}\Big|_{z=x}$ indicates, that first one has to evaluate the derivatives with respect to w and set $w=z$ and afterwards evaluate the derivatives with respect to z and then set $z=x$. The second term of Eq. A.28 can be calculated analogously

$$
\begin{aligned}
f^{(2)}(|x|) = &-\frac{e^2}{2} 2\pi^2 |x|^3 \frac{1}{(2\pi)^8} \frac{-4\pi^2 c_\pi^2}{\Lambda^2 - m_V^2} ((p\cdot q)(k\cdot(p+k)) - (p\cdot(p+k))(k\cdot q))^{k=-i\nabla_z, p=i\nabla_w}_{q=-i\nabla_x} \\
&\int_0^\infty d|p| \frac{|p|\,\tilde{h}(p^2)}{p^2+m_V^2} \int_0^1 \frac{d\alpha}{|z-\alpha x|} \int_0^\infty d|k| \frac{|k|}{k^2+m_\pi^2} \\
&\Big[K_0\Big(|x|\sqrt{\alpha(1-\alpha)k^2+m_V^2}\Big) - \Big(K_0\Big(|x|\sqrt{\alpha(1-\alpha)k^2+\alpha m_V^2+(1-\alpha)\Lambda^2}\Big)\Big] \\
&\frac{1}{|w|} \sum_{n=0}^{\infty} Z^{(m_V)\ n+1}_{|k|,|p|} J_{n+1}(|k||z-\alpha x|)\, J_{n+1}(|p||w|)\, C_n^{(1)}(\hat{w}\cdot\widehat{z-\alpha x}) \Big|_{w=z} \Big|_{z=x}.
\end{aligned}
\tag{A.36}
$$

The final result for the integrand is obtained from the sum

$$
f(|x|) = f^{(1)}(|x|) + f^{(2)}(|x|) \tag{A.37}
$$

A.4 Additional plots

In this section we want to display the integrands of Eq. 10.22 computed on all the ensembles from table 11.1 in addition to the integrand on the ensemble D450 shown in Fig. 11.7

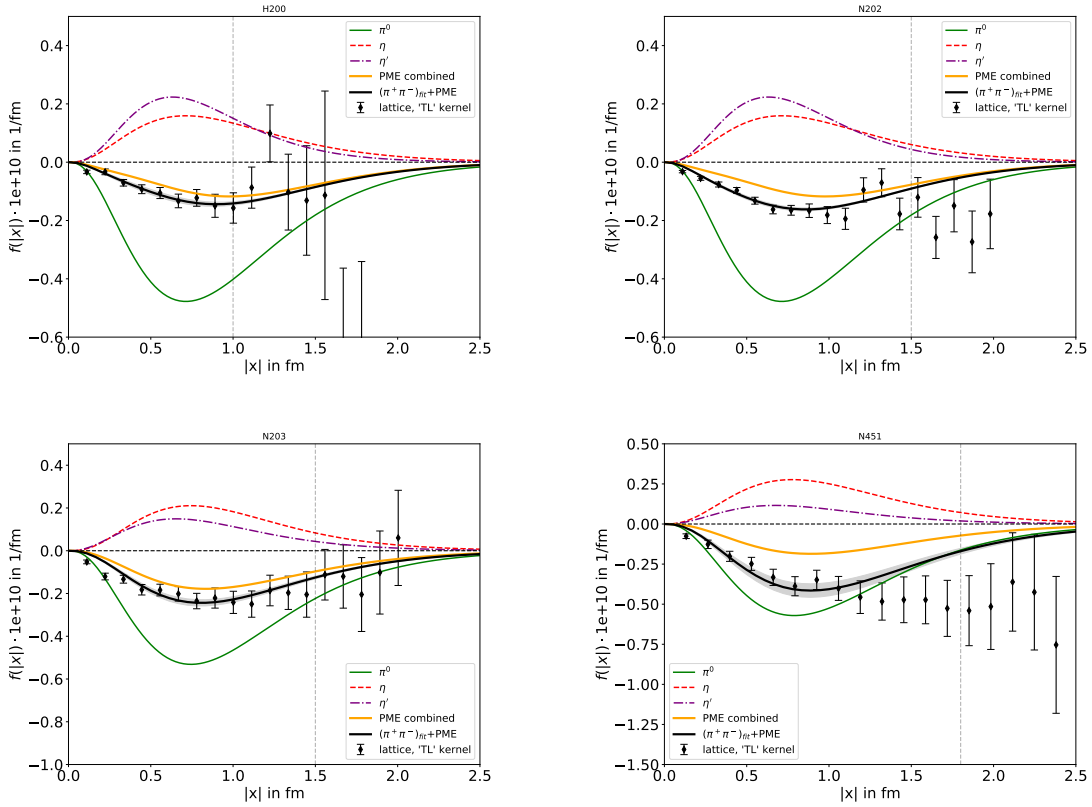

Figure A.1: Plots of the integrand of the $a_\mu^{(2+2)a-ll}$ contribution 10.22 for four of the ensemble in Table 9.1, where the tail is approximated with the method described in 11.5, with the titel of the plot being the ID of the ensemble. Additional descriptions can be found in Fig. 11.7.

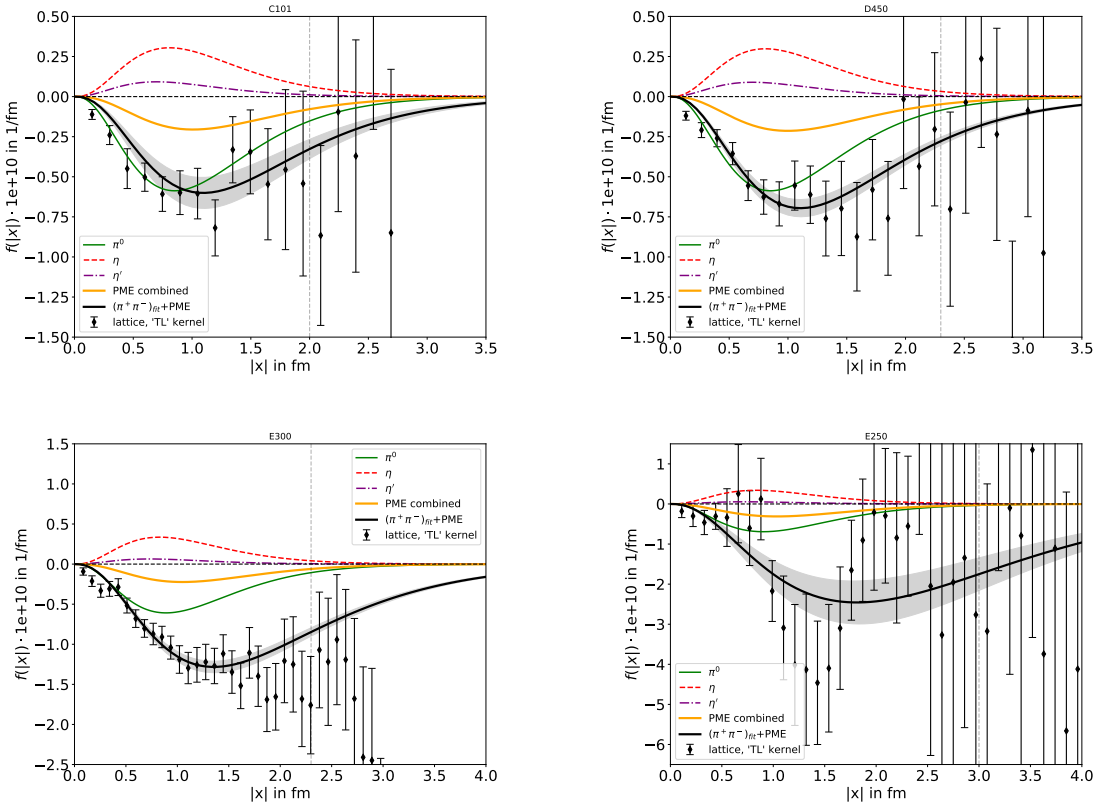

Figure A.2: Plots of the integrand of the $a_\mu^{(2+2)a-ll}$ contribution 10.22 for four of the ensemble in Table 9.1, where the tail is approximated with the method described in 11.5, with the titel of the plot being the ID of the ensemble. Additional descriptions can be found in Fig. 11.7.

A.5 Bibliography

[1] MUON $g-2$ collaboration, *Final Report of the Muon E821 Anomalous Magnetic Moment Measurement at BNL, Phys. Rev.* **D73** (2006) 072003 [hep-ex/0602035].

[2] S. Weinberg, *The Quantum Theory of Fields*. 1995.

[3] D. V. S. Michael E. Peskin, *An introduction to quantum field theory*. 1995.

[4] F. Gross et al., *50 Years of Quantum Chromodynamics, Eur. Phys. J. C* **83** (2023) 1125 [2212.11107].

[5] S. Scherer, *Introduction to chiral perturbation theory, Adv. Nucl. Phys.* **27** (2003) 277 [hep-ph/0210398].

[6] B. Zwiebach, *A First Course in String Theory*. Cambridge University Press, 2 ed., 2009.

[7] ATLAS collaboration, *Observation of a new particle in the search for the Standard Model Higgs boson with the ATLAS detector at the LHC, Phys. Lett. B* **716** (2012) 1 [1207.7214].

[8] SUPER-KAMIOKANDE, KAMLAND collaboration, *Combined Pre-Supernova Alert System with Kamland and Super-Kamiokande*, 2404.09920.

[9] M. Sajjad Athar et al., *Status and perspectives of neutrino physics, Prog. Part. Nucl. Phys.* **124** (2022) 103947 [2111.07586].

[10] NOVA collaboration, *Improved measurement of neutrino oscillation parameters by the NOvA experiment, Phys. Rev. D* **106** (2022) 032004 [2108.08219].

[11] D. Hanneke, S. Fogwell and G. Gabrielse, *New Measurement of the Electron Magnetic Moment and the Fine Structure Constant, Phys. Rev. Lett.* **100** (2008) 120801 [0801.1134].

[12] D. Hanneke, S. F. Hoogerheide and G. Gabrielse, *Cavity Control of a Single-Electron Quantum Cyclotron: Measuring the Electron Magnetic Moment, Phys. Rev. A* **83** (2011) 052122 [1009.4831].

[13] T. Aoyama, M. Hayakawa, T. Kinoshita and M. Nio, *Tenth-Order QED Contribution to the Electron g-2 and an Improved Value of the Fine Structure Constant, Phys. Rev. Lett.* **109** (2012) 111807 [1205.5368].

[14] T. Aoyama, M. Hayakawa, T. Kinoshita and M. Nio, *Tenth-Order Electron Anomalous Magnetic Moment — Contribution of Diagrams without Closed Lepton Loops, Phys. Rev. D* **91** (2015) 033006 [1412.8284].

[15] B. Abi et al., *Measurement of the Positive Muon Anomalous Magnetic Moment to 0.46 ppm, Phys. Rev. Lett.* **126** (2021) 141801 [2104.03281].

[16] MUON G-2 collaboration, *Measurement of the Positive Muon Anomalous Magnetic Moment to 0.20 ppm*, 2308.06230.

[17] T. Aoyama et al., *The anomalous magnetic moment of the muon in the Standard Model, Phys. Rept.* **887** (2020) 1 [2006.04822].

[18] F. Jegerlehner and A. Nyffeler, *The Muon g-2, Phys. Rept.* **477** (2009) 1 [0902.3360].

[19] J. S. Schwinger, *On Quantum electrodynamics and the magnetic moment of the electron, Phys. Rev.* **73** (1948) 416.

[20] F. Jegerlehner, *The Anomalous Magnetic Moment of the Muon, Springer Tracts Mod. Phys.* **274** (2017) 1.

[21] S. Borsanyi et al., *Leading hadronic contribution to the muon magnetic moment from lattice QCD, Nature* **593** (2021) 51 [2002.12347].

[22] A. Boccaletti et al., *High precision calculation of the hadronic vacuum polarisation contribution to the muon anomaly*, 2407.10913.

[23] M. Cè et al., *Window observable for the hadronic vacuum polarization contribution to the muon g-2 from lattice QCD, Phys. Rev. D* **106** (2022) 114502 [2206.06582].

[24] EXTENDED TWISTED MASS collaboration, *Lattice calculation of the short and intermediate time-distance hadronic vacuum polarization contributions to the muon magnetic moment using twisted-mass fermions, Phys. Rev. D* **107** (2023) 074506 [2206.15084].

[25] RBC, UKQCD collaboration, *Update of Euclidean windows of the hadronic vacuum polarization, Phys. Rev. D* **108** (2023) 054507 [2301.08696].

[26] C. Lehner and A. S. Meyer, *Consistency of hadronic vacuum polarization between lattice QCD and the R-ratio, Phys. Rev. D* **101** (2020) 074515 [2003.04177].

[27] CHIQCD collaboration, *Muon g-2 with overlap valence fermions, Phys. Rev. D* **107** (2023) 034513 [2204.01280].

[28] C. Aubin, T. Blum, M. Golterman and S. Peris, *Muon anomalous magnetic moment with staggered fermions: Is the lattice spacing small enough?, Phys. Rev. D* **106** (2022) 054503 [2204.12256].

[29] FERMILAB LATTICE, HPQCD,, MILC collaboration, *Light-quark connected intermediate-window contributions to the muon g-2 hadronic vacuum polarization from lattice QCD, Phys. Rev. D* **107** (2023) 114514 [2301.08274].

[30] M. Davier, Z. Fodor, A. Gerardin, L. Lellouch, B. Malaescu, F. M. Stokes et al., *Hadronic vacuum polarization: Comparing lattice QCD and data-driven results in systematically improvable ways*, *Phys. Rev. D* **109** (2024) 076019 [2308.04221].

[31] P. Stoffer, G. Colangelo and M. Hoferichter, *Puzzles in the hadronic contributions to the muon anomalous magnetic moment*, *JINST* **18** (2023) C10021 [2308.04217].

[32] G. Colangelo, A. X. El-Khadra, M. Hoferichter, A. Keshavarzi, C. Lehner, P. Stoffer et al., *Data-driven evaluations of Euclidean windows to scrutinize hadronic vacuum polarization*, *Phys. Lett. B* **833** (2022) 137313 [2205.12963].

[33] G. Benton, D. Boito, M. Golterman, A. Keshavarzi, K. Maltman and S. Peris, *Data-Driven Determination of the Light-Quark Connected Component of the Intermediate-Window Contribution to the Muon g-2*, *Phys. Rev. Lett.* **131** (2023) 251803 [2306.16808].

[34] M. Davier, A. Hoecker, B. Malaescu and Z. Zhang, *Reevaluation of the hadronic vacuum polarisation contributions to the Standard Model predictions of the muon $g-2$ and $\alpha(m_Z^2)$ using newest hadronic cross-section data*, *Eur. Phys. J.* **C77** (2017) 827 [1706.09436].

[35] A. Keshavarzi, D. Nomura and T. Teubner, *Muon $g-2$ and $\alpha(M_Z^2)$: a new data-based analysis*, *Phys. Rev.* **D97** (2018) 114025 [1802.02995].

[36] G. Colangelo, M. Hoferichter and P. Stoffer, *Two-pion contribution to hadronic vacuum polarization*, *JHEP* **02** (2019) 006 [1810.00007].

[37] M. Hoferichter, B.-L. Hoid and B. Kubis, *Three-pion contribution to hadronic vacuum polarization*, *JHEP* **08** (2019) 137 [1907.01556].

[38] M. Davier, A. Hoecker, B. Malaescu and Z. Zhang, *A new evaluation of the hadronic vacuum polarisation contributions to the muon anomalous magnetic moment and to $\boldsymbol{\alpha(m_Z^2)}$*, *Eur. Phys. J.* **C80** (2020) 241 [1908.00921].

[39] A. Keshavarzi, D. Nomura and T. Teubner, *The $g-2$ of charged leptons, $\alpha(M_Z^2)$ and the hyperfine splitting of muonium*, *Phys. Rev.* **D101** (2020) 014029 [1911.00367].

[40] A. Kurz, T. Liu, P. Marquard and M. Steinhauser, *Hadronic contribution to the muon anomalous magnetic moment to next-to-next-to-leading order*, *Phys. Lett.* **B734** (2014) 144 [1403.6400].

[41] FERMILAB LATTICE, LATTICE-HPQCD, MILC collaboration, *Strong-Isospin-Breaking Correction to the Muon Anomalous Magnetic Moment from Lattice QCD at the Physical Point*, *Phys. Rev. Lett.* **120** (2018) 152001 [1710.11212].

[42] BUDAPEST-MARSEILLE-WUPPERTAL collaboration, *Hadronic vacuum polarization contribution to the anomalous magnetic moments of leptons from first principles*, *Phys. Rev. Lett.* **121** (2018) 022002 [1711.04980].

[43] RBC, UKQCD collaboration, *Calculation of the hadronic vacuum polarization contribution to the muon anomalous magnetic moment, Phys. Rev. Lett.* **121** (2018) 022003 [1801.07224].

[44] ETM collaboration, *Electromagnetic and strong isospin-breaking corrections to the muon $g-2$ from Lattice QCD+QED, Phys. Rev.* **D99** (2019) 114502 [1901.10462].

[45] E. Shintani and Y. Kuramashi, *Study of systematic uncertainties in hadronic vacuum polarization contribution to muon $g-2$ with 2+1 flavor lattice QCD, Phys. Rev.* **D100** (2019) 034517 [1902.00885].

[46] FERMILAB LATTICE, LATTICE-HPQCD, MILC collaboration, *Hadronic-vacuum-polarization contribution to the muon's anomalous magnetic moment from four-flavor lattice QCD, Phys. Rev.* **D101** (2020) 034512 [1902.04223].

[47] A. Gérardin, M. Cè, G. von Hippel, B. Hörz, H. B. Meyer, D. Mohler et al., *The leading hadronic contribution to $(g-2)_\mu$ from lattice QCD with $N_\mathrm{f}=2+1$ flavours of O(a) improved Wilson quarks, Phys. Rev.* **D100** (2019) 014510 [1904.03120].

[48] C. Aubin, T. Blum, C. Tu, M. Golterman, C. Jung and S. Peris, *Light quark vacuum polarization at the physical point and contribution to the muon $g-2$, Phys. Rev.* **D101** (2020) 014503 [1905.09307].

[49] D. Giusti and S. Simula, *Lepton anomalous magnetic moments in Lattice QCD+QED, PoS* **LATTICE2019** (2019) 104 [1910.03874].

[50] K. Melnikov and A. Vainshtein, *Hadronic light-by-light scattering contribution to the muon anomalous magnetic moment revisited, Phys. Rev.* **D70** (2004) 113006 [hep-ph/0312226].

[51] P. Masjuan and P. Sánchez-Puertas, *Pseudoscalar-pole contribution to the $(g_\mu-2)$: a rational approach, Phys. Rev.* **D95** (2017) 054026 [1701.05829].

[52] G. Colangelo, M. Hoferichter, M. Procura and P. Stoffer, *Dispersion relation for hadronic light-by-light scattering: two-pion contributions, JHEP* **04** (2017) 161 [1702.07347].

[53] M. Hoferichter, B.-L. Hoid, B. Kubis, S. Leupold and S. P. Schneider, *Dispersion relation for hadronic light-by-light scattering: pion pole, JHEP* **10** (2018) 141 [1808.04823].

[54] A. Gérardin, H. B. Meyer and A. Nyffeler, *Lattice calculation of the pion transition form factor with $N_f=2+1$ Wilson quarks, Phys. Rev.* **D100** (2019) 034520 [1903.09471].

[55] J. Bijnens, N. Hermansson-Truedsson and A. Rodríguez-Sánchez, *Short-distance constraints for the HLbL contribution to the muon anomalous magnetic moment, Phys. Lett.* **B798** (2019) 134994 [1908.03331].

[56] G. Colangelo, F. Hagelstein, M. Hoferichter, L. Laub and P. Stoffer, *Longitudinal short-distance constraints for the hadronic light-by-light contribution to* $(g-2)_\mu$ *with large-*N_c *Regge models*, *JHEP* **03** (2020) 101 [1910.13432].

[57] V. Pauk and M. Vanderhaeghen, *Single meson contributions to the muon's anomalous magnetic moment*, *Eur. Phys. J.* **C74** (2014) 3008 [1401.0832].

[58] I. Danilkin and M. Vanderhaeghen, *Light-by-light scattering sum rules in light of new data*, *Phys. Rev.* **D95** (2017) 014019 [1611.04646].

[59] M. Knecht, S. Narison, A. Rabemananjara and D. Rabetiarivony, *Scalar meson contributions to* a_μ *from hadronic light-by-light scattering*, *Phys. Lett.* **B787** (2018) 111 [1808.03848].

[60] G. Eichmann, C. S. Fischer and R. Williams, *Kaon-box contribution to the anomalous magnetic moment of the muon*, *Phys. Rev.* **D101** (2020) 054015 [1910.06795].

[61] P. Roig and P. Sánchez-Puertas, *Axial-vector exchange contribution to the hadronic light-by-light piece of the muon anomalous magnetic moment*, *Phys. Rev.* **D101** (2020) 074019 [1910.02881].

[62] G. Colangelo, M. Hoferichter, A. Nyffeler, M. Passera and P. Stoffer, *Remarks on higher-order hadronic corrections to the muon* $g-2$, *Phys. Lett.* **B735** (2014) 90 [1403.7512].

[63] T. Blum, N. Christ, M. Hayakawa, T. Izubuchi, L. Jin, C. Jung et al., *The hadronic light-by-light scattering contribution to the muon anomalous magnetic moment from lattice QCD*, *Phys. Rev. Lett.* **124** (2020) 132002 [1911.08123].

[64] T. Aoyama, T. Kinoshita and M. Nio*Atoms* **7** (2019) .

[65] A. Czarnecki, W. J. Marciano and A. Vainshtein, *Refinements in electroweak contributions to the muon anomalous magnetic moment*, *Phys. Rev. D* **67** (2003) 073006 [hep-ph/0212229].

[66] C. Gnendiger, D. Stöckinger and H. Stöckinger-Kim, *The electroweak contributions to* $(g-2)_\mu$ *after the Higgs boson mass measurement*, *Phys. Rev. D* **88** (2013) 053005 [1306.5546].

[67] M. Srednicki, *Quantum field theory*. 2007.

[68] J. Parrino, *The two-loop vacuum polarization in euclidean coordinate space*, 2019.

[69] Z. Hong-Hao, F. Kai-Xi, Q. Si-Wei, Z. An and L. Xue-Song, *On analytic formulas of feynman propagators in position space*, *Chinese Physics C* **34** (2010) 1576–1582.

[70] K. Osterwalder and R. Schrader, *Axioms for Euclidean Green's functions*, *Communications in Mathematical Physics* **31** (1973) 83 .

[71] V. Shtabovenko, R. Mertig and F. Orellana, *FeynCalc 10: Do multiloop integrals dream of computer codes?*, 2312.14089.

[72] K. G. Chetyrkin, A. L. Kataev and F. V. Tkachov, *New Approach to Evaluation of Multiloop Feynman Integrals: The Gegenbauer Polynomial x Space Technique*, *Nucl. Phys. B* **174** (1980) 345.

[73] A. Kotikov, *The gegenbauer polynomial technique: the evaluation of a class of feynman diagrams*, *Physics Letters B* **375** (1996) 240.

[74] A. V. Kotikov, *The Gegenbauer polynomial technique: The Evaluation of complicated Feynman integrals*, in *15th International Workshop on High-Energy Physics and Quantum Field Theory (QFTHEP 2000)*, pp. 211–217, 7, 2000, hep-ph/0102177.

[75] S. Groote, J. G. Korner and A. A. Pivovarov, *On the evaluation of a certain class of Feynman diagrams in x-space: Sunrise-type topologies at any loop order*, *Annals Phys.* **322** (2007) 2374 [hep-ph/0506286].

[76] S. Groote and J. G. Körner, *Coordinate space calculation of two- and three-loop sunrise-type diagrams, elliptic functions and truncated Bessel integral identities*, *Nucl. Phys. B* **938** (2019) 416 [1804.10570].

[77] P. Skands, *Introduction to QCD*, in *Theoretical Advanced Study Institute in Elementary Particle Physics: Searching for New Physics at Small and Large Scales*, pp. 341–420, 2013, 1207.2389, DOI.

[78] C. B. L. Christof Gattringer, *Quantum Chromodynamics on the Lattice*. 2010.

[79] M. L. Mangano, *Introduction to QCD*, in *1998 European School of High-Energy Physics*, pp. 53–97, 1998.

[80] A. Risch, *Isospin breaking effects in hadronic matrix elements on the lattice*, Ph.D. thesis, Mainz, 2021. http://doi.org/10.25358/openscience-6314.

[81] M. T. S. J. Pérez, *The hadronic contribution to the running of the electromagnetic coupling and the electroweak mixing angle*, Ph.D. thesis, Mainz, 2022. http://doi.org/10.25358/openscience-7115.

[82] E.-H. Chao, *Hadronic light-by-light scattering contribution to the anomalous magnetic moment of the muon from Lattice Quantum Chromodynamics*, Ph.D. thesis, Mainz, 2022. http://doi.org/10.25358/openscience-6720.

[83] P. Etingof, *Lie groups and Lie algebras*, 2201.09397.

[84] H. Sazdjian, *Introduction to chiral symmetry in QCD*, *EPJ Web Conf.* **137** (2017) 02001 [1612.04078].

[85] E. Laenen, *QCD*, in *2014 European School of High-Energy Physics*, pp. 1–58, 2016, 1708.00770, DOI.

[86] A. Deur, S. J. Brodsky and G. F. de Teramond, *The QCD Running Coupling*, *Nucl. Phys.* **90** (2016) 1 [1604.08082].

[87] D. J. Gross and F. Wilczek, *Ultraviolet behavior of non-abelian gauge theories*, *Phys. Rev. Lett.* **30** (1973) 1343.

[88] W. E. Caswell, *Asymptotic behavior of non-abelian gauge theories to two-loop order*, *Phys. Rev. Lett.* **33** (1974) 244.

[89] S. A. Larin and J. A. M. Vermaseren, *The Three loop QCD Beta function and anomalous dimensions*, *Phys. Lett. B* **303** (1993) 334 [hep-ph/9302208].

[90] S. N. et al. (Particle Data Group).

[91] W. Hollik, *Electroweak theory*, *J. Phys. Conf. Ser.* **53** (2006) 7.

[92] J. Gasser and H. Leutwyler, *Chiral perturbation theory to one loop*, *Annals of Physics* **158** (1984) 142.

[93] J. Gasser and H. Leutwyler, *Chiral perturbation theory: Expansions in the mass of the strange quark*, *Nuclear Physics B* **250** (1985) 465.

[94] M. Rho, "The "Folk Theorem" on Effective Field Theory: How Does It Fare in Nuclear Physics?." Sept., 2017.

[95] S. Scherer and M. R. Schindler, *Chiral perturbation theory*, 11, 2022, 2211.17031.

[96] F. Jegerlehner and R. Szafron, $\rho^0 - \gamma$ *mixing in the neutral channel pion form factor* F_π^e *and its role in comparing* e^+e^- *with* τ *spectral functions*, *Eur. Phys. J. C* **71** (2011) 1632 [1101.2872].

[97] E.-H. Chao, H. B. Meyer and J. Parrino, *Coordinate-space calculation of the window observable for the hadronic vacuum polarization contribution to (g-2)*μ, *Phys. Rev. D* **107** (2023) 054505 [2211.15581].

[98] S. Weinberg, *Phenomenological lagrangians*, *Physica A: Statistical Mechanics and its Applications* **96** (1979) 327.

[99] P. Bickert and S. Scherer, *Two-photon decays and transition form factors of* π^0, η, *and* η' *in large-*N_c *chiral perturbation theory*, *Phys. Rev. D* **102** (2020) 074019 [2005.08550].

[100] J. Wess and B. Zumino, *Consequences of anomalous ward identities*, *Physics Letters B* **37** (1971) 95.

[101] E. Witten, *Global aspects of current algebra*, *Nuclear Physics B* **223** (1983) 422.

[102] E.-H. Chao, A. Gérardin, J. R. Green, R. J. Hudspith and H. B. Meyer, *Hadronic light-by-light contribution to* $(g-2)_\mu$ *from lattice QCD with SU(3) flavor symmetry*, *Eur. Phys. J. C* **80** (2020) 869 [2006.16224].

[103] W. Detmold, B. C. Tiburzi and A. Walker-Loud, *Electromagnetic and spin polarisabilities in lattice QCD*, *Phys. Rev. D* **73** (2006) 114505 [hep-lat/0603026].

[104] G. 't Hooft, *Symmetry breaking through bell-jackiw anomalies*, *Phys. Rev. Lett.* **37** (1976) 8.

[105] E. Witten, *Current algebra theorems for the u(1) "goldstone boson"*, *Nuclear Physics B* **156** (1979) 269.

[106] G. Veneziano, *U(1) without instantons*, *Nuclear Physics B* **159** (1979) 213.

[107] P. Bickert, P. Masjuan and S. Scherer, η-η' *Mixing in Large-*N_c *Chiral Perturbation Theory*, *Phys. Rev. D* **95** (2017) 054023 [1612.05473].

[108] J. J. Sakurai, *Theory of strong interactions*, *Annals Phys.* **11** (1960) 1.

[109] PARTICLE DATA GROUP collaboration, *Review of Particle Physics*, *PTEP* **2022** (2022) 083C01.

[110] M. Bruno, T. Korzec and S. Schaefer, *Setting the scale for the CLS* $2+1$ *flavor ensembles*, *Phys. Rev. D* **95** (2017) 074504 [1608.08900].

[111] J. Smit, *Introduction to quantum fields on a lattice: A robust mate*, *Cambridge Lect. Notes Phys.* **15** (2002) 1.

[112] P. Knechtli, Günther, *Lattice Quantum Chromodynamics*. 2017.

[113] M. Luscher and S. Schaefer, *Lattice QCD without topology barriers*, *JHEP* **07** (2011) 036 [1105.4749].

[114] K. Symanzik, *Continuum limit and improved action in lattice theories: (i). principles and 4 theory*, *Nuclear Physics B* **226** (1983) 187.

[115] K. Symanzik, *Continuum limit and improved action in lattice theories: (ii). o(n) non-linear sigma model in perturbation theory*, *Nuclear Physics B* **226** (1983) 205.

[116] M. Luscher and P. Weisz, *On-shell improved lattice gauge theories*, *Commun. Math. Phys.* **98** (1985) 433.

[117] M. Lüscher and P. Weisz, *Computation of the action for on-shell improved lattice gauge theories at weak coupling*, *Physics Letters B* **158** (1985) 250.

[118] H. Nielsen and M. Ninomiya, *Absence of neutrinos on a lattice: (i). proof by homotopy theory*, *Nuclear Physics B* **185** (1981) 20.

[119] H. Nielsen and M. Ninomiya, *A no-go theorem for regularizing chiral fermions, Physics Letters B* **105** (1981) 219.

[120] M. Luscher, *Exact chiral symmetry on the lattice and the Ginsparg-Wilson relation, Phys. Lett. B* **428** (1998) 342 [hep-lat/9802011].

[121] K. G. Wilson, *Confinement of quarks, Phys. Rev. D* **10** (1974) 2445.

[122] B. Sheikholeslami and R. Wohlert, *Improved continuum limit lattice action for qcd with wilson fermions, Nuclear Physics B* **259** (1985) 572.

[123] J. Bulava and S. Schaefer, *Improvement of $N_f = 3$ lattice QCD with Wilson fermions and tree-level improved gauge action, Nucl. Phys. B* **874** (2013) 188 [1304.7093].

[124] A. S. Kronfeld, *Lattice Gauge Theory with Staggered Fermions: How, Where, and Why (Not), PoS* **LATTICE2007** (2007) 016 [0711.0699].

[125] M. Golterman, *Staggered fermions*, 2406.02906.

[126] R. C. Brower, H. Neff and K. Orginos, *The Möbius domain wall fermion algorithm, Comput. Phys. Commun.* **220** (2017) 1 [1206.5214].

[127] K. Jansen, *Domain wall fermions and chiral gauge theories, Physics Reports* **273** (1996) 1.

[128] R. Frezzotti, P. A. Grassi, S. Sint and P. Weisz, *A Local formulation of lattice QCD without unphysical fermion zero modes, Nucl. Phys. B Proc. Suppl.* **83** (2000) 941 [hep-lat/9909003].

[129] C. Alexandrou, S. Bacchio, P. Charalambous, P. Dimopoulos, J. Finkenrath, R. Frezzotti et al., *Simulating twisted mass fermions at physical light, strange, and charm quark masses, Phys. Rev. D* **98** (2018) 054518.

[130] A. Shindler, *Twisted mass lattice QCD, Phys. Rept.* **461** (2008) 37 [0707.4093].

[131] C. Gattringer and K. Langfeld, *Approaches to the sign problem in lattice field theory, Int. J. Mod. Phys. A* **31** (2016) 1643007 [1603.09517].

[132] C. Gattringer and K. Langfeld, *Approaches to the sign problem in lattice field theory, International Journal of Modern Physics A* **31** (2016) .

[133] K. Nagata, *Finite-density lattice qcd and sign problem: Current status and open problems, Progress in Particle and Nuclear Physics* **127** (2022) 103991.

[134] S. Duane, A. Kennedy, B. J. Pendleton and D. Roweth, *Hybrid monte carlo, Physics Letters B* **195** (1987) 216.

[135] D. Weingarten and D. Petcher, *Monte carlo integration for lattice gauge theories with fermions*, *Physics Letters B* **99** (1981) 333.

[136] I. Omelyan, I. Mryglod and R. Folk, *Symplectic analytically integrable decomposition algorithms: classification, derivation, and application to molecular dynamics, quantum and celestial mechanics simulations*, *Computer Physics Communications* **151** (2003) 272.

[137] M. Bruno et al., *Simulation of QCD with $N_f = 2 + 1$ flavors of non-perturbatively improved Wilson fermions*, *JHEP* **02** (2015) 043 [1411.3982].

[138] M. Luscher and F. Palombi, *Fluctuations and reweighting of the quark determinant on large lattices*, *PoS* **LATTICE2008** (2008) 049 [0810.0946].

[139] M. Lüscher, *Properties and uses of the Wilson flow in lattice QCD*, *JHEP* **08** (2010) 071 [1006.4518].

[140] ALPHA collaboration, *On the N_f-dependence of gluonic observables*, *PoS* **LATTICE2013** (2014) 321 [1311.5585].

[141] RQCD collaboration, *Scale setting and the light baryon spectrum in $N_f = 2 + 1$ QCD with Wilson fermions*, *JHEP* **05** (2023) 035 [2211.03744].

[142] M. Luscher, *Computational Strategies in Lattice QCD*, in *Les Houches Summer School: Session 93: Modern perspectives in lattice QCD: Quantum field theory and high performance computing*, pp. 331–399, 2, 2010, 1002.4232.

[143] H. Bozdogan, *Model selection and akaike's information criterion (aic): The general theory and its analytical extensions*, *Psychometrika* **52** (1987) 345.

[144] K. Kimura and H. Waki, *Minimization of Akaike's Information Criterion in Linear Regression Analysis via Mixed Integer Nonlinear Program*, *arXiv e-prints* (2016) arXiv:1606.05030 [1606.05030].

[145] CMD-3 collaboration, *Measurement of the e+e-→π+π- cross section from threshold to 1.2 GeV with the CMD-3 detector*, *Phys. Rev. D* **109** (2024) 112002 [2302.08834].

[146] D. Bernecker and H. B. Meyer, *Vector Correlators in Lattice QCD: Methods and applications*, *Eur.Phys.J.* **A47** (2011) 148 [1107.4388].

[147] M. Della Morte, A. Francis, V. Gülpers, G. Herdoíza, G. von Hippel, H. Horch et al., *The hadronic vacuum polarization contribution to the muon $g-2$ from lattice QCD*, *JHEP* **10** (2017) 020 [1705.01775].

[148] RBC, UKQCD collaboration, *Calculation of the hadronic vacuum polarization contribution to the muon anomalous magnetic moment*, *Phys. Rev. Lett.* **121** (2018) 022003 [1801.07224].

[149] H. B. Meyer, *Lorentz-covariant coordinate-space representation of the leading hadronic contribution to the anomalous magnetic moment of the muon*, *Eur. Phys. J. C* **77** (2017) 616 [1706.01139].

[150] M. Bruno, M. Cè, A. Francis, P. Fritzsch, J. R. Green, M. T. Hansen et al., *Exploiting stochastic locality in lattice QCD: hadronic observables and their uncertainties*, *JHEP* **11** (2023) 167 [2307.15674].

[151] M. Cè, M. Bruno, J. Bulava, A. Francis, P. Fritzsch, J. R. Green et al., *Hadronic observables from master-field simulations*, *PoS* **LATTICE2022** (2023) 052 [2301.05156].

[152] M. Cè, A. Gérardin, K. Ottnad and H. B. Meyer, *The leading hadronic contribution to the running of the Weinberg angle using covariant coordinate-space methods*, *PoS* **LATTICE2018** (2018) 137 [1811.08669].

[153] M. Cè, A. Gérardin, G. von Hippel, H. B. Meyer, K. Miura, K. Ottnad et al., *The hadronic running of the electromagnetic coupling and the electroweak mixing angle from lattice QCD*, *JHEP* **08** (2022) 220 [2203.08676].

[154] H. B. Meyer, *Lattice QCD and the Timelike Pion Form Factor*, *Phys. Rev. Lett.* **107** (2011) 072002 [1105.1892].

[155] A. Francis, B. Jäger, H. B. Meyer and H. Wittig, *A new representation of the Adler function for lattice QCD*, *Phys.Rev.* **D88** (2013) 054502 [1306.2532].

[156] M. T. Hansen and A. Patella, *Finite-volume effects in* $(g-2)_\mu^{HVP,LO}$, *Phys. Rev. Lett.* **123** (2019) 172001 [1904.10010].

[157] M. T. Hansen and A. Patella, *Finite-volume and thermal effects in the leading-HVP contribution to muonic* $(g-2)$, *JHEP* **10** (2020) 029 [2004.03935].

[158] T. Bhattacharya, R. Gupta, W. Lee, S. R. Sharpe and J. M. S. Wu, *Improved bilinears in lattice QCD with non-degenerate quarks*, *Phys. Rev. D* **73** (2006) 034504 [hep-lat/0511014].

[159] A. Gerardin, T. Harris and H. B. Meyer, *Nonperturbative renormalization and* $O(a)$*-improvement of the nonsinglet vector current with* $N_f = 2+1$ *Wilson fermions and tree-level Symanzik improved gauge action*, *Phys. Rev. D* **99** (2019) 014519 [1811.08209].

[160] M. D. Hirschhorn, *Partial fractions and four classical theorems of number theory*, *The American Mathematical Monthly* **107** (2000) 260 [https://doi.org/10.1080/00029890.2000.12005191].

[161] P. Fritzsch, J. Bulava, M. Cè, A. Francis, M. Lüscher and A. Rago, *Master-field simulations of QCD*, *PoS* **LATTICE2021** (2022) 465 [2111.11544].

[162] R. Kitano and H. Takaura, *Quantum electrodynamics on the lattice and numerical perturbative computation of g − 2, PTEP* **2023** (2023) 103B02 [2210.05569].

[163] M. A. Clark, M. Della Morte, Z. Hall, B. Hörz, A. Nicholson, A. Shindler et al., *QED with massive photons for precision physics: zero modes and first result for the hadron spectrum, PoS* **LATTICE2021** (2022) 281 [2201.03251].

[164] X. Feng, L. Jin and M. J. Riberdy, *Lattice QCD Calculation of the Pion Mass Splitting, Phys. Rev. Lett.* **128** (2022) 052003 [2108.05311].

[165] V. Biloshytskyi, E.-H. Chao, A. Gérardin, J. R. Green, F. Hagelstein, H. B. Meyer et al., *Forward light-by-light scattering and electromagnetic correction to hadronic vacuum polarization, JHEP* **03** (2023) 194 [2209.02149].

[166] E.-H. Chao, R. J. Hudspith, A. Gérardin, J. R. Green and H. B. Meyer, *The charm-quark contribution to light-by-light scattering in the muon* $(g-2)$ *from lattice QCD, Eur. Phys. J. C* **82** (2022) 664 [2204.08844].

[167] E.-H. Chao, H. B. Meyer and J. Parrino, *Coordinate-space calculation of QED corrections to the hadronic vacuum polarization contribution to* $(g-2)_\mu$, *PoS* **LATTICE2023** (2024) 256 [2310.20556].

[168] E.-H. Chao, R. J. Hudspith, A. Gérardin, J. R. Green, H. B. Meyer and K. Ottnad, *Hadronic light-by-light contribution to* $(g-2)_\mu$ *from lattice QCD: a complete calculation, Eur. Phys. J. C* **81** (2021) 651 [2104.02632].

[169] B. Strassberger et al., *Scale setting for CLS 2+1 simulations, PoS* **LATTICE2021** (2022) 135 [2112.06696].

[170] M. Knecht and A. Nyffeler, *Hadronic light by light corrections to the muon g-2: The Pion pole contribution, Phys. Rev. D* **65** (2002) 073034 [hep-ph/0111058].

[171] RQCD collaboration, *Masses and decay constants of the η and η' mesons from lattice QCD, JHEP* **08** (2021) 137 [2106.05398].

[172] A. Nyffeler, *Precision of a data-driven estimate of hadronic light-by-light scattering in the muon* $g-2$*: Pseudoscalar-pole contribution, Phys. Rev. D* **94** (2016) 053006 [1602.03398].

[173] M. Lüscher and S. Schaefer, *Lattice QCD with open boundary conditions and twisted-mass reweighting, Comput. Phys. Commun.* **184** (2013) 519 [1206.2809].

[174] SciDAC, LHPC, UKQCD collaboration, *The Chroma software system for lattice QCD, Nucl. Phys. B (Proc. Suppl.)* **140** (2005) 832 [hep-lat/0409003].